

Fall 2000

Determination of Anisotropy of Granular Materials and Its Relation to Liquefaction Resistance Under Cyclic Loading

Omer Faruk Capar
Old Dominion University

Follow this and additional works at: https://digitalcommons.odu.edu/cee_etds

 Part of the [Civil Engineering Commons](#)

Recommended Citation

Capar, Omer F. "Determination of Anisotropy of Granular Materials and Its Relation to Liquefaction Resistance Under Cyclic Loading" (2000). Doctor of Philosophy (PhD), dissertation, Civil/Environmental Engineering, Old Dominion University, DOI: 10.25777/n63s-w233
https://digitalcommons.odu.edu/cee_etds/38

This Dissertation is brought to you for free and open access by the Civil & Environmental Engineering at ODU Digital Commons. It has been accepted for inclusion in Civil & Environmental Engineering Theses & Dissertations by an authorized administrator of ODU Digital Commons. For more information, please contact digitalcommons@odu.edu.

**DETERMINATION OF ANISOTROPY OF GRANULAR MATERIALS AND ITS
RELATION TO LIQUEFACTION RESISTANCE UNDER CYCLIC LOADING**

by

Omer Faruk Capar
B.S. Civil Engineering, Cukurova University, Adana, Turkey, 1989
M.S. Civil Engineering, Cukurova University, Adana, Turkey, 1992

A Dissertation Submitted to the Faculty of Old Dominion University in Partial
Fulfillment of the Requirement for the Degree of

DOCTOR OF PHILOSOPHY

CIVIL ENGINEERING

OLD DOMINION UNIVERSITY
December 2000

Approved by:

Isao Ishibashi (Director)

Zia Razzaq (Member)

Ramamurthy Prabhakaran (Member)

ABSTRACT

DETERMINATION OF ANISOTROPY OF GRANULAR MATERIALS AND ITS RELATION TO LIQUEFACTION RESISTANCE UNDER CYCLIC LOADING

Omer Faruk Capar
Old Dominion University, December 2000
Director: Dr. Isao Ishibashi

Granular materials such as sand deposits have anisotropic characteristics due to the gravitational forces during depositional process and various stress histories. These anisotropic characteristics make evaluation of liquefaction resistance of soil very complex. Since obtaining undisturbed soil specimens for laboratory tests from discrete elements like sandy soils is very laborious, the soil specimens are reconstituted in laboratory with regards to the in-situ density of soil. Reconstituting the soil changes the soil fabric or anisotropic characteristics in comparison with field conditions. Many researchers have pointed out that liquefaction resistance is highly influenced by differences in the structure of the soil (or soil fabric) produced by different sample preparation techniques. Liquefaction resistance could vary with different soil fabrics even for the same soil with a specific density.

The objective of this research is to investigate the anisotropy of granular materials and to establish its relation to the liquefaction resistance. Anisotropy can be expressed by the directional mechanical properties of the soil. In order to investigate the effects of the anisotropy on the liquefaction resistance in a quantitative way, uniform medium dense sand specimens were prepared using three different techniques to create the different initial soil fabrics. Undrained cyclic triaxial tests were performed to determine the liquefaction resistance of each soil specimen. A relationship between liquefaction

resistance and the number of cyclic loads was established for three types of specimens with different soil fabrics. The results clearly demonstrate that the preparation methods significantly affect the liquefaction behavior.

After preparation of the soil specimens, vertical and horizontal compression (P) wave velocity and vertical shear (S) wave velocity were measured, and the soil fabric effects on elastic properties of the soil were investigated under dry and saturated conditions. P-wave velocities in both directions showed small difference for all sample preparation techniques except for air pluviated (AP) specimens. AP specimens reflected cross anisotropy. However, S-wave velocities turned out to be very affected by soil-fabric. S-wave promised to distinguish nature of inherent anisotropy with regarding to liquefaction resistance.

Anisotropic elastic constants of soil specimens were recovered quantitatively from elastic wave measurements and consolidation test data. Induced anisotropy due to different preparation techniques was identified by recovered anisotropic constants. The recovered elastic constants were found sufficient to express anisotropy of specimens. Accordingly, by using directional variation of elastic constants, three anisotropy indices were created. The anisotropy indices were then used to create pseudo cyclic stress ratio. Liquefaction cyclic stress ratios of the specimens were normalized with corresponding pseudo cyclic stress ratios. It was observed that the anisotropy effects on liquefaction resistance can be eliminated with those anisotropy indices. It was found that under cyclic loading, anisotropy indices obtained from experimental S-wave measurements were able to express anisotropy of granular materials and a relation to the liquefaction resistance.

Dedicated to my parents and family

ACKNOWLEDGEMENTS

There are many people whom I would like to thank for helping me complete this study. Without their support, aid and friendship, it would have been impossible to complete this research.

I express my sincere thanks to my advisor, Dr. Isao Ishibashi for his endless time and efforts to help me during this Ph.D. program. He provided me with the essential feedback that was invaluable in completing this research. It has been a great experience working with him.

I would like to thank my committee members, Dr. Zia Razzaq, and Dr. Ramamurthy Prabhakaran for their priceless advice and suggestions during the course of this project.

Special thanks goes to Dr. Jaewan Yoon for his infinite knowledge and generous help with computers and software when I needed them most.

I would like to thank Mr. Tom Galloway in the electrical shop for helping in the development of piezoelectric transducers and the data acquisition system for the cyclic triaxial test. In addition, I would like to thank the entire crew in the engineering machine shop for help in modifying the dynamic triaxial test device.

I received financial support from Zonguldak Karaelmas University via a fellowship. This support is greatly appreciated.

I would like to thank the following fellow graduate students and co-workers for their friendship and support: Erdem Altan, Nurettin Altundeger, Salim Balik, Ilhan and

Tugba Bayraktar, Mehmet Bektasoglu, Hilmi and Meltem Coskun, Onur Coskun, Mustafa Dogan, Mehmet Ekici, Selim Ergen, Supad Gosh, Bulent Imamoglu, Omer Kabil, Nilgun Kaya, Ceyhan Kilic, Artun Kockug, Saha Mrinal, Huseyin Ozkan, Zafer Pirim, Yasar Sari, Ibrahim Sahin, Sethapong Sethabouppha, Murat and Ceyda Utku, Yalcin Yamak and Huseyin Yerlikaya.

I am grateful for the love and support of my parents, Mahmut and Sema Capar, and my brothers, Murat Samil and Oguz Capar.

Finally, I would like to thank my wife, Jacqueline Ann, for being my partner, editor and best friend.

TABLE OF CONTENTS

LIST OF TABLES	x
LIST OF FIGURES	xii
NOMENCLATURE	xvii
CHAPTER 1	INTRODUCTION
1.1 Statement of Problem	1
1.2 Scope of Research.....	2
1.3 Outline of Dissertation.....	2
CHAPTER 2	LITERATURE REVIEW
2.1 Introduction.....	4
2.2 Definition of Liquefaction	4
2.3 Methods of Evaluating Liquefaction Resistance of Sands	5
2.3.1 Cyclic Stress Ratio	5
2.3.2 In-situ Evaluation Methods	8
2.3.3 Laboratory Cyclic Loading Tests	11
2.4 Anisotropy of Granular Materials	11
2.5 Elastic Wave Speed Measurement	21
2.6 Liquefaction and Wave Speed Measurements	23
2.6.1 Directional Wave Velocities and Anisotropy.....	23
2.6.2 Evaluation of Liquefaction Resistance with Shear Wave Velocity	29
CHAPTER 3	LABORATORY EXPERIMENTS
3.1 Introduction.....	36
3.2 Properties of Material	37
3.2.1 Grain Size Distributions	37
3.2.2 Index Properties	38
3.2.3 Relative Density	39
3.3 Cyclic Triaxial Test Setup and Procedure	43
3.3.1 Dynamic Triaxial Test Setup	43
3.3.2 Loading System.....	46
3.3.3 Variables Tested.....	47
3.3.4 Data Acquisition System.....	48
3.4 Wave Generation and Measuring System.....	48
3.4.1 Compression and Shear Wave Transducers Design	48
3.4.1.1 Compressional Wave Transducer Design	51
3.4.1.2 Shear Wave Transducer Design	52
3.4.2 Electrical Connections	55
3.4.3 Frequency of Elastic Waves.....	60
3.4.4 Corrections on Wave Measurements	67

3.4.4.1	Correction on Delay Time	67
3.4.4.2	Corrections on Shear Wave Arrival Time	69
3.4.4.3	Corrections on Shear Wave Travelling Distance	70
3.5	Determination of Elastic Constants	72
3.6	Saturation Effects on Laboratory Testing and Saturation Procedure	79
3.6.1	Saturation Effects on Elastic Wave Propagation	79
3.6.2	Pore Water Pressure Parameter B	83
3.6.3	Numerical Example of Saturation Effects on Elastic Wave Propagation	84
3.6.4	Saturation Effects on Cyclic Stress Ratio	87
3.6.5	Saturation Procedure	90
3.7	Methods of Sample Preparation.....	92
3.7.1	Air Pluviation.....	94
3.7.2	Moist Tamping.....	95
3.7.3	Moist Vibration.....	96
3.8	Summary of Laboratory Testing Programs	97
3.8.1	Preparation of Soil Specimens	97
3.8.2	Saturation of Soil Specimens	97
3.8.3	Cyclic Triaxial Testing Program.....	97
3.8.4	Measurement of Elastic Wave Velocities	98
3.8.4.1	Elastic Wave Velocities at Dry Condition (S=0%)	98
3.8.4.2	Elastic Wave Velocities at Full Water Saturation(S=100%).....	98
3.8.4.3	Elastic Wave Velocities under Different Effective Pressures	98
3.8.4.4	Measurement of Volume Change Under Isotropic Stresses.....	98

CHAPTER 4 EXPERIMENTAL RESULTS AND ANALYSIS

4.1	Introduction.....	100
4.2	Liquefaction Resistance of Specimens	101
4.3	Elastic Wave Measurements.....	104
4.3.1	Effects of Initial Water Content	105
4.3.2	Effect of Saturation Degree (S).....	106
4.3.3	Effect of Effective Confining Pressure	109
4.4	Consolidation Test.....	115
4.5	Analysis of Results	117
4.5.1	Elastic Wave Velocities	117
4.5.2	Recovery of Elastic Constants	118
4.5.2.1	Isotropic Material Constants.....	118
4.5.2.2	Transversely Isotropic Material Constants.....	123
4.5.3	Determination of Inherent Anisotropy	134
4.5.4	Relationship between Anisotropy Index and Liquefaction Resistance	135
4.5.5	Relationship between Liquefaction Resistance and Shear Wave Velocity	139
4.5.6	Examination of Liquefaction Resistance by Anisotropy Index Parameters.....	145

CHAPTER 5 SUMMARY AND CONCLUSIONS

5.1 Summary of Research.....	148
5.2 Conclusions.....	149
5.3 Recommendations for Future Work	152
REFERENCES	153
APPENDICIES	159
A. Cyclic Triaxial Test Records.....	163
B. Frequency Effect on Elastic Waves.....	169
C. Saturation Effect on Elastic Wave Velocities	198
D. Elastic Wave Measurements under Different Effective Confining Pressure at Dry Condition	207
E. Elastic Wave Measurements under Different Effective Confining Pressure at Saturated Condition	225
VITA.....	238

LIST OF TABLES

Table 2.1 Correlation between magnitude of an earthquake and number of cyclic stresses (Seed et al., 1985).....	7
Table 2.2 Comparison of undisturbed and remolded strength (Mulilis et al., 1977).....	17
Table 2.3 Laboratory measurements of cyclic stress ratio required to cause liquefaction with electrical parameter $A^3 / \bar{F} \cdot \bar{f}_m$ (Arulmoli and Arulanandan, 1994).....	20
Table 2.4 Average adjusted wave velocities in Schertman's experiment (1977).....	24
Table 2.5 Constants in proposed empirical equations on small strain shear modulus: $G_0 = A F(e) (\sigma_0')^n$ (Ishihara, 1996).....	31
Table 3.1 Material characteristics of Virginia Beach sand.....	38
Table 3.2 Geometric and index parameters of AP specimens.....	41
Table 3.3 Geometric and index parameters of MT and MV specimens.....	41
Table 3.4 Wave path configurations.....	76
Table 3.5 Wave velocity and B values computed from typical values of compressibility, porosity, and saturation degree for loose sand.....	86
Table 3.6 An example of the saturation procedure.....	92
Table 4.1 Initial conditions of soil specimens prior to the cyclic loading.....	101
Table 4.2 Cyclic stress ratio required to cause liquefaction at different cycles.....	104
Table 4.3 Saturation effect on elastic wave velocities based on Ishihara's (1970) data..	105
Table 4.4 Measurements of elastic waves for AP Specimens at dry and saturated conditions under different effective pressures.....	110
Table 4.5 Measurements of elastic waves for MT Specimens at dry and saturated conditions under different effective pressures.....	110
Table 4.6 Measurements of elastic waves for MV Specimens at dry and saturated conditions under different effective pressures.....	110
Table 4.7 Consolidation test results of reconstituted soil specimens.....	116

Table 4.8 Consolidation test results of AP, MT and MV specimens.....	120
Table 4.9 Computed and measured elastic wave velocity ratios	121
Table 4.10 Initial input values of AP specimens at different effective pressures.....	125
Table 4.11 Values of recovered elastic constants for AP specimens.....	125
Table 4.12 Errors of the non-linear equations for AP specimens	125
Table 4.13 Initial input values of MT specimens at different effective pressures.....	127
Table 4.14 Values of recovered elastic constants for MT specimens.....	127
Table 4.15 Errors of the non-linear equations for MT specimens	127
Table 4.16 Initial input values of MV specimens at different effective pressure.....	129
Table 4.17 Values of recovered elastic constants for MV specimens	129
Table 4.18 Errors of the non-linear equations for MV specimens.....	129
Table 4.19 Values of anisotropy index (A^E) for the specimens under different effective pressures.....	136
Table 4.20 Experimental CSR and pseudo CSR* at different number of cycles (N).....	138
Table 4.21 Ratio of experimental CSR to pseudo CSR*	139
Table 4.22 Shear wave anisotropic index A^S for AP, MT and MV under different effective confining pressures (S=0 %).....	142
Table 4.23 Experimental CSR and pseudo CSR** at different number of cycles (N) (S=0%).....	142
Table 4.24 Ratio of experimental CSR to pseudo CSR**	143
Table 4.25 Shear wave anisotropy index A^S for AP, MT and MV under different effective pressures (S=100%)	144
Table 4.26 Experimental CSR and pseudo CSR*** at different number of cycles (N) (S=100%).....	145
Table 4.27 Ratio of experimental CSR to pseudo CSR***	145
Table 4.28 Pseudo cyclic stress ratios of AP, MT and MV specimens	147

LIST OF FIGURES

Figure 2.1 A typical example of liquefaction resistance curve.....	8
Figure 2.2 Cyclic stress ratio of sands based on the normalized SPT N value (Ishihara, 1993).....	9
Figure 2.3 Cyclic stress ratio of sands based on the normalized CPT q_c value (Ishihara, 1993).....	10
Figure 2.4 A comparison of liquefaction characteristics between in-situ frozen sample sand tube samples (Yoshimi et al., 1989).....	12
Figure 2.5 Relationship between the cyclic stress ratio and number of cycles for differently prepared specimens (Ladd, 1974).....	14
Figure 2.6 Relationship between the cyclic stress ratio and number of cycles for Monterey No 0 sand with different preparation methods (Mulilis et al., 1977).....	15
Figure 2.7 Relationship between the cyclic stress ratio and the formation factor (Mulilis et al., 1977).....	16
Figure 2.8 Correlation between K_{2max} and electrical index $\bar{F}/(A \cdot \bar{f})^{1/2}$ (Arulmoli and Arulanandan, 1994).....	21
Figure 2.9 Comparison of s-wave velocities obtained from in-situ and laboratory tests (Nakagawa et al., 1997).....	23
Figure 2.10 Effects of inherent and stress-induced anisotropy on elastic waves (Schmertman, 1977).....	25
Figure 2.11 Shear-wave velocity versus the liquefaction resistance (De Alba et al., 1984).....	27
Figure 2.12 Fluid-wave velocity versus liquefaction resistance (De Alba et al., 1984).....	27
Figure 2.13 Liquefaction resistance under uniform cyclic strains (Ishibashi and Kiku, 1995).....	28
Figure 2.14 Normalized liquefaction resistance under uniform cyclic strains (Ishibashi and Kiku, 1995).....	28

Figure 2.15 Correlation of shear wave velocity and shear modulus with the void ratio and the confining pressure for dry sands (Hardin and Richart, 1963).....	30
Figure 2.16 Correlation between normalized shear modulus and liquefaction cyclic stress ratio (Tokimatsu and Uchida, 1990).....	33
Figure 2.17 Empirical correlation between cyclic stress ratio (CSR) and shear wave velocity (Andrus, 1999).....	34
Figure 3.1 Grain size distribution of Virginia Beach sand	38
Figure 3.2 Relationship between relative density and liquefaction resistance (DeAlba et al., 1975).....	40
Figure 3.3 Effect of relative density on vertical P-wave velocities (V_{pv}) of AP specimens.....	42
Figure 3.4 Effect of relative density on horizontal S-wave velocities (V_{sv}) of AP specimens.....	42
Figure 3.5 Effect of relative density on horizontal P-wave velocities (V_{ph}) of AP specimens.....	43
Figure 3.6 Cyclic triaxial test apparatus	44
Figure 3.7 Two load cells used	45
Figure 3.8 Axial (A) and cyclic (B) pneumatic loading system	45
Figure 3.9 Schema of the cylindrical loading piston	46
Figure 3.10 Calibration chart of the isotropic loading system.....	47
Figure 3.11 Design of the bender element wiring (adapted from Matroc Inc. manual)	49
Figure 3.12 Bender elements installed in the triaxial cell.....	53
Figure 3.13 Design layout of compression and shear wave transducers (a) view of transducers at the top and pedestal (b) side view of transducers for radial application.....	54
Figure 3.14 Electrical connections of bender elements (adapted from Agarwal, 1990)....	57
Figure 3.15 Calibration chart for amplified pulse amplitude.....	58
Figure 3.16 Correlation of trigger voltage to reference voltage output	58

Figure 3.17 Schema of the pulse/function generator and the digitizing oscilloscope	59
Figure 3.18 Typical transmitted and received wave signals from oscilloscope	59
Figure 3.19 Effect of frequency on vertical P-wave velocities of AP specimens.....	61
Figure 3.20 Effect of frequency on vertical S-wave velocities of AP specimens.....	61
Figure 3.21 Effect of frequency on horizontal P-wave velocities in AP specimens.....	62
Figure 3.22 Shear wave velocity measurement under the near-field effect (Brignoli et al., 1996)	63
Figure 3.23 Near field effect on the output signal due to the dimensions of the bender element (I_b) (Arulnathan et al., 1998)	65
Figure 3.24 Calibration chart for near field effects.....	66
Figure 3.25 Time delay due to the electrical connections	69
Figure 3.26 Calibration chart for effective distance for shear wave velocity measurement	72
Figure 3.27 Direction cosines of propagation directions	74
Figure 3.28 Wave path configurations.....	75
Figure 3.29 Phase diagram for a soil element.....	80
Figure 3.30 Typical relation of pore pressure parameter B vs. saturation degree	85
Figure 3.31 Relation between P-wave and S-wave velocities and the degree of saturation.....	87
Figure 3.32 Saturation effect on liquefaction resistance (Sheriff et al., 1977)	88
Figure 3.33 Assembly of cyclic triaxial test	89
Figure 4.1 The results of cyclic triaxial test on VB sand : $\sigma_1 = \sigma_3 = 70$ psi, $u = 60$ psi, $\sigma'_v = 10$ psi	102
Figure 4.2 Liquefaction resistance for AP, MT, and MV specimens	104
Figure 4.3 Saturation effect on P-wave velocities of AP, MT and MV specimens	107
Figure 4.4 Saturation effect on S-wave velocities of AP, MT and MV specimens	108

Figure 4.5 P-wave velocities in vertical direction against effective confining pressure at dry condition (S=0.0%).....	111
Figure 4.6 P-wave velocities in the horizontal direction against effective confining pressure at dry condition (S=0.0%)	111
Figure 4.7 P-wave velocities in the vertical direction against effective confining pressure at saturated condition (S=100%).....	112
Figure 4.8 S-wave velocities in the vertical direction against effective confining pressure at dry condition (S=0.0%).....	112
Figure 4.9 S-wave velocities in the horizontal direction against effective confining pressure at saturated condition (S=100%)	113
Figure 4.10 Volumetric strain against consolidation pressure for AP, MT and MV specimens.....	116
Figure 4.11 Axial strain against consolidation pressure for AP, MT and MV specimens.....	117
Figure 4.12 Measured and computed elastic wave velocity ratio for AP specimens	122
Figure 4.13 Measured and computed elastic wave velocity ratio for MT specimens.....	122
Figure 4.14 Measured and computed elastic wave velocity ratio for MV specimens	123
Figure 4.15 Transversely isotropic, elastic constants of AP specimens (a) longitudinal modulus (b) shear modulus (c) Poisson's ratio	126
Figure 4.16 Transversely isotropic elastic constants of MT specimens (a) longitudinal modulus (b) shear modulus (c) Poisson's ratio.....	128
Figure 4.17 Transversely isotropic elastic constants of MV specimens (a) longitudinal modulus (b) shear modulus (c) Poisson's ratio.....	130
Figure 4.18 Influence of preparation techniques on longitudinal modulus in vertical direction, E_1	133
Figure 4.19 Influence of preparation techniques on longitudinal modulus in horizontal direction, E_2	133
Figure 4.20 Influence of preparation techniques on shear modulus in vertical plane, G_{12}	134

Figure 4.21 Influence of preparation techniques on shear modulus in vertical plane, G_{23}	134
Figure 4.22 Anisotropy index (A^E) calculated from elastic constants	136
Figure 4.23 Ratio of CSR to CSR* against the number of cycles.....	139
Figure 4.24 Ratio of CSR to CSR** against the number of cycles	143
Figure 4.25 Ratio of CSR to CSR*** against the number of cycles	145

NOMENCLATURE

A	Amplitude of strain
A	Anisotropy index
A^E	Anisotropy index from elastic constants
A^S	Anisotropy index from S-wave measurements
a, b	Curve fitting parameter
a_{max}	Maximum ground surface acceleration
AP	Air pluviation
B	Pore water pressure parameter
C	Grain characteristics
C_a	Compressibility of air
C_{aw}	Compressibility of air-water mixture
C_b	Compressibility of bulk or soil skeleton
C_c	Coefficient of curvature
C_{ij}	Constitutive tensor
C_s	Compressibility of solid
CSR	Cyclic stress ratio ($\frac{\sigma_u}{2\sigma}$)
C_r	Correction factor due to the non-similarity of stress conditions
C_w	Compressibility of water
C_u	Coefficient of uniformity
d, L_{tt}	Travel distance
d_1, d_2, d_3	Direction cosines
D_{50}	Mean diameter of grains
D_r	Relative Density
E^E	Ratio of longitudinal moduli in vertical and horizontal plane
e	Void ratio
e_{min}	Minimum void ratio
e_{max}	Maximum void ratio
e_n	Natural void ratio

E_1, E_2, E_3	Longitudinal modulus in principle directions
E_θ	Directional longitudinal moduli
E_v	Longitudinal modulus in vertical direction
E_h	Longitudinal modulus in horizontal direction
EA	Electrical parameter
EI	Electric index
f	Frequency of vibration
f	Wave frequency
F	Formation factor
\bar{j}	Shape factor
\bar{F}	Average formation factor
$\bar{j}_{m.}$	Mean shape factor
\bar{j}_{max}	Maximum shape factor
\bar{j}_{min}	Minimum shape factor
F_v	Vertical formation factor
F_H	Horizontal formation factor
G	Shear modulus
g	Gravitational acceleration
G _s	Specific gravity
G _{ij}	Shear modulus in plane ij
G _θ	Directional shear moduli
G _{avg}	Average shear modulus on all directions
G _{max}	Maximum shear modulus
G _N	Normalized shear modulus
H	Ambient stress and vibration history
I _p	Plasticity index
K	Bulk modulus
K _{2max}	Correction factor to express maximum shear modulus
M _w	Magnitude of an earthquake
MT	Moist tamping

MV	Moist vibration
n	Porosity
R	Nearfield correction factor due to dimensions of bender elements
R	Stress ratio
Rd	Nearfield correction factor due to wave length
r_d	Stress reduction factor
r_c	Factor representing the effects of multidirectional shaking
S	Degree of saturation
S^E	Ratio of shear moduli in vertical and horizontal plane
S_1	Shear wave in direction 1
S_2	Shear wave in direction 2
S_{ij}	Components of elastic matrix
t	Travel time
T	Temperature parameter
V_p	Vertical P-wave velocity
V_{ph}	Horizontal P-wave velocity
V_{sv}	Vertical S-wave velocity
V_a, V_w, V_v	Volume of air, water, and void, respectively
V_T, V_S	Total volume and volume of solid, respectively
V_{p1}	P-wave velocity in direction 1
V_{p3}	P-wave velocity in direction 3
V_{pf}	Fluid wave velocity
V_s	S-wave velocity
V_{s1}	Corrected S-wave velocity
V_{s1}^*	Corrected S-wave velocity due to fine content
u	Pore water pressure
σ_0	Total vertical pressure acting on the soil stratum
σ_0'	Effective vertical pressure in the field
σ_{d1}	Axial cyclic stress acting on the triaxial specimen
σ_1	Principle stress in direction 1
σ_3	Principal stress in direction 3

σ_{ij}	Stress tensor
σ'	Effective confining pressure
ϵ_v	Volumetric strain
ϵ_1	Axial strain in direction 1
ϵ_2	Axial strain in direction 2
ϵ_3	Axial strain in direction 3
ϵ_{ij}	Strain tensor
γ_{dmin}	Minimum dry density of soil
γ_{dmax}	Maximum dry density of soil
γ_d	Dry density of soil
λ	Wave length
λ	Lame's constant
ν_{ij}	Poisson's ratio in direction i due to the force applied in direction j
ρ	Mass density
τ_{av}	Average or equivalent uniform cyclic shear stress amplitude
τ_{max}	Maximum cyclic shear stress
τ_0	Octahedral shear stress
ϑ	Soil structure

CHAPTER 1

INTRODUCTION

1.1 Statement of Problem

Niigata and Alaska earthquakes in 1964 led many researchers to deal with liquefaction problem over the past 30 years. The evaluation techniques of liquefaction resistance of saturated sand deposits have been improved by means of laboratory and in-situ testing techniques.

In the laboratory studies, cyclic triaxial test, cyclic simple shear test, resonant column test, etc., have been conducted to investigate the effects of soil density, gradation, cyclic stress amplitude and other parameters on liquefaction resistance. Since it is very difficult and expensive to obtain completely undisturbed granular specimens from the fields, soil specimens had to be reconstituted in the laboratory with regards to the in-situ density of soil. At the same time, researchers found out that laboratory reconstituted specimens and undisturbed specimens yielded a quite different liquefaction resistance. Furthermore, they realized that different sample preparation techniques in the laboratory produced significantly different liquefaction resistance for the same soil with same density. It is believed that those differences are due to soil fabric or inherent anisotropy created by different sample preparation techniques. Many researchers (Ladd, 1974; Mulilis et al., 1977; Toki et al., 1986; Tatsuoka et al., 1986)* experimentally showed that the liquefaction resistance is highly influenced by differences in the structure of the soil produced by different sample preparation techniques.

**Geotechnique* is used as a format model for reference cited.

De Alba et al. (1984) noticed experimentally that elastic waves are also affected by anisotropy of soils. Ishibashi and Agarwal (1991) and Agarwal and Ishibashi (1992) measured P-wave and S-wave velocities along several directions relative to the principal stress axes in the cubical granular specimens. Their works suggested that the directional wave velocity measurements could identify the anisotropy of the granular materials. In addition, Ishibashi and Kiku (1995) presented three-dimensional discrete element model simulations to relate the effect of initial anisotropy by means of directional elastic moduli to liquefaction resistance. Tokimatsu et al.'s (1986) and Tokimatsu and Uchida (1990) and Stokoe (1997) and Andrus et al.'s (1999) work proposed promising empirical correlations between liquefaction resistance of sand deposits and shear wave velocities measured in the field.

1.2 Scope of Research

In this research, laboratory experiments are conducted to describe anisotropy and to evaluate liquefaction resistance under cyclic loading for a specific soil. Different sample preparation techniques are utilized to obtain different soil fabrics. By measuring P-wave and S-wave velocities in the vertical direction and additional P-wave velocity in the horizontal directions through the specimens, the anisotropy is quantified. Cyclic triaxial test are then conducted to determine liquefaction resistance for each soil sample. The relationship between anisotropy and liquefaction resistance is quantitatively established based on those experimental results.

1.3 Outline of Dissertation

This dissertation is presented in five chapters. This chapter introduces the problem and the objectives of this research. Chapter Two first identifies the liquefaction phenomenon and represents the currently available evaluation techniques of liquefaction

resistance of soils in the field and in the laboratories. Then it gives reviews of published researches related to the subject and makes discussions of the various solutions from the case studies.

In Chapter Three, experimental testing programs chosen for this research are introduced. Since cyclic triaxial test device and pulse transmission method are mainly used in this research, the criteria of the testing devices and their installation process are presented. Some correction factors applied to experimental measurements are introduced and those are quantitatively identified.

Chapter Four represents experimental results and their analyses. In the chapter, the results of experiments are discussed in detail. Based on the results, relationships between anisotropy and liquefaction resistance are quantitatively established.

Finally, conclusions of this research are presented in Chapter Five, and recommendations for future works are pointed out.

CHAPTER 2

LITERATURE REVIEW

2.1 Introduction

Since the Niigata and Alaska earthquakes in 1964, liquefaction resistance of saturated sand under cyclic loading has been intensively studied. Field and laboratory studies revealed that soil-fabric, or anisotropy of soil, is one of the key factors affecting the liquefaction resistance. One of the most liquefiable granular materials is fully saturated, uniform, loose, medium to fine sand deposits. Therefore, liquefaction evaluation projects are generally focused on that type of soil. In this chapter, anisotropy effects on the liquefaction resistance of loose sand and the developments concerning the recovery of anisotropic characteristics of sands are reviewed.

2.2 Definition of Liquefaction

Mogami and Kubo (1953) coined the term “liquefaction” to signify the behavior of saturated sand deposits during vibration. Liquefaction phenomenon was then dramatically observed during the Niigata and Alaska earthquakes in 1964. Extensive research on liquefaction has started after those two major earthquakes. Seed and Idriss (1982) state that “if a saturated sand is subjected to ground vibrations, it tends to compact and decrease in volume; if drainage is unable to occur, the tendency to decrease in volume results in an increase in pore water pressure and if pore water pressure builds up to the point at which it is equal to overburden pressure, the effective stress becomes zero, the sand loses its strength completely, and it develops a liquefied state.”

Numerous studies have been conducted focusing on the assessment of the liquefaction resistance of soils in both laboratory and field studies. The results indicated

that the liquefaction resistance of any soil deposit can be influenced by soil parameters, earthquake characteristics, and environmental factors. These factors are listed below:

Soil parameters:

Stiffness

Damping characteristics

Unit weight

Grain characteristics

Relative density

Soil fabric

Earthquake characteristics:

Intensity of ground shaking

Duration of ground shaking

Environmental factors:

Method of soil formation

Seismic history

Geologic history (aging and cementation)

Lateral earth pressure coefficient

Effective confining pressure

2.3 Methods of Evaluating Liquefaction Resistance of Sands

Field (in-situ) testing as well as laboratory testing procedures have been developed in order to evaluate the liquefaction resistance of soil deposits. The basic purpose of those methodologies is to establish the liquefaction resistance of soils by considering the affecting factors mentioned above.

2.3.1 Cyclic Stress Ratio

For the evaluation of liquefaction resistance in the field as well as in the laboratory, cyclic stress ratio is conveniently used. The cyclic stress ratio generated by an earthquake was first defined by Seed and Peacock (1971) and Seed and Idriss (1971) as:

$$\left(\frac{\tau_{av}}{\sigma'_0} \right) = 0.65 \left(\frac{a_{max}}{g} \right) \left(\frac{\sigma_0}{\sigma'_0} \right) r_d \quad (2.1)$$

where τ_{av} is the average or equivalent uniform cyclic shear stress amplitude developed by the earthquake. a_{max} is the maximum ground surface acceleration, g is the gravitational acceleration and σ_0 is the total pressure acting on the soil stratum. σ_0' is the effective pressure acting on the soil stratum before the earthquake and r_d is a stress reduction factor due to the flexibility of a soil deposit, which reduces with increasing depth. Due to the nature of earthquakes, the time history of real shear stress shows irregularity. The irregular cyclic shear stress is converted to an equivalent uniform shear stress by 65% of the maximum shear stress for simplification.

Later, the stress ratio τ_{av}/σ_0' in the field was modified by Seed (1979) and Yoshimi (1989) in terms of cyclic triaxial test parameters as:

$$\left(\frac{\tau_{av}}{\sigma_0} \right)_{field} = C_r \left(\frac{\sigma_{dl}}{2\sigma_0'} \right)_{triaxial} r_c \quad (2.2)$$

$$C_r = \frac{1 + 2K_0}{3} \quad (2.3)$$

where r_c is a factor representing the effects of multidirectional shaking with a value from 0.9 to 1.0. C_r is a correction factor due to the non-similarity of stress conditions between the field and laboratory triaxial tests (K_0 effect). σ_{dl} is axial cyclic stress acting on the triaxial specimen due to cyclic loading.

In the laboratory triaxial test, the specimen is saturated and consolidated under a certain confining pressure and then subjected to uniform cyclic axial stresses. The axial cyclic stress (σ_{dl}) generates the maximum shear stress condition on a plane of 45° in the specimen with a maximum shear stress of $\sigma_{dl}/2$. When a certain axial strain is exceeded, or pore water pressure (u) builds-up until u becomes equal to the initially applied effective stress (σ_0'), the state of liquefaction will be developed. The critical axial strain

of 5% double amplitude (DA) is usually used for loose and medium sand specimens. This state has been defined as “initial liquefaction” or simply “liquefaction.” When the initial liquefaction takes place, especially for loose sand, a large amount of deformation occurs just before the magnitude of pore water pressure and confining pressure becomes equal (complete liquefaction).

Correlation between the magnitude of an earthquake and the number of cyclic shear stress was established by Seed et al. (1985) and is shown in Table 2.1. Several cyclic loading tests must be conducted under different values of cyclic stress to establish the relationship between the cyclic stress ratio to cause liquefaction and the number of load cycles for a given soil with a given density. A typical liquefaction curve is illustrated in Figure 2.1.

Table 2.1 Correlation between magnitude of an earthquake and number of cyclic stresses (Seed et al., 1985)

Earthquake Magnitude M	Number of Representative Cycles at $0.65 \tau_{max}$
8-1/2	26
7-1/2	15
6-3/4	10
6	5-6
5-1/4	2-3

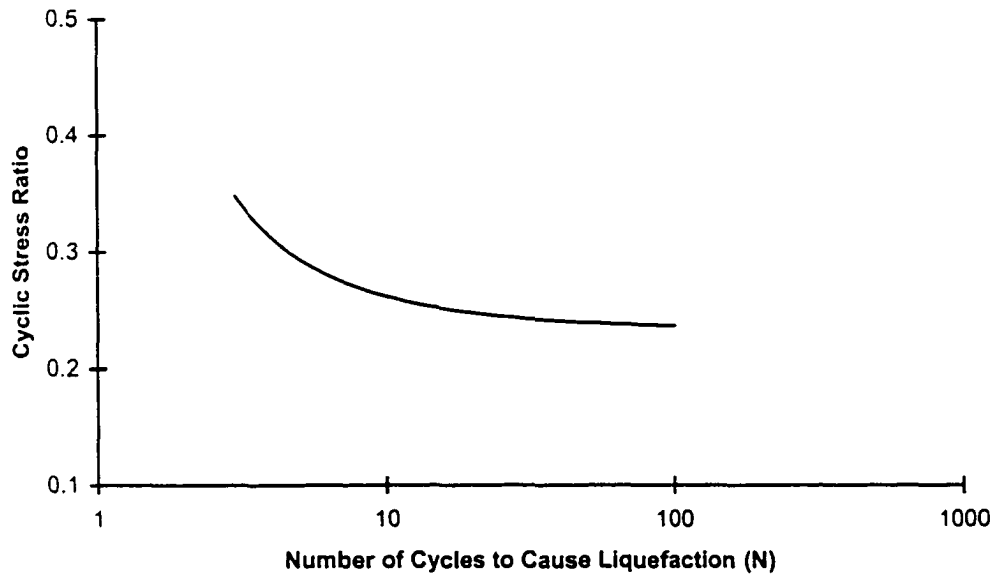


Figure 2.1 A typical example of liquefaction resistance curve

2.3.2 In-situ Evaluation Methods

Field measured values reflect all soil parameters and the environmental factors, which the soil possesses in an undisturbed condition. Field tests do not require the sampling of specimens. Especially for sand and gravel deposits, obtaining high-quality undisturbed specimens requires extremely difficult and expensive procedures such as in-situ freezing methods (Yoshimi et al., 1984 and 1989). In addition, to represent the properties of one specific soil deposit from laboratory tests, it requires large volumes of the soil sampling. Therefore, in-situ testing methods are economically feasible for the measurement of soil properties that correlate to liquefaction resistance in usual situations.

The most popular field tests are the Standard Penetration Test (SPT) and the Cone Penetration Test (CPT). These two tests have been successfully applied for the evaluation of the cyclic strength of sands in terms of cyclic stress ratios shown in Figures 2.2 and 2.3 (Ishihara, 1993).

However, in-situ testing methods can not simulate the pore water pressure generation and dissipation mechanisms that occur during earthquake vibrations, and those play a highly influential role on the liquefaction phenomenon. The soil parameters have to be identified by empirical correlation or theoretical analysis; these parameters can not be measured individually in the field tests.

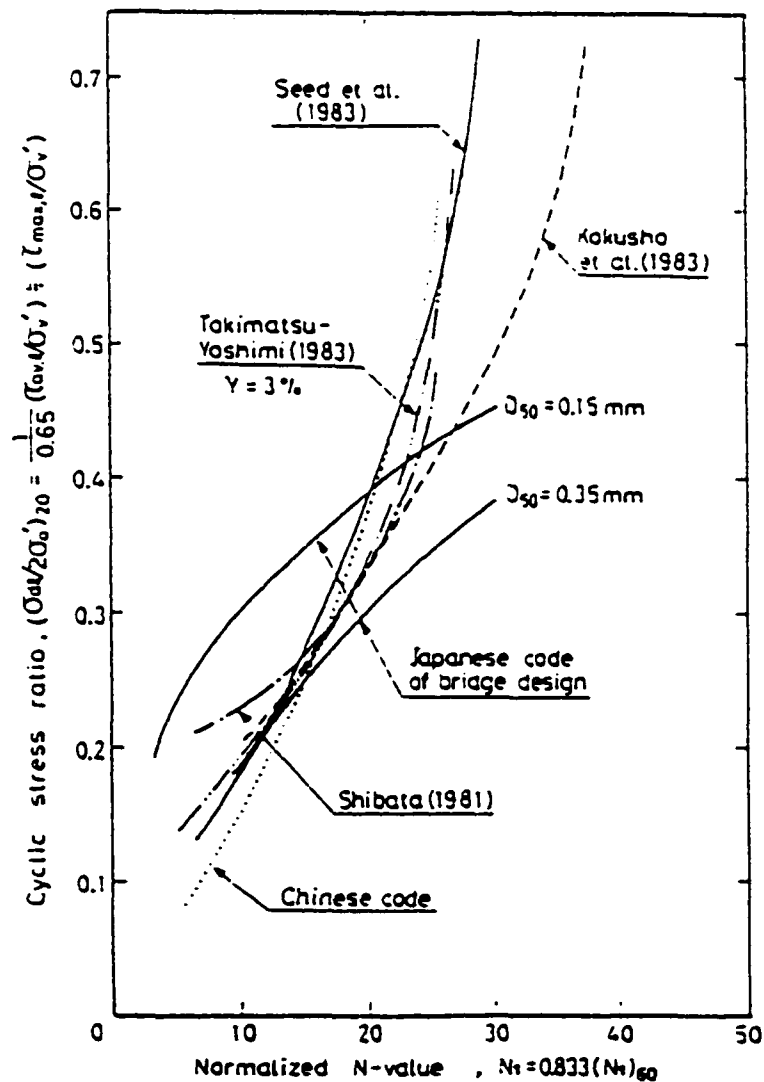


Figure 2.2. Cyclic stress ratio of sands based on the normalized SPT N value (Ishihara, 1993)

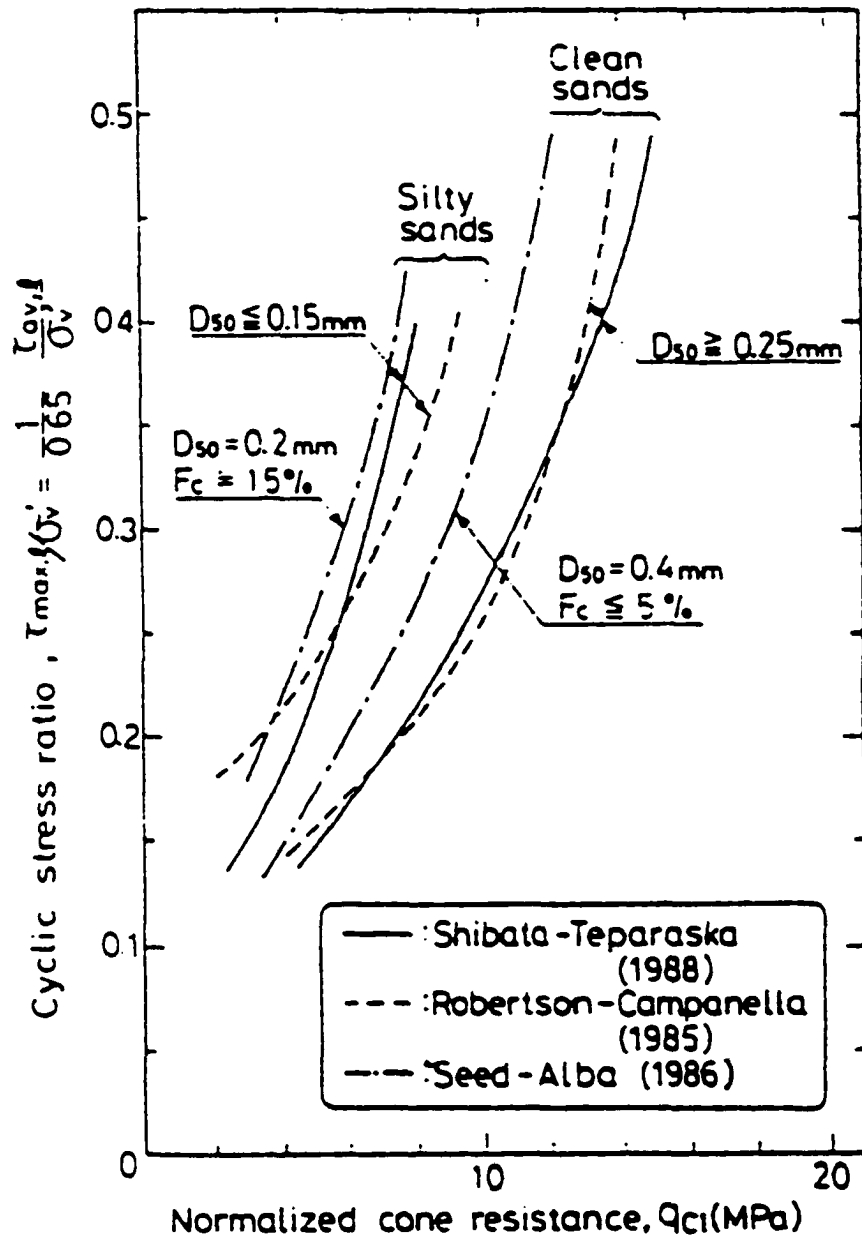


Figure 2.3 Cyclic stress ratio of sands based on the normalized CPT q_c value (Ishihara, 1993)

2.3.3 Laboratory Cyclic Loading Tests

As mentioned previously, field tests have some limitations. Specific soil properties need to be investigated thoroughly in laboratory conditions. Various parameters which affect the liquefaction resistance of fully saturated sands under cyclic loading conditions have been thoroughly investigated through various types of laboratory cyclic tests. Commonly used cyclic laboratory tests are:

- 1) cyclic triaxial test
- 2) cyclic simple shear test
- 3) cyclic torsional shear test
- 4) shaking table test

Some basic differences among these tests are how to model the dynamic behaviors of soil based on the initial stress and the cyclic loading condition. Factors such as the initial stress, the pore water drainage condition, the density and the sample preparation technique have been investigated using those cyclic devices.

In this research, a laboratory dynamic triaxial test apparatus is used on reconstituted sand specimens. Although the cyclic triaxial test has some disadvantages, like non-similarity to in-situ stress and no rotation of principle stress axes, it has a simple mechanism and is widely used in engineering practice. It makes sample preparation easier than other types of cyclic shear devices. The cyclic triaxial setup and the basic mechanism will be discussed in Section 3.3.1.

2.4 Anisotropy of Granular Materials

Granular materials such as sand deposits have anisotropic characteristics due to gravity, formation process and various stress histories. It has been shown that the liquefaction resistance of sand is highly affected by seismic history (Seed et al., 1975),

aging (Seed, 1979 and Schmertman, 1992), in-situ lateral stress conditions [K_0 conditions] (Seed and Peacock., 1971), and soil structure (Ladd, 1974; Mullilus et al., 1977; Nemet-Nasser and Tobita, 1982; Nemet-Nasser and Takahashi, 1984; Ochiai et al., 1984; De Alba et al., 1984; Toki et al., 1986; and Tatsuoka et al., 1986; and Ashraf et al., 1991).

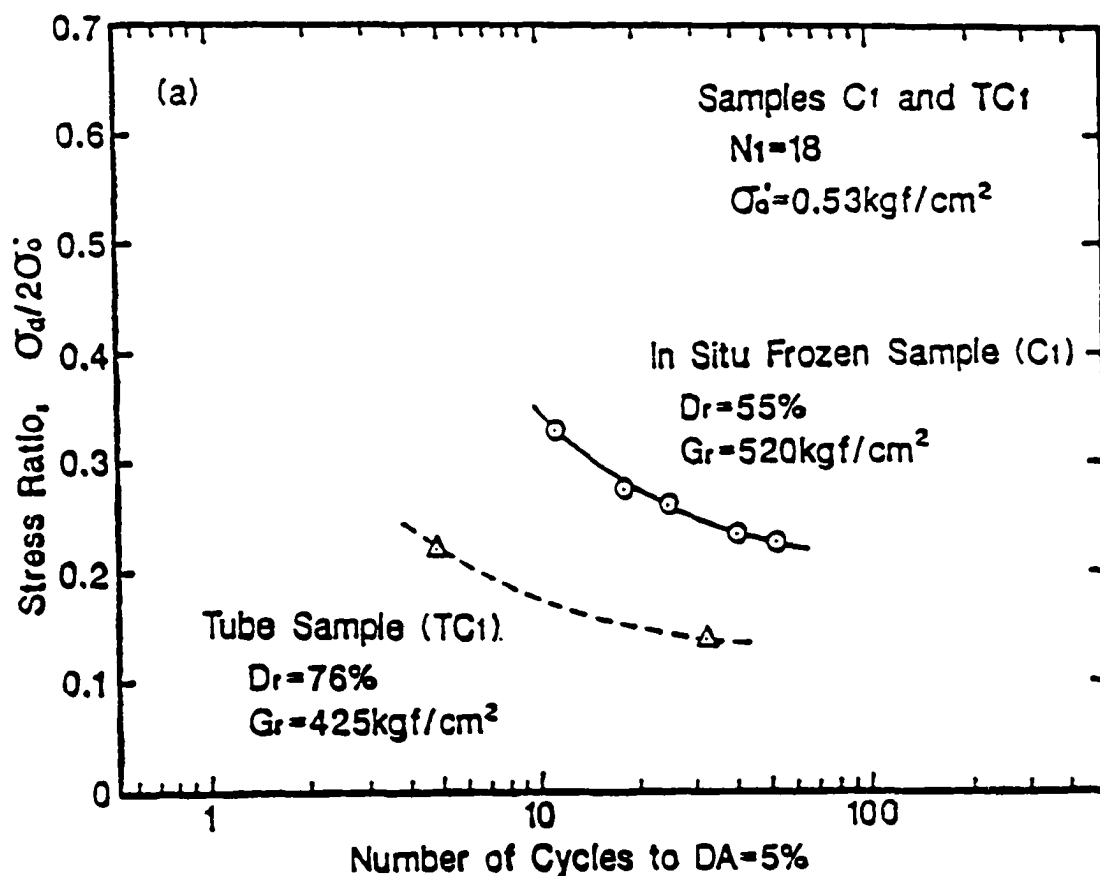


Figure 2.4 A comparison of liquefaction characteristics between in-situ frozen samples and tube samples (Yoshimi et al., 1989)

In order to investigate anisotropic effects on the liquefaction resistance, high-quality undisturbed specimens have been used for laboratory testing. These specimens allow a more reliable and accurate evaluation of the cyclic strength. Granular materials do not have cohesion, and thus the physical molecular forces between particles within

substances that unite them do not exist. Therefore, advanced sampling techniques are required. In-situ freezing, one type of advanced sampling techniques, is used for sands (Yoshimi et al., 1984 and 1989). Figure 2.4 shows a distinguishable difference between the specimens obtained by the freezing technique and a conventional sampling method in regard to the cyclic stress ratio versus number of cycles to reach the state of liquefaction. Obtaining and handling undisturbed specimens of granular materials is difficult and highly expensive. The freezing procedure is primarily used, therefore, for very essential construction projects.

Previous studies indicated that the initial density of soils has a major effect on the liquefaction and the settlement characteristics. If other factors remain unchanged, increasing the density of one specific soil increases the liquefaction resistance. In the laboratory cyclic tests, however, different sample preparation techniques have given quite different liquefaction resistance even for a same soil with a same density. The pioneering works of Ladd (1974) and Mulilis et al. (1977) shown in Figure 2.5 and Figure 2.6 pointed out that using different preparation techniques created different soil fabric and that these techniques influenced the liquefaction resistance significantly. The soil density was kept the same but preparation techniques were changed. Ladd suggested that the structure of sand should be considered as a very important factor; thus to reduce the effects of reconstituted structure on the laboratory cyclic strength, undisturbed specimens should be used if possible.

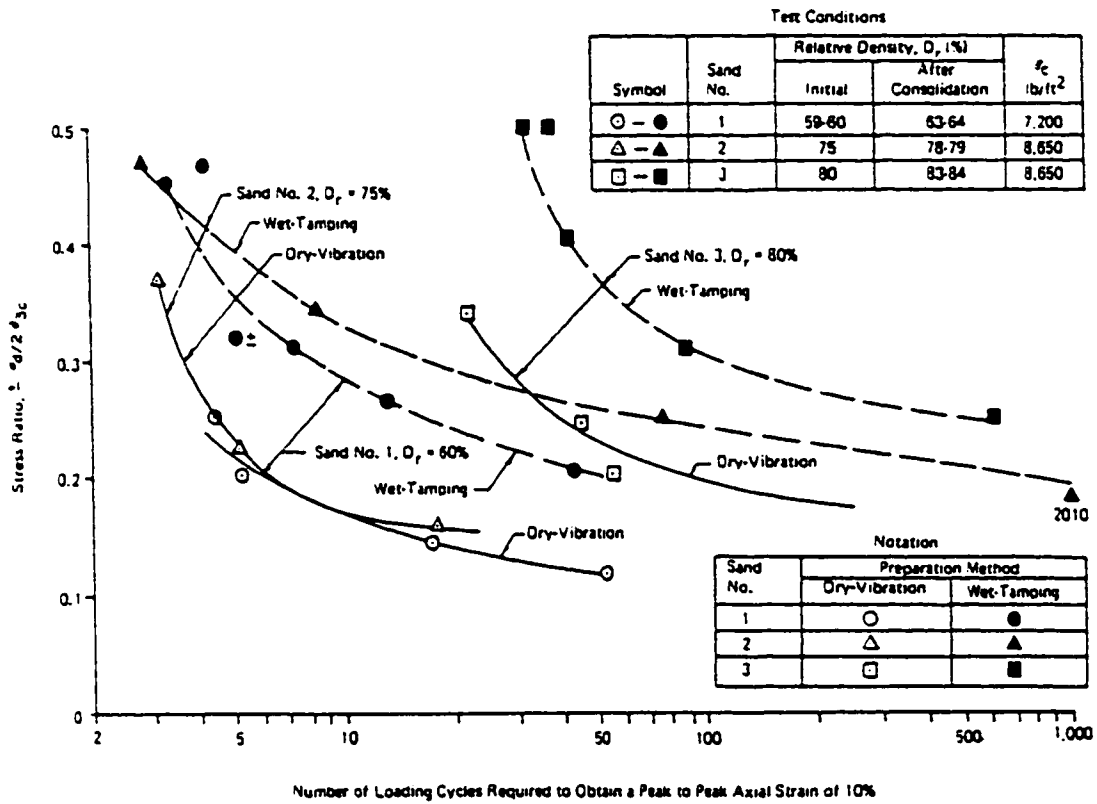


Figure 2.5 Relationship between the cyclic stress ratio and number of cycles for differently prepared specimens (Ladd, 1974)

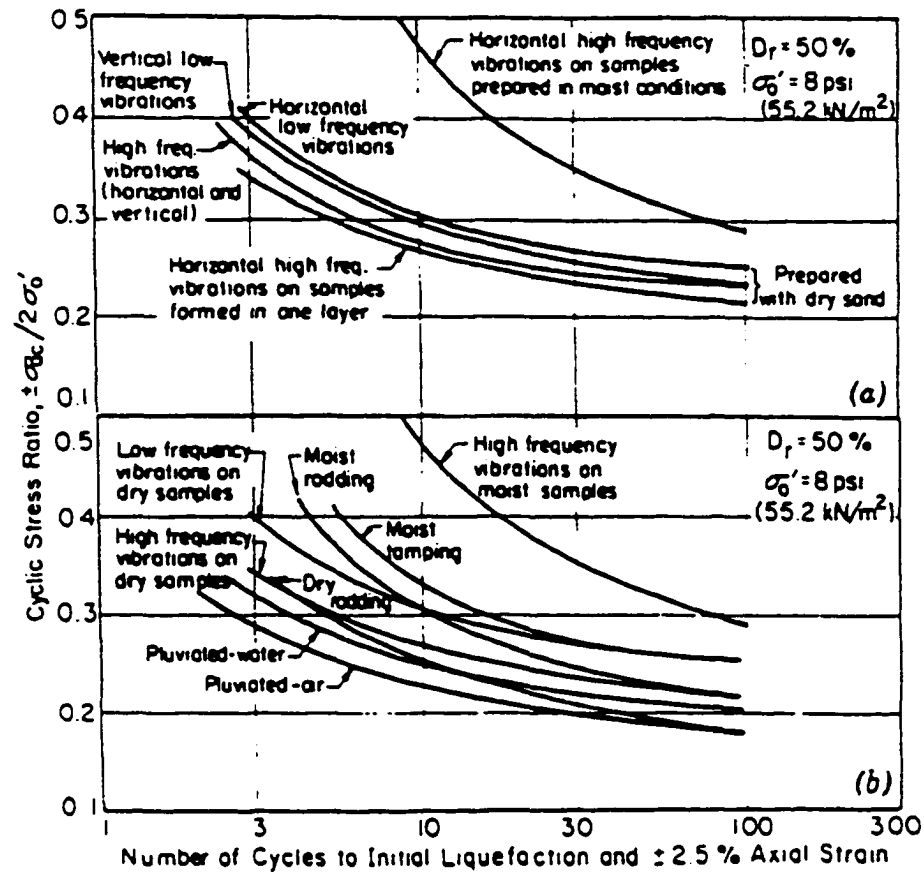


Figure 2.6 Relationship between the cyclic stress ratio and number of cycles for Monterey No 0 sand with different preparation methods (Mulilis et al., 1977)

Mulilis et al. (1977) attempted to explain the effects of soil fabric on liquefaction. In their extensive experimental research, eleven different preparation techniques were used. The effects of air-pluviation, moist-tamping and moist-vibration techniques on the liquefaction resistance were extensively examined. The weakest specimens were created by pluviating the soil through air (air-pluviation), while the strongest ones were by vibrating soil in a moist condition (moist vibration).

They verified their assumption by means of the distribution of density, x-ray analysis and the electrical conductivity of the specimens. Qualitative x-ray analyses were

used for observing the fabric diagram and determining the statistical orientation of contacts between grains.

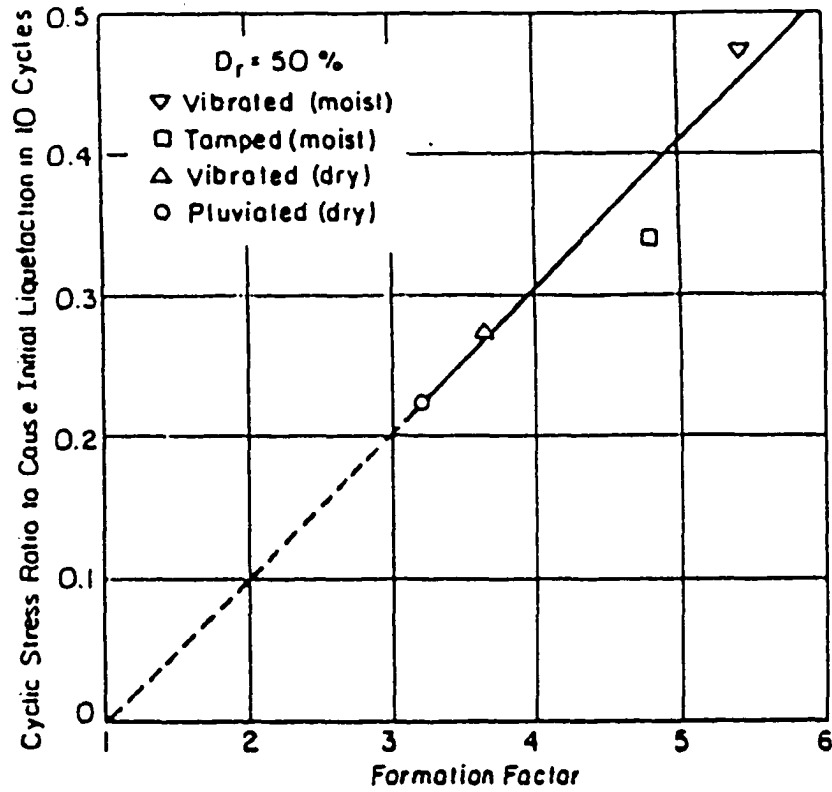


Figure 2.7 Relationship between the cyclic stress ratio and the formation factor (Mulilis et al., 1977)

Table 2.2 Comparison of undisturbed and remolded strength (Mulilis et al., 1977)

Firm (1)	Project (2)	Ratio of undisturbed to remolded strength (3)	Soil type (4)	Method of remolding (5)
Woodward-Clyde (Oakland, Calif.)	South Texas	1.00	Silty fine, $D_{50}=0.07$ mm-0.27 mm	Moist tamping, ½-in. diameter tamping foot
Woodward-Clyde (Orange, Calif.)	San Onofre	1.15	Well-graded coarse to fine sand, 15%--No. 200 sieve slightly cemented	Moist tamping, ½-in. diameter tamping foot
University of California Berkeley, California	Blue Hills Texas	1.15	Uniform fine silty sand, $D_{50}=0.4$ mm, 8%-15%--No. 200 sieve	Moist tamping, ½-in. diameter tamping foot
Dames & Moore (San Francisco, California)	Allens Creek (heat sink area)	1.20	Fine silty clayey sand, $D_{50}=0.03$ mm-1.6mm, 0%--40%--No. 200 sieve	Moist tamping, 1-in. diameter tamping foot
Dames & Moore (San Francisco, California)	Allens Creek (plant area)	1.27	Fine silty clayey sand, $D_{50}=0.03$ mm-1.6mm, 0%--40%--No. 200 sieve	Moist tamping, 1-in. diameter. tamping foot
Converse-Davis	Perris Dam	1.45	Clayey sand, LL = 26, PI = 11, 44%--No. 200 sieve	Moist tamping, ½-in. diameter. tamping foot
Law Engineering and Testing	Florida sand	1.30	Silty sand with shells	Dry vertical vibrations, frequency = 120 cps
Waterways Experiment Station	Ft. Peck Dam (foundation)	1.65-1.80	Uniform fine silty sand	Dry rodding (3/8-in. diameter. foot), followed by static compaction
Waterways Experiment Station	Ft. Peck Dam (shell)	1.70-2.00	Uniform fine to medium sand	Dry rodding (3/8-in. diameter foot), followed by static compaction

Electrical conductivity measurements were also used to characterize the pore structure of specimens. Sand particles are not electrically conductive, especially when clean. In the electrical conductivity test, the voids of the sand specimens were saturated with an electrolyte, 0.001N NaCl, so that the conductivity of the fully saturated soil specimen was able to be measured in a direction by an impedance comparator. Taking the magnitude of conductivity of 0.001N NaCl solution as a reference, a formation factor (F) was identified. F is the ratio of the conductivity of the NaCl solution to the one of the soil

specimen saturated by the same solution. The results concluded that there is a linear relationship between the cyclic stress ratio and the formation factor as seen in Figure 2.7. It is, therefore, concluded that the formation factor could recover the effects of the soil fabric on the cyclic stress ratio.

Mulilis et al. (1977) compared data of the liquefaction resistance of reconstituted specimens with undisturbed specimens of different sands as seen in Table 2.2. It was suggested that although some disturbance occurred during sampling, the liquefaction resistance of the samples prepared by moist tamping or moist vibrating might be similar to the liquefaction characteristics of the undisturbed specimens.

Based on the works of Mulilis et al. (1977) and other similar studies, Arulmoli and Arulanandan (1994) proposed an electrical method for a correlation between the cyclic stress ratio and electrical parameters. Since soil samples were considered to be transversely isotropic, the formation factor was determined in both vertical and horizontal directions. It was pointed out that the formation factor (F) is function of void ratio, the shape of grain particle, contact orientation and grain size distribution based on experimental results. The following parameters were defined:

Anisotropy index:

$$A = \sqrt{\frac{F_V}{F_H}} \quad (2.4)$$

Average formation factor:

$$\bar{F} = \frac{(F_V + 2F_H)}{3} \quad (2.5)$$

where F_v and F_h are vertical and horizontal formation factors, respectively. Considering particle shapes and porosity (n), the following empirical correlation was found among \bar{F} , n and \bar{f} (shape factor):

$$\bar{F} = n^{-j} \quad (2.6)$$

$$\bar{f}_m = \frac{(\bar{f}_{\max} + \bar{f}_{\min})}{2} \quad (2.7)$$

\bar{f} depends on the shape of the particles and on the orientation of the particles. For practical purposes, \bar{f} is determined as the negative slope of the $\log \bar{F} - \log n$ plot as given in Equation 2.6, and \bar{f}_{\max} and \bar{f}_{\min} are the values of \bar{f} at maximum and minimum values of porosities for a specimen.

It was found that the liquefaction resistance of soil specimens varies with A , \bar{F} and \bar{f}_m . The summary of these correlations is shown in Table 2.3. An electrical parameter (EA) and electric index (EI) were then defined in the following equations:

$$EA = \frac{A^3}{(\bar{F} \cdot \bar{f}_m)} \quad (2.8)$$

$$EI = \left(\frac{\bar{F}}{A \cdot \bar{f}_m} \right)^{1.2} \quad (2.9)$$

In addition, by using an empirical relationship between the dynamic shear modulus, G , and the effective confining pressure (σ_0') given by Seed and Idriss (1970), correlation of $K_{2\max}$ to the electrical index (EI) was established as shown in Figure 2.8, in which maximum shear modulus is represented by $G_{\max} = 1000 \times K_{2\max} (\sigma_0')^{1/2}$. $K_{2\max}$ is the function of void ratio, age of deposit, and in-situ stress (K_0) condition.

Table 2.3 Laboratory measurements of cyclic stress ratio required to cause liquefaction with electrical parameter $A^3 / \bar{F} \cdot \bar{f}_m$ (Arulmoli and Arulanandan, 1994)

Sand Type	Method Of Preparation	Porosity n	Average Formation Factor, \bar{F}	Anisotropy Index, A	$A^3 / \bar{F} \cdot \bar{f}_m$	Cyclic Stress Ratio to Cause Liquefaction ($\pm\sigma_d/2\sigma_0$) in.					Reference for Cyclic Testing
						5 Cyc.	10 Cyc.	15 Cyc.	30 Cyc.	50Cyc	
Monterey O Sand	Moist Tamping	0.416	3.72	0.989	0.174	0.400	0.330	0.305	0.280	0.270	Mulilis et al. 1975
	Dry Pluviation	0.416	3.72	1.029	0.196	0.260	0.230	0.215	0.200	0.190	
		0.395	3.96	1.027	0.182	0.350	0.305	0.290	0.265	0.255	
		0.379	4.18	1.025	0.172	...	0.455	0.410	0.345	...	
Ottawa C-109" Sand	Dry Pluviation	0.406	3.44	1.00	0.217	0.185	0.170	0.165	0.160	0.155	Harder 1977
		0.380	3.74	1.01	0.199	0.277	0.232	0.217	0.200	0.191	
		0.366	3.90	1.00	0.191	0.370	0.270	0.237	0.210	0.203	
Sierra Diamond Sand	Dry Pluviation	0.463	3.35	1.035	0.213	0.252	0.195	0.170	0.145	0.132	Arulmoli 1982
	Moist Tamping	0.463	3.35	0.972	0.177	0.417	0.350	0.315	0.265	0.235	
Nigata Site Sand	Natural	0.505	3.00	1.091	0.271	0.150	0.145	0.140	0.138	...	Silver and Ishihara 1977
		0.487	3.16	1.107	0.268	0.157	0.140	0.132	
		0.482	3.21	1.148	0.295	0.132	0.118	0.106	0.100	0.095	
Red Belford Sand	Moist Tamping	0.424	3.56	0.985	0.182	0.328	0.287	0.270	0.250	0.238	Townsend et al. 1978
		0.404	3.77	0.978	0.168	0.495	0.435	0.408	0.382	0.372	
		0.381	4.08	0.970	0.152	0.485	0.450	
Lawson's Landing Site Sand	Pluviation Through Water	0.429	3.62	1.031	0.201	0.255	0.225	0.212	0.195	0.188	Arulmoli 1982
		0.419	3.74	1.032	0.495	0.305	0.275	0.258	0.240	0.228	
		0.412	3.84	1.032	0.190	0.350	0.320	0.285	0.260	0.255	

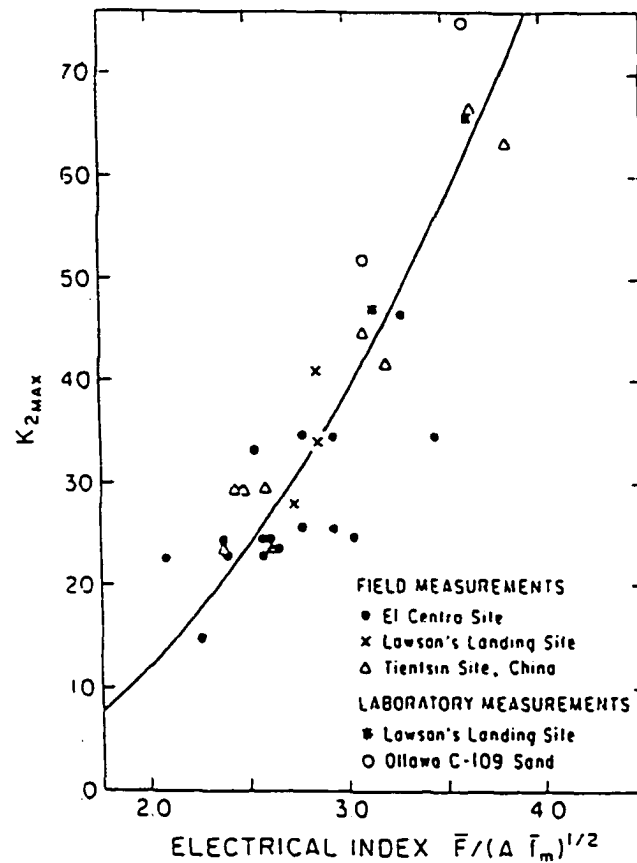


Figure 2.8 Correlation between K_{2max} and electrical index $\bar{F}/(A \cdot \bar{f})^{1/2}$ (Arulmoli and Arulanandan, 1994)

2.5 Elastic Wave Speed Measurement

Elastic-waves passing through soils are affected by the mechanical properties of soils. Wave speed measurements, which are low-strain tests, can be conducted without compromising the stress history of the soils. If an approximate magnitude of strain falls into the range between 10^{-6} to 10^{-5} , the range is acceptable to determine elastic characteristics of soils (Ishihara, 1996). Many applications of wave speed measurements have been developed in the field and laboratory. Elastic constants, such as longitudinal modulus and shear modulus, have been determined from wave speed measurements in

different directions. These measurements and recovered elastic constants have been used to quantitatively identify soil anisotropy.

In the laboratory, elastic constants of granular materials have been measured by means of the resonant column test (Hardin and Richart, 1963), plate-hammer impact test with accelerometers (Schmertman, 1977), a motor driven excitor (Roesler, 1979) and pulse transmission by piezoelectric transducers (De Alba et al., 1984; Ishibashi and Agarwal (1991), Agarwal and Ishibashi (1992); Nakagawa et al. 1996 and 1997; Zeng and Ni, 1998 and 1999). The pulse transmission method by piezoelectric transducer has been proved to be applicable to evaluate elastic waves and this system can be installed easily in a triaxial setup. The pulse transmission, thus, has become the most popular method to measure elastic waves propagating in soils in the laboratory.

Nakagawa et al. (1996) compared laboratory elastic shear wave velocities measured by the resonant column method (RCM) and the pulse transmission method (PTM) to in-situ wave velocities. Laboratory PTM gave very similar results to the in-situ values for both sands and clays as shown in Figure 2.9.

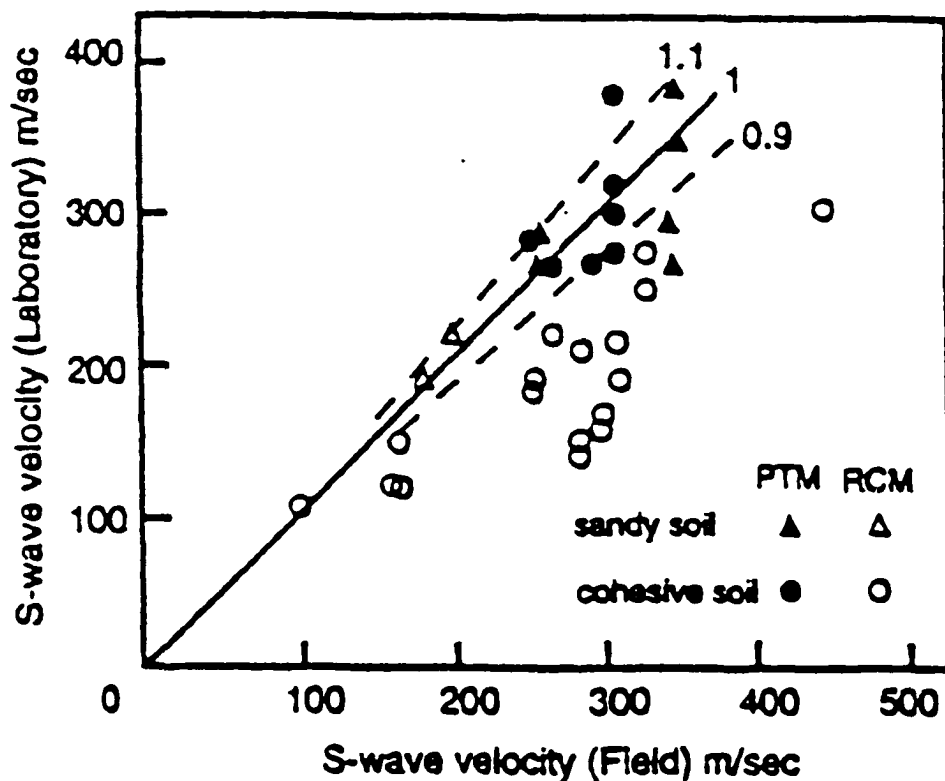


Figure 2.9 Comparison of S-wave velocities obtained from in-situ and laboratory tests (Nakagawa et al., 1996)

In this research, the pulse transmission method is used to measure the elastic wave velocities through the soil specimens.

2.6 Liquefaction and Wave Velocity Measurement

2.6.1 Directional Wave Velocities and Anisotropy

The anisotropy of soils can be qualitatively identified by elastic constants determined in different directions in the granular materials (Schmertman, 1977; Ishibashi and Agarwal, 1991, Agarwal and Ishibashi, 1992; Ishibashi and Kiku, 1995; Zeng and Ni, 1998 and 1999).

Schmertman (1977) applied isotropic ($R=1$) and anisotropic ($R=3$) ambient stress and conducted wave speed measurements in both vertical and horizontal directions on a

sand specimen prepared by the air-pluviation technique. R is the ratio of the major to minor effective principle stresses (σ_1/σ_3). The results of the wave velocity measurements are given in Table 2.4 and Figure 2.10. According to the results, the soil specimens obtained by air-pluviation show inherent and stress induced anisotropy in terms of compressional (P) wave velocities as formulated by:

$$\frac{V_{P1}}{V_{P3}} = 0.89R^{n \cdot 2} \quad (2.10)$$

where n is porosity and was 0.5 in his experiment, and V_{P1} and V_{P3} are compressional wave velocities in axial and radial directions, respectively. Under isotropic stress condition, ($\sigma_1=\sigma_3$ or $R=1$), the ratio of V_{P1} to V_{P3} was 0.89. Likewise, the ratio of shear waves (S_1/S_3) was 0.79 when $R=1$. It showed that inherent and stress induced anisotropy existed and was identified by wave speed measurements.

Table 2.4 Average adjusted wave velocities in Schertman's experiment (1977)

R	Propagation Direction (degrees)	S-Wave			P-wave		
		Velocity m/s	Std Dev m/s	Num	Velocity m/s	Std Dev m/sec	Num
1	90	272	21	14	417	25	14
	60	290	17	14	427	29	14
	30	287	27	12	441	39	12
	0	---	---	---	470	33	9
3	90	289	32	11	528	37	12
	60	301	39	12	490	35	12
	30	313	46	12	473	34	12
	0	---	---	---	424	14	6

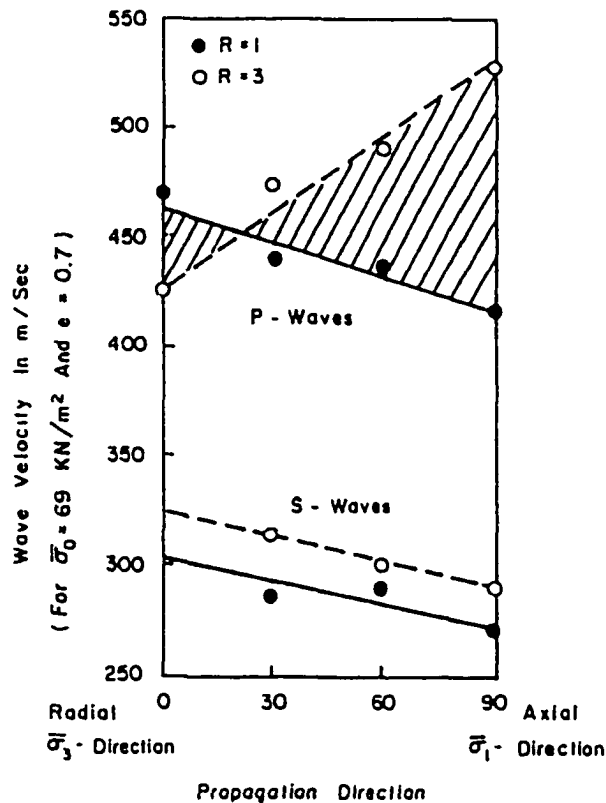


Figure 2.10 Effects of inherent and stress-induced anisotropy on elastic waves (Schmertman, 1977)

De Alba (1984) experimentally showed relationships between the elastic wave velocities and the liquefaction resistance of sands in terms of different sample preparation methods as seen in Figures 2.11 and 2.12. In his study, six different sands and three different preparation methods were used to show the effects of soil fabrics on the liquefaction resistance. The range of relative density was between 50% and 80%. Before soil specimens were saturated, shear and compressional waves were attempted to be measured by the pulse transmission method, but compressional waves could not be detected with the compression/expansion piezoelectric transducers until a saturation degree exceeded more than 99%. According to the results of De Alba's work, fluid wave velocity (V_{pf}) as well as shear wave velocity (V_s) showed a sensitivity of different fabrics

and had good relationships to the liquefaction resistance of soil specimens prepared by different preparation techniques. It was suggested that to simulate the dynamic characteristics of a soil deposit by using the reconstituted soil specimen, laboratory and field measurements of elastic-wave velocities should be considered. However, it was mentioned that those measurements were not enough to identify relationship between soil structure and the liquefaction resistance, and thus other soil parameters should be considered.

Ishibashi and Agarwal (1991) and Agarwal and Ishibashi (1992) measured P-wave and S-wave velocities along several directions relative to the principal stress axis in the cubical granular specimens. They modified the pulse transmission setup to detect elastic waves in dry granular media. The granular specimens were considered transversely isotropic and anisotropic dynamic elastic constants were recovered based on the elastic wave propagation theory and the experimental measurements. It was suggested that the anisotropy of granular materials could be identified by dynamic elastic constants.

Ishibashi and Kiku (1995) conducted a three dimensional discrete element model simulation to identify the effect of initial anisotropy on the liquefaction resistance. In the simulation study, directional longitudinal moduli (E_θ) and shear moduli (G_θ) were computed for the specimen, and it was noticed that those parameters significantly affect the liquefaction resistance but with different magnitudes. They suggested a parameter, $G_{avg}/(E_v/E_h)^3$, would be an influential parameter on liquefaction as shown in Figures 2.13 and 2.14, where G_{avg} is the average shear modulus on all directions, and E_v and E_h are the longitudinal moduli in vertical and horizontal directions, respectively.

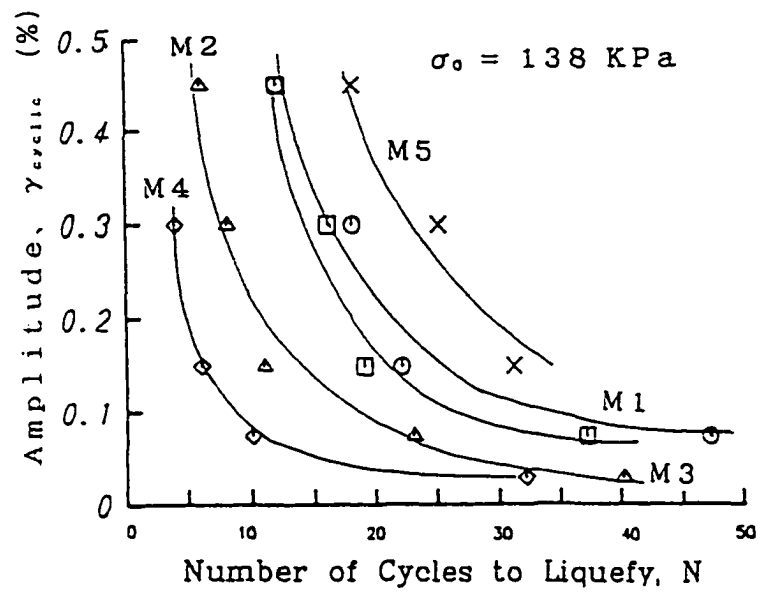


Figure 2.13 Liquefaction resistance under uniform cyclic strains (Ishibashi and Kiku, 1995)

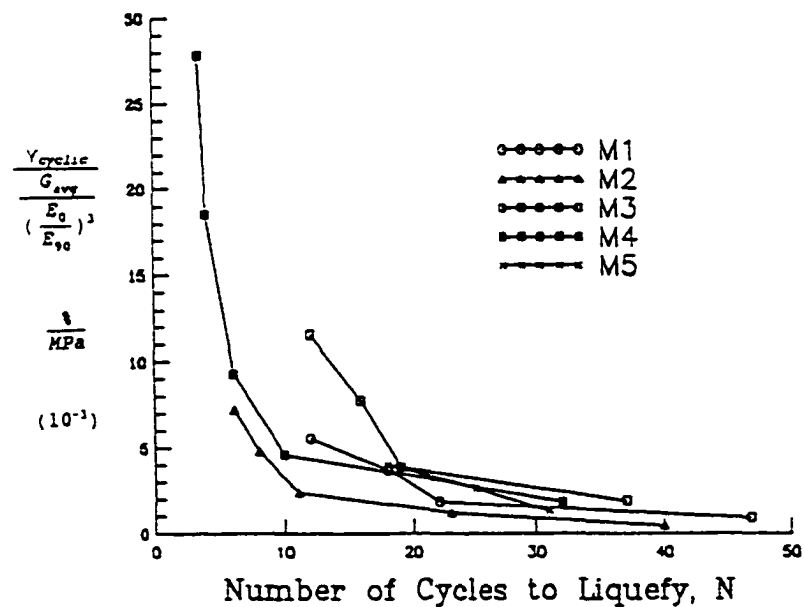


Figure 2.14 Normalized liquefaction resistance under uniform cyclic strains (Ishibashi and Kiku, 1995)

2.6.2 Evaluation of Liquefaction Resistance with Shear Wave Velocity

The pioneering work of Hardin and Richart (1963) found that shear modulus of sand is a function of void ratio and the n^{th} power of effective confining pressure. The empirical relationship among V_s (shear wave velocity), G (shear modulus), void ratio, and effective confining pressure are shown in Figure 2.15. The shear wave velocity and the dynamic shear modulus for dry round sands were expressed by the following equations:

$$V_s = [170 - 78.2e](\sigma')^{0.25} \text{ for } e < 80 \% \quad (2.11)$$

$$G = \frac{2630(2.17 - e)^2}{1 + e} (\sigma')^{0.5} \quad (2.12)$$

where V_s is shear wave velocity in ft/sec, e is void ratio, σ' is effective confining pressure in lb/in² and G is dynamic shear modulus in lb/in². Similar correlations for the angular-grained materials were proposed as:

$$V_s = [159 - 53.5e](\sigma')^{0.25} \quad (2.13)$$

$$G = \frac{2630(2.97 - e)^2}{1 + e} (\sigma')^{0.5} \quad (2.14)$$

After Hardin and Richart (1963), Hardin and Black (1968) investigated many other expected affecting parameters on shear modulus. They specified shear modulus as:

$$G = A \cdot F(e) \cdot g(\sigma') \quad (2.15)$$

$$A = f(H, S, \tau_0, C, a, f, \vartheta, T) \quad (2.16)$$

Where A is a function of several parameters: H , ambient stress and vibration history; S , degree of saturation; τ_0 , octahedral shear stress; C , grain characteristics; a , amplitude of strain; f , frequency of vibration; ϑ , soil structure; and T , temperature parameter. $F(e)$ is a

function of void ratio. Since then, numerous empirical relations have been established for different soils as shown in Table 2.5 (Ishihara, 1996).

Imai (1977) analyzed in-situ specimens using hundreds of P-wave and S-wave velocities measured in Japan, and showed that P-wave velocities ranged from 1700 to 1800 m/sec for soils with N-values varying between 5 to 200. He pointed out that the fluid P-wave velocity was almost unrelated to the stiffness of a soil skeleton, but S-wave velocities showed a satisfactory correlation to the liquefaction resistance. This correlation led many researchers to work on formulating the liquefaction resistance of soils in terms of V_S velocity and shear modulus.

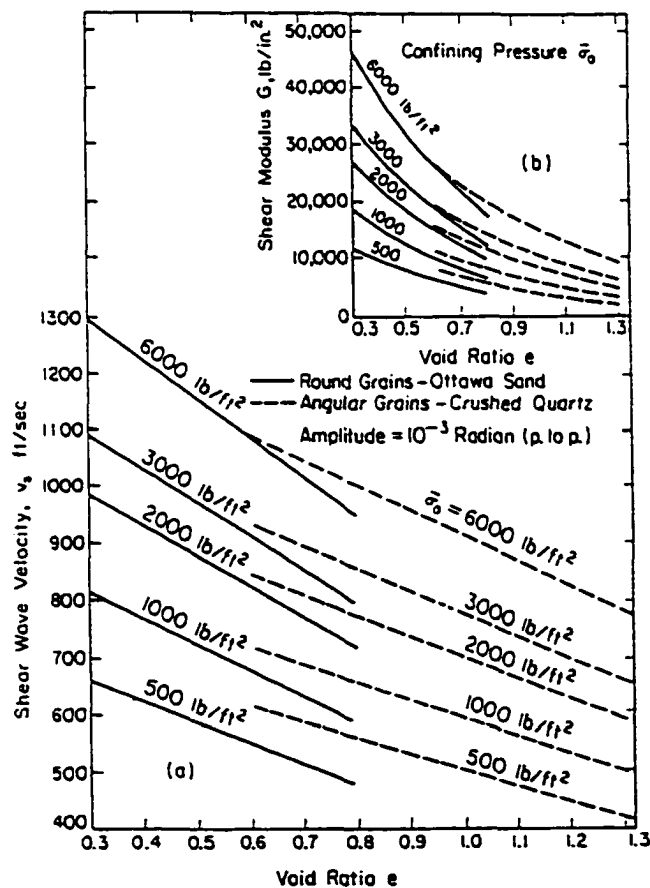


Figure 2.15 Correlation of shear wave velocity and shear modulus with the void ratio and the confining pressure for dry sands (Hardin and Richart, 1963)

Table 2.5 Constants in proposed empirical equations on small strain shear modulus:

$$G_0 = A F(e) (\sigma_0')^n \quad (\text{Ishihara, 1996})$$

	References	A	$F(e)$	n	Soil Material	Test Method
Sand	Hardin-Richart (1963)	7000	$(2.17 - e)^2 / (1 + e)$	0.5	Round grained Ottawa sand	Resonant column
		3300	$(2.97 - e)^2 / (1 + e)$	0.5	Angular grained crushed quartz	Resonant column
	Shibata-Soelamo (1975)	42000	$(67 - e)^2 / (1 + e)$	0.5	Three kinds of clean sand	Ultrasonic pulse
	Iwasaki et al. (1978)	9000	$(2.17 - e)^2 / (1 + e)$	0.38	Eleven kinds of clean sand	Resonant column
	Kokusho (1980)	8400	$(2.17 - e)^2 / (1 + e)$	0.5	Toyoura sand	Cyclic triaxial
	Yu-Richart (1984)	7000	$(2.97 - e)^2 / (1 + e)$	0.5	Three kinds of clean sand	Resonant column
Clay	Hardin-Black (1968)	3300	$(2.97 - e)^2 / (1 + e)$	0.5	Kaolinite, etc.	Resonant column
	Marcuson-Wahls (1972)	4500	$(2.17 - e)^2 / (1 + e)$	0.5	Kaolinite, $I_p^{**} = 35$	Resonant column
		450	$(4.4 - e)^2 / (1 + e)$	0.5	Bentonite, $I_p = 60$	Resonant column
	Zen-Umehara (1978)	2000 - 4000	$(2.97 - e)^2 / (1 + e)$	0.5	Remolded clay, $I_p = 0 \sim 50$	Resonant column
	Kokusho et al. (1982)	141	$(7.32 - e)^2 / (1 + e)$	0.6	Undisturbed clay, $I_p = 40 \sim 85$	Cyclic Triaxial

* σ' : kPa, ** I_p : Plasticity Index

After proving the dependency among the soil parameters and shear wave velocities, Tokimatsu et al. (1986 and 1990) created the definition of normalized shear modulus as:

$$G_v = \frac{G_0}{(\sigma_0')^n F(e_{min})} \quad (2.17)$$

where G_0 is the shear modulus specified in Equation 2.15. The constant n was defined as 0.5 by Hardin and Richart (1963), but they chose n as $2/3$ because it provided a better

correlation. $F(e_{min})$ is a function of minimum void ratio representing the effect of soil density. By substituting, Eq.2.15 to Eq.2.17, and G_N becomes:

$$G_N = A [F(e)/F(e_{min})] \quad (2.18)$$

$$F(e) = (2.17 - e)^2 / (1 + e) \quad (2.19)$$

where $F(e)/F(e_{min})$ shows the effect of density, and e_{min} is the minimum void ratio of soil. "A" represents the effects of soil fabric created by stress and strain histories and is defined from 500 to 900 when effective confining pressure and G_0 were in kgf/cm^2 . It was concluded that after the corrections, no matter the kind of soil type or confining pressure, the normalized shear modulus has a positive parallel relationship with the liquefaction resistance for Toyoura and Niigata sands as seen in Figure 2.16.

Based on the work of Tokimatsu et al. (1986) and Tokimatsu and Uchida (1990), another empirical correlation between cyclic stress ratio (CSR) and shear wave velocity was given by Andrus (1999). An extensive research was conducted based on field data consisting of 70 different sites and 26 different earthquakes covering from clean fine sand to sandy gravel with cobbles as seen in Figure 2.17. The empirical correlation of the cyclic stress ratio to shear wave velocity was expressed in the following special equation

$$CSR = \left\{ a \left(\frac{CV_{s1}}{100} \right)^2 + b \left(\frac{1}{V_{s1}^* - CV_{s1}} - \frac{1}{V_{s1}^*} \right) \right\} \left(\frac{M_w}{7.5} \right)^{-2.56} \quad (2.20)$$

where M_w is the magnitude of an earthquake, and the range of magnitude is from 5.9 to 8.3 on the Richter scale. C is the correction factor due to the causes of aging, cementation and negative pore water pressure. "a" and "b" are curve fitting parameters and are defined as 0.022 and 2.8, respectively. V_{s1} is the corrected shear wave velocity in the field in terms of effective overburden pressure (σ'_0). It is shown as:

$$V_{s1} = V_s \left(\frac{P_a}{\sigma'} \right)^{0.25} \quad (2.21)$$

where V_s is the real field shear wave velocity through soil deposits under the water table. P_a is 100 kPa or atmospheric pressure approximately 1 atm, and σ' is the effective overburden pressure. The following V_{s1}^* values were used as the upper limit value of V_{s1} at the state of liquefaction. It varies with fine content (F_C) as:

$$\left. \begin{aligned} V_{s1}^* &: 215 \text{ m/sec} && \text{for } F_C \leq 5\% \\ V_{s1}^* &= 215 - 0.5(F_C - 5) \text{ m/sec} && \text{for } 5\% < F_C < 35\% \\ V_{s1}^* &= 200 \text{ m/sec} && \text{for } F_C \geq 35\% \end{aligned} \right\} \quad (2.22)$$

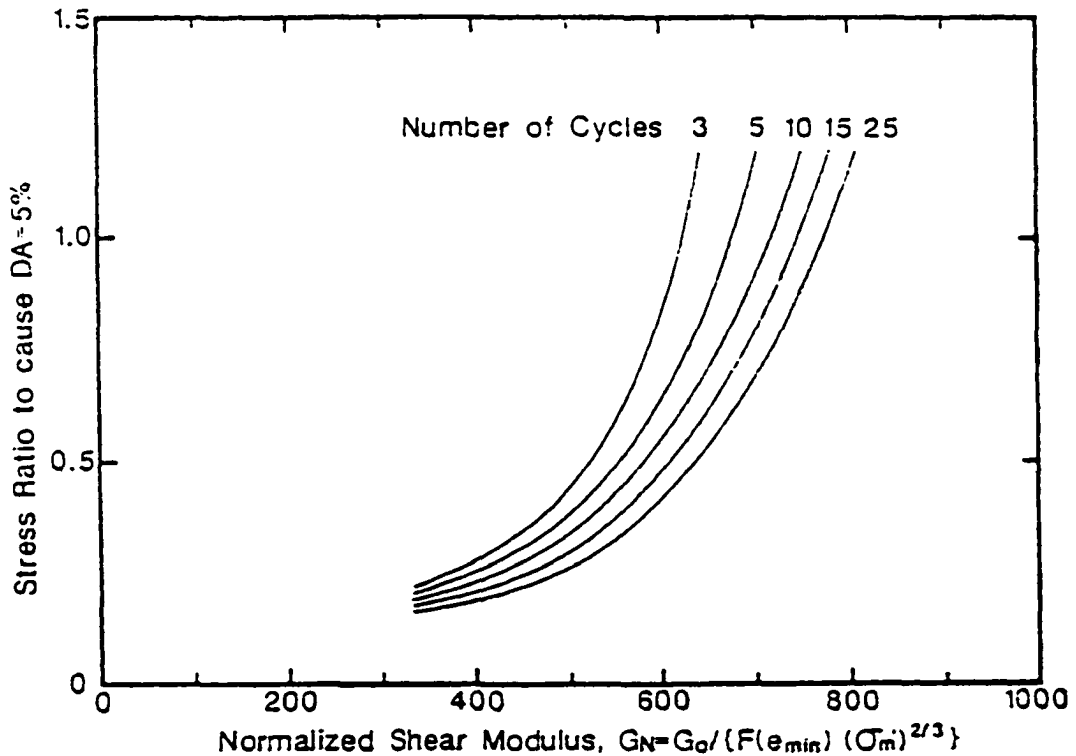


Figure 2.16 Correlation between normalized shear modulus and liquefaction cyclic stress ratio (Tokimatsu and Uchida, 1990)

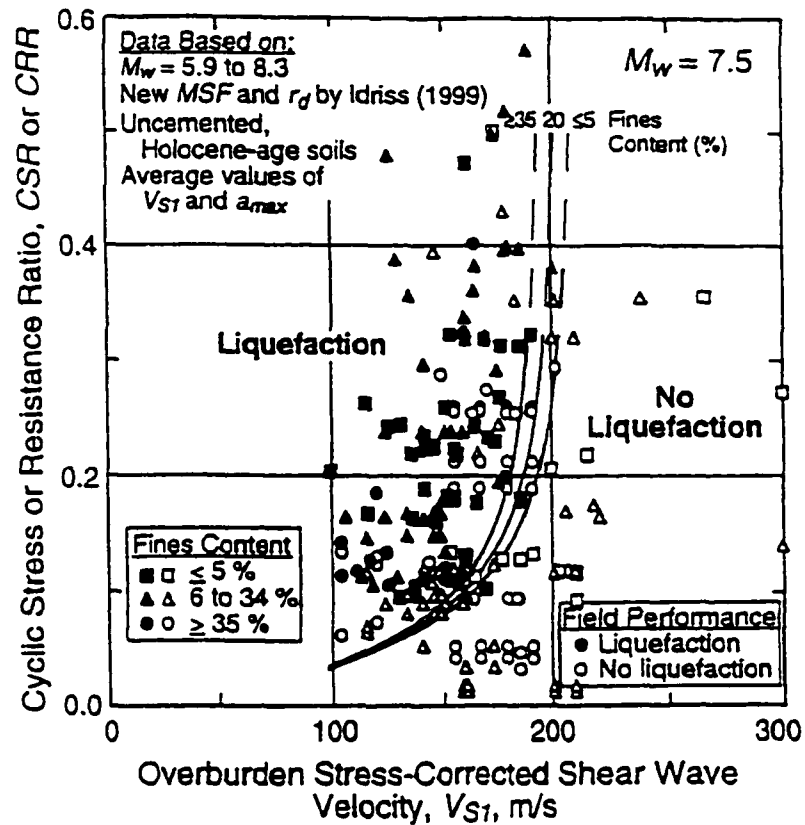


Figure 2.17 Empirical correlation between cyclic stress ratio (CSR) and shear wave velocity (Andrus, 1999)

In summary, according to good relationships between V_s and the liquefaction resistance of soil by field data (Andrus and Stokoe, 1997, Andrus, 1999), and by laboratory experimental data (De Alba et al., 1984), it can be concluded that anisotropy of soil are significantly related to shear wave velocities and shear modulus.

Concerning the fact that the density of a soil deposit alone is not enough to evaluate the dynamic characteristics of soil, reconstituted soil specimens can not fully represent inherent anisotropy of the soil in the field. Nevertheless, by using a correlation between field and laboratory shear wave velocity measurements, the gap can be closed.

Lastly, existing empirical formulations of shear modulus and shear wave velocity by means of void ratio and effective confining stress need to be improved and should be combined with a factor including soil fabric or the effect of anisotropy.

CHAPTER 3

LABORATORY EXPERIMENTS

3.1 Introduction

The focus of this research is to quantitatively determine the anisotropic characteristics of granular materials and to establish their relationship to the liquefaction resistance. As mentioned in the previous chapter, the liquefaction resistance could vary due to the initial soil fabrics (anisotropy) even for the same soil with a specific density. Anisotropy can be expressed by the directional mechanical properties of the soil, such as longitudinal moduli, shear moduli, and Poisson's ratios. In order to investigate the effects of the anisotropy on the liquefaction resistance in a quantitative way, the following experiments were carried out:

- Properties of the sand used in this research were determined.
- Three different specimen preparation techniques, air pluviation (AP), moist tamping (MT), and moist vibration (MV) were employed to investigate the different initial soil fabrics.
- Specimens were fully saturated and consolidated under the same effective stress, and undrained cyclic triaxial tests were performed to determine the liquefaction resistance of each soil specimen.
- After the specimen was prepared, elastic wave velocities were measured by means of a pulse transmission method during saturation process, and before cyclic triaxial test.
- Isotropic consolidation tests were conducted to determine the compressibility of each specimen.

- During the consolidation tests, elastic wave velocities were also measured to examine the effects of effective consolidation stress and saturation.
- To obtain comprehensive information about the saturation and effective confining stress on the characteristics of elastic waves, each specimen was subjected to different effective confining stresses under dry and saturated conditions

In this chapter, details on the soil sample, the experimental setups and the tests procedures are explained.

3.2 Properties of Material

One of the most liquefiable granular materials is fully saturated, uniform and loose fine to medium sand deposits. Therefore, a uniform medium dense sand was chosen for the testing program. The properties of the material are given in the following sections.

3.2.1 Grain Size Distribution

Virginia Beach (VB) sand was used in this study. A sieve analysis was performed to determine the grain size distribution of the VB sand and is presented in Figure 3.1. Based on the characteristics of the grain size distribution, VB sand is a uniformly graded, subangular sand. Previous studies confirmed that there is a considerable fine-content effect on the liquefaction resistance. The material contains less than 0.74% fine. Therefore, the effect of fine content on the liquefaction resistance is considered to be insignificant in this study.

Table 3.1 Material characteristics of VA Beach sand

USCS Parameters			Dry Unit Weight		Specific Gravity
D_{50} (mm)	C_u	C_c	Minimum $\gamma_{dmin}(\text{lb}/\text{ft}^3)$	Maximum $\gamma_{dmax}(\text{lb}/\text{ft}^3)$	Gs
0.291	2.044	0.914	92.142±0.108	105.384±0.106	2.685±0.012

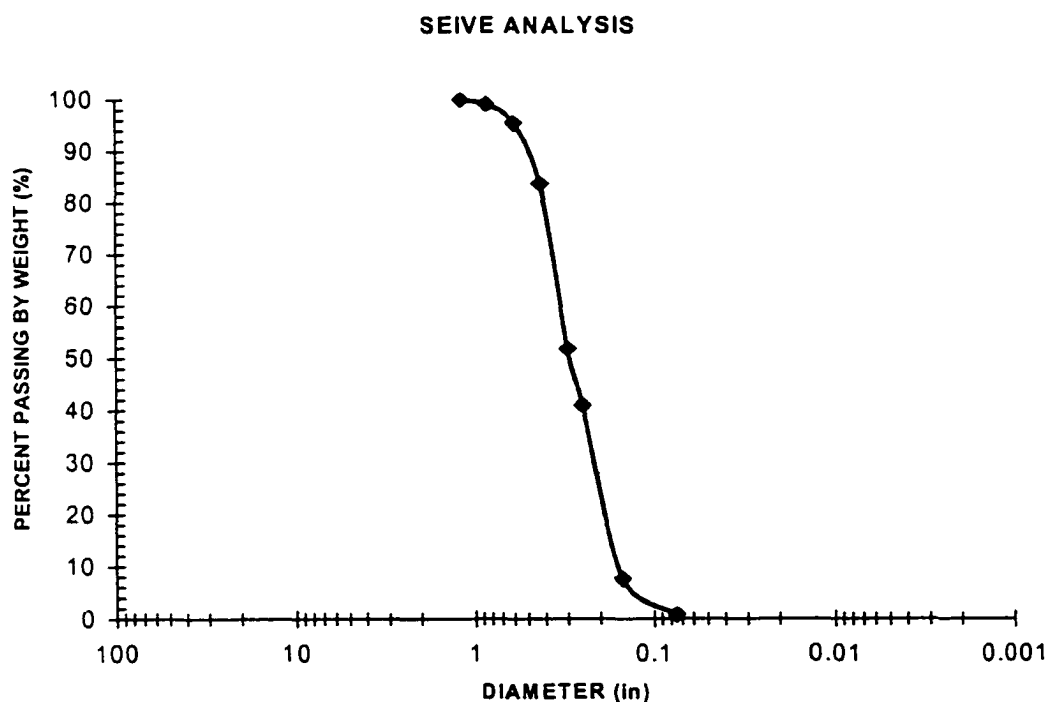


Figure 3.1 The grain size distribution of Virginia Beach sand

3.2.2 Index Properties

The laboratory classification parameters, the coefficient of uniformity, and the coefficient of curvature are given in Table 3.1. According to Unified Soil Classification System (USCS), the range of grain size for the sand is between 4.75 and 0.075 mm. Virginia Beach sand falls in this range. The uniform coefficient (C_u) is less than 6, and the coefficient of curvature (C_c) is less than one. All these indicate that Virginia Beach

sand is uniformly graded sand. The specific gravity (G_s) of the sand was determined as 2.685 ± 0.012 .

3.2.3 Relative Density

The maximum and minimum dry densities were determined in accordance with ASTM D4253-83 and D4254-83 for the five dry soil specimens. The minimum and maximum dry densities are $\gamma_{dmin}=92.142 \pm 0.108$ lb/ft³ and $\gamma_{dmax}=105.384 \pm 0.106$ lb/ft³, respectively. Relative density (D_r) was determined by the following equation:

$$D_r = \frac{e_{max} - e_n}{e_{max} - e_{min}} \times 100(\%) = \left(\frac{\frac{1}{\gamma_{dmin}} - \frac{1}{\gamma_{dn}}}{\frac{1}{\gamma_{dmin}} - \frac{1}{\gamma_{dmax}}} \right) \times 100(\%) \quad (3.1)$$

where e_{max} and e_{min} are void ratios of the soil in the loosest and the densest conditions, respectively, and e_n is the current void ratio of the soil. The minimum (e_{min}) and maximum (e_{max}) void ratios of VB sand were determined to be 0.590 and 0.819, respectively. The relative density describes the denseness of granular soils based on the current void ratio, and this relates approximately to many engineering properties such as strength and stiffness. Therefore, it is one of the key parameters to identify the liquefaction resistance of the soil as shown in Figure 3.2 (De Alba et al., 1975).

In this study, the relative density of the reconstituted specimens was chosen to be 50% which represents a loose to medium-dense material; in other words, the void ratio (e_n) of each specimen should be 0.705. Since the grain size distribution emphasizes a uniformity of VB sand, there is a very close range between the maximum and minimum dry densities. The relative densities of each specimen had to be between 48% and 52% to be accepted. Otherwise, specimen was rejected.

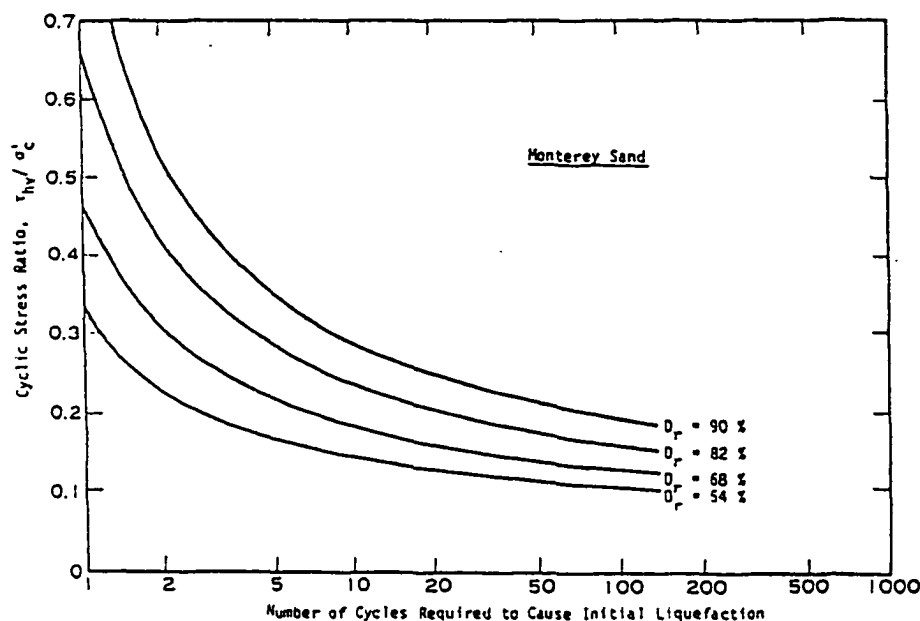


Figure 3.2 Relationship between relative density and liquefaction resistance (De Alba et al., 1975)

In order to obtain the desired relative density, the changes of the diameter and height of soil specimens were investigated. It was observed that during trials of preparations of soil specimens, readings of diameters of specimens fell in between 2.800 to 2.815 inch. It was figured out that preparation techniques affected the dimension of diameter. Especially, the tamping rod for moist tamping technique and the surcharge load for moist vibration technique push the membrane in lateral direction. The specimens were 2.2046 lbs of air-dried Virginia Beach sand for AP specimens and 2.1561 lbs for MT and MV specimens. By considering the dry weight and the minimum and maximum diameters of soil specimens, the desired heights of the specimens were calculated as shown in Table 3.2 and 3.3. It was observed that the relative densities of specimens were very sensitive by small changes in the dimensions of the specimens.

Table 3.2 Geometric and index parameters of AP specimens

Dr	e	γ_{dry}	Weight	Volume	Minimum Diameter	Maximum Diameter	Maximum Height	Minimum Height
%	%	lb/ft ³	lb.	ft ³	In.	In.	in.	in.
48	70.94	98.06	2.2046	0.0225	2.8000	2.8150	6.3095	6.2425
49	70.71	98.19	2.2046	0.0225	2.8000	2.8150	6.3011	6.2341
50	70.48	98.32	2.2046	0.0224	2.8000	2.8150	6.2926	6.2258
51	70.26	98.45	2.2046	0.0224	2.8000	2.8150	6.2842	6.2174
52	70.03	98.58	2.2046	0.0224	2.8000	2.8150	6.2758	6.2091

Table 3.3 Geometric and index parameters of MT and MV specimens.

Dr	e	γ_{dry}	Weight	Volume	Minimum Diameter	Maximum Diameter	Maximum Height	Minimum Height	S
%	%	lb/ft ³	lb.	ft ³	In.	in.	in.	in.	%
48	70.94	98.06	2.1561	0.0220	2.8000	2.8150	6.1707	6.1051	0.3028
49	70.71	98.19	2.1561	0.0220	2.8000	2.8150	6.1625	6.0970	0.3038
50	70.48	98.32	2.1561	0.0219	2.8000	2.8150	6.1542	6.0888	0.3047
51	70.26	98.45	2.1561	0.0219	2.8000	2.8150	6.1460	6.0806	0.3057
52	70.03	98.58	2.1561	0.0219	2.8000	2.8150	6.1377	6.0725	0.3067

In addition, elastic wave velocities were measured in vertical and horizontal directions (V_{pv} , V_{sv} , and V_{ph}), with various D_r of specimens. The results of the tests are illustrated in Figures 3.3, 3.4 and 3.5. As seen in those figures, there is no significant correlation between D_r and the velocities with the range of this relative density. The variations in the values of V_{pv} , V_{sv} and V_{ph} for $D_r=48\%$ to 52% under the 5 psi effective pressure were approximately ± 2.1 , ± 3.8 and $\pm 3.2\%$, respectively. When 10 psi effective pressure was applied on the specimens, the variations in the values of V_{pv} , V_{sv} , and V_{ph} reduced to ± 1.4 , ± 3.1 and $\pm 3.3\%$, respectively. Therefore, based on the measured elastic wave velocities, the range of relative densities (48 to 52%) of the specimens is to be considered very small.

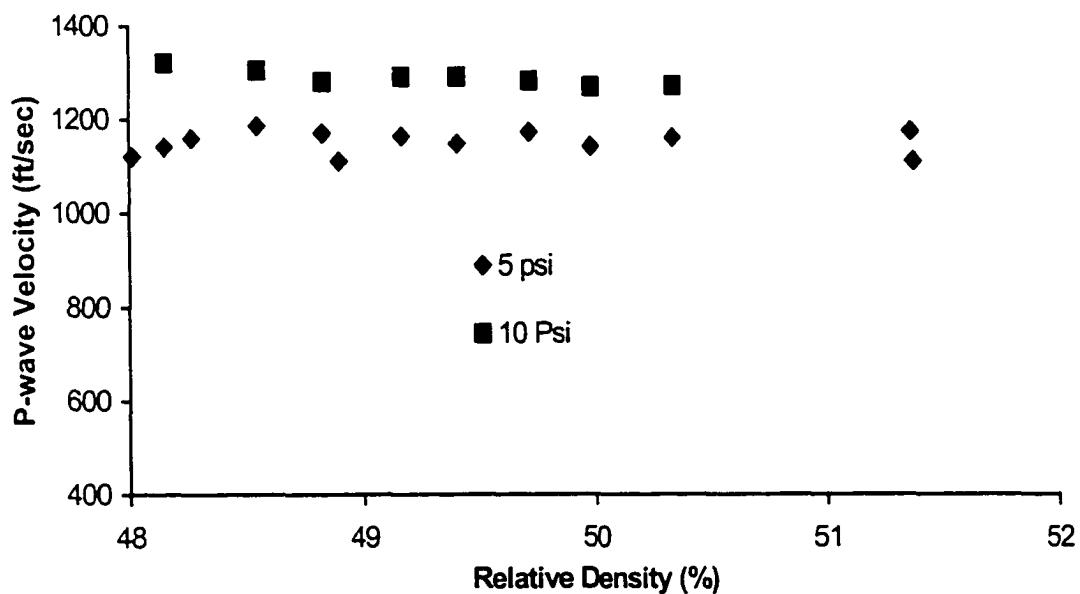


Figure 3.3 Effect of relative density on vertical P-wave velocities (V_{p_v}) of AP specimens

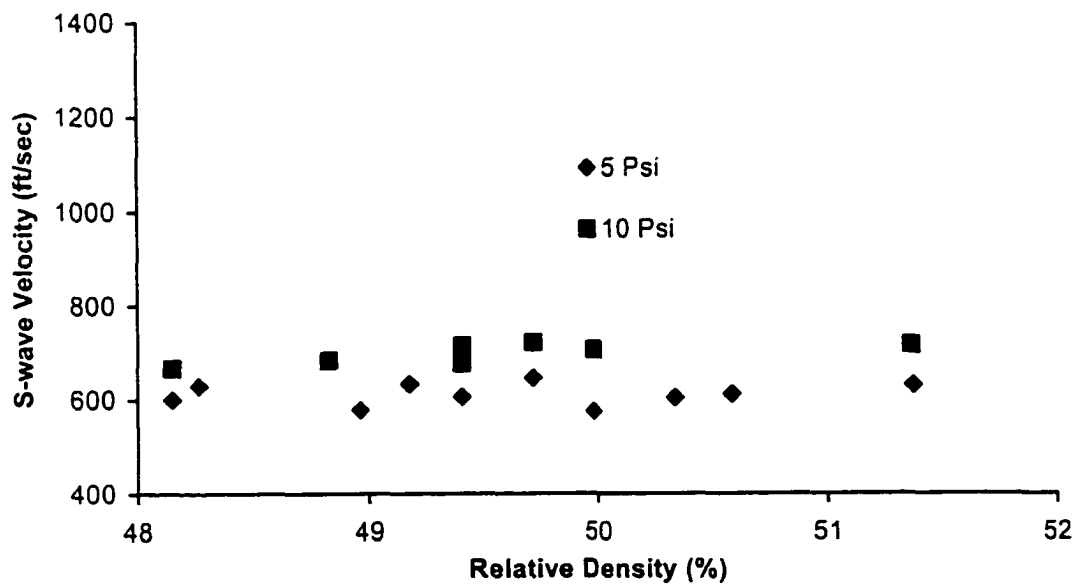


Figure 3.4 Effect of relative density on horizontal S-wave velocities (V_{s_v}) of AP specimens

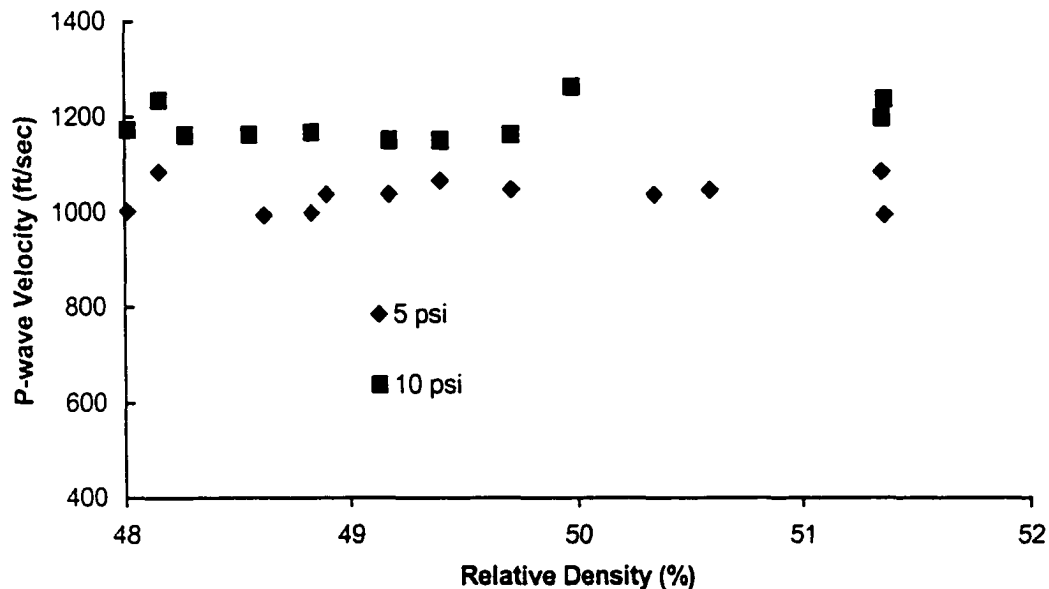


Figure 3.5 Effect of relative density on horizontal P-wave velocities (V_{ph}) of AP specimens

3.3 Cyclic Triaxial Test Setup and Procedure

The liquefaction resistance is determined by undrained cyclic triaxial tests. The triaxial test allows the application of axial and horizontal stresses to a cylindrical specimen. Although this test has some disadvantages, like non-similarity to in-situ stress, no rotation of the principle stress axes, etc., it has a simple mechanism and is commonly used by engineers around the world. In addition, the triaxial test makes sample preparation much easier than other types of cyclic shear devices.

3.3.1 Dynamic Triaxial Test Setup

The standard triaxial cell was modified for this research as seen in Figure 3.6, and air pressure was used as a confining pressure through a cell pressure line. Considering the duration of the test procedures and the possibility of air penetrating through the membrane, another cell was installed inside of the triaxial test chamber; the Perspex inner

cell (PI-cell). The PI-cell was filled with water to prevent air from migrating through the membrane into the soil specimen.

Two load cells were installed into the setup. The first one (LC1) was assembled directly under the pedestal to record axial cyclic loading. The second one (LC2) was used as a loading controller and was attached to the top of the triaxial cell (the top of the loading rod) as shown in Figures 3.6 and 3.7. Monotonic and cyclic loading were introduced independently by two different pneumatic loaders, which were located at the top and the bottom of the triaxial apparatus as seen in Figures 3.6 and 3.8. The loading system will be discussed further in the following section.

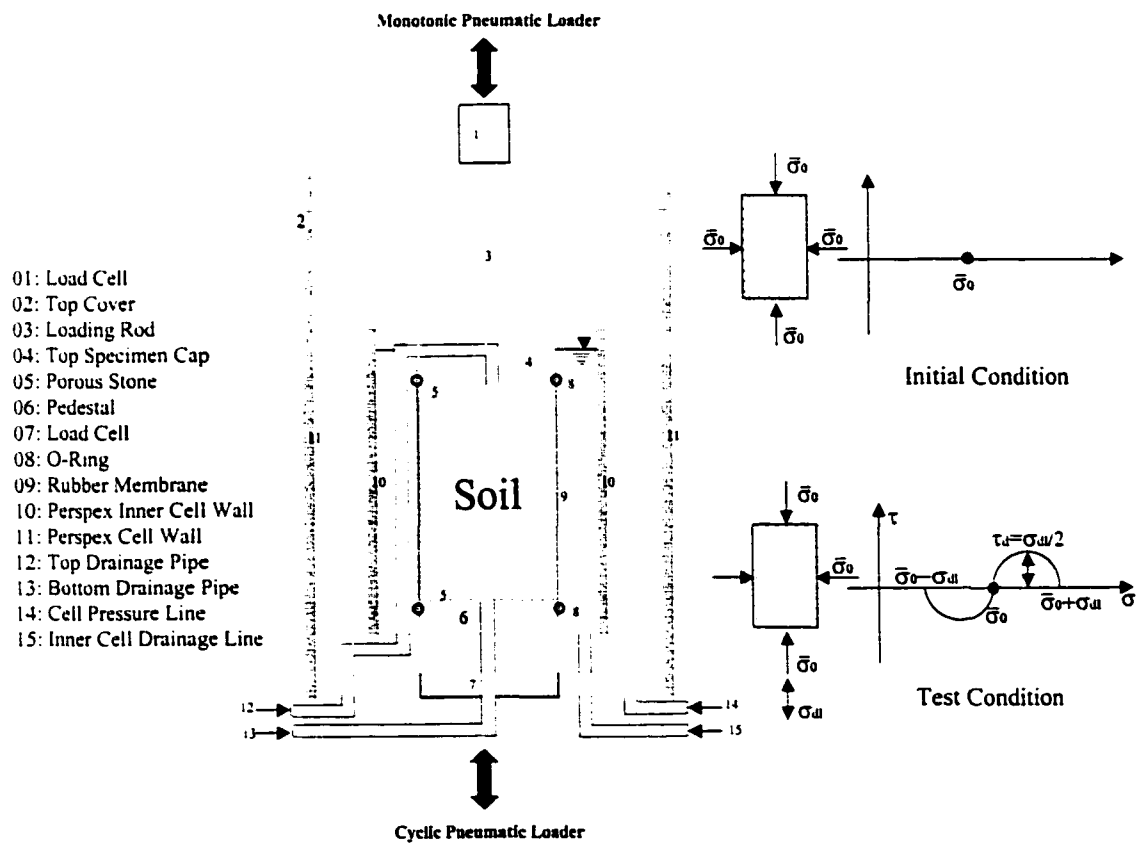


Figure 3.6 Cyclic triaxial test apparatus

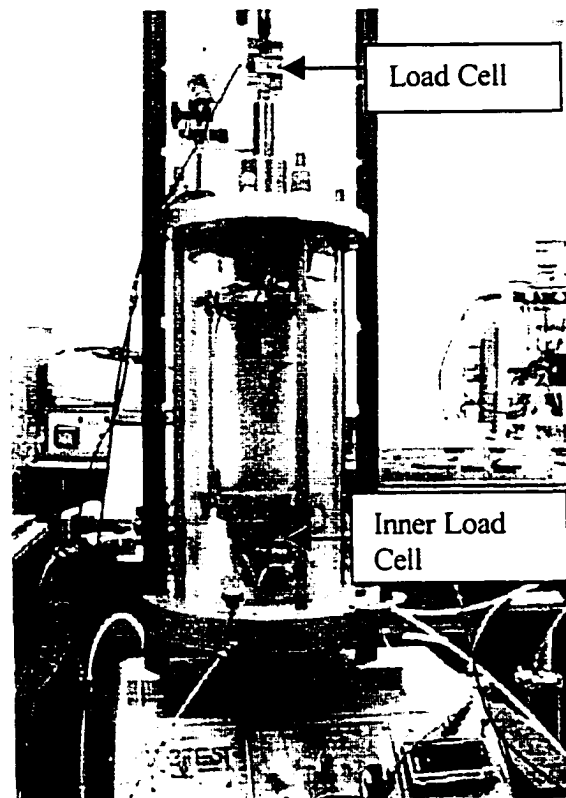


Figure 3.7 Two load cells used

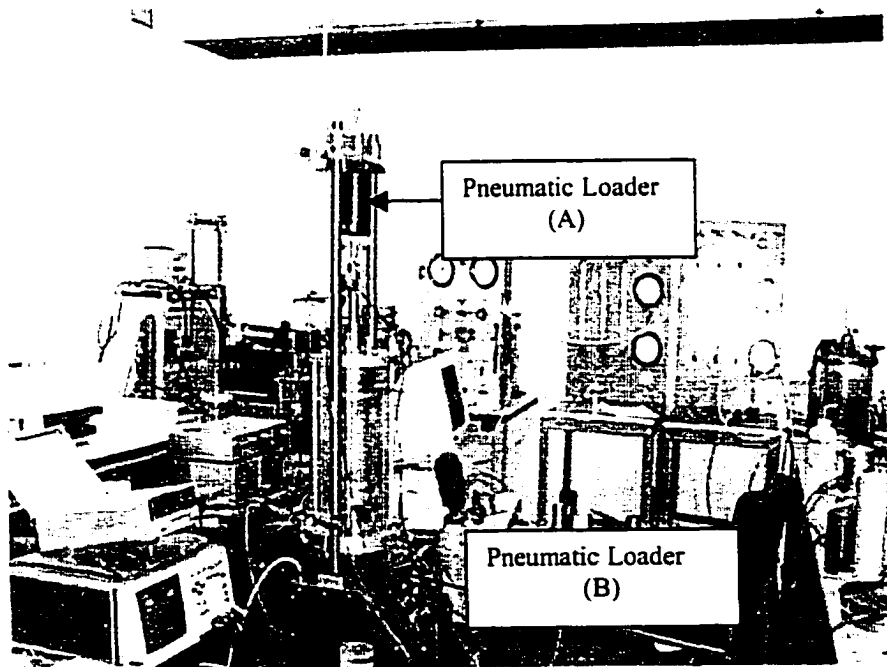


Figure 3.8 Axial (A) and cyclic (B) pneumatic loading system

3.3.2 Loading System

To control the axial (σ_1) and confining (σ_3) stresses independently, a special loading piston was constructed and connected to the specimen cap by means of a loading rod as seen in Figure 3.9. A steel disc 2.8 inches in diameter, which is the same as the specimen diameter, was tightly attached to the loading rod and smoothly fitted within a frictionless cylinder. When cell pressure σ_3 is applied on the specimen, σ_3 is also applied under the disc, so that σ_3 does not create any stress change in vertical direction of the specimen.

A pneumatic loader (A) was installed at the top of the loading rod in order to apply σ_1 during the consolidation and the saturation processes, as seen in Figures 3.8 and 3.9. σ_1 and σ_3 were increased manually at the same time, but independently, for isotropic loading. A calibration chart of σ_1 vs. σ_3 is plotted in Figure 3.10 with different specimen diameters (D).

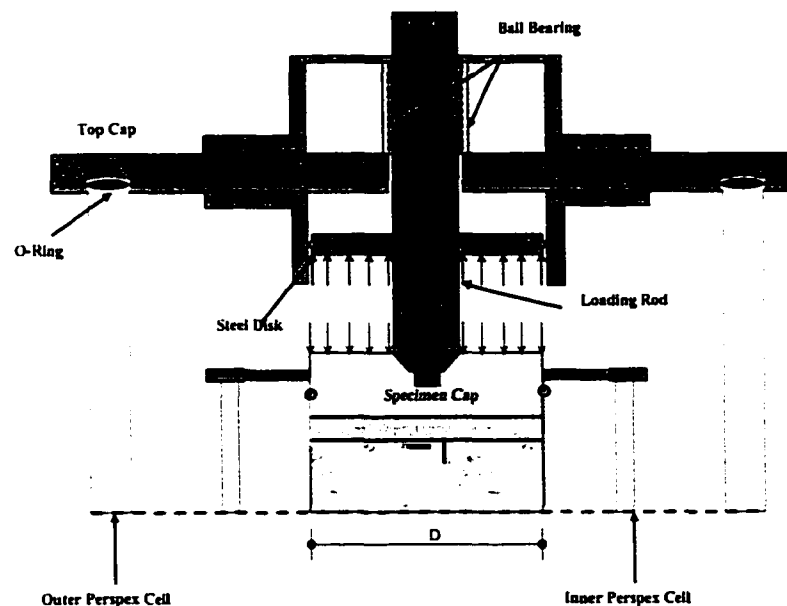


Figure 3.9 Schema of the cylindrical loading piston

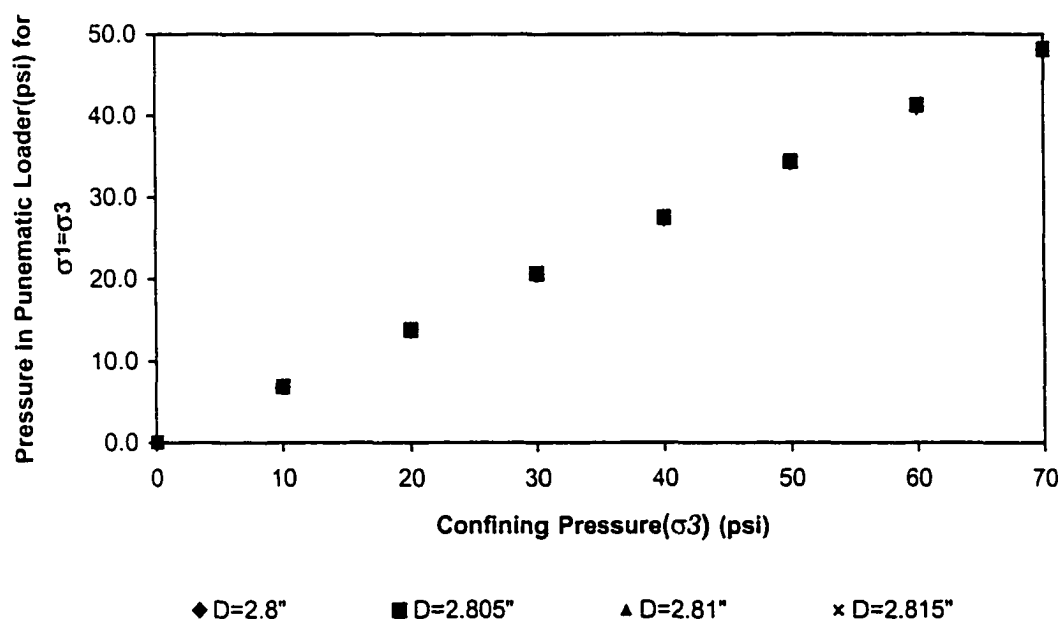


Figure 3.10 Calibration chart of the isotropic loading system

3.3.3 Variables Tested

Two load cells (LC1 and LC2) were installed on the triaxial apparatus. LC2 is attached to the top of the triaxial frame as shown in Figure 3.6 and 3.7, and LC1 is installed inside the triaxial cell. During the dynamic test, LC1 was used for reading the cyclic axial stress. LC2 was used to verify that σ_1 and σ_3 remained equal during the saturation and consolidation processes. The inner load cell (LC1) is a Sensotec model 41 tension/extension. It is extremely sensitive and has a reading range from 0 to 1000 lbs. The output sensitivity is 3mv/v. Temperature affects this reading $\pm 0.0002\%$ per $^{\circ}\text{F}$. It operates in temperatures ranging from -65°F to 250°F .

Pore water pressure was measured by a Sensotec porewater transducer, model THE 1708-12. The pressure range is 0 to 200 psi, output sensitivity is 2mv/v, and the excitation voltage is 10 VDC. It is connected to the bottom drainage line of the specimen.

Static axial displacement, generated by saturation and consolidation processes, was measured by a mechanical dial gauge with 0.001 inch resolution. Dynamic axial strain was measured by a Logic-basic digital gauge model BG1110-0-36, which was attached outside of the triaxial cell. Its range is 0-1.0 inches and the resolution is 0.001 inch.

3.3.4 Data Acquisition System

A 486DX33-PC computer was used for data acquisition. Communication between the cyclic triaxial test apparatus and the computer was established by means of Lab-PC⁺ interface card, which is a multifunctional analog and digital input/output board. This controlled and recorded the pneumatic loading system generating cyclic axial stress. During the cyclic tests, axial displacement, pore water pressure, and dynamic axial force were recorded with sensitivities of 0.0001 inches, 0.1 psi, and 0.1 lbs., respectively. Data storage rate was 400 data/sec.

3.4 Wave Generation and Measuring System

A pulse transmission by piezoelectric transducer method was used to measure elastic waves propagating in soil specimens. These elements are capable of generating and detecting waves even through a highly dispersed dry soil specimen.

Compression-expansion piezoelectric discs have been commonly used for generating compressional waves (De Alba et al., 1984 and Nagakawa et al., 1996 and 1997). When a specimen is dry, the amplitude of a received signal could be unmeasurable due to the high dispersive characteristics of dry soil. Agarwal et al. (1991) found that the compression-expansion disc can not generate a high amplitude of compressional waves passing through granular materials even if the input signals are amplified.

Previous studies showed that bender elements with two transversely expanding double piezoelectric plates can generate notable shear wave through soil (Dyvik and Madhus, 1985; Thomann and Hryciw, 1990; Ishibashi and Agarwal, 1991, Agarwal and Ishibashi, 1992; Zeng and Ni., 1998 and 1999). A bender element consists of two piezoceramic plates bonded together as shown in Figure 3.11. If the two piezoceramic plates are polarized in the same direction (serial connected), the expansion and contraction of the plates creates a bending motion, which thus creates waves. In addition, bender elements are affected by any mechanical disturbance such as bending of the elements. This mechanical bending of the element lets the piezoelectric plates generate a voltage. It works like a motion detector.

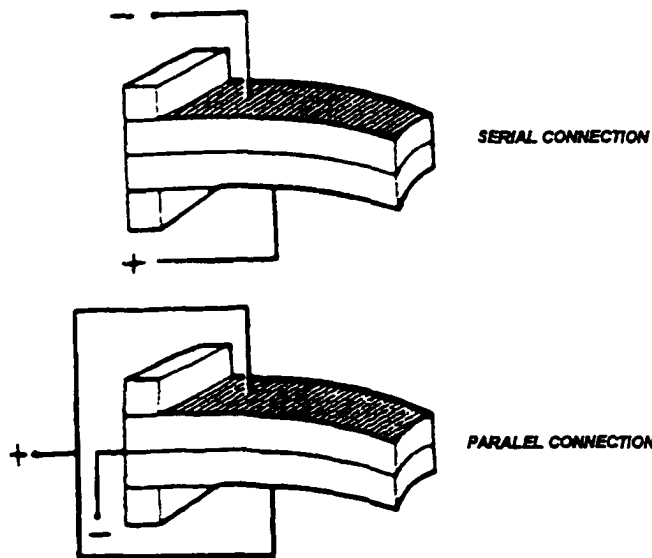


Figure 3.11 Design of the bender element wiring (adapted from Matroc Inc. manual)

3.4.1 Compressional and Shear Wave Transducers Design

The bender elements (0.41x0.41x0.024 inches), model number PZT-5B, were purchased from Morgan Matroc Inc. As seen in Figure 3.11, there are two different wiring connection possibilities for bender elements: serial and parallel connections. Dyvik and Madshus (1985) and Thomann and Hryciw (1990) mentioned that series connected bender elements generate a higher voltage, but a lower motion, almost half, than parallel connected bender elements. Because of these differences, they suggested that the serial connected bender elements should be installed as a receiver and the parallel connected bender elements should be used as transmitters. However, the wiring of parallel bender elements is a very formidable task. It is possible to damage bender elements during the process. In addition, bender elements need to be re-cut and this could reduce the efficiency of the bender elements. If an input signal was highly amplified, it can be easily detected by the serial connected bender elements. Therefore, serial connected bender elements were used for this research.

Two bender elements are embedded in the top cap and the pedestal of the triaxial device as receivers and transmitters in the vertical direction for P- and S-waves. In addition, two bender elements are attached to the membrane surrounding the soil specimen to measure horizontal P-wave velocities as seen in Figure 3.12.

The properties of bender elements change due to time and mechanical stress. Aging and time should be considered. It has been experienced that some time after installing bender elements, the efficiency gradually dropped. Therefore, the bender elements were replaced frequently. It is hard to give an exact lifetime of these elements because the life expectancy depends on the amplitude of output signals and the mechanical stress induced by the cyclic triaxial test. In addition, because of the wiring

design and the mechanism of bender elements, precaution must be taken to protect the bender elements from short circuit due to the presence of water or any conductive materials in the soil. Therefore, a water-resist coating, M-Coat-A air-drying polyurethane was applied over the bender elements and wires. Considering the effect of the thickness of the coating on the mechanical behavior of the bender elements, the elements before and after coating were tested on conductive dried sand specimens. By observing the first arrival time of received waves, no noticeable effects were experienced. The thickness of the coating layers did not pass 0.12 inch.

In order to install the bender elements into the triaxial test cell, a Teflon disc with a diameter of 1 inch and 0.275-inch thickness was embedded at the center of the top cap and the pedestal of the triaxial cell. A hole drilled in the center of each disc allowed the electrical wires to come out and to be soldered to the bender elements. As mentioned before, the bender element characteristics gradually change due to time and the loading test. Therefore, when the efficiency dropped, the bender elements were changed and the system was recalibrated.

3.4.1.1 Compressional Wave Transducer Design

Two bender elements, the receiver and transmitter, are embedded in the top cap and the pedestal of the triaxial device. These were used to generate and measure compressional (P) waves in the longer axial direction of the specimen as seen in Figure 3.13a. After insulating the bender element with M-Coat-A air-drying polyurethane, the bender element was embedded into two Teflon plates and the effective cantilever length was fixed at 0.325 inches.

Two other bender elements are attached to the membrane surrounding the soil specimen to measure horizontal compressional (P) wave velocities as seen in Figure

3.13b. The bender element was mounted on a 0.5-inch square hard PVC plate with epoxy. After mounting the element, a 0.335 inch long cantilever action was achieved. Then the plate was attached on a see-saw aluminum beam (0.50x5.8x0.130 inches) with a screw as seen in Figure 3.12. The tip of the aluminum beam was attached to a 0.125 inch diameter and 4.1 inch long screw with a rubber joint in order to be pushed/pulled from outside of the cell manually. The rubber joint allowed adjustment of the angular movement of the beam and the horizontal back and forth movement of the screw. A small amount of petrolatum was put on the surface membrane before attaching the horizontal bender elements. It is experimentally observed that petrolatum allows good coupling between the bender elements and the specimen.

3.4.1.2 Shear Wave Transducer Design

As can be seen in Figure 3.13(a), one edge of the shear bender elements was glued into 0.025-inch wide and 0.5-inch deep slots opened into the Teflon discs, which are embedded in the top cap and the pedestal of the triaxial device to create cantilever action. They were also insulated with a M-Coat-A air-drying polyurethane.

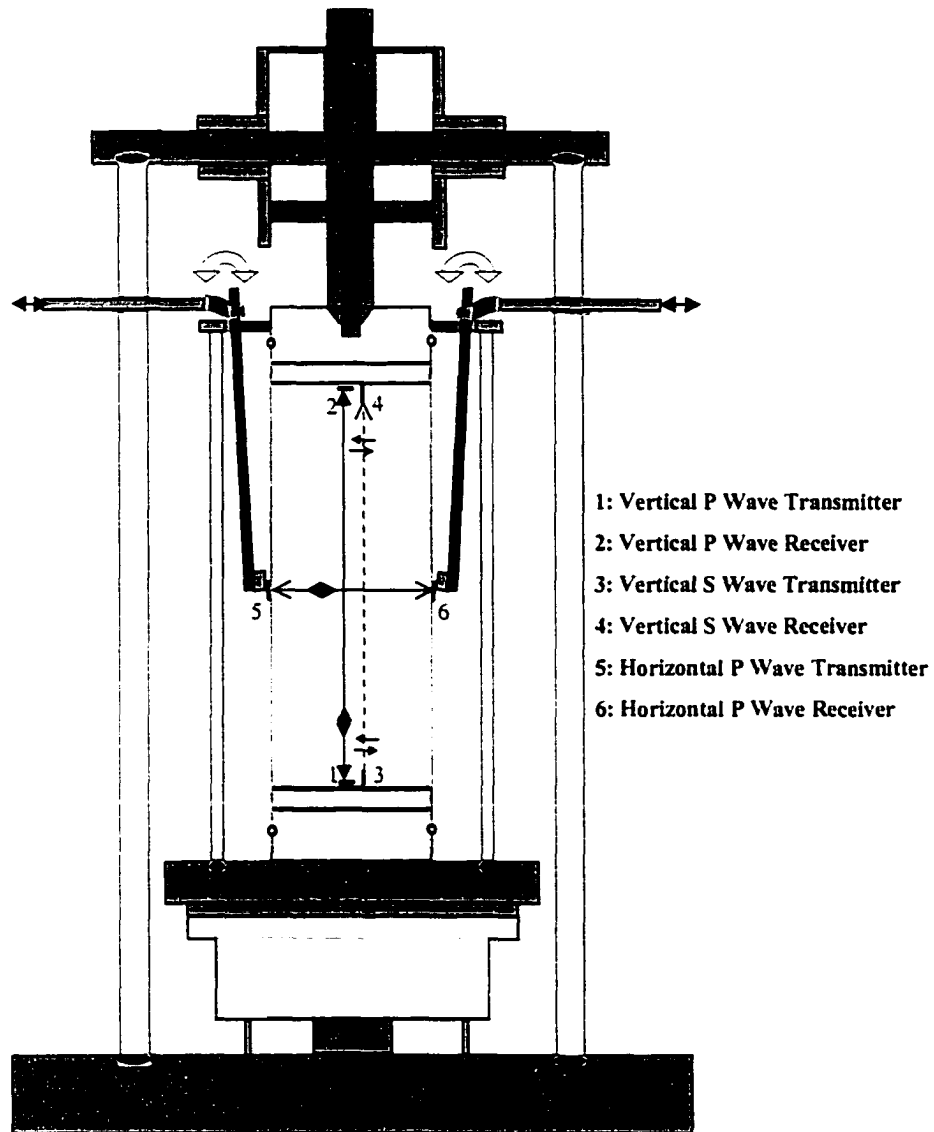
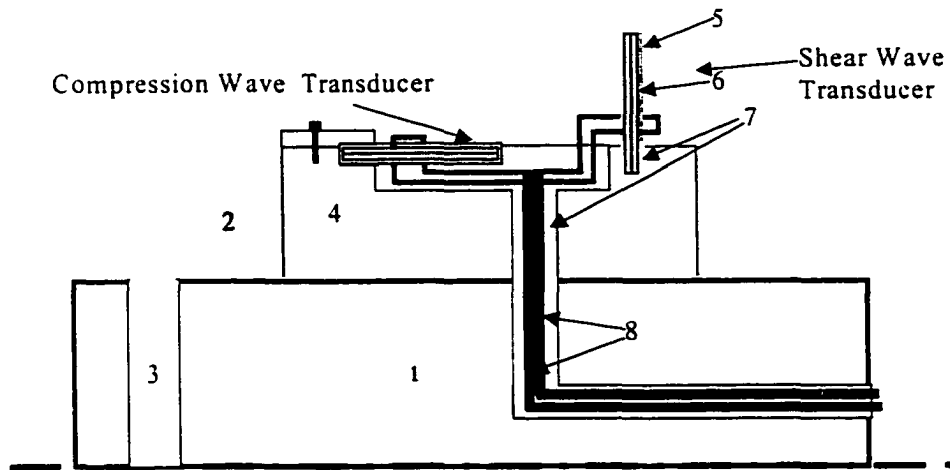
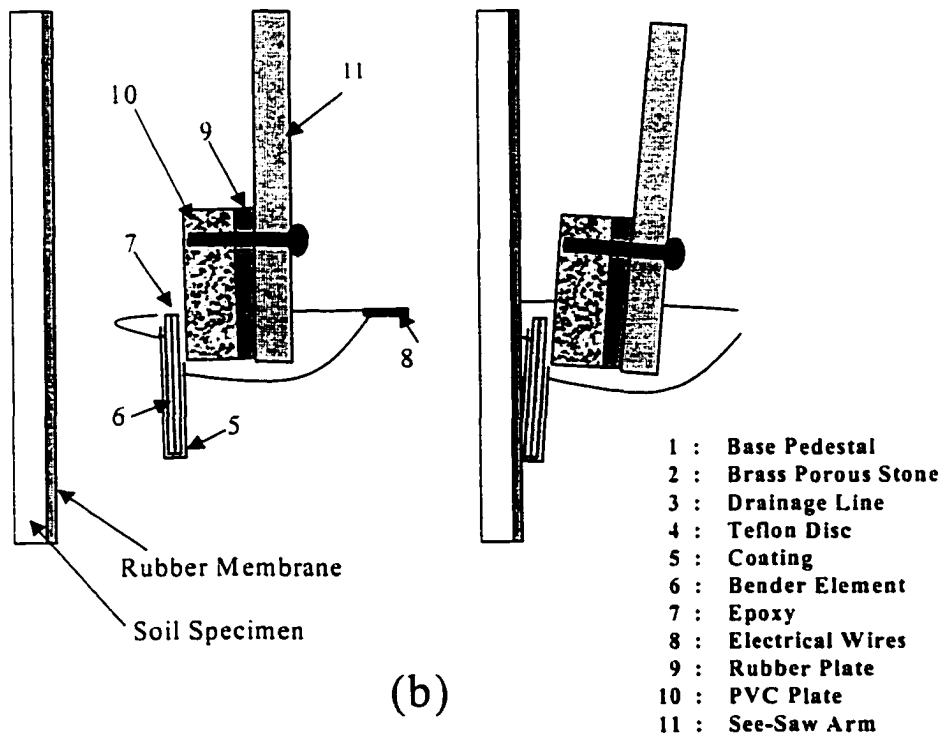


Figure 3.12 Bender elements installed in the triaxial cell



(a)



(b)

Figure 3.13 Design layout of compression and shear wave transducers (a) view of transducers at the top and pedestal (b) side view of transducers for radial application

3.4.2 Electrical Connections

Electrical connections of bender elements are shown in Figure 3.14. The pulse transmission system developed at Old Dominion University by Ishibashi and Agarwal (1991) was modified for this research. The electrical source wave was generated by using a Hewlett Packard HP811A pulse/function generator. The pulse/function generator is capable of generating different shaped pulses such as sinusoidal, square, half square and triangle wave forms. All waveforms, except sinusoidal, contain more than one frequency. After amplifying the input signals, the shapes of these waveforms are deformed easily, and interpreting the time difference between input and output signals becomes difficult. Therefore, a single-frequency sinusoidal waveform was chosen as the input signal. The output range of the generator is from 0.15 to 15 volts. The frequency range for generating pulse is from 0.1 Hz to 20 MHz.

The amplitude of generated wave signals was 10 volts. However, loose sandy materials have large damping characteristics and it is very difficult to detect the transmitted wave signals if the amplitude of input wave signal is not enough. Therefore, a generated signal was amplified by a special amplifier, which was developed at Old Dominion University in 1996. The output voltage of the function generator could be amplified up to 1000 peak to peak volts. The calibration chart for amplified generator voltage in terms of input voltage of the function generator is given in Figure 3.15. The output voltage of the function generator was changed from 1.5 to 11.0 volts to identify the effect on the received signals. When the soil specimens were dry, any output voltage of transmitted signal gave measurable data. When water was present in the material, an immediate reduction on the amplitude of received signals data was observed. It was found experimentally that if an output voltage was higher than 5 volts, measurable signals

were received. Therefore, 10 volts was chosen to generate measurable compressional waves by the receivers. It should be noted that 10 volts of input signal were amplified to 160 volts by means of the power amplifier and further amplified through a transformer to step up the voltage up to 960 volts AC. This is very high amplitude. However, to pass noise levels and to transmit the wave on a highly dispersive soil specimen, this high amplitude was necessary. The magnitude of this reference wave signal that was directly sent to the oscilloscope was gradually reduced by a 1 megaohm resistor to protect the oscilloscope from the high voltage input. A correlation showing a reduction on the magnitude of the reference wave signal is illustrated in Figure 3.16.

RG58/U-type coaxial shielded cables were used to minimize the electrical noise because the amplitude of received signals is in the minimum range of 5 mV to 100 mV. This amplitude is very small compared to the amplitude of transmitting signals. Therefore, electrical noise must be minimized. Input and output signals produced by piezoelectric bender elements were recorded by an HP54201A digitizing oscilloscope to calculate the travel time. It is a two-channel waveform acquiring digital storage oscilloscope. The sampling rate is 200×10^6 samples per second and are sufficient for this research and the minimum time resolution of the oscilloscope is 1 μ s. The pulse/function generator and the digitizing oscilloscope are shown in Figure 3.17. The oscilloscope is automatically triggered by the pulse from the step up transformer. The delay time between transmitted and received signals shows the travel time (t) as seen in Figure 3.18. The ratio of corrected distance (d) between the transmitting and receiving bender elements to the travel time (t) gives the wave velocity as:

$$V = \frac{d}{t_i} \quad (3.2)$$

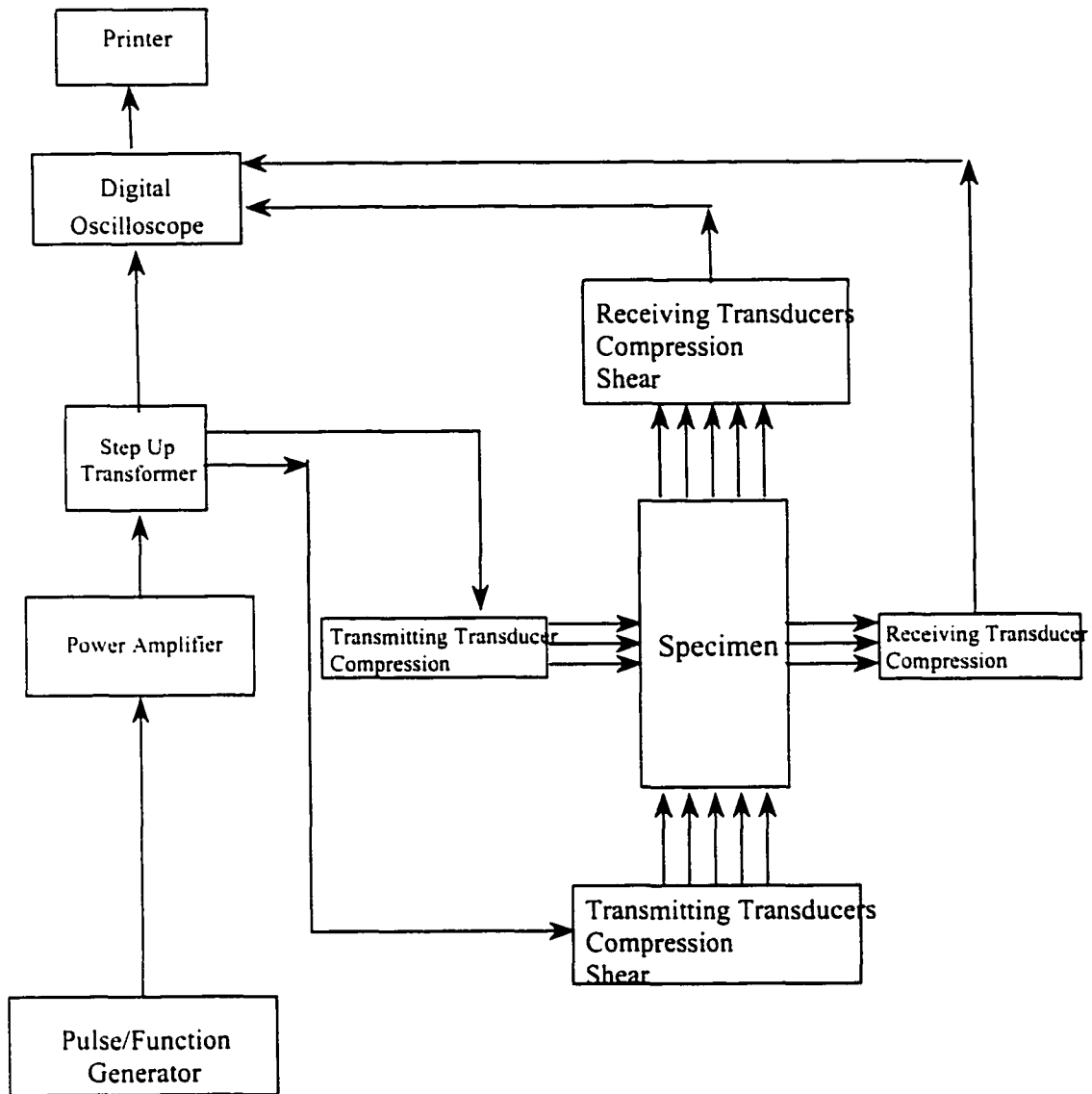


Figure 3.14 Electrical connections of bender elements (adapted from Agarwal, 1991)

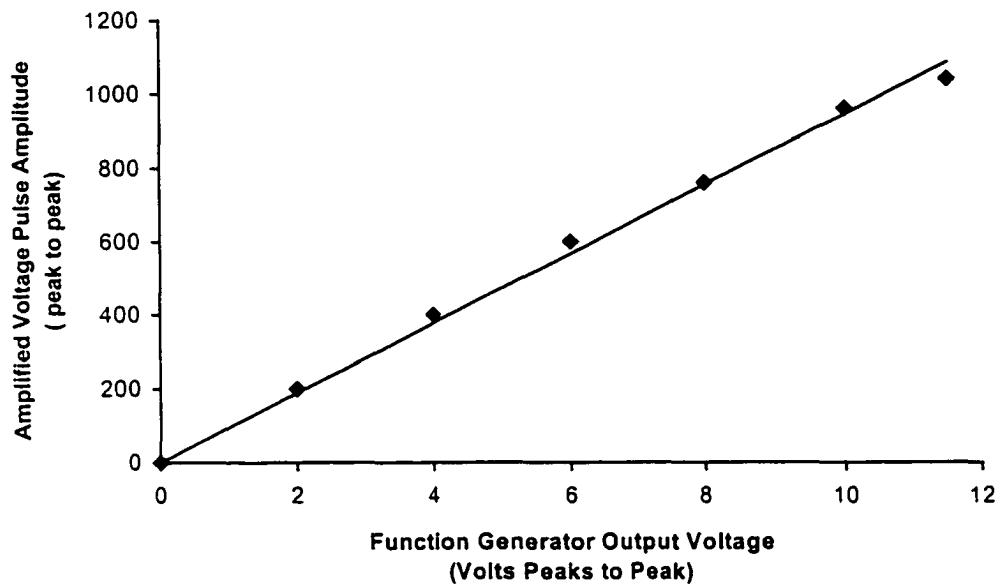


Figure 3.15 Calibration chart for amplified pulse amplitude

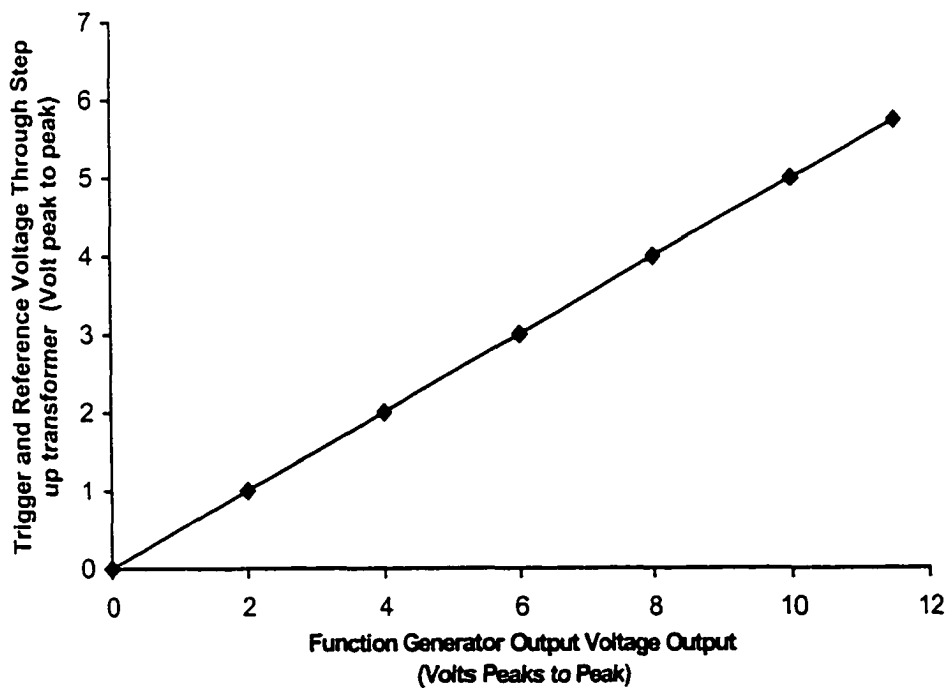


Figure 3.16 Correlation of trigger voltage to reference voltage output

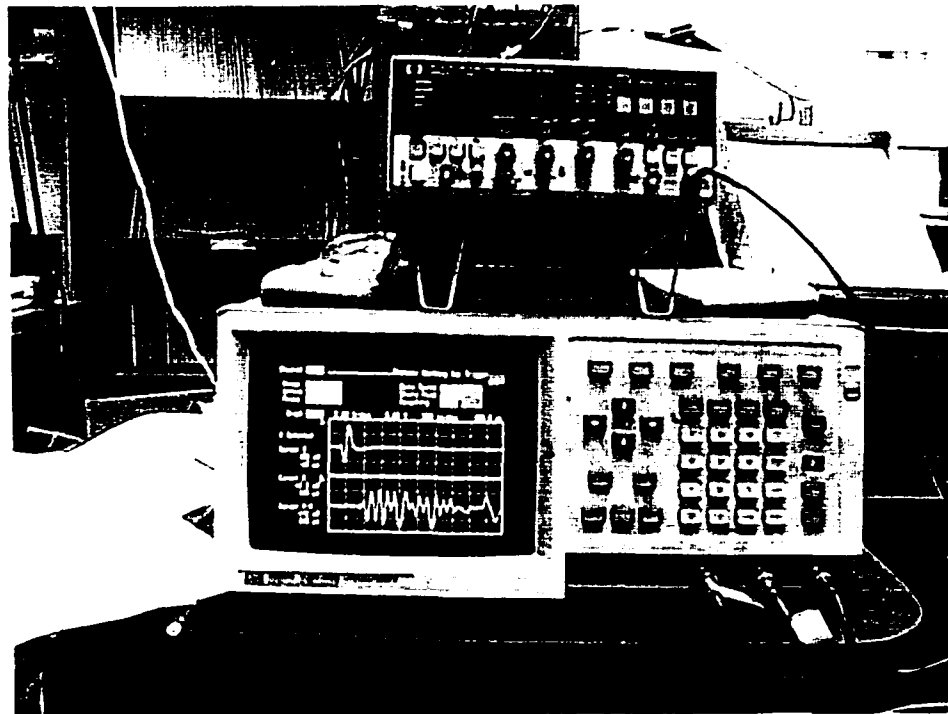


Figure 3.17 Schema of the pulse/function generator and the digitizing oscilloscope

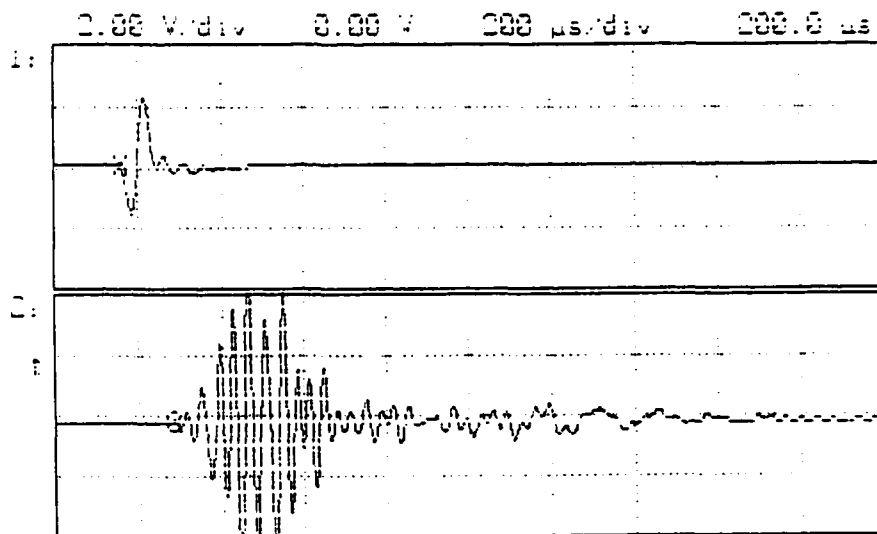


Figure 3.18 Typical transmitted and received wave signals from oscilloscope

All compressional and shear wave bender elements in the triaxial cell were wired by an RG-174 coaxial cable because of the availability of small space. On the outside of the cell, an RG 58/U coaxial cable was used to connect the transducers to the step up transformer and the digital oscilloscope. The reference signals were displayed after the signal came out from the step up transformer. The amplifier can produce a minimal change on the shape of the output signals, and it affects the arrival time. Since a perfectly designed amplifier can affect the shape of the signal, the reference signal must be taken just before a transmitter generates a pulse in the step-up transformer as seen in Figure 3.14.

3.4.3. Frequency of Elastic Waves

Firstly, specimens prepared by air-pluviation (AP) technique were used to investigate the frequency effects on bender elements performance. The soil specimens were first prepared under 5 psi vacuum pressure. Input amplitude of function generator was selected 10 volts, which corresponds to 960 volts to the bender elements after the amplifications. By changing the frequency of sinusoidal input signal from 1 to 30 kHz, elastic waves were measured under 5 psi and 10 psi effective stresses. The results are shown in Figures 3.19, 3.20 and 3.21. Indeed, frequency did not show any significant effect on wave measurements.

According to Nakagawa et al. (1997), P-wave and S-wave are not affected by the frequency of the waves. However, a certain frequency, close to the natural frequency of bender elements, can provide high output signals. Experimental trials showed that the best readings occurred between 17 to 22 kHz for vertical P-wave bender elements and between 20 to 30 kHz for horizontal P-waves.

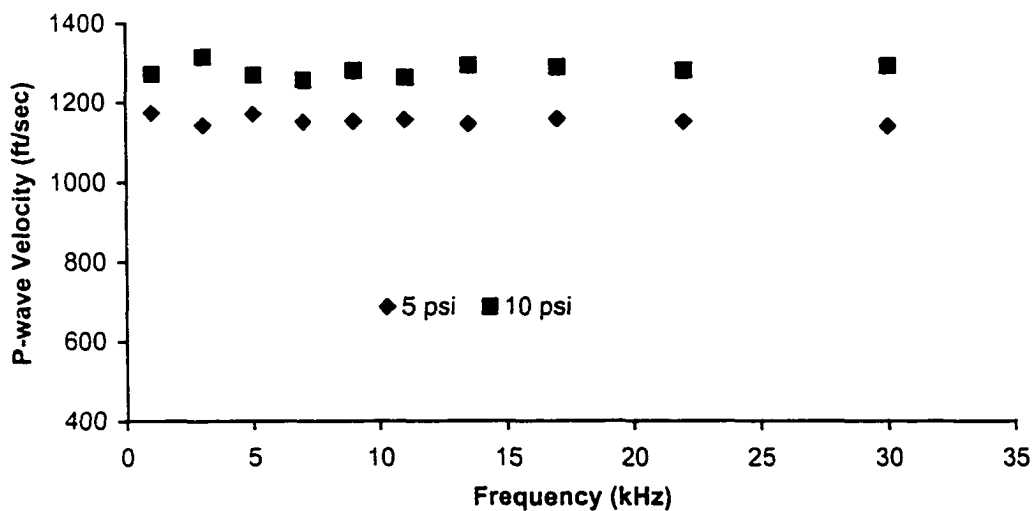


Figure 3.19 Effect of frequency on vertical P-wave velocities of AP specimens

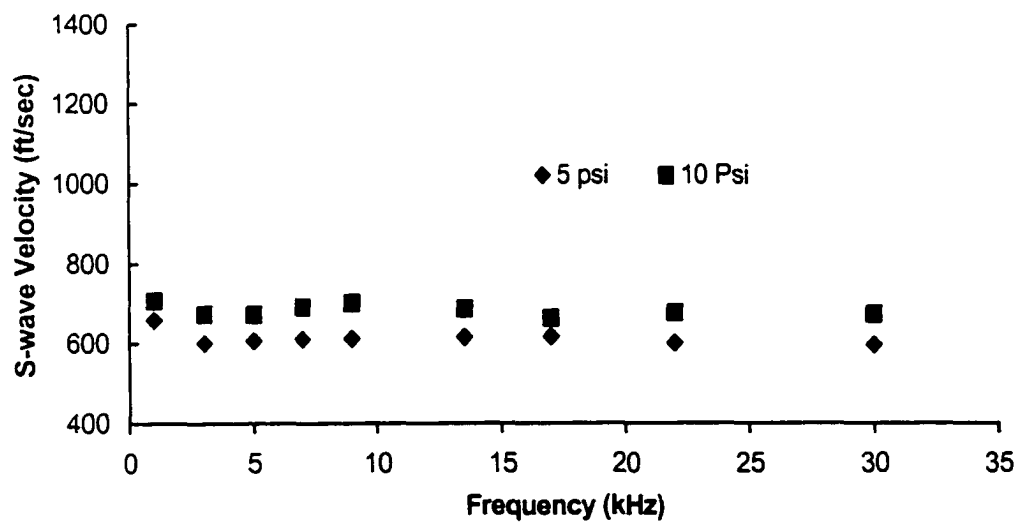


Figure 3.20 Effect of frequency on vertical S-wave velocities of AP specimens

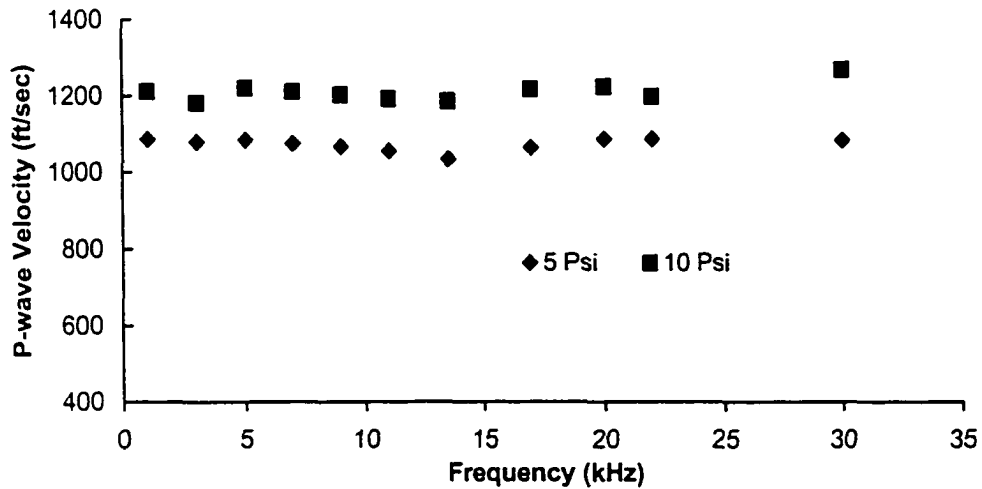


Figure 3.21 Effect of frequency on horizontal P-wave velocities in AP specimens

Another observation was that when the input frequency of S-wave bender element was higher than 9 kHz, P-wave or unknown waves were generated by S-wave bender elements, and those were overlapped on the first arrivals of S-waves. The graphical data of various frequencies test are given in Appendix B.

Additional consideration regarding to frequency of input signal is needed. Previous studies emphasized that the first arrival disturbance of a received wave may not represent the arrival of shear wave. Some other waves could overlap shear wave signals as seen in Figure 3.22. The first arrival wave was called a near-field component propagating in the specimen with the velocity of a compressional wave.

Viggianni et al. (1995a and b) suggested that because of a near-field effect, corresponding peaks of input-output signals can be more accurate to measure the travel time instead of using time difference between the first arrival time of input and output signals. Therefore, the near-field effects can be neglected.

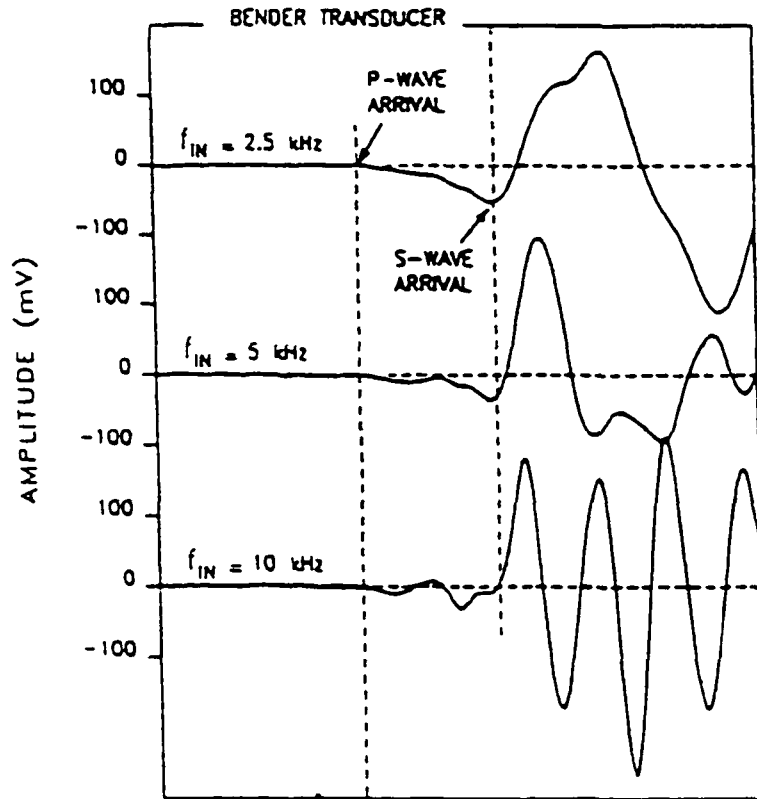


Figure 3.22 Shear wave velocity measurement under the near-field effect (Brignoli et al., 1996)

Brignoli et al. (1996) suggested that a specific frequency was needed to generate an input signal to reduce near-field effect. The frequency was obtained from the following relations:

$$V_s = \lambda f \quad (3.3)$$

$$R_d = \frac{d}{\lambda} \quad (3.4)$$

where V_s is the shear wave velocity measured from the experiment, λ is the wave length and f is the frequency of input pulse. R_d is a ratio showing the number of wave lengths between the bender elements. It was assumed that shear wave velocity was not affected by the frequency. As seen in Figure 3.22, it was experimentally found that the effect of

the near-field component begins to decrease with an increase in the frequency of the input pulse. The higher frequency gives a higher number of wave lengths and R_d increases. If R_d is around 4 or more, the effect of the near-field component significantly decreases.

Jovicic et al. (1996) reviewed Vigianni et al.'s work experimentally and theoretically. The near-field effect was investigated at $R_d=1.1$ to 8.1 and V_s was measured with an accuracy of $\pm 1\%$. It was pointed out that at a low value of R_d the near-field effect influences the first arrival time of the shear wave peak. It was also suggested that without conducting complex numerical analyses direct measurement from an oscilloscope is enough to determine the shear wave velocity.

Boulander et al. (1998) and Arulnathan et al. (1998) reported that R_d is not a sufficient parameter to evaluate enough to reduce the near-field effect and the dimensions of the bender element should be considered. They defined R value as:

$$R = \lambda / I_b \quad (3.5)$$

where I_b is the length of both transmitter and receiver bender elements.

They indicated that observation of input-output signals of V_s decreases with increasing R_d and increases with decreasing λ/I_b . The results are illustrated in Figure 3.23. R values were changed 3 to 18 by using a different frequency of the input signals. As seen in Figure 3.24, the best reading can be obtained when R is less than 8. They also indicated that the measured shear waves of different soils could be differently influenced by R and R_d ratios.

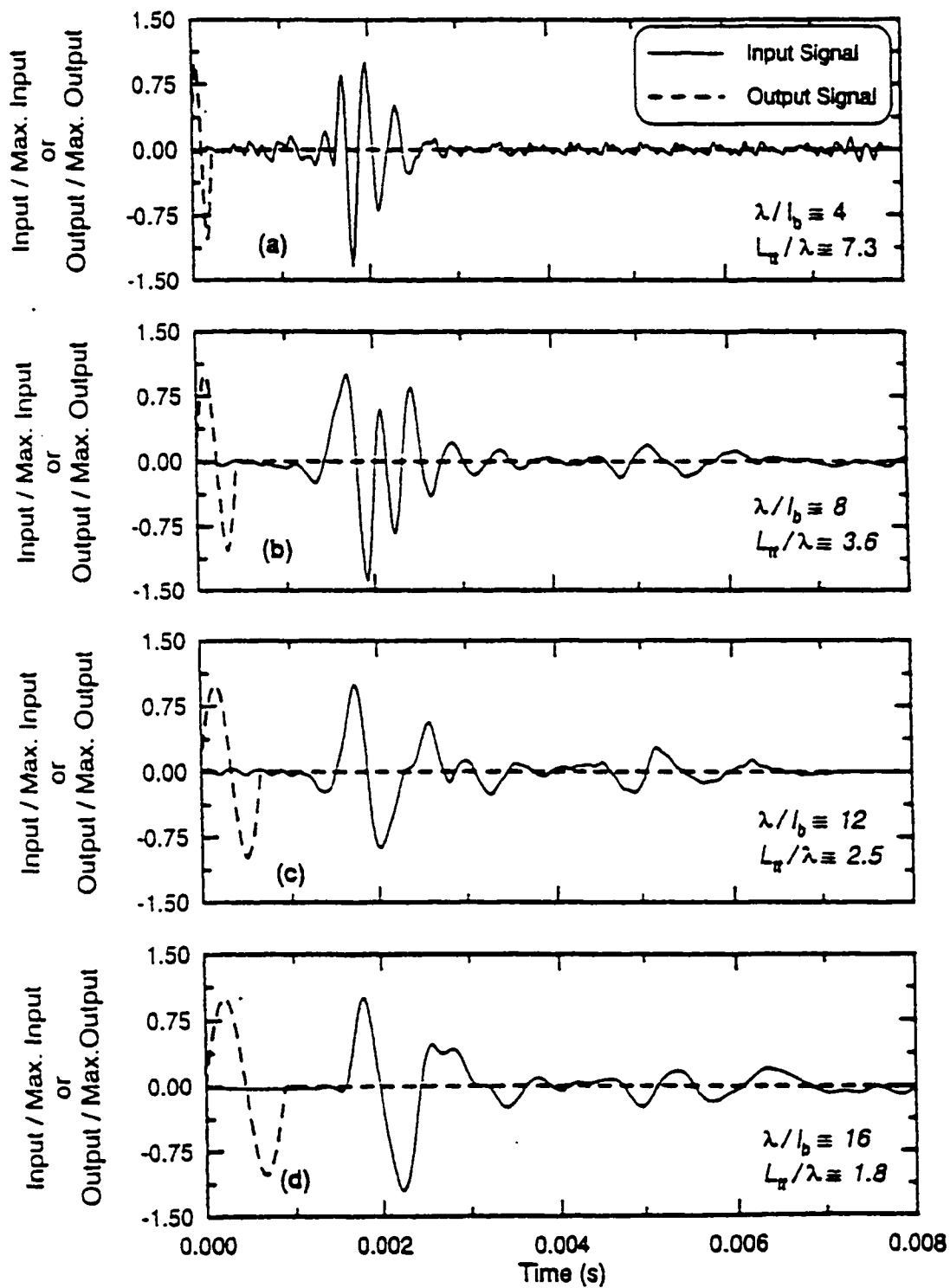


Figure 3.23 Near field effect on the output signal due to the dimensions of the bender element (l_b) (Arulnathan et al., 1998)

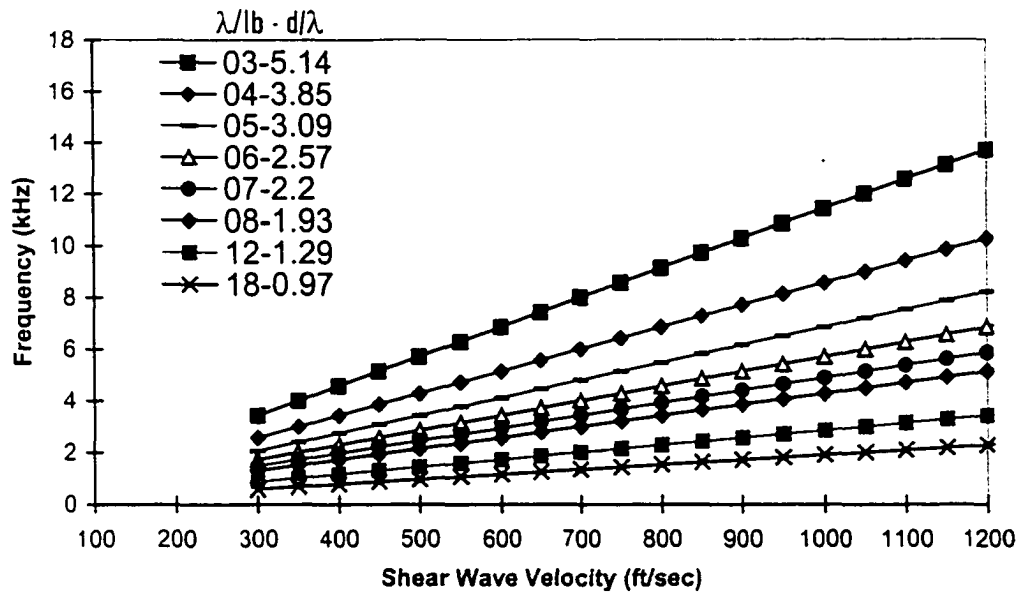


Figure 3.24 Calibration chart for near field effects

In this research, to reduce the near-field effect, the following procedure was established:

- A single sinusoidal pulse was chosen to stimulate a transmitting bender element.
- Because of the difficulties of obtaining the first arrival time of shear wave, the time difference of the first peaks of input-output signals was used to determine the travel time of shear waves.
- To measure the travel time more accurately, optimum frequency was investigated as seen in Figure 3.24 by theoretically changing R value from 3 to 18 and assuming V_s value of 300 to 1200 ft/sec based on previous experimental studies.
- Figure 3.24 was used to select proper frequency range for the shear wave velocity measurement for VB sand specimens.

In this research, the length of bender elements (l_b) is 0.35 inches and the travel distance from tip to tip (d) is 5.4 ~5.8 inches. It was found that S-wave velocities

traveling through the soil specimen under 5 and 10 psi effective pressures fall into between 600 and 700 ft/sec. By using Equations 3.4 and 3.5, R and R_d ratios were calculated. R should be less than 8 and also R_d should be around 4. According to these findings and Figure 3.24, the input frequencies of S-waves were selected as 5 to 10 kHz. Arrival times of shear wave were visually measured with the time difference between the peaks of the transmitted signal to the first peak of the received signal.

When the soil is saturated, output signals of S-wave were very clear and easy to detect as seen in Appendix C. Especially, if the input frequency was less than a certain value (approximately 11 kHz), P-wave and unknown waves did not disturb the first peak of S wave arrivals.

3.4.4 Corrections on Wave Measurements

3.4.4.1 Correction on Delay Time

A single-frequency sinusoidal pulse was generated by a transmitter. The first arrival of the wave was detected by the receiver and both were recorded by the oscilloscope as shown in Figure 3.18. The time difference between input and output signals shows the travel time (t_t). t_t needs to be calibrated in terms of the delay time due to the electrical setup. The reference of input signals was obtained just after it comes out from step up amplifier as shown in Figure 3.14. Still, time delay exists and needs to be corrected due to different lengths of electric cables and connections. To make a correction on this effect, two bender elements (the transmitter and receiver) were in direct contact, and a single pulse was sent to the transmitter and the arrival of the first waveform was recorded. The time difference between the initial input (reference) signal and initial arrival of the wave recorded by the receiver gives the delay time. This delay time was 5 μ sec, as shown in Figure 3.25. This 5 μ sec correction was subtracted from the

measured delay time for all tests except for S-wave measurement as discussed in Section 3.4.4.3.

In addition, horizontal P-wave reading corrections were needed due to the specimen membrane. Rubber membranes 0.025 inch thick were directly sandwiched between two bender elements and without applying aggressive pressure on the bender elements, a good contact surface for the elements with petrolatum was provided. A single frequency sinusoidal pulse was generated by the transmitter and the first arrival of the wave was detected by the receiver. The time difference between an input and output signal fell into a range of 4 μsec to 6 μsec . A similar delay time was observed by the time delay due to cable length correction; therefore, no additional time delay correction due to the membrane was made.

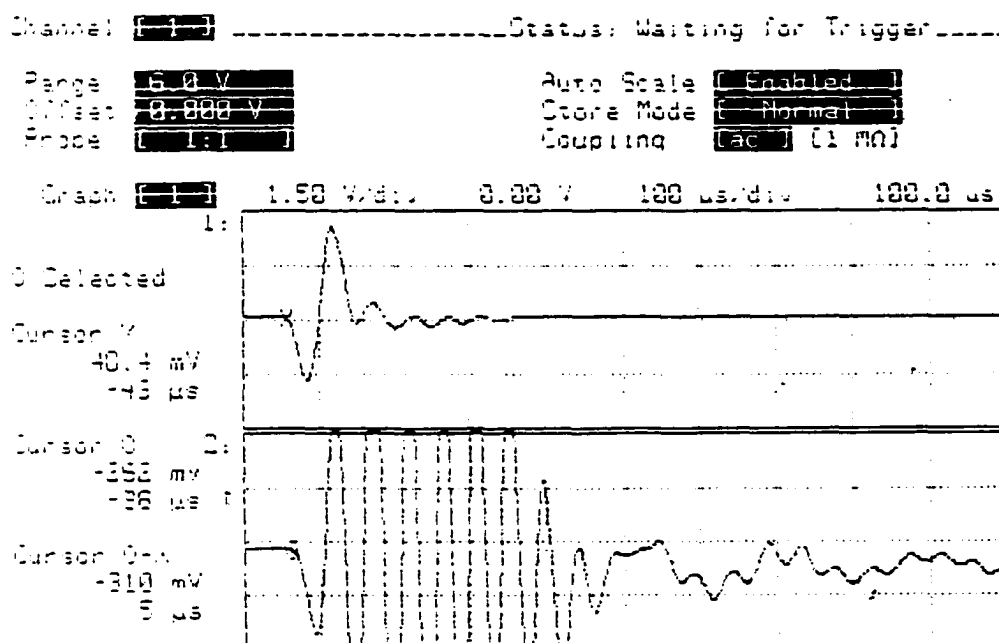


Figure 3.25 Time delay due to the electrical connections

Vertical and horizontal compressional waves were easily identified. Travel distance does not need to be corrected as long as the distance between the transmitter and receiver bender elements is known.

3.4.4.2 Corrections on Shear Wave Arrival Time

Interpretation of shear waveform requires more attention. The waveform received contains not only shear waves but also some unknown waves. To determine the arrival time of a shear wave is somewhat complex. It can be identified by using different techniques such as:

- Observing the first peak of the transmitted signal and the first peak of the received signal.
- Using some numerical analysis to distinguish the frequency and the first arrival time of shear wave velocity such as Fast Fourier Transform (FFT) analysis.

Viggiani et al. (1995a and b) determined the shear wave travel time by using bender elements on a reconstituted clay specimen using different techniques. The shear wave frequency ranged between 1 kHz to 10 kHz for a single sinusoidal input pulse. Arrival times of shear wave were visually inspected by measuring the time difference between the peaks of the transmitted signal to the first peak of the received signal. Their research showed that using peak to peak reading introduces 1.0 % and 1.02% errors that overestimated the measurements in comparison with cross-correlation functions and cross-power spectrum analyses, respectively. This is considered to be very small errors for this kind of experimental studies.

Another numerical analysis of bender elements experiments on different media was conducted by Arulnathan et al. (1998). Shear wave velocities were calculated using different methods of the finite element model of a two-dimensional elastic plane-strain

specimen. The modeled value of shear wave velocity was 80 m/sec. By using characteristic maximum and minimum peaks of input and output waveforms, shear wave velocity was ranged between 82.1 and 84.8 m/sec. The cross-correlation method gave 83 m/sec for shear wave velocity. They suggested that these overestimated errors could be eliminated if the arrival time of second shear wave, which was reflected on the cap and base of the specimen, was considered.

Accordingly, during this investigation, first peak-to-peak signals were analyzed to determine the traveling time of shear waves. No corrections were made in this regard.

3.4.4.3 Corrections on Shear Wave Travelling Distance

According to Viggiani et al. (1995a and b) and Arulnathan et al. (1998), to obtain more accurate results, determination of shear wave velocity with the visual peak to peak reading needs some corrections by considering determination of the effective travel distance, and near field effect.

First, Dyvik and Madshus (1985) suggested that instead of using the real height of the specimen, the distance between the tips of the bender elements should be used. Total length of the bender elements into the soil specimen was 8% of the total specimen height and their results were checked with conventional resonant column test results. About 8% correction on shear wave velocity was needed. This correction led researchers to use travel distance between the tips of the bender elements for shear wave measurement (Thoman and Hryciw, 1990; Viggiani et al., 1995a and b; Brignoli et al., 1996; Jovicic et al., 1996; Arulnathan et al., 1998; Boulanger et al., 1998; and Zeng and Ni, 1998).

Brignoli et al. (1996) and Zeng and Ni (1998) paid attention to the determination of effective distance. In Brignoli et al.'s study, by changing the height of the bender elements, the shear wave velocity was determined on one specific soil. The correlation

between the effective distance and shear wave velocity was established based on the distance between the tips of bender elements. Their results supported Dyvik and Madshus's assumption. Zeng and Ni (1998) used different sized bender elements to find the best output for S-wave velocity measurements. It was reported that output signals were highly affected by the size of the bender elements and the optimum size could be chosen for each type of soil. Increasing the size also increases the flexibility of the bender elements and this helped to detect low amplitude input signals.

In fact, after transmitting the pulse, the first arrival wave may not be a shear wave as mentioned earlier. The first arrival wave could be unknown waves or even a P-wave if the frequency was high enough to make the shear bender elements generate a compressional wave parallel to the polarization direction. Still, those waves other than shear wave are generated by the bender elements. When the transmitter bender element is triggered by a single pulse, the whole body of the element generates these waves, not just at the tip of the element.

In this study, in order to find the effective travel distance for shear wave propagation, a special experiment was conducted. By changing the distance between the transmitter and receiver bender elements in the air, the first arrival time of a received wave was measured. Travel distance in Figure 3.26 represents the total space between the specimen cap and pedestal, in which bender elements are installed. According to the experimental results, when the arrival time is zero, there still exists a small distance (x_d). The total length of the bender elements intruded into the specimen is 0.773 inches. If the bender element generates and receives the wave at the tip, x_d should be around 0.773 inches. In fact, it was 0.02 inches. This implies that shear bender elements might not generate the wave or receive it at the tip. The amount of x_d was subtracted from the total

height of the specimen to compute shear wave velocity. In this shear wave experiment, the arrival time correction (5 μsec) due to electrical cables was not made since the corrected height also includes delay time problems due to the electrical cable connections.

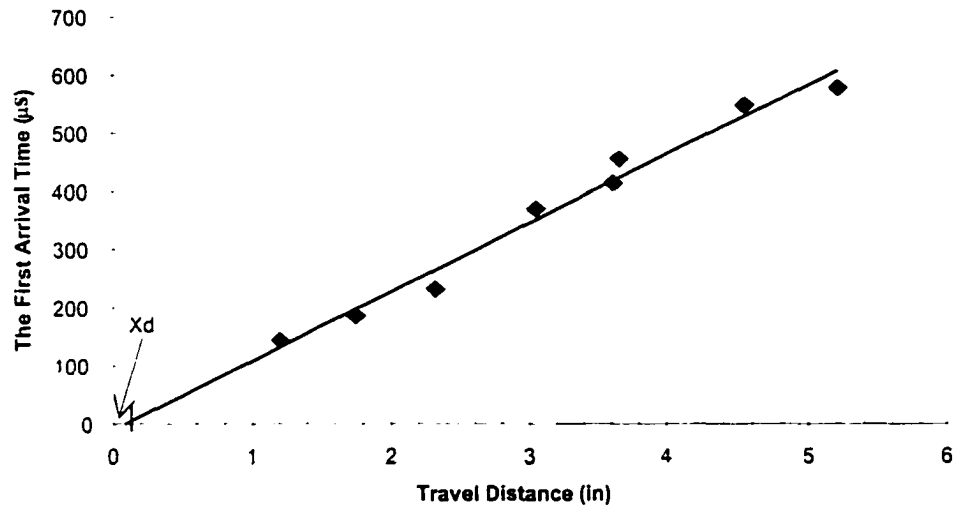


Figure 3.26 Calibration chart for effective distance for shear wave velocity measurement

3.5 Determination of Elastic Constants

For engineering applications, reactions of any elastic materials, subjected by various stresses, can be identified by a set of well-known constitutive equations:

$$\sigma_{ij} = C_{ijkl} \varepsilon_{kl} \quad i,j,k,l = 1,2,3 \quad (3.6)$$

or

$$\varepsilon_{ij} = S_{ijkl} \sigma_{kl} \quad (3.7)$$

where σ_{ij} and ε_{kl} are the stress and the strain tensors, respectively. C_{ijkl} and S_{ijkl} are the elastic stiffness and the elastic compliance tensors, respectively. The stiffness tensor contains eighty-one elastic constants that have to be dealt with. Because of the definition

of the shear stresses and strains, the total numbers of non-equal elastic constants reduces to thirty-six. Since one kind of material exists in one direction, the stiffness and compliance tensors must be symmetric. So the constitutive equations can be simplified in a matrix form for a three-dimensional body in a 1-2-3 orthogonal Cartesian coordinate system as given in Equation 3.8. An anisotropic material contains 21 non-equal elastic constants which are required to express the mechanical behavior of the material and Equation 3.8 refers to an anisotropic material that has no plane of symmetry.

$$\begin{bmatrix} \sigma_1 \\ \sigma_2 \\ \sigma_3 \\ \tau_{12} \\ \tau_{13} \\ \tau_{23} \end{bmatrix} = \begin{bmatrix} C_{11} & C_{12} & C_{13} & C_{14} & C_{15} & C_{16} \\ & C_{22} & C_{23} & C_{24} & C_{25} & C_{26} \\ & & C_{33} & C_{34} & C_{35} & C_{36} \\ & & & C_{44} & C_{45} & C_{46} \\ & & & & C_{55} & C_{56} \\ & & & & & C_{66} \end{bmatrix} \begin{bmatrix} \varepsilon_1 \\ \varepsilon_2 \\ \varepsilon_3 \\ \gamma_{12} \\ \gamma_{13} \\ \gamma_{23} \end{bmatrix} \quad (3.8)$$

If the material in direction '1' which is normal to plane 2-3, has the same properties or behaves isotropically in one symmetry plane, the material is called a transversely isotropic material. Its stiffness matrix can be given as:

$$\begin{bmatrix} \sigma_1 \\ \sigma_2 \\ \sigma_3 \\ \tau_{12} \\ \tau_{13} \\ \tau_{23} \end{bmatrix} = \begin{bmatrix} C_{11} & C_{12} & C_{12} & 0 & 0 & 0 \\ C_{12} & C_{22} & C_{23} & 0 & 0 & 0 \\ C_{12} & C_{23} & C_{22} & 0 & 0 & 0 \\ 0 & 0 & 0 & C_{44} & 0 & 0 \\ 0 & 0 & 0 & 0 & C_{44} & 0 \\ 0 & 0 & 0 & 0 & 0 & (C_{11} - C_{12}) \end{bmatrix} \begin{bmatrix} \varepsilon_1 \\ \varepsilon_2 \\ \varepsilon_3 \\ \gamma_{12} \\ \gamma_{13} \\ \gamma_{23} \end{bmatrix} \quad (3.9)$$

where plane 2-3 is considered as the plane of isotropy. Therefore, plane 1-2 and plane 1-3 are similar. Based on this assumption, the number of the terms reduces to five independent elastic constants.

In this study, soil is assumed transversely isotropic due to the cylindrical triaxial specimen shape and specimen preparation techniques. In the transversely isotropic cases,

still five elastic constants must be determined independently. Therefore, the measurements of the directional elastic waves through a granular media have been one of experimental tools to recover elastic characteristics of soils. Based on the theory of plane wave propagation within an elastic body, longitudinal wave (P-wave) and shear wave (S-wave) can be identified as:

$$\text{P-wave : } V_p = f_1(\rho, C_{ij}, d_1, d_2, d_3) \quad (3.10)$$

$$\text{S-wave : } V_s = f_2(\rho, C_{ij}, d_1, d_2, d_3) \quad (3.11)$$

where ρ is mass density of the elastic body, and d_1 , d_2 and d_3 are direction cosines of the wave normal with respect to axes 1,2,3 as seen in Figure 3.27.

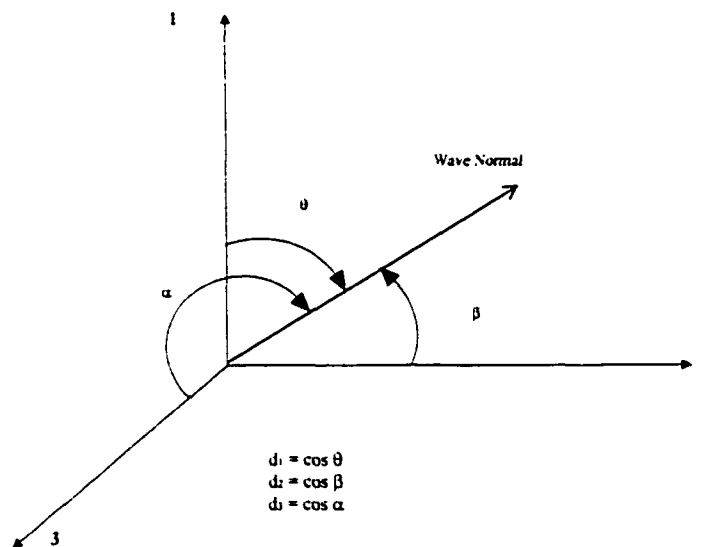


Figure 3.27 Direction cosines of propagation directions

According to Equation 3.10 and 3.11, longitudinal and shear wave velocities in any direction can be determined in terms of the stiffness constants, the propagation direction, and the density of the material in any arbitrary directions. If the propagation planes are chosen as the principle planes, an instant reduction in Equation 3.10 and 3.11

may be achieved. Therefore, in this study, two measurements of P-wave velocity and one S-wave measurement were performed in the plane 1-2.

Two sets of bender elements are embedded in the top cap and the pedestal of the triaxial device as receivers and transmitters in the vertical direction for P- and S-waves. In addition, two bender elements are attached to the membrane surrounding the soil specimen to measure horizontal compressional (P) wave velocities. All the paths are arranged in plane 1-2 and those are illustrated in Figure 3.28.

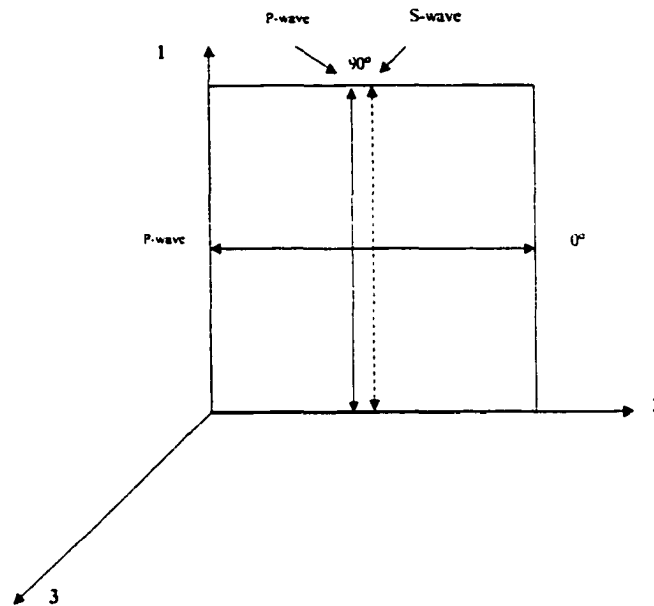


Figure 3.28 Wave path configurations

Elastic wave velocities in the plane 1-2 ($d_3 = \cos 90 = 0$) are:

$$\text{P-wave: } V_p = \sqrt{\frac{b + \sqrt{b^2 - 4c}}{2\rho}} \quad (3.12)$$

$$\text{S-wave: } V_s = \sqrt{\frac{d_1^2 C_{44} + \frac{d_2^2}{2}(C_{22} - C_{23})}{\rho}} \quad (3.13)$$

where

$$b = d_1^2(C_{11} + C_{44}) + d_2^2(C_{22} + C_{44}) \quad (3.14)$$

$$c = (d_1^2 C_{11} + d_2^2 C_{44}) \cdot (d_1^2 C_{44} + d_2^2 C_{22}) - (C_{12} + C_{44})^2 d_1^2 d_2^2 \quad (3.15)$$

Table 3.4 Wave path configurations

Wave Type	Wave Symbol	Wave Plane	d_1	d_2	d_3
Compressional Wave	V_{pv}	1-2	1	0	0
Compressional Wave	V_{ph}	1-2	0	1	0
Shear Wave	V_{sv}	1-2	1	0	0

The next simplification was that the directions of wave measurements were chosen perpendicular or parallel to the principle axes. The summary of the simplifications are shown in Table 3.4 and these wave velocities thus turn out as:

P-wave velocity in the direction 1:

$$V_{p_1} = \sqrt{\frac{C_{11}}{\rho}} \quad (3.16)$$

P-wave velocity in the direction 2:

$$V_{p_2} = \sqrt{\frac{C_{22}}{\rho}} \quad (3.17)$$

S-wave velocity in the direction 1:

$$V_s = \sqrt{\frac{C_{44}}{\rho}} \quad (3.18)$$

If the stiffness components (C_{ij}) are expressed by the elastic properties of the material such as longitudinal modulus, Poisson's ratio, and shear modulus for a

transversely isotropic material, the elastic compliance matrix S_{ij} can be identified by means of elastic constants as:

$$[S] = \begin{bmatrix} 1/E_1 & -\nu_{12}/E_1 & -\nu_{12}/E_1 & 0 & 0 & 0 \\ -\nu_{21}/E_2 & 1/E_2 & -\nu_{32}/E_2 & 0 & 0 & 0 \\ -\nu_{21}/E_2 & -\nu_{23}/E_2 & 1/E_2 & 0 & 0 & 0 \\ 0 & 0 & 0 & 1/G_{12} & 0 & 0 \\ 0 & 0 & 0 & 0 & 1/G_{12} & 0 \\ 0 & 0 & 0 & 0 & 0 & 1/G_{23} \end{bmatrix} \quad (3.19)$$

where E_i is the Young's modulus in direction i and the material properties are the same in direction 2 and 3. ν_{ij} and G_{ij} are Poisson's ratio and shear modulus in direction i due to the force being applied in direction j , respectively.

In addition, because of the symmetry of the compliance matrix:

$$\frac{\nu_{ij}}{E_i} = \frac{\nu_{ji}}{E_j} \xrightarrow{\text{Symmetry}} \frac{\nu_{12}}{E_1} = \frac{\nu_{21}}{E_2} \quad (3.20)$$

and because of isotropic conditions in direction 2 and 3:

$$\nu_{32} = \nu_{23} \quad (3.21)$$

and

$$G_{23} = \frac{E_2}{2(1 + \nu_{23})} \quad (3.22)$$

Therefore, to identify this transversely isotropic material, five constants are needed: E_1 , E_2 , ν_{21} , ν_{23} and G_{12} . Using the relationship between the elastic stiffness $[C]_{ij}$ and the elastic compliance $[S]_{ij}$ matrixes:

$$[C] = [S]^{-1} \quad (3.23)$$

C_{11} , C_{22} , C_{44} and C_{66} can be identified by the following elastic constants:

$$C_{11} = \frac{E_1 E_2 (-1 + \nu_{32})}{-E_2 + 2E_1 \nu_{21}^2 + E_2 \nu_{32}} \quad (3.24)$$

$$C_{22} = \frac{E_2 (E_2 - E_1 \nu_{21}^2)}{(1 + \nu_{32})(E_2 - 2E_1 \nu_{21}^2 - E_2 \nu_{32})} \quad (3.25)$$

$$C_{44} = G_{12} \quad (3.26)$$

$$C_{66} = G_{23} \xrightarrow{or} = \frac{E_2}{2(1 + \nu_{23})} \quad (3.27)$$

Next the material is considered linear and isotropic in any direction, the elastic constants are:

$$\left. \begin{aligned} E_1 = E_2 = E_3 = E \\ \nu_{12} = \nu_{21} = \nu_{23} = \nu_{32} = \nu \\ G_{12} = G_{13} = G_{23} = G \end{aligned} \right\} \quad (3.28)$$

Then,

$$C_{44} = C_{66} = G \xrightarrow{or} = \frac{E}{2(1 + \nu)} \quad (3.29)$$

$$C_{11} = C_{22} = \frac{E}{(1 + \nu)} + \frac{E\nu}{(1 + \nu)(1 - 2\nu)} \xrightarrow{or} = 2G + \lambda \quad (3.30)$$

where λ is the Lamé's constant:

$$\lambda = \frac{E\nu}{(1 + \nu)(1 - 2\nu)} \quad (3.31)$$

In many geotechnical applications where the anisotropy in soil fabric is not significant, soil is simply assumed isotropic and has infinite planes of symmetry. In such a case, elastic wave velocities can be expressed for a linear and isotropic granular material as:

P-wave velocity in horizontal and vertical directions:

$$V_{pH} = V_{p.} = \sqrt{\frac{\lambda + 2G}{\rho}} \quad (3.32)$$

and S-wave velocity:

$$V_s = \sqrt{\frac{G}{\rho}} \quad (3.33)$$

3.6 Saturation Effects on Laboratory Testing and Saturation Procedure

3.6.1 Saturation Effects on Elastic Wave Propagation

An element of soil may be symbolized by a column of unit cross-sectional area and total height V_T as shown in Figure 3.29. The volume of solid particles is then represented by a height V_s and the total volume of voids by a height V_v . The porosity n describes the portion of the total volume represented by the void space and the saturation degree S describes the ratio of the volume of water to the total void volume:

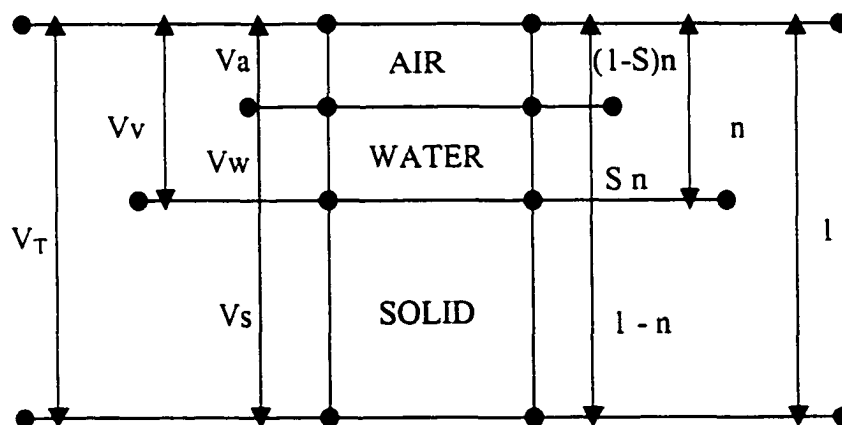


Figure 3.29 Phase diagram for a soil element

$$n = \frac{V_v}{V_T} \quad \text{and} \quad S = \frac{V_w}{V_v} \quad (3.34)$$

$$\gamma = nS\gamma_w + (1-n)\gamma_s \quad (3.35)$$

The unit weight γ of soils at various conditions of water content can be defined in terms of porosity (n), saturation degree (S) and the unit weight of the solid (γ_s). In addition, total volume is:

$$V_T = V_{solid} + V_{air} + V_{water} \quad (3.36)$$

If stress-strain relationship is rewritten for a linear isotropic material subjected to ambient stress ($\sigma_1=\sigma_2=\sigma_3=\sigma_T$ and $\tau_{12}=\tau_{13}=\tau_{23}=0$) in an orthogonal Cartesian coordinate system, it would be:

$$\varepsilon_{1,2,3} = \frac{(1-2\nu)}{E} \sigma_T \quad (3.37)$$

and volumetric strain is :

$$\varepsilon_v = \frac{\Delta V}{V_T} = \varepsilon_1 + \varepsilon_2 + \varepsilon_3 \quad (3.38)$$

$$\frac{\Delta V}{V_T} = \frac{3(1-2\nu)}{E} \sigma_T = \frac{\sigma_T}{K} \quad (3.39)$$

where K is the bulk modulus. σ_T and $\Delta V/V_T$ represent the total stress acting on the soil and volumetric strain, respectively. ΔV is equal to the total volume change that can be evaluated with summation of volume change of the elements:

$$\Delta V = \Delta V_{solid} + \Delta V_{water} + \Delta V_{air} \quad (3.40)$$

$$\frac{\Delta V_{solid}}{V_{solid}} = C_s u \quad V_{solid} = (1-n)V_T \quad (3.41)$$

$$\frac{\Delta V_{water}}{V_{water}} = C_w u \quad V_{water} = n S V_T \quad (3.42)$$

$$\frac{\Delta V_{air}}{V_{air}} = C_a u \quad V_{air} = (1-S)n V_T \quad (3.43)$$

where C_a , C_w , C_s are compressibilities of air, water and solid, respectively. u is pore water pressure. Using Equations 3.41, 3.42 and 3.43, Equation 3.40 can be rewritten in the following form:

$$\Delta V = [(1-n)C_s + nSC_w + (1-S)nC_a](\sigma_T - \sigma')V_T \quad (3.44)$$

$$\sigma_T - \sigma' = u \quad (3.45)$$

In Equation 3.45, σ' is effective stress or intergranular stress. In addition, one more compressibility coefficient that should be considered is the compressibility of the soil skeleton:

$$\frac{\Delta V}{V_T} = C_b \sigma' \quad (3.46)$$

This relation is present if the drained condition occurs during an increment of deviator stress. Substitution of Equation 3.39 into 3.44 creates a relationship between the volumetric strain and the total stress as:

$$K = \frac{\sigma_T}{\frac{\Delta V}{V_T}} = \frac{1}{A} + \frac{1}{C_b} \quad (3.47)$$

where

$$A = [(1-S)nC_a + nC_w + (1-n)C_s] \quad (3.48)$$

If we specify boundary conditions in terms of the saturation degree, Equation 3.49 and 3.50 can be obtained as:

$$S = 1 \quad K = \frac{1}{nC_w + (1-n)C_s} + \frac{1}{C_b} \quad (\text{fully saturation condition}) \quad (3.49)$$

$$S = 0 \quad K = \frac{1}{nC_a + (1-n)C_s} + \frac{1}{C_b} \quad (\text{dry condition}) \quad (3.50)$$

It should be noted again that soil is assumed to be isotropic and has infinite planes of symmetry so that bulk modulus can be described by the stiffness matrix components as in Equation 3.39:

$$K = \frac{E}{3(1-2\nu)} \quad (3.51)$$

or

$$K = \lambda + \frac{2}{3}G \quad (3.52)$$

where λ and G are the Lamé's constant and the shear modulus, respectively. If compressional velocity is reviewed in terms of K and Equation 3.35:

$$V_p = \sqrt{\frac{K + \frac{4}{3}G}{\frac{(nS\gamma_w + (1-n)\gamma_s)}{g}}} \quad (3.53)$$

$$V_s = \sqrt{\frac{G}{\frac{(nS\gamma_w + (1-n)\gamma_s)}{g}}} \quad (3.54)$$

According to Equations 3.49 and 3.50 and the fact that K value is influenced greatly by S , the velocity of the P-wave is changed dramatically with a very small decrement in saturation degree. Meanwhile the S-wave is only slightly affected. Since Equation 3.54 does not include K value, V_s slightly decreases when S value changes from 0.0 to 1.0. This observation will be discussed in a later section.

3.6.2 Pore Water Pressure Parameter B

In laboratory testing, to evaluate pore water pressure development in undrained loading due to isotropic cell pressure ($\Delta\sigma_3$), a B value was proposed by Skempton (1954). as:

$$B = \frac{\Delta u}{\Delta\sigma_3} \quad (3.55)$$

where Δu is the increment of pore water pressure due to the increment of isotropic cell pressure $\Delta\sigma_3$. If a soil specimen is not fully saturated, or some air is present in the specimen, the B value changes, and this makes it easy to understand the behavior of a partially saturated soil. By means of the compressibilities of soil skeleton and voids, B is also formulated as:

$$B = \frac{1}{1 + n \frac{C_{aw}}{C_b}} \quad (3.56)$$

where C_{aw} is the compressibility of the fluid (air and water mixture). C_b is the compressibility of the soil skeleton. The compressibility of air-water mixture was made clear by Wood (1970). According to Wood's comprehensive work, the compressibility of mixture can be obtained from following equation:

$$C_{aw} = SC_w + (1 - S)C_a \quad (3.57)$$

where C_w is the compressibility of de-aired water at atmospheric pressure and is equal to 2.048×10^{-8} to 2.34×10^{-8} ft²/lb. C_a is the compressibility of air and is equal to 3.33×10^{-4} ft²/lb at the atmospheric pressure. S is the degree of saturation. Considering the influence of air bubbles in the water on the compressibility of the air-water mixture, the compressibility is reduced dramatically by the presence of a very small percentage of air-bubbles because the compressibility of air is much bigger than that of de-aired water.

Now, in saturated soils (zero air voids), C_{aw}/C_b is approximately equal to zero, since the compressibility of water is negligible in comparison with that of the soil skeleton. It leads to $B=1$ when $S=1$. On the contrary, if soil is dry, C_{aw}/C_b approaches infinity due to the high value of compressibility of air. Thus, for dry soil ($S=0$), B is equal to zero. For partially saturated soils, even for $0.90 < S < 1.0$, the values of B range typically from about 0.1 to 0.5 (Skempton, 1954). This behavior is easily pointed out in Figure 3.30.

3.6.3 Numerical Examples of Saturation Effects on Elastic Wave Propagation

The effect of saturation on elastic wave propagation was investigated by using Ishihara's (1968 and 1970) data for a loose sand. These computed results are shown in Table.3.5 and Figure 3.31. P-wave velocity was obtained by Equations 3.47, and 3.53. According to these results, P-wave velocity and B values decrease dramatically when the degree of saturation drops slightly from 100%. Those phenomena were also mentioned by Skempton(1954), and Nakagawa et al.(1996 and 1997). According to Nakagawa et al. (1996 and 1997), the P-wave velocity decreased approximately 30% with very small decrease in saturation degree such as from 100% to 99.99%.

Hardin and Richart (1963) showed that shear wave velocity in saturated soils easily is affected by some power of effective confining pressure, but also it depends on the shapes of the particles. They also found experimentally that shear wave velocity slightly reduced when soils are saturated. It was assumed that the presence of water in sand is to attach with soil skeleton and the mass of water in the sand moves with soil structure. When the mass of water increases, the mass of soil structure also increases when compared to the dry condition, and thus it reduces the stiffness of soil structure.

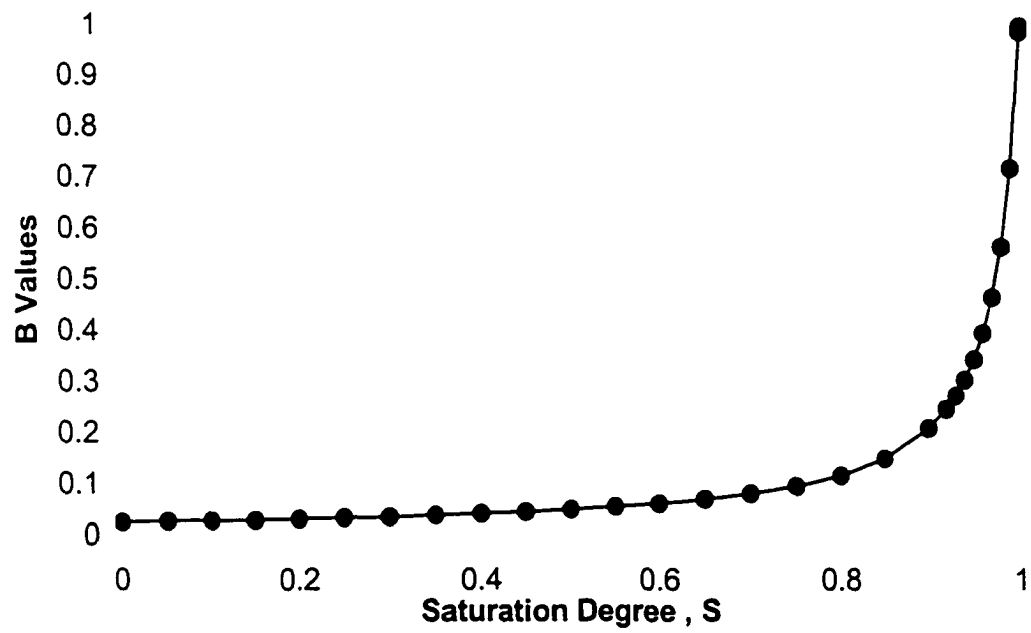


Figure 3.30 Typical relation of pore pressure parameter B vs. saturation degree

Table 3.5. Wave velocity and B values computed from typical values of compressibility, porosity and saturation degree for loose sand.

Cb	4.394E-06 ft ² /lb	N	0.5
Cs	1.32E-09 ft ² /lb	G	2048160 lb/ft ²
Ca	3.331E-04 ft ² /lb	γ_s	162.312 lb/ft ³
Cw	2.34E-08 ft ² /lb	γ_w	62.4278 lb/ft ³

Sa	Sw	K	γ	Vp	Vs	Caw	B
%	%	Lb/ft ²	lb/ft ³	ft/sec	ft/sec	ft ³ /lb	
0.0001	99.9999	8.00E+07	112.37	4865.532	765.789	2.38E-08	0.9973
0.001	99.999	7.14E+07	112.37	4608.379	765.79	2.68E-08	0.99696
0.01	99.99	3.47E+07	112.367	3272.676	765.8	5.67E-08	0.99359
0.1	99.9	5.82E+06	112.339	1564.66	765.895	3.56E-07	0.96102
0.2	99.8	3.12E+06	112.308	1294.944	766.002	6.90E-07	0.92725
0.3	99.7	2.18E+06	112.276	1186.384	766.108	1.02E-06	0.89577
0.4	99.6	1.70E+06	112.245	1127.156	766.215	1.36E-06	0.86636
0.5	99.5	1.41E+06	112.214	1089.75	766.321	1.69E-06	0.83882
0.6	99.4	1.22E+06	112.183	1063.96	766.428	2.02E-06	0.81297
0.7	99.3	1.08E+06	112.152	1045.101	766.535	2.35E-06	0.78868
0.8	99.2	9.71E+05	112.12	1030.714	766.641	2.69E-06	0.76579
1	99	8.24E+05	112.058	1010.234	766.855	3.35E-06	0.72378
2	98	5.27E+05	111.746	968.4679	767.925	6.68E-06	0.56798
3	97	4.27E+05	111.434	954.9024	769	1.00E-05	0.46738
5	95	3.47E+05	110.809	945.4205	771.163	1.67E-05	0.34512
10	90	2.88E+05	109.249	942.8379	776.652	3.33E-05	0.20866
20	80	2.58E+05	106.127	951.8384	787.99	6.66E-05	0.11652
30	70	2.48E+05	103.006	964.5343	799.84	9.99E-05	0.08083
35	65	2.45E+05	101.445	971.4591	805.97	1.17E-04	0.07009
40	60	2.43E+05	99.8845	978.6664	812.242	1.33E-04	0.06188
45	55	2.41E+05	98.3238	986.1264	818.663	1.50E-04	0.05538
50	50	2.40E+05	96.7631	993.8241	825.239	1.67E-04	0.05012
55	45	2.38E+05	95.2024	1001.753	831.975	1.83E-04	0.04577
60	40	2.38E+05	93.6417	1009.912	838.88	2.00E-04	0.04212
65	35	2.37E+05	92.081	1018.302	845.959	2.17E-04	0.03901
70	30	2.36E+05	90.5203	1026.929	853.221	2.33E-04	0.03632
75	25	2.36E+05	88.9597	1035.798	860.672	2.50E-04	0.03398
100	0	2.34E+05	81.1562	1084.088	901.101	3.33E-04	0.02571

Note: where S_a , S_w are gas saturation and water saturation degree of the specimen in percentage, respectively. ($S_a + S_w = 100\%$).

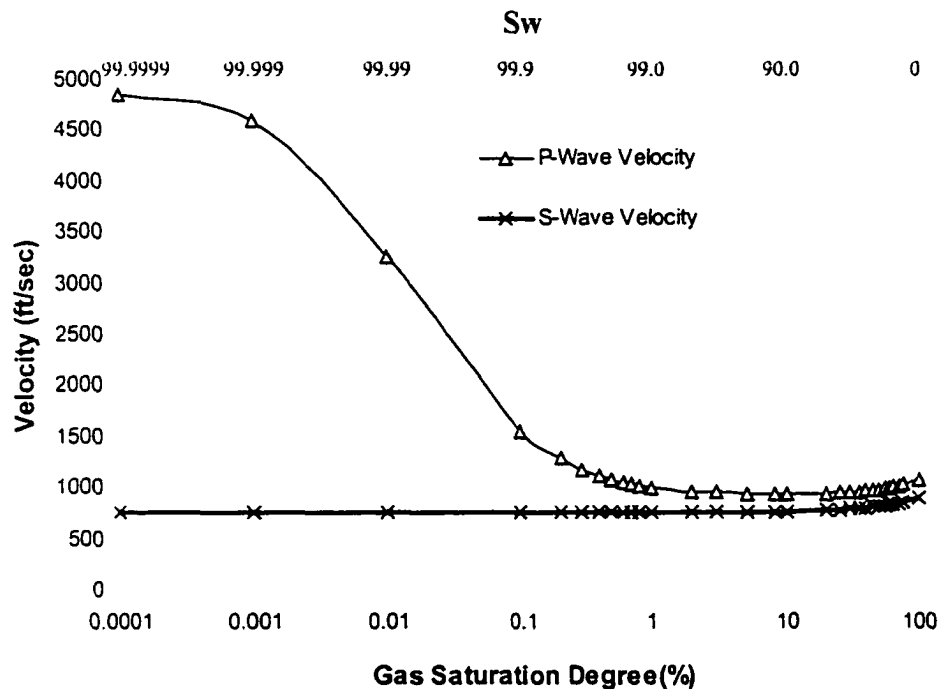
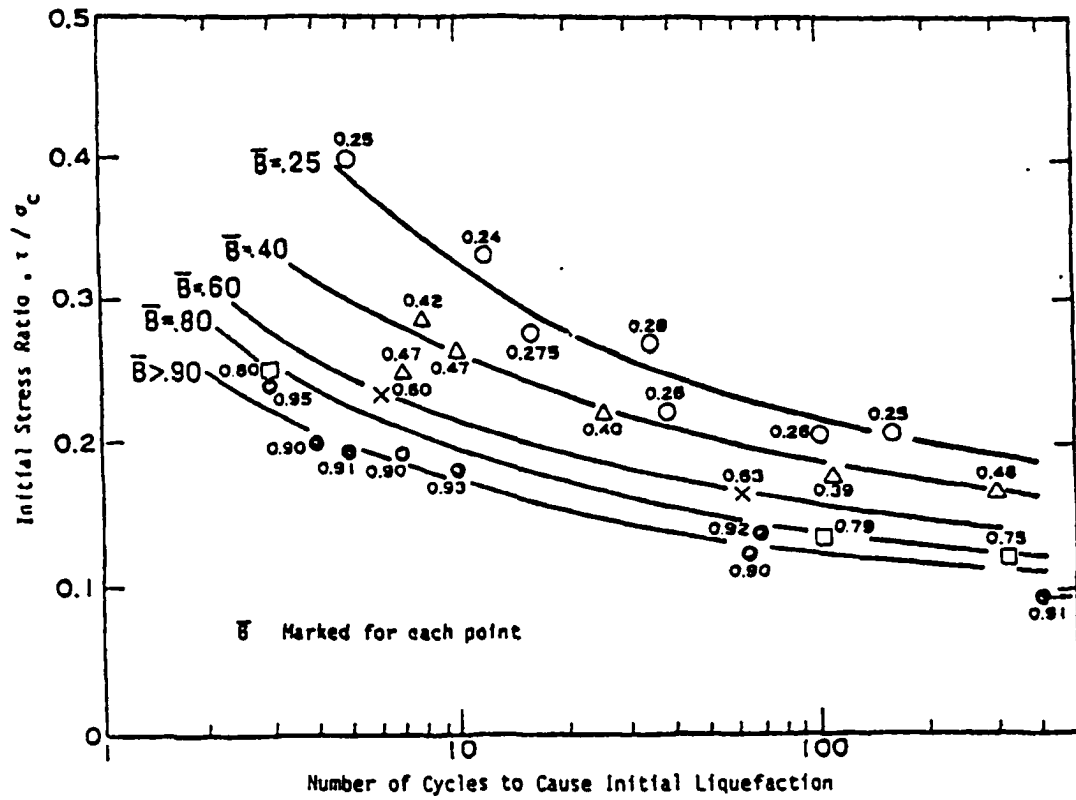


Figure 3.31 Relation between P-wave and S-wave velocities and the degree of saturation

3.6.4 Saturation Effects on Cyclic Stress Ratio

Early studies of liquefaction showed that the initial saturation degree of a soil specimen is the major factor to adequately describe the liquefaction resistance of soil. The buildup of pore pressure affects the amount of permanent deformation under the cyclic loading. When a very small percentage of air-bubbles is present in a porous space, the pore compressibility increases dramatically, and the pore water pressure does not build up as seen in Table 3.5. The earlier works of Sheriff et al. (1977) showed that the liquefaction resistance of sand varies with pore pressure parameter B in Figure 3.32. It was suggested that most soil deposits are not fully saturated and B values should be considered to obtain liquefaction resistance of a specific soil for engineering application.



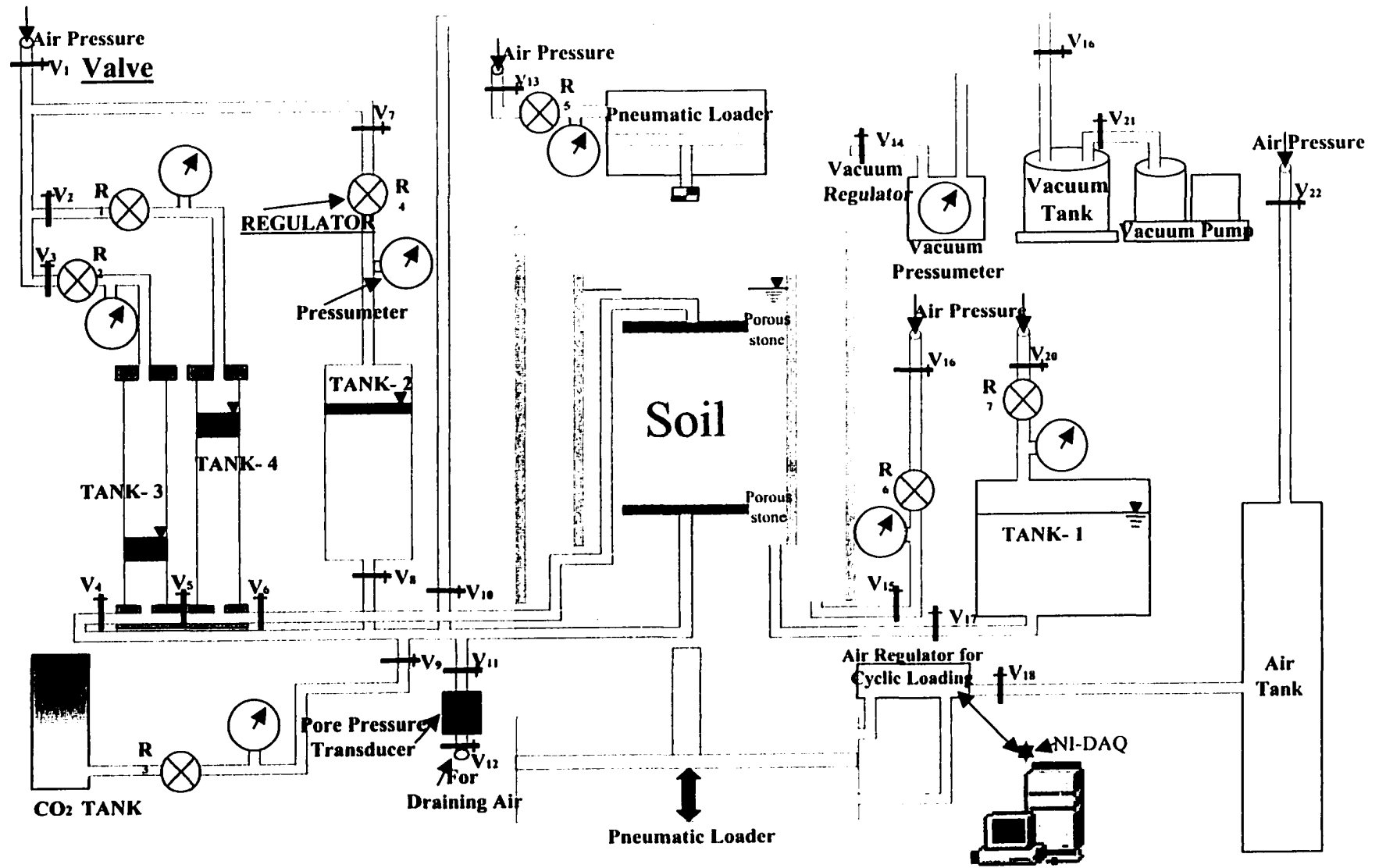


Figure 3.33 The assembly of cyclic triaxial Test

3.6.5 Saturation Procedure

The saturation degree is very important factor to evaluate liquefaction resistance. Especially in this research, the full saturation must be achieved to investigate the anisotropy effects on liquefaction resistance. Achieving 100% saturation of the soil specimen is a formidable task. As seen in Table 3.5, even 99.8% of saturation gives 0.92 of B value. In this research, 0.94 or higher values of B values ($S > 99.9\%$) were accepted as full saturation. According to Sheriff et al. (1977), the high B values can be obtained by:

- Circulating de-aired water through the specimen (percolation method): the aired-water is circulated through the soil specimen by using different pressure at the bottom and the top, so that the air bubbles are forced to leave the specimen.
- Applying the back pressure to the specimen (the back pressure method): by keeping the effective pressure (σ') constant, both the confining pressure (σ_3) and back pressure are increased to diminish air-bubbles under the high pressure.

As seen in Figure 3.33, cyclic triaxial setup was modified to have high B values for all reconstituted specimens. Both saturation methods were used. Before using the percolation method, CO₂ gas was circulated through the specimen. This process is very useful to eliminate air bubbles before saturation of the specimen. CO₂ is heavier than air and does not associate with air. CO₂ can also be dissolved easily in water at a low back pressure. Therefore, de-aired water can occupy porous space without any problems.

The following step-by-step procedure was applied on each specimen. If more than 0.94 B values were obtained before finishing all steps, the procedure was continued to have the same confining and pore water pressure for all specimens. The details of the following steps are shown in Table 3.6:

- 1) Specimen was first prepared under 5 psi vacuum pressure.
- 2) Confining pressure was increased to 5 psi ($\sigma_1=\sigma_2=\sigma_3=5$ psi).
- 3) Vacuum pressure inside of the soil specimen was gradually reduced to 0 psi.
- 4) After vacuum pressure was reduced to 0 psi, the confining pressure was increased to 10 psi.
- 5) A CO₂ tank was connected to the bottom of the specimen and CO₂ pressure was gradually increased to 5 psi. The top drainage line of the specimen was open to let CO₂ circulate. The pressure at the top of the specimen was 0 psi at this time.
- 6) The specimen was slowly saturated by CO₂ for one hour.
- 7) After CO₂ saturation, a de-aired water tank (tank2), as seen in Figure 3.33, was connected to bottom of drainage line. The specimen was saturated by de-aired water for 1 hour
- 8) After saturation was complete, water tank 3 at the top and water tank 4 at the bottom were connected as seen Figure 3.33.
- 9) After closing both drainage valves, the confining pressure was increased manually to 20 psi and B values measured.
- 10) After B values measurement back pressure was fixed at 15 psi at the bottom and 10 psi at the top and de-aired water circulation was continued for another 30 minutes.
- 11) After saturation and closing the drainage valves, the confining pressure was increased to 30 psi and B value was checked.
- 12) When confining pressure was 70 psi and B value was more than 0.94, saturation was considered to be completed.

Table 3.6 An example of the saturation procedure

Trial No	σ_1	σ_3	W. Pressure in Specimen		Pore Water Pressure	$\Delta\sigma_3$	Δu	B
			At Top	At Bottom				
	psi	psi	psi	psi	psi	psi	psi	
	10	10	0	5				
1	10	10	Closed	5	5			
	20	20	Closed	Closed	10.3	10	5.3	0.53
	20	20	10	15				
2	20	30	Closed	15	15			
	30	30	Closed	Closed	22.5	10	7.5	0.75
	30	30	20	25				
3	30	30	Closed	25	25			
	40	40	Closed	Closed	33.4	10	8.4	0.84
	40	40	30	35				
4	40	40	Closed	35	35			
	50	50	Closed	Closed	44.2	10	9.2	0.92
	50	50	40	45				
5	50	50	Closed	45	45			
	60	60	Closed	Closed	54.3	10	9.3	0.93
	60	50	50	55				
6	60	50	Closed	55	55			
	70	60	Closed	Closed	64.8	10	9.8	0.98

3.7 Methods of Sample Preparation

Taking into consideration of the experimental results of Mulilis et al. (1977) as shown in Figure 2.6, three different sample preparation methods were selected for this study:

- air pluviation (AP)
- moist tamping(MT)
- moist vibration(MV)

According to Mulilis et al.'s (1977) research on Montreal 0 sand, the weakest soil specimen was the one prepared by air pluviation and the strongest one was obtained by moist vibration. The moist tamping method created the second strongest specimen in terms of the liquefaction resistance, and it is very applicable and requires rather easy testing procedures. Therefore, this method was also used for the comparisons of the preparation techniques by many researchers (Ladd, 1974; De Alba et al., 1984; Ochiai et al., 1984; Ashraf et al., 1991; Lee et al., 1996 and Vaid et al., 1999).

During this research, the following step-by-step preparation procedures were carried out:

- Step 1. A rubber membrane (0.0125 inch thickness) was mounted on the inside of the split mold. The membrane was stretched length-wise to cover the inside and the edges of the mold. It was overlapped over the outside of the split mold to prevent leakage. 700 mmHg (13.53 psi) vacuum pressure was applied between the membrane and the inner side of the mold. The split mold was placed to the base pedestal of the triaxial cell.
- Step 2. Formation of the soil by different techniques, which will be discussed later in detail.
- Step 3. The specimen cap was placed on the mold, and the top edge of the membrane that overlapped the split mold was rolled back around the cap and sealed by a rubber O-ring. The top drainage pipe was connected and 5 psi vacuum pressure was applied inside the specimen from the bottom drainage pipe. After applying vacuum pressure, the bottom edge of the membrane that overlapped the split mold membrane was rolled down to the base of the pedestal of the triaxial cell and sealed with another rubber O-ring. The split mold was then removed.

- Step 4. Using a caliper and pie-tape, the height and diameter of the specimen were measured. Height and diameter readings were made at four different points. An average of all the readings was used for computing specimen volume with correction of membrane thickness. Knowing the volume and the weight of the specimen, the specimen density was calculated. Sensitivity of height and diameter reading was ± 0.001 inch. The desired range of the relative density was 48%~52%. If the relative density of the specimen was not in this range, the specimen was rejected.

Steps 1, 3 and 4 are the same for all the techniques. In step 2, soil specimens are formed by using different techniques. These techniques will be discussed in the following sections.

3.7.1 Air Pluviation

2.2046 lbs (1000 gram) of air-dried Virginia Beach sand was poured into a 0.0353 ft³ (1000 ml) flask. The flask was closed by a rubber stopper with a 0.25 inches diameter nozzle. The flask was placed upside-down above the mold. By rotating the flask, sand was poured into the mold from a controlled height until all of the sand was dispersed. To obtain a desired density, three factors have to be considered: the nozzle size, height of the drop and the rotation speed. Mulilis et al. (1975) mentioned that changing the height of the drop did not greatly affect the density. It was suggested to use a certain height of drop to keep compaction energy the same. In this study, the height was kept constant at 6 inches. The relationship between the density of the specimen and the nozzle size was investigated by changing the nozzle size. Decreasing the nozzle size changes the flow rate from high intensity down to a few grains per second. A higher flow rate gives a lower density and vice versa. A proper nozzle size was chosen by trials and error to get a relative density of 50%.

The other consideration is how sand is poured into the mold. The flask must be moved in a circular motion to have a homogeneous specimen. The speed of rotation is important. A higher speed of motion could create a sample with a higher density. After some practice, the necessary rotational rate was experimentally established. To have 50% relative density for the VB sand specimen, the rotation speed was approximately 40-50 circles to have a one-inch soil layer in the mold.

3.7.2 Moist Tamping

To have a uniform soil specimen, the specimen was formed in five layers. Locations of layers were marked on the interior of the mold for vision before sand was dispersed into the mold. The first layer thickness at the bottom was 1.9 inches to protect the piezoelectric transducers at the bottom from the tamping effects. The other layers are one inch thick. In total, 2.1561 lbs (978 gram) air-dried Virginia Beach sand was used to constitute a soil specimen by the moist tamping technique.

The desired weight of air-dried sand for the first layer was poured into a pan and mixed with a certain amount of de-aired water to have moisture content of 8%. After creating a homogeneous mixture of moist sand, the mixture was poured into the mold. The surface was leveled. The mixture was compacted with a tamping rod. The rod consisted of a 7-inch long brass rod with a changeable tamping foot. The tamping foot was 2.75 inches in diameter and 0.3 inches thick. To control the height of drop, a restraining disc was used. The restraining disc was adjusted on the brass rod to produce the desired height for the first layer, then the tamping rod was placed inside the mold. The tamping rod was dropped from a height of one inch until the desired layer thickness was achieved. The compactor procedure was repeated for each layer. After the compaction of all layers was done, step 3 and step 4 were applied.

3.7.3 Moist Vibration

Vibration is one of the most popular methods to compact cohesionless soil. Changing the frequency and the amplitude of the vibrations affects the soil fabric and density. In the laboratory conditions, using the vibration technique on partially saturated cohesionless soils such as sand is highly difficult. The amplitude of vibration can not be high due to the small specimen size, and moist saturated soils show some pseudo cohesion by water films between the particles. A large amount of vibration energy is needed to achieve even medium density ($D_r=50\%$). In order to have a uniform soil specimen and to apply large amount of vibration energy, a soil specimen was formed in 10 layers. The first two layers were 0.95 inches each to protect the piezoelectric bender elements at the surface of the pedestal and all other layers were 0.5 inches. Totally, 2.1561 lbs (978 gram) air-dried Virginia Beach sand was used to constitute a soil specimen by the moist vibration technique. A beaker was filled with the desired weight of dry soil and a certain amount of de-aired water. They were mixed enough to have a homogeneous moist mixture with 8% water content. The mixture was poured into a split mold and the surface was leveled. The surcharge load was placed on the layer. The surcharge produced 1.12 psi on the layer. A modified hand vibrator was contacted firmly at the side of the mold until the desired height was achieved. The frequency of vibration was 1 kHz. These procedures were repeated for each layer. After finishing all layers, step 3 and step 4 were applied.

3.8 Summary of Laboratory Testing Program

3.8.1 Preparation of Soil Specimens

After the properties of the sand used in this research were determined. Three different specimen preparation techniques were used.

- air pluviation (AP)
- moist tamping (MT)
- moist vibration (MV)

During the preparation procedures, the vacuum pressure between the specimen mold and rubber membrane was kept constant (5 psi) to eliminate the effect of the vacuum pressure on the soil specimens and soil structure. Relative density (D_r) was chosen at 50% to obtain a medium dense soil specimen and the range of (D_r) was chosen between 48% and 52% to consider the densities of each specimen be the same. Otherwise, the specimen was rejected.

3.8.2 Saturation of Soil Specimens

The soil specimen was saturated by de-aired water until achieving 0.94 or higher B values to reduce the saturation effect on the liquefaction resistance. The saturation procedure was continued to have a confining pressure (σ_3) of 70 psi, no matter if desired B value was achieved earlier or not. Back pressure was increased to 60 psi to have effective pressure of 10 psi. If required B value did not pass 0.94, the specimen was rejected.

3.8.3 Cyclic Triaxial Testing Program

After a specimen was fully saturated and consolidated under 10 psi effective isotropic confining pressure, the cyclic triaxial test was performed to determine the liquefaction resistance. It should be noted that all cyclic triaxial tests were conducted

under an isotropic stress condition to eliminate stress-induced anisotropy. By changing the amplitude of cyclic stress, the relationship between the cyclic stress ratio and the number of cycles causing initial liquefaction was obtained.

3.8.4 Measurements of Elastic Wave Velocities

3.8.4.1 Elastic Wave Velocities at Dry Condition(S=0%)

After the preparation of the soil specimen was completed under 5 psi, vertical and horizontal P-wave velocities and vertical shear wave velocity were measured. Elastic wave velocity tests were repeated for all specimens prepared by the different techniques so that the soil fabric effects on elastic properties of soil structure were investigated for dry or moist specimens (8% water content).

3.8.4.2 Elastic Wave Velocities at Full Water Saturation(S=100%)

After the saturation of the soil specimens was completed under 5 psi effective confining pressure, vertical P-wave and vertical shear wave velocities were measured. Horizontal P-wave velocity was not able to be measured at this time, because of a high disturbance on wave form due to water in the inner cell. The first arrival time was not clearly detected.

3.8.4.3 Elastic Wave Velocity under Different Effective Confining Pressures

The specimens prepared by different techniques were subjected to different effective confining pressure at dry and saturated conditions. Elastic wave velocities were measured at the effective confining pressures 10, 20, 30, 40 and 50 psi.

3.8.4.4 Measurements of Volume Change under Isotropic Stresses

As separated tests, consolidation tests were conducted to determine the compressibility (bulk modulus) of the soil skeleton of each specimen. For consolidation tests, the triaxial test setup was used. After saturated soils specimen under 10 psi

confining and 5 psi back pressure, the specimens were consolidated under different effective confining pressure, 10, 20 30, 40, and 50 psi. Volumetric change (ΔV) and axial strain (ϵ_1) were measured under the consolidation pressures.

CHAPTER 4

EXPERIMENTAL RESULTS AND ANALYSIS

4.1 Introduction

A laboratory experimental program was developed to investigate anisotropy of granular materials and its relation to liquefaction resistance. Cyclic triaxial tests were performed on Virginia Beach (VB) sand specimens prepared by three different preparation methods:

- Air Pluviation (AP)
- Moist Tamping (MT)
- Moist Vibration (MV)

In order to investigate the effects of inherent anisotropy on the liquefaction resistance, elastic wave velocities were measured by means of a pulse transmission method on the same specimens with dry ($S=0\%$) and saturated ($S=100\%$) conditions. Isotropic consolidation tests were also conducted to determine the compressibility of each specimen under different effective confining pressures.

Based on the results of experiments, firstly, soil specimens (AP, MT, MV) were assumed to be isotropic materials. The isotropic mechanical properties of each specimen were obtained. Secondly, the specimens were assumed to be transversely isotropic and the anisotropic mechanical properties were recovered.

In this chapter, the results of the laboratory testing programs are presented and anisotropic characteristics of granular materials and its relation to liquefaction resistance are discussed.

4.2 Liquefaction Resistance of Specimens

Series of stress-controlled cyclic triaxial tests were performed on three different specimens created by air pluviation (AP), moist tamping (MT), and moist vibration (MV) techniques. All tests were conducted under an isotropic confining stress condition. The specimens were consolidated under an effective confining pressure (σ'_v) of 10 psi for 20 minutes. The initial conditions prior to the cyclic testing are given in Table 4.1.

Table 4.1 Initial conditions of soil specimens prior to the cyclic loading

Preparation Technique	Dr (%)	B (%)	Confining Pressure (σ_3) psi	Pore Water Pressure psi	Effective Confining Pressure psi
AP	50.1±0.97	97.0±1.25	70	60	10
MT	48.81±0.58	96.16±1.88	70	60	10
MV	49.20±0.77	95.77±1.75	70	60	10

During the liquefaction tests, modified cyclic triaxial test equipment was used. Cyclic loading frequency was 0.5 Hz. After the specimen was fully consolidated, the drainage valves were closed. The specimens were then subjected to uniform sinusoidal cyclic stresses. The axial deformations of the specimen with increasing number of cyclic loads were recorded. The numbers of cycles causing initial liquefaction with 5% of double axial strain were determined. Figure 4.1 represents the result of a cyclic triaxial test on VB sand. The number of cycles causing liquefaction are 14 with 5% double amplitude axial strain in this case. Other graphical results of cyclic triaxial test are given in Appendix A.

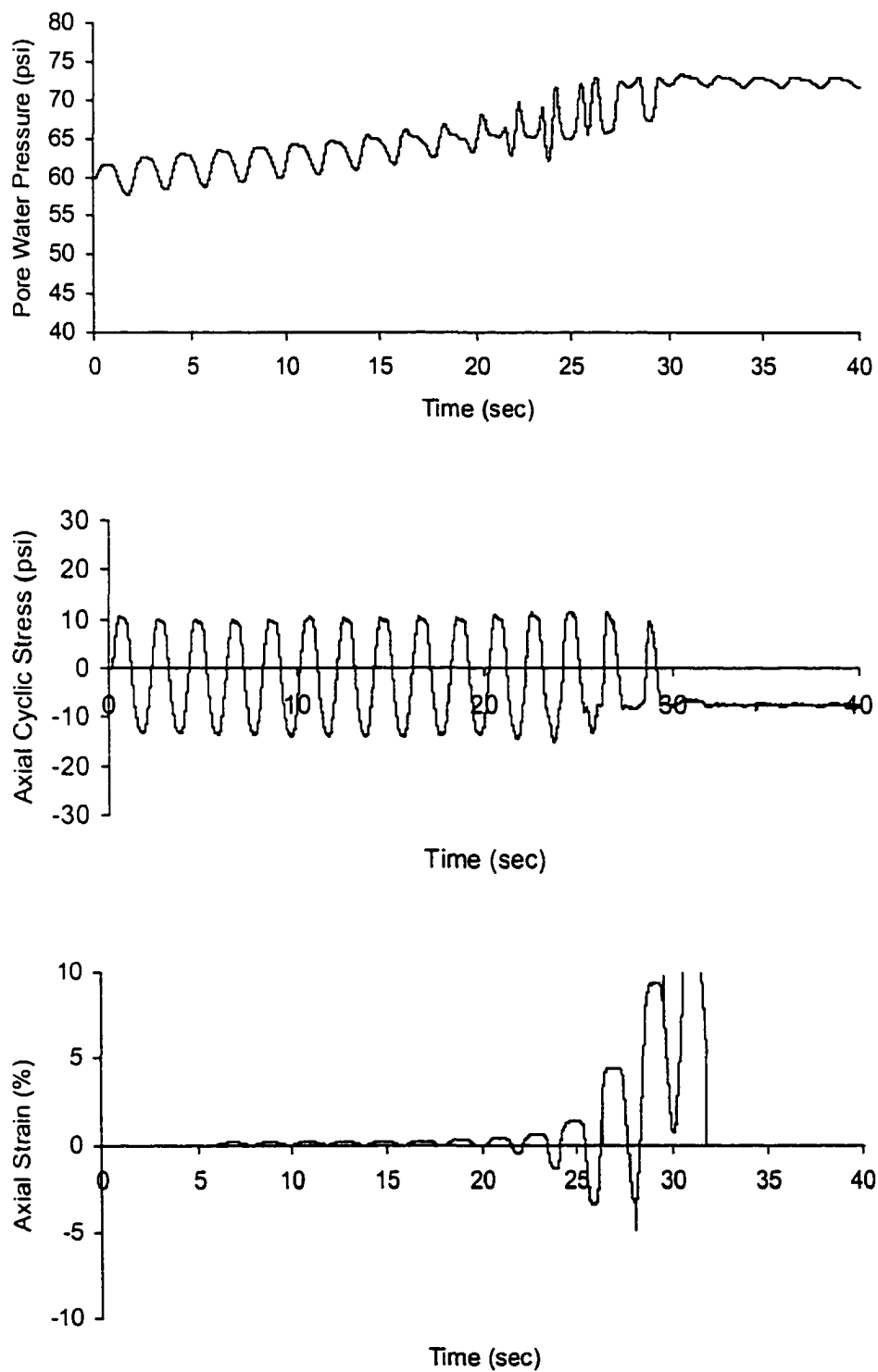


Figure 4.1 The results of cyclic triaxial test on VB sand: $\sigma_1 = \sigma_3 = 70$ psi, $u = 60$ psi, $\sigma' = 10$ psi

The relationship of liquefaction resistance in terms of cyclic stress ratio (CSR) to the number of cyclic loads was established for AP, MT and MV specimens as seen in Figure 4.2. The cyclic stress ratio (CSR) was defined as the ratio of cyclic deviator stress to initial effective confining stress ($\sigma_{d1}/2 \sigma'_v$) when the double amplitude axial strain reaches 5%. The results clearly demonstrate that the preparation methods significantly affect the liquefaction behavior. According to the results of the cyclic loading test, the differences in cyclic stress ratios of MV and AP specimens were about to 144 % at 10 cycles and 116% at 100 cycles. Specimens formed by MT method had a slightly lower strength in comparison with MV specimens. MT specimens were about 9% lower at 10 cycles and lower 11% at 100 cycles than MV specimens. The differences in cyclic stress ratios of MT and AP specimens were about to 124 % at 10 cycles and 94% at 100 cycles. These results showed that there were enormous differences between the cyclic stress ratios of reconstituted Virginia Beach sand specimens depending on the sample preparation techniques. This is in agreement with data obtained by Mulilis et al. (1977).

Table 4.2 Cyclic stress ratio required to cause liquefaction at different cycles

Earthquake Magnitude M	Number of Cycles	CSR		
		AP	MT	MV
6	5	0.295	0.693	0.798
6-3/4	10	0.262	0.588	0.639
7-1/2	15	0.252	0.544	0.591
8	20	0.247	0.521	0.567
8-1/2	25	0.245	0.506	0.553
>9	30	0.243	0.496	0.544

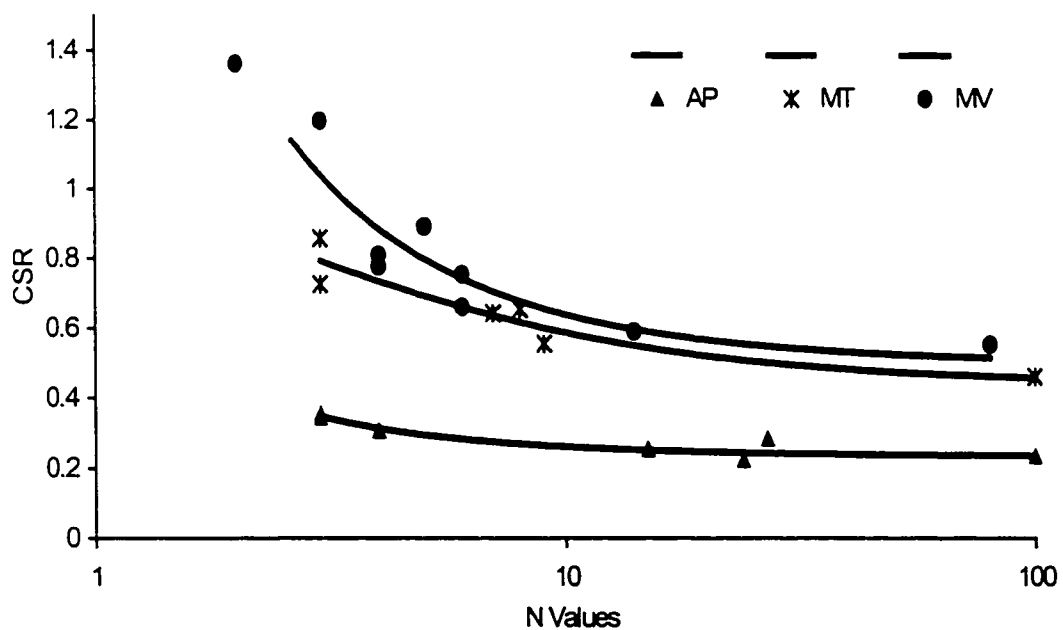


Figure 4.2 Liquefaction resistance for AP, MT, and MV specimens

4.3 Elastic Wave Measurements

4.3.1 Effect of Initial Water Content

The basic differences among AP, MT, and MV specimens are initial water content of the compacted materials. AP specimens were prepared under totally dry condition ($S=0\%$), while MT and MV specimens were compacted with 8% water content. The 8% water content implies $S=0.3\%$ for Virginia Beach specimens. By using Equations 3.51 and 3.52 for bulk modulus, Equation 3.58 for P-wave velocity (V_p), and Equation 3.59 for S-wave (V_s) velocity, elastic waves were numerically calculated as functions of S and B values based on Ishihara's (1970) data. Equations 3.60 and 3.61 were utilized to compute B values. Those are shown in Table 4.3. When saturation degree is 0.3 %, B values is 0.0258. The values of V_p , and V_s at $S=0.3\%$ are reduced 0.057, and 0.058 % smaller than the values at $S=0\%$, respectively. Therefore, initial MT and MV specimens can be considered practically as dry soil samples.

Table 4.3 Saturation effect on elastic wave velocities based on Ishihara's (1970) data

S	K	γ	V_p	V_s	C_{aw}	B
%	lb/ft ²	lb/ft ³	ft/sec	ft/sec	ft ² /lb	
100	8.10E+07	112.37	4896.99	765.79	2.34E-08	0.9973
99.999	7.14E+07	112.37	4608.38	765.79	2.68E-08	0.9970
99.99	3.47E+07	112.37	3272.68	765.80	5.67E-08	0.9936
99.9	5.82E+06	112.34	1564.66	765.90	3.56E-07	0.9610
99	8.24E+05	112.06	1010.23	766.85	3.35E-06	0.7238
98	5.27E+05	111.75	968.47	767.93	6.68E-06	0.5680
95	3.47E+05	110.81	945.42	771.16	1.67E-05	0.3451
50	2.40E+05	96.76	993.82	825.24	1.67E-04	0.0501
1	2.34E+05	81.47	1082.02	899.37	3.30E-04	0.0260
0.5	2.34E+05	81.31	1083.05	900.24	3.31E-04	0.0258
0.3	2.34E+05	81.25	1083.47	900.58	3.32E-04	0.0258
0	2.34E+05	81.16	1084.09	901.10	3.33E-04	0.0257

4.3.2 Effect of Saturation Degree

During the specimen saturation process, and before each cyclic triaxial test, elastic wave velocities were measured at every increments of back pressure application, except P-wave in horizontal direction. Horizontal P-wave velocity was not able to be measured. Since a high disturbance coming from coupling between water and bender elements, the first arrival time of P-wave was hidden. The results of vertical P-wave and S-wave measurements are illustrated in Figure 4.3 and 4.10.

As seen in Table 4.3 and Figure 4.3, water saturation degree has a big effect on the P-wave velocities. In Section 3.6.3, it was reported that after full water saturation is completed, the bulk compressibility of the pore fluid is a main factor affecting P-wave velocities. It was experimentally proved that the small amount of air bubbles dramatically changes the compressibility of pore fluid. Especially flushing CO₂ gas and deaired water through soil specimens gives small B values in low back pressures. Increasing back pressure forces gas bubbles to resolve into water till B value reaches a desirable magnitude such as 0.94.

Strachan (1985) stated that the small gas bubbles could not be distributed uniformly through the soil specimen. As CO₂ gas and de-aired water were pushed into the soil specimen to eliminate air in the pore, de-aired water could find its own pathways and travels in that direction during the flushing process. Therefore, small amounts of gas could be present in the soil. However, P-wave can be transmitted through the fully saturated pathways in the media, and further flushing water causes less gas bubbles to be present and more fully saturated pathways let P-wave energy increase. During the saturation process, it was observed that after a certain B value was accomplished, the amplitudes of received signals were increased. It is shown in Appendix C.

In Figure 4.3, the numerical data from Table 4.3 differs from the experimental values. Flushing de-aired water travels from the bottom of the specimens to the top and air bubbles could be stacked at the top. That affects the P-wave velocity and B values and the gas bubbles might not be distributed uniformly in the direction of P-wave propagation. All these difficulties are beyond the control and it might change the magnitude of P-wave velocities with time. It might explain the difference between theoretical P-wave velocities calculated in Section 3.6.3 and the measured P-wave velocities.

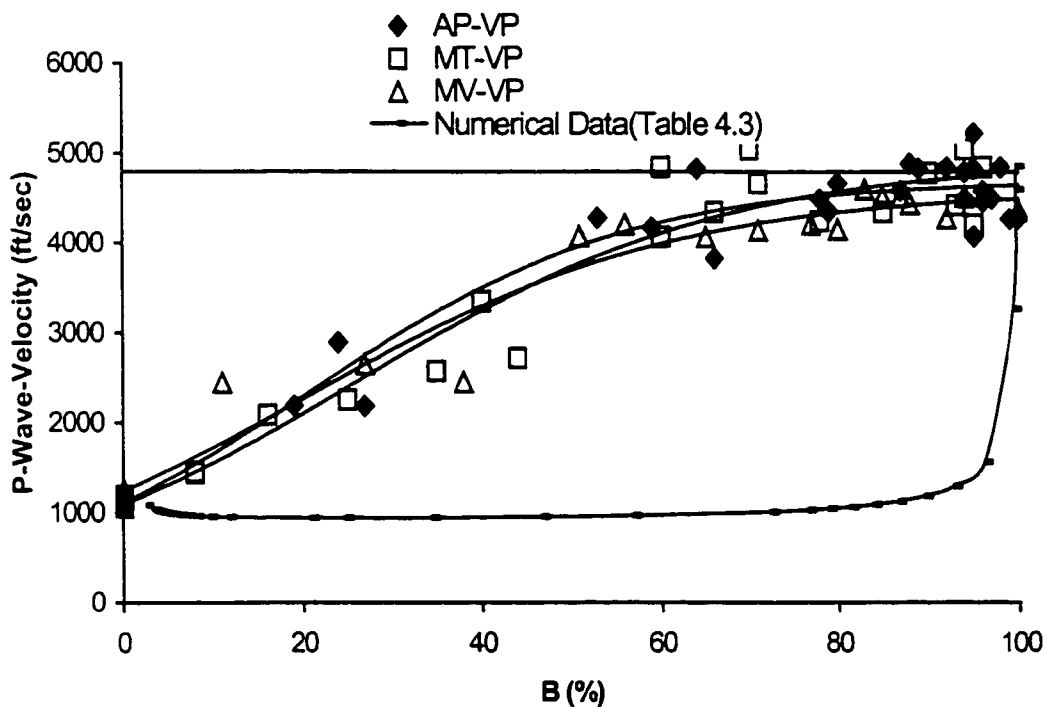


Figure 4.3 Saturation effect on P-wave velocities of AP, MT, and MV specimens

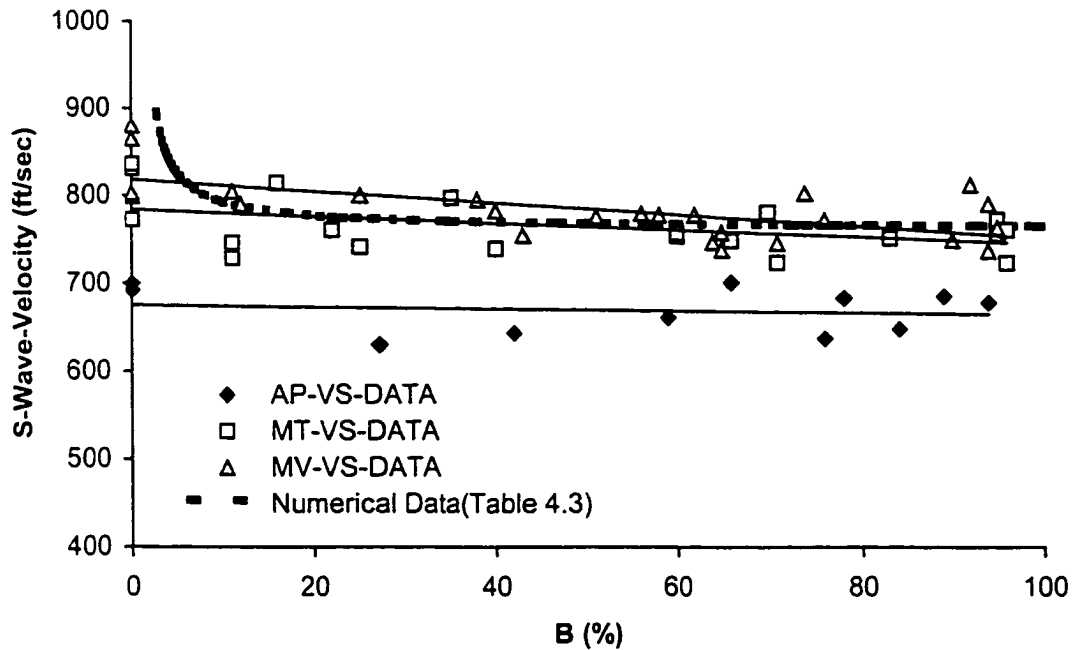


Figure 4.4 Saturation effect on S-wave velocities of AP, MT, and MV specimens

As identified in Section 3.5.1, while P-wave propagation is function of the bulk modulus of the specimens, S-wave is not only a function of the effective pressures but also depends on the direction of particle motion. The measurements of S-wave velocity show a small variation over various B values as seen in Figure 4.4. Water may influence the coupling between solid particles by wetting the contacts of solid particles. After saturation, the experimental results indicated that the values of V_{sv} of AP, MT and MV specimens under 5 psi effective pressure decrease approximately 8, 6 and 6%, respectively, in comparison with the values of V_{sv} of dry specimens. The measured S-wave velocities during the saturation showed generally a good agreement with the numerical data. Hardin and Richart (1963) showed that shear wave velocity in saturated soils is a power function of effective confining pressure, but also it depends on the shapes of the particles. They also found experimentally that shear wave velocity decreased slightly due to the presence of water in a sand since water is attached to soil particles and

it moves with the soil. As the mass of water increases the mass of the soil structure compared to dry condition, the shear wave velocity decreases for the same G values as seen in Equation 3.59.

4.3.5 Effect of Effective Confining Pressure

To investigate the effect of effective confining pressure (σ') on elastic wave velocities, three series of experiments were conducted for each sample preparation techniques. Specimens were first prepared at 5 psi vacuum pressure and effective pressure (σ) was then increased to 10, 20, 30, 40, and 50 psi. P-wave velocities in vertical and horizontal directions (V_{pv} and V_{ph}) and S-wave velocity in vertical direction (V_{sv}) were measured. Those are presented in Tables 4.4, 4.5 and 4. 6 and in Figures 4.5, 4.6 and 4.8. During the test, frequencies for V_{pv} were 17 and 22 kHz, for V_{sv} those were 5, 7 and 9 KHz, and for V_{ph} , frequencies of 20 and 30 kHz were used. Average values were reported for different readings at different frequencies. Some graphical results are also presented in Appendix D

It was experimentally observed that under different effective pressures (σ') in the range from 5 to 50 psi, P-wave velocities in vertical and horizontal directions, and also S-wave velocities in vertical direction increased with increasing the effective pressure. Since air was present in the porous media in the cases of $S=0\%$, the compressibility of soil skeleton or bulk modulus affected strongly the measurement of wave velocities with different σ' as seen in Figures 4.5 and 4.6.

Table 4.4 Measurements of elastic waves for AP specimens at dry and saturated conditions under different effective pressures

AP							
σ	S	V _{p_v}	V _{s_v}	V _{p_h}	S	V _{p_v}	V _{s_v}
psi	%	ft/sec	ft/sec	ft/sec	%	ft/sec	ft/sec
5	0.0	1149.65	613.25	1036.07	100	4447.76	576.52
10	0.0	1288.32	687.15	1187.17	100	4373.16	635.76
20	0.0	1424.90	821.02	1402.41	100	4325.73	722.16
30	0.0	1514.99	905.92	1523.05	100	4246.85	872.12
40	0.0	1582.11	1023.87	1584.20	100	4490.36	919.44
50	0.0	1651.11	1072.92	1699.60	100	4446.27	995.92

Table 4.5 Measurements of elastic waves for MT specimens at dry and saturated conditions under different effective pressures

MT							
σ	S	V _{p_v}	V _{s_v}	V _{p_h}	S	V _{p_v}	V _{s_v}
psi	%	ft/sec	ft/sec	ft/sec	%	ft/sec	ft/sec
5	0.0	1114.6	687.27	1089.08	100	4657.87	655.94
10	0.0	1217.6	813.12	1208.25	100	4591.33	761.93
20	0.0	1400.4	926.51	1390.63	100	4560.53	858.09
30	0.0	1541.7	1086.29	1543.29	100	4557.39	962.50
40	0.0	1606.3	1133.26	1617.17	100	4509.46	1046.25
50	0.0	1647.8	1220.29	1651.42	100	4670.60	1125.55

Table 4.6. Measurements of elastic waves for MV specimens at dry and saturated conditions under different effective pressures

MV							
σ	S	V _{p_v}	V _{s_v}	V _{p_h}	S	V _{p_v}	V _{s_v}
psi	%	ft/sec	ft/sec	ft/sec	%	ft/sec	ft/sec
5	0.0	1167.51	725.64	1126.17	100	4573.92	688.79
10	0.0	1293.50	836.52	1295.14	100	4292.93	772.62
20	0.0	1483.07	971.42	1461.40	100	4450.87	923.71
30	0.0	1575.82	1112.93	1585.09	100	4342.67	986.25
40	0.0	1692.87	1201.61	1688.80	100	4463.16	1116.63
50	0.0	1779.87	1271.61	1737.42	100	4601.72	1152.48

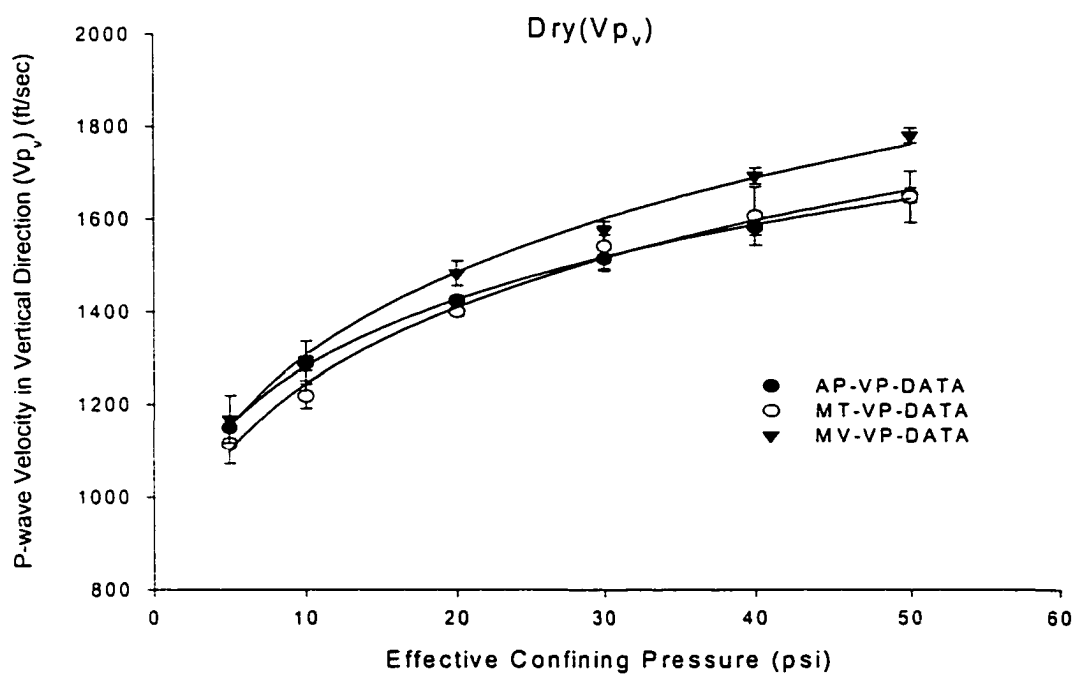


Figure 4.5 P-wave velocities in vertical direction against effective confining pressure at dry condition ($S=0.0\%$)

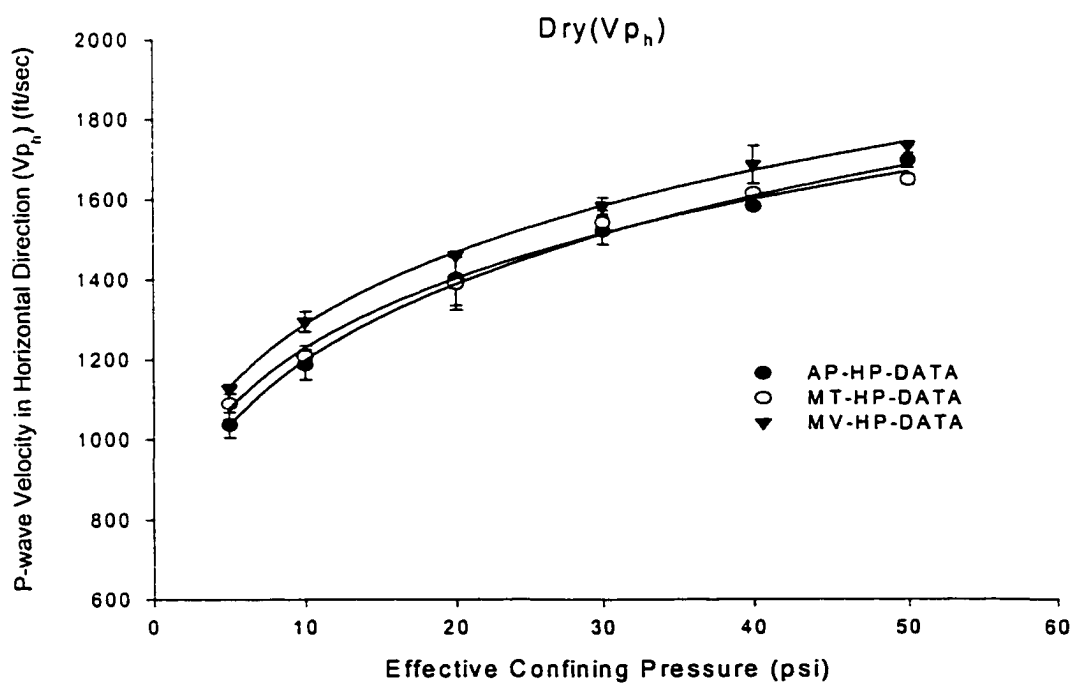


Figure 4.6 P-wave velocities in the horizontal direction against effective confining pressure at dry condition ($S=0.0\%$)

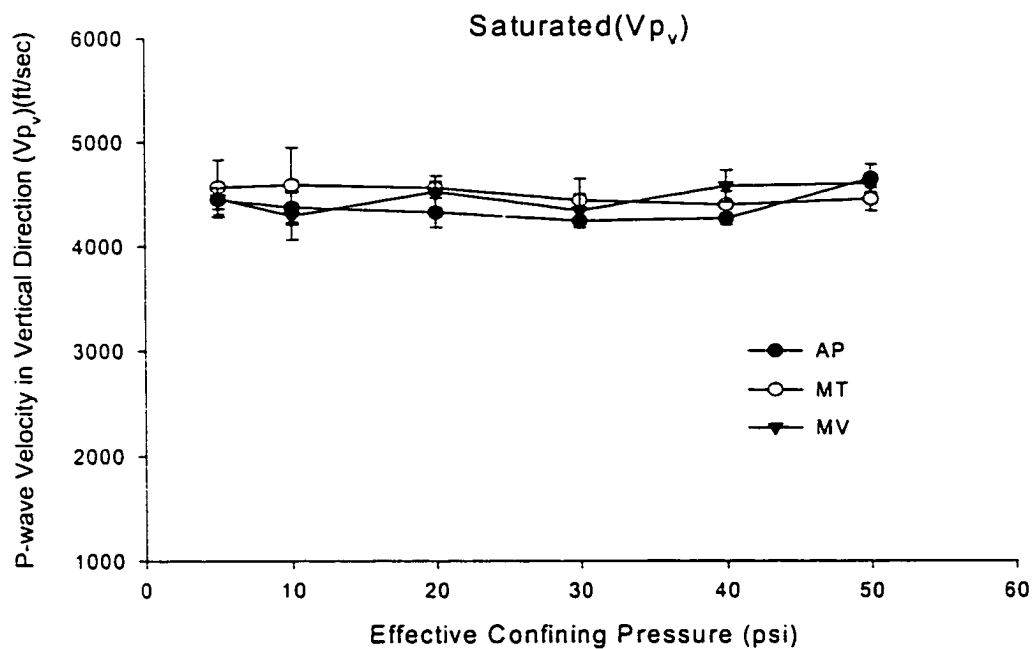


Figure 4.7 P-wave velocities in the vertical direction against effective confining pressure at saturated condition ($S=100\%$)

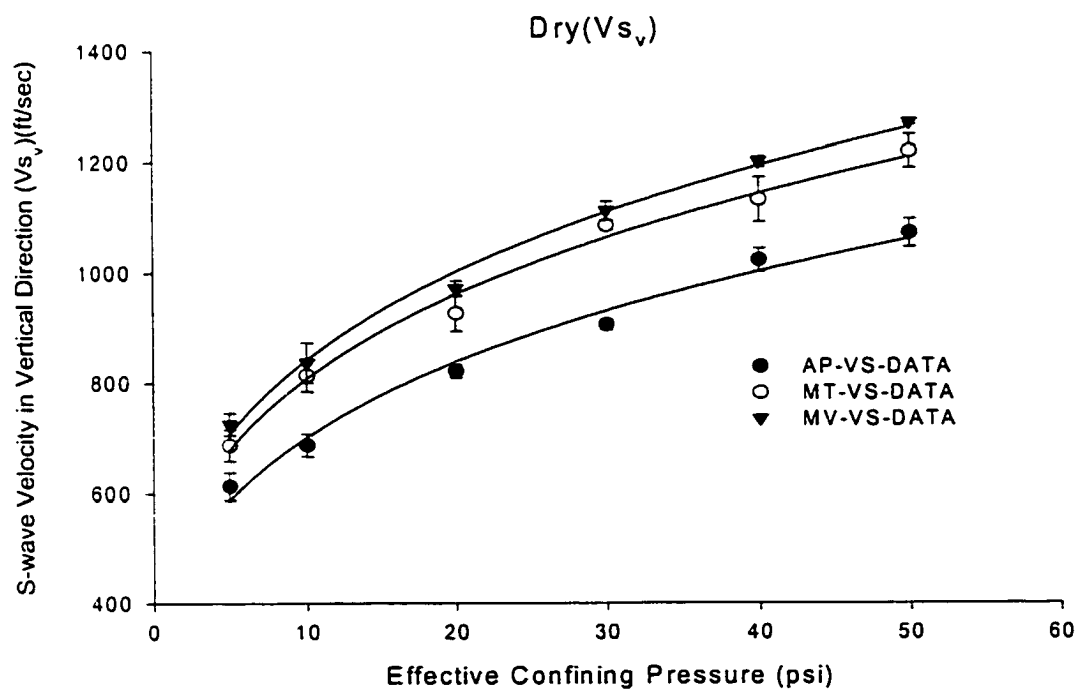


Figure 4.8 S-wave velocities in the vertical direction against effective confining pressure at dry condition ($S=0.0\%$)

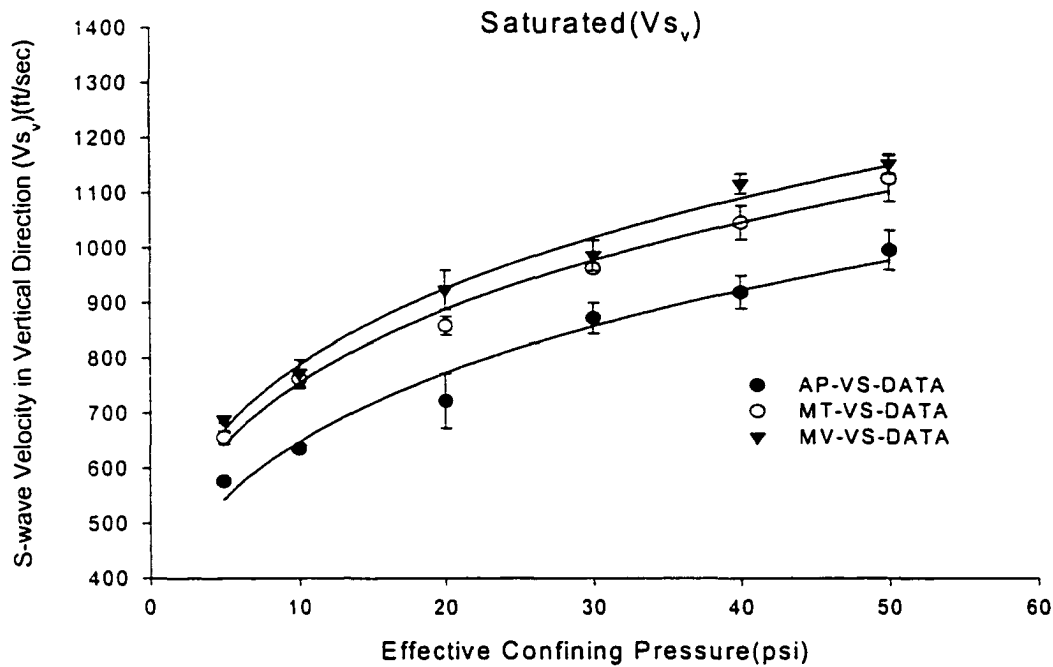


Figure 4.9 S-wave velocities in the horizontal direction against effective confining pressure at saturated condition ($S=100\%$)

In case of dry specimens, the values of V_{p_v} were measured as 1288, 1217 and 1293 ft/sec for AP, MT and MT specimens under 10 psi effective confining pressure as seen in Tables 4.4 through 4.5, respectively. The differences in vertical P-wave velocities of MV and AP specimens are just about 0.38%. The results indicate that in vertical direction P-wave velocities are nearly identical.

The ratios of V_{p_v} to V_{p_h} for AP, MT and MV specimens are 1.085, 1.007 and 0.998, respectively. It implies that P-wave velocities in both directions are nearly identical for MT and MV, but not for AP specimens. It appears that AP technique in comparison with the others creates more rigid structures in vertical direction, while MT and MV techniques create rather isotropic structures. In addition, the highest P-wave velocities in any direction were given by MV technique. Since there is a very small difference in the V_{p_v}/V_{p_h} ratio (0.998), MV technique creates the strongest specimen.

From Figures 4.5, and 6, another conclusion can be made that V_{pv} and V_{ph} velocities are highly affected by the presence of water in the porous media. The compressibility of air in comparison with the compressibility of sand particles is very high. Therefore, P-wave velocity increases with increasing confining pressure when specimens are dry. When the same porous volume is filled with de-aired water, fully saturated specimens give similar magnitudes of V_{pv} at any effective pressures as seen in Figure 4.7 and in Appendix E.

As seen in Figure 4.8 and 4.9, under dry and saturated conditions, S-waves of all reconstituted specimens increase with increasing effective confining pressure. As stresses increased at the contacts between the particles, frictional forces go up. It creates stronger stiffness. Some wave records are also presented in Appendix D and E.

In case of dry specimens, the values of V_{sv} were measured as 687, 813, and 836 ft/sec for AP, MT and MV specimens under 10 psi effective confining pressure as seen in Tables 4.4, 4.5, and 4.6, respectively. The difference in vertical S-wave velocities of MV and AP specimens are about 21.6%. In the case of saturated specimens, the difference is also 21.52%. Those fact implies that S-waves can clearly distinguished the differences of AP, MT and MV techniques as compared with the curves of P-wave velocities. The smallest magnitudes of S-wave velocities under dry and saturated conditions were created by AP techniques while the highest S-wave velocities occurred for MV specimens for all levels of the effective confining pressure. There could be a strong relationship between inherent anisotropy, shear wave velocities, and hence shear modulus of the specimens.

4.4 Consolidation Test

In order to obtain the compressibility (bulk modulus) of the soil specimens, three series of consolidation tests were conducted by using the triaxial test setup. Specimens were prepared at 5 psi vacuum pressure first. Those were saturated under 10 psi confining pressure and 5 psi back pressure with CO₂ gas and then de-aired water circulations. Saturation process was checked by pulse transmission method. P-wave arrival time in vertical direction was chosen as a reference. When the saturation degree was increased, it transmitted faster and higher amplitude P-waves. When the velocity of saturated specimens was reached, it was assumed that the specimens were saturated.

After specimens were saturated under 10 psi confining and 5 psi back pressure, isotropic consolidation stresses were increased step by step from 10, 20 30, 40, and to 50 psi. Volumetric and axial strains were measured. Relationships between different soil fabrics created by the different preparation methods and the volumetric stress-strain behavior were established from the consolidation tests. Volumetric (ϵ_v) and axial (ϵ_l) strain were measured under the consolidation pressures. The values of volumetric and axial strain changes were recorded at 15 and 30 seconds and at 1, 2, 4, 8 and 15 minutes. The consolidation time of specimens generally took place in 2 minutes and there was no significant volumetric or axial strain changes observed thereafter. The results are seen in Table 4.7 and Figures 4.10 and 4.11. It is clear that the preparation techniques caused significant differences in terms of the volumetric and axial strains. It was observed that the amount of volumetric strain (ϵ_v), and the axial strain (ϵ_l) were the highest for AP specimens, followed by MT, and MV specimens in the order. It implies that AP specimens had the lowest stiffness and the highest tendency for volume changes

and thus lowest resistance against liquefaction.

Table 4.7 Consolidation test results of reconstituted soil specimens

Consolidation Pressure	ϵ_v			ϵ_1		
	AP	MT	MV	AP	MT	MV
psi	%	%	%	%	%	%
10	0.05517	0.04287	0.04193	0.012737	0.012012	0.013953
20	0.17432	0.10966	0.11380	0.043205	0.032441	0.038257
30	0.26563	0.16749	0.17371	0.070058	0.051338	0.058565
40	0.33888	0.21634	0.22312	0.090545	0.066413	0.077231
50	0.40138	0.25920	0.26356	0.106257	0.080396	0.092614

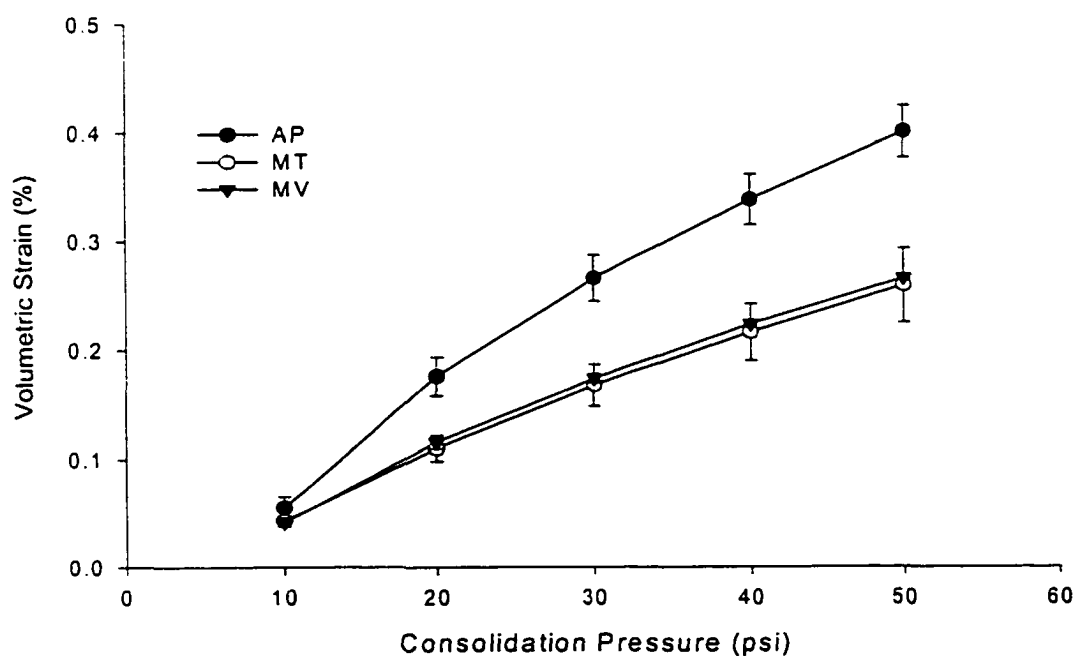


Figure 4.10 Volumetric strain against consolidation pressure for AP, MT, and MV specimens

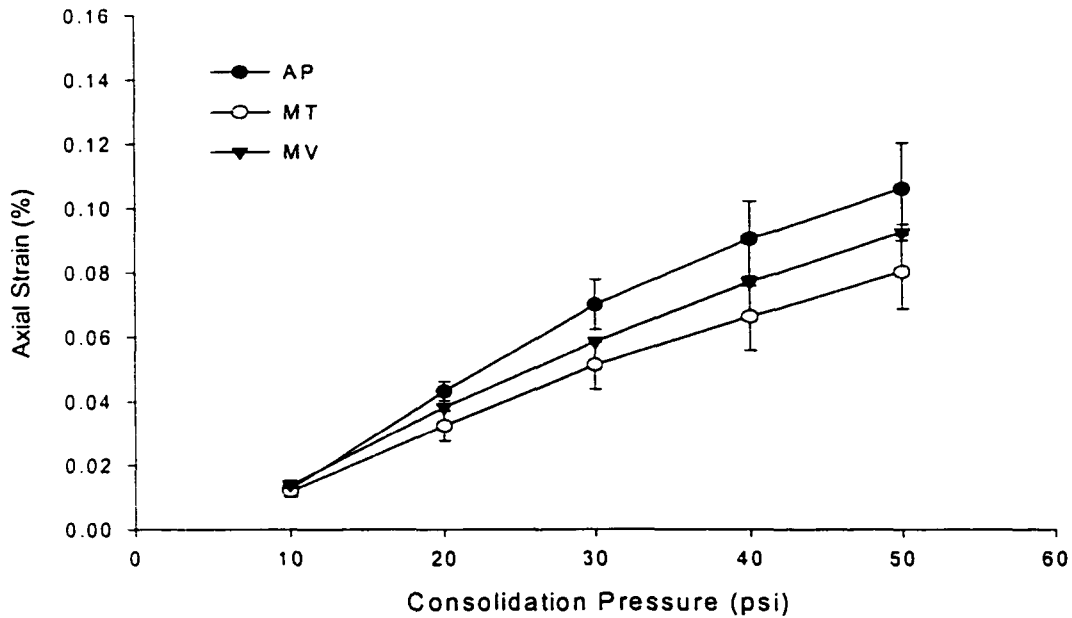


Figure 4.11 Axial strain against consolidation pressure for AP, MT and MV specimens

4.5 Analysis of Results

4.5.1 Elastic Wave Velocities

It was observed that under dry condition, elastic waves were a function of effective confining stress. The relationships between effective stress and elastic wave velocity were investigated. As mentioned in Section 2.6.2, it was found that elastic waves have a good correlation with effective confining pressure (σ'). Elastic waves, which were measured during this investigation, can be well expressed by the following formula:

Air Pluviation:

$$V_{pv} = 898.55(\sigma')^{0.1543} \quad R^2 = 0.999 \quad S = 0\% \quad (4.1a)$$

$$V_{ph} = 733.21(\sigma')^{0.2132} \quad R^2 = 0.997 \quad S = 0\% \quad (4.1b)$$

$$V_{sv} = 398.25(\sigma')^{0.2489} \quad R^2 = 0.984 \quad S = 0\% \quad (4.1c)$$

$$V_{sv} = 373.96(\sigma')^{0.2427} \quad R^2 = 0.963 \quad S = 100\% \quad (4.1d)$$

Moist Tamping:

$$V_{pv} = 823.81(\sigma')^{0.1793} \quad R^2 = 0.991 \quad S = 0\% \quad (4.2a)$$

$$V_{ph} = 792.56(\sigma')^{0.1907} \quad R^2 = 0.993 \quad S = 0\% \quad (4.2b)$$

$$V_{sv} = 457.57(\sigma')^{0.2479} \quad R^2 = 0.991 \quad S = 0\% \quad (4.2c)$$

$$V_{sv} = 447.77(\sigma')^{0.2289} \quad R^2 = 0.988 \quad S = 100\% \quad (4.2d)$$

Moist Vibration

$$V_{pv} = 859.6(\sigma')^{0.1827} \quad R^2 = 0.995 \quad S = 0\% \quad (4.3a)$$

$$V_{ph} = 832.2(\sigma')^{0.1896} \quad R^2 = 0.990 \quad S = 0\% \quad (4.3b)$$

$$V_{sv} = 478.86(\sigma')^{0.2468} \quad R^2 = 0.993 \quad S = 0\% \quad (4.3c)$$

$$V_{sv} = 466.09(\sigma')^{0.2294} \quad R^2 = 0.987 \quad S = 100\% \quad (4.3d)$$

4.5.2 Recovery of Elastic Constant

It should be noted that during the following analyses and numerical calculations, all the soil specimens were assumed to have relative density of 50% and their elastic wave velocities were calculated from Equations 4.1, 4.2 and 4.3 for simplifications rather than using the raw data values.

4.5.2.1 Isotropic Material Constants

First, it is assumed that AP, MT and MV preparation techniques create isotropic materials. From the elastic theory for isotropic materials, P-wave velocities in horizontal and vertical directions are:

$$V_{pH} = V_{pV} = \sqrt{\frac{\lambda + 2G}{\rho}} \quad \text{or} \quad = \sqrt{\frac{K + \frac{4}{3}G}{\rho}} \quad (4.4)$$

and S-wave velocity is:

$$V_s = \sqrt{\frac{G}{\rho}} \quad (4.5)$$

and the ratio of V_p to V_s is:

$$\frac{V_p}{V_s} = \sqrt{\frac{K}{G} + \frac{4}{3}} \quad (4.6)$$

where λ is Lamé's constant. G is shear modulus and K is bulk modulus of linear isotropic materials.

During the consolidation test, the instantaneous increase of confining pressure $\Delta\sigma_c$ is applied on a fully saturated soil and the pore water pressure in the soil initially increases. Because of allowed drainage, $\Delta\sigma_c$ is gradually transferred from water in the porous of soil to the assembly of soil particles. Then the increment of confining pressure is carried by the soil skeleton. Eventually, a volume change occurs. The volume change is a function of the compressibility or bulk modulus of soil structure. Therefore, the bulk modulus of soil structure can be determined from the consolidation test as follows:

$$\varepsilon_v = \frac{\Delta V}{V} = \varepsilon_1 + \varepsilon_2 + \varepsilon_3 \quad (\text{Isotropic condition } \varepsilon_1 = \varepsilon_2 = \varepsilon_3) \quad (4.7)$$

$$\frac{\Delta V}{V} = \frac{\sigma}{K} \quad (4.8)$$

where ε_v is volumetric strain. ε_1 , ε_2 and ε_3 , are axial strains in principal stress directions 1, 2 and 3, respectively.

As seen in Figures 4.10 and 4.11, during the consolidation test, soil specimens produce non-linear (curved) behavior. However, bulk modulus is linearly related with the volumetric strain and effective stress as expressed in Equation 4.8. To reduce any complication, within a small stress interval, the following relation can be used to obtain

tangent bulk modulus (K):

$$K_n = \frac{\sigma_n - \sigma_{n-1}}{\varepsilon_{vn} - \varepsilon_{vn-1}} \quad (4.9)$$

where ε_{vn} and ε_{vn-1} are the volumetric strain at effective pressure σ_n' , σ_{n-1}' , respectively.

K values of AP, MT, and MV specimens in terms of effective pressures are given in Table 4.8.

Table 4.8 Consolidation test results of AP, MT, MV specimens

AP					
σ	ε_v	ε_1	ε_2	$\varepsilon_v/\varepsilon_1$	K
psi	%	%	%		psi
10	0.055172	0.012737	0.021218	4.331706	9062.57
20	0.175784	0.043205	0.06629	4.068604	8291.018
30	0.266122	0.070058	0.098032	3.798572	11069.65
40	0.338878	0.090545	0.124166	3.742631	13744.49
50	0.401376	0.106257	0.14756	3.777403	16000.45
MT					
10	0.042868	0.012012	0.015428	3.568694	11663.8
20	0.109664	0.032441	0.038612	3.380435	14970.88
30	0.167488	0.051338	0.058075	3.262452	17293.88
40	0.216336	0.066413	0.074962	3.257442	20471.45
50	0.259202	0.080396	0.089403	3.224054	23328.82
MV					
10	0.041927	0.013953	0.013987	3.004919	11925.5
20	0.115302	0.038257	0.038523	3.013892	13628.54
30	0.173706	0.058565	0.05757	2.966039	17122.35
40	0.223873	0.077231	0.073321	2.898746	19933.16
50	0.265803	0.092614	0.086594	2.870005	23849.53

The direct measurement of shear modulus with applied shear strain is not experimentally possible by using the triaxial test device. However, shear modulus (G) of

the specimens can be computed from elastic S-wave measurements using Equation 4.5. Computed K values in Table 4.8, and G values obtained from S-wave measurements are used to compute V_{p_v}/V_{s_v} ratio (Equation 4.6) for consolidation test. Computed V_{p_v}/V_{s_v} values from the consolidation test and from actual wave measurements are compared in Table 4.9, and in Figures 4.12, 13, and 14 for AP, MT and MV specimens, respectively.

Table 4.9 Computed and measured elastic wave velocity ratios

σ	Consolidation Test			Wave Measurement Test		
	V_{p_v}/V_{s_v}			V_{p_v}/V_{s_v}		
	AP	MT	MV	AP	MT	MV
psi						
10	1.479	1.452	1.436	1.815	1.537	1.549
20	1.376	1.428	1.387	1.699	1.466	1.481
30	1.389	1.414	1.393	1.636	1.426	1.443
40	1.406	1.420	1.395	1.592	1.398	1.417
50	1.417	1.425	1.411	1.558	1.377	1.397

As seen in Figures 4.13 and 14, MT and MV specimens show good agreements. It should be noted that V_p/V_s ratios from the consolidation test use the measured bulk modulus from isotropic loading tests based on the isotropic material assumption, and thus good agreement of two curves implies that the isotropic material assumption is nearly valid. It can be said that MT and MV specimens had nearly isotropic soil fabrics. Figure 4.12, however, shows a significant difference on two curves, which implies that isotropic material assumption is not valid for AP specimens. It was mentioned before that the ratios of V_{p_v} to V_{p_h} for AP, MT, and MV specimens are 1.085, 1.007 and 0.998, respectively. P-wave velocities in both directions are nearly identical for MT and MV,

but not for AP specimens. It appears that AP technique in comparison with the others creates highly anisotropic structure. In addition, as seen in Table 4.8, the ratio of ε_v to ε_1 for AP specimens is higher than 4. It implies that AP specimens are highly anisotropic. Meanwhile, the ratios of ε_v to ε_1 for MT and MV specimens are rather close to the value of 3.33, which is for ideal isotropic materials.

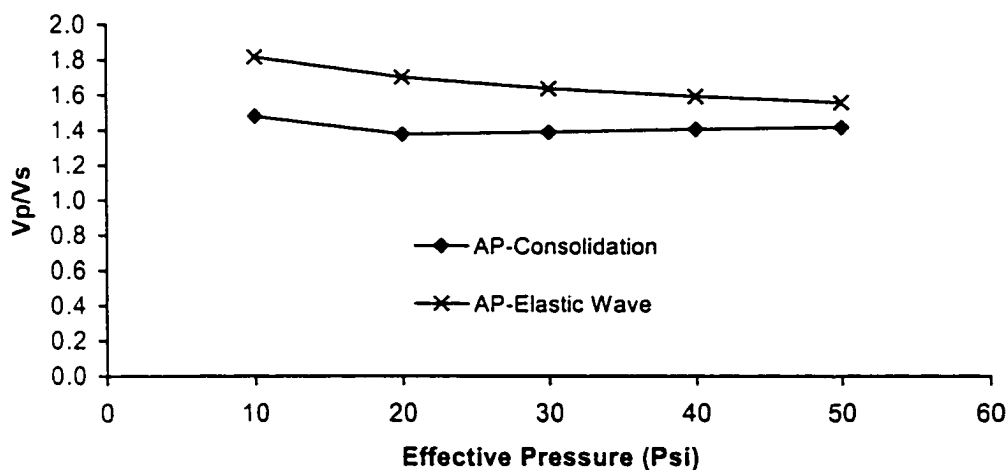


Figure 4.12 Measured and computed elastic wave velocity ratio for AP specimens

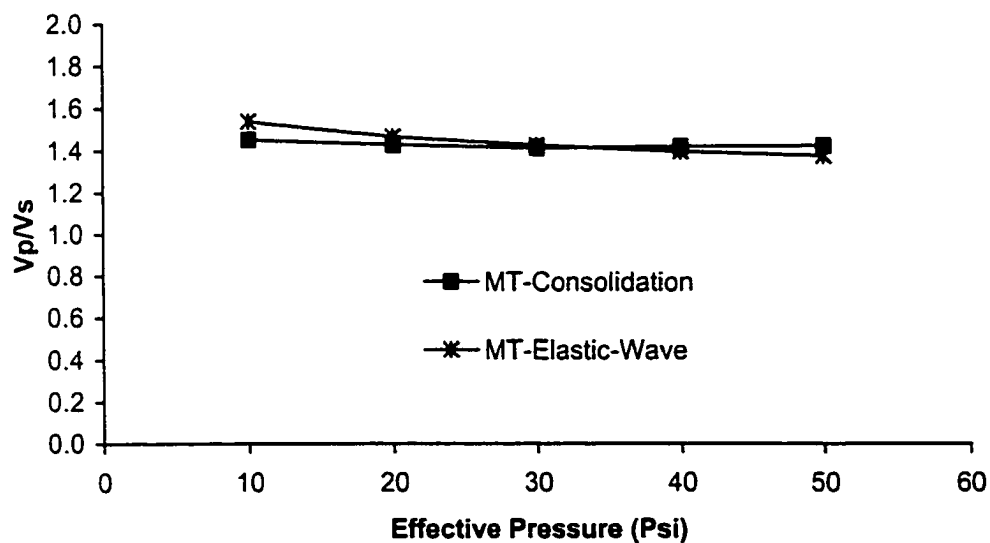


Figure 4.13 Measured and computed elastic wave velocity ratio for MT specimens

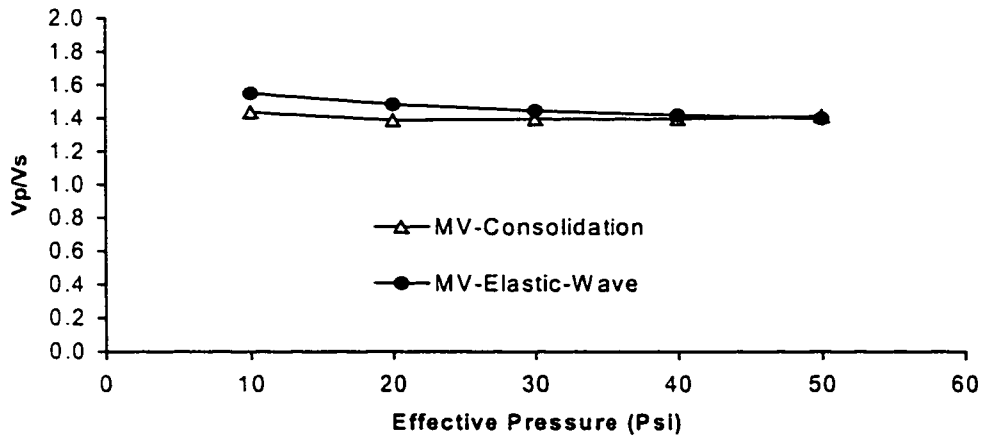


Figure 4.14 Measured and computed elastic wave velocity ratio for MV specimens

4.5.2.2 Transversely Isotropic Material Constants

It is a logical assumption that AP, MT and MV preparation techniques in a cylindrical triaxial device create transversely isotropic materials. As mentioned in Chapter 3, the specimens considered in direction '1', which is normal to plane 2-3, has the same properties or behaves isotropically on one symmetry plane (plane 2-3). During the experiments, two measurements of P-wave velocities and one S-wave velocity were obtained in the plane 1-2. In transversely isotropic condition, P-wave and S-wave can be expressed as:

P-wave velocity in vertical direction in the plane 1-2:

$$V_{pv} = \sqrt{\frac{C_{11}}{\rho}} \quad (4.10)$$

P-wave velocity in horizontal direction in the plane 1-2:

$$V_{ph} = \sqrt{\frac{C_{22}}{\rho}} \quad (4.11)$$

S-wave velocity in the vertical direction in the plane 1-2:

$$V_s = \sqrt{\frac{C_{44}}{\rho}} \quad (4.12)$$

where C_{11}, C_{22} and C_{44} are the components of the stiffness matrix of transversely isotropic materials. Those were identified in Section 3.5.1. In the transversely isotropic cases, the five elastic constants ($E_1, E_2, G_{12}, \nu_{21}$ and ν_{23}) must be defined independently. G_{12} can be directly calculated by Equation 4.12 from S-wave measurement.

During the consolidation test, a hydrostatic state of stress ($\sigma_1=\sigma_2=\sigma_3$) exists and every directions are principle directions. Because of the transversely isotropic condition ($\varepsilon_2 = \varepsilon_3$), Equation 4.7 can be rewritten as:

$$\varepsilon_v = \varepsilon_1 + 2\varepsilon_2 \quad (4.13)$$

$$\varepsilon_1 = \frac{\sigma_1}{E_1} - \frac{\nu_{21}}{E_2} \sigma_2 - \frac{\nu_{21}}{E_2} \sigma_3 \quad (4.14)$$

$$\varepsilon_2 = \frac{\sigma_2}{E_2} - \frac{\nu_{21}}{E_2} \sigma_1 - \frac{\nu_{23}}{E_2} \sigma_3 \quad (4.15)$$

ε_2 can be obtained from Equation 4.13 using consolidation test results shown in Table 4.8. As observed earlier in this section, under the consolidation test, volumetric strain curves were non-linear (curved). Therefore to utilize Equations 4.14 and 4.15, the following modifications are made:

$$\Delta\varepsilon_{k,n} = \varepsilon_{k,n} - \varepsilon_{k,n-1} \quad (4.16)$$

$$\Delta\sigma_{k,n} = \sigma_{k,n} - \sigma_{k,n-1} \quad (4.17)$$

where k represents the direction of the strain, and n shows the step number of increments of the effective confining pressure.

Finally, Equations 4.10, 4.11, 4.16 and 4.17 were used for the recovery of other four independent elastic constants (E_1, E_2, ν_{21} and ν_{23}). It should be noted that these equations are non-linear. Therefore, those need to be solved numerically. A commercial

computer program, Mathematica, was used to solve the problem. First, initial values of elastic constants were assigned, and E_1 , E_2 , ν_{21} and ν_{23} were obtained for AP, MT and MV specimens under different effective confining pressures. All initial data and results are given in Tables 4.10 through 4.18, and the results are plotted in Figures 4.15, 4.16 and 4.17.

Table 4.10 Initial input values of AP specimens at different effective pressures

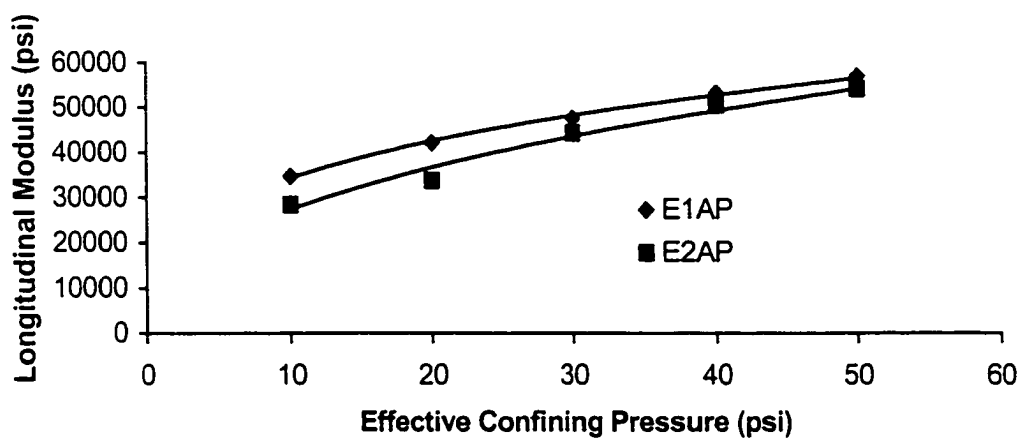
σ'	ϵ_v	ϵ_1	ϵ_2	V_{sv}	G_{12}	V_{pv}	V_{ph}
psi	%	%	%	ft/sec	psi	ft/sec	ft/sec
10	0.055172	0.01274	0.021218	706.408	10589.811	1281.865	1197.922
20	0.175784	0.04321	0.06629	839.425	14953.434	1426.564	1388.699
30	0.266122	0.07006	0.098032	928.563	18297.813	1518.665	1514.086
40	0.338878	0.09055	0.124166	997.490	21115.126	1587.596	1609.858
50	0.401376	0.10626	0.14756	1054.458	23595.842	1643.211	1688.297

Table 4.11 Values of recovered elastic constants for AP specimens

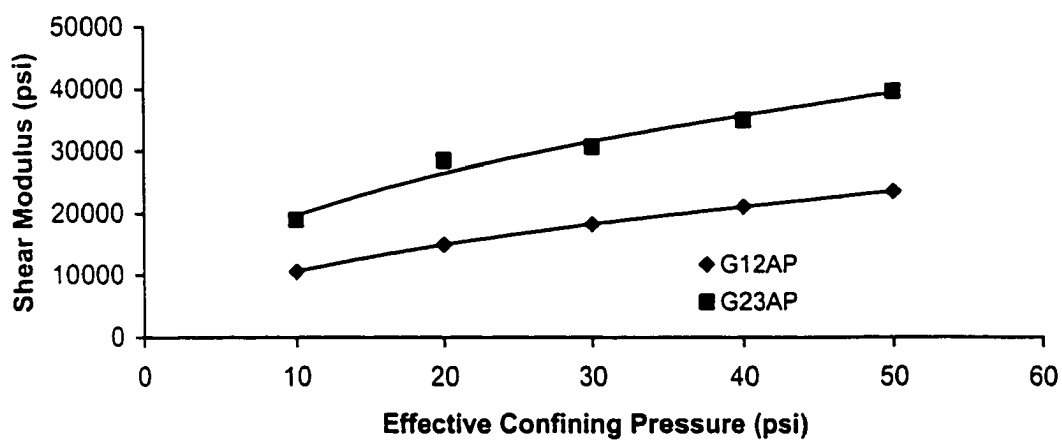
σ'	ν_{32AP}	ν_{21AP}	E_{1AP}	E_{2AP}	G_{12AP}	G_{23AP}
psi			psi	psi	psi	psi
10	-0.253	0.048	34624.023	28383.345	10589.811	18998.401
20	-0.409	-0.113	42098.160	33771.539	14953.434	28556.012
30	-0.278	-0.128	47475.501	44314.466	18297.813	30702.636
40	-0.278	-0.043	53192.749	50556.017	21115.126	35025.549
50	-0.318	0.050	56926.003	54178.134	23595.842	39692.220

Table 4.12 Errors of the non-linear equations for AP specimens

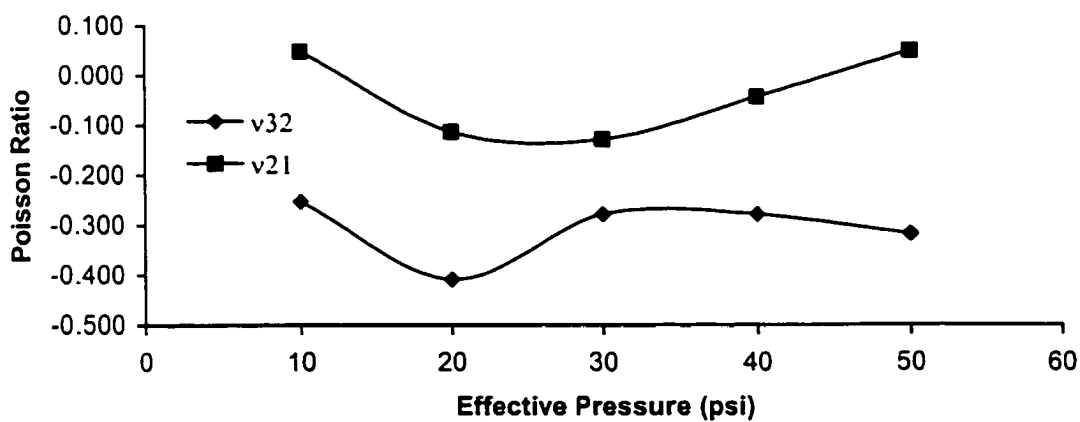
σ'	Equation 4.10	Equation 4.11	Equation 4.16	Equation 4.17
psi				
10	0	0	1.69E-18	-1.69E-18
20	0	2.84E-14	-6.78E-18	1.69E-18
30	0	0.00E+00	-8.47E-19	-8.47E-19
40	2.84E-14	0	1.69E-18	1.06E-18
50	0	0	-8.47E-19	-2.12E-19



(a)



(b)



(c)

Figure 4.15 Transversely isotropic, elastic constants of AP specimens (a) longitudinal modulus (b) shear modulus (c) Poisson's ratio

Table 4.13 Initial input values of MT specimens at different effective pressures

σ'	ε_v	ε_1	ε_2	V_{sv}	G_{12}	V_{pv}	V_{pH}
psi	%	%	%	ft/sec	psi	ft/sec	ft/sec
10	0.0428677	0.012012	0.0154278	809.762	15028.414	1244.879	1229.510
20	0.109664	0.032441	0.0386116	961.574	21191.604	1409.619	1403.261
30	0.1674879	0.051338	0.0580749	1063.251	25910.147	1515.915	1516.070
40	0.2163365	0.066413	0.0749617	1141.848	29882.333	1596.160	1601.567
50	0.2592019	0.080396	0.0894028	1206.791	33378.167	1661.317	1671.190

Table 4.14 Values of recovered elastic constants for MT specimens

σ'	V_{32MT}	V_{21MT}	E_{1MT}	E_{2MT}	G_{12MT}	G_{23MT}
psi			psi	Psi	psi	psi
10	-0.123	0.075	35143.447	33959.295	15028.414	19367.351
20	-0.075	0.035	45427.897	44826.053	21191.604	24218.402
30	-0.027	0.002	52661.897	52635.576	25910.147	27037.866
40	-0.051	0.064	57933.986	58414.911	29882.333	30764.836
50	0.017	0.062	62757.746	63729.850	33378.167	31317.874

Table 4.15 Errors of the non-linear equations for MT specimens

σ'	Equation 4.10	Equation 4.11	Equation 4.16	Equation 4.17
psi				
10	0.00E+00	2.84E-14	-3.81E-18	4.24E-18
20	2.84E-14	2.84E-14	8.47E-19	1.48E-18
30	-2.84E-14	1.28E-12	1.70E-16	6.20E-17
40	3.12E-13	1.71E-13	-7.41E-19	-1.74E-17
50	-2.84E-14	2.84E-14	3.71E-19	1.69E-18

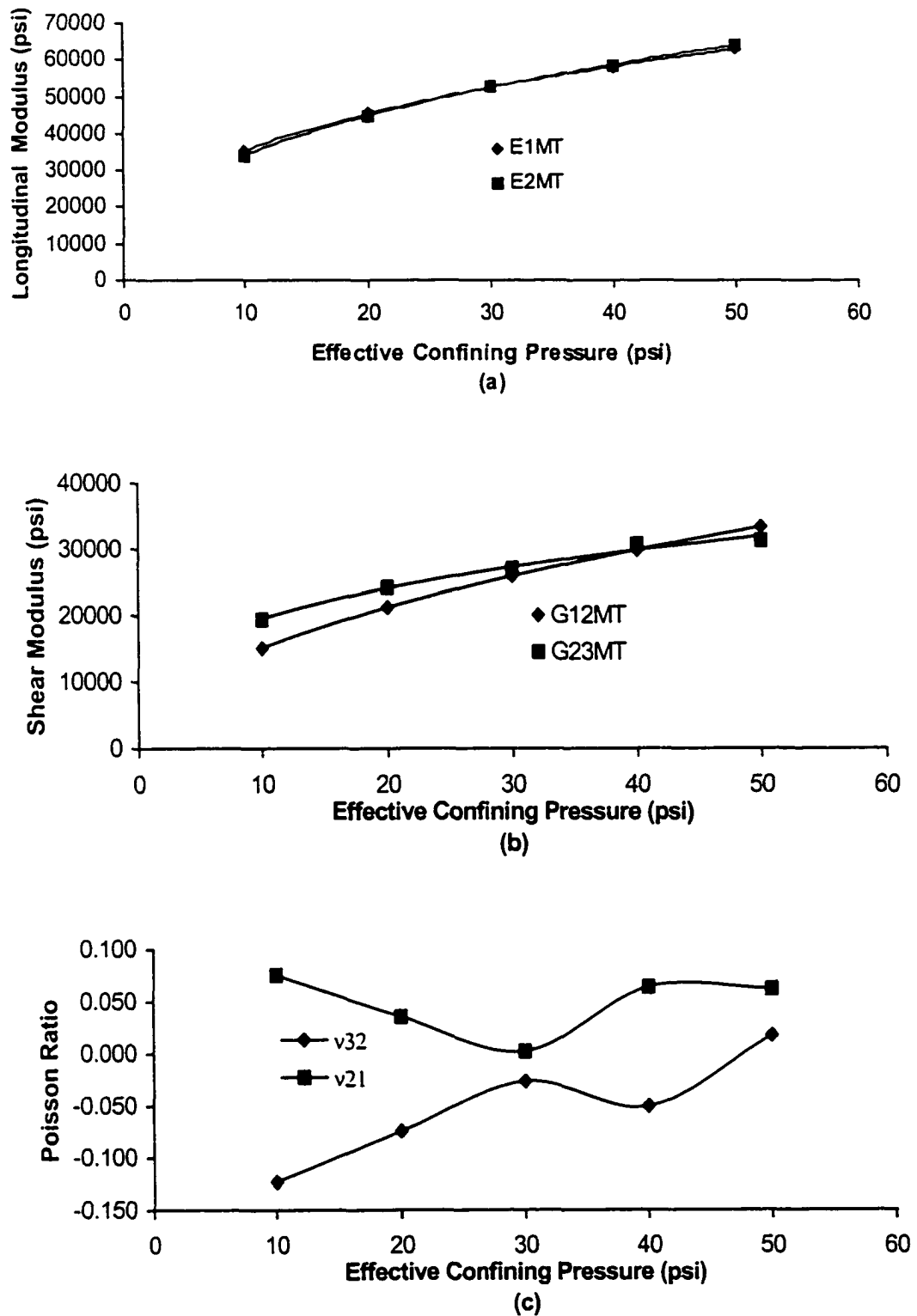


Figure 4.16 Transversely isotropic elastic constants of MT specimens (a) longitudinal modulus (b) shear modulus (c) Poisson's ratio

Table 4.16 Initial input values of MV specimens at different effective pressure

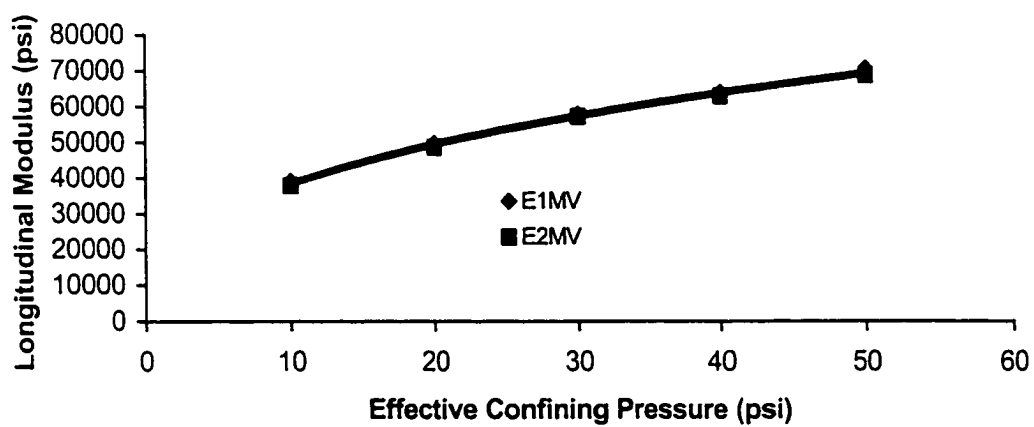
σ'	ε_v	ε_1	ε_2	V_{sv}	G_{12}	V_{pv}	V_{ph}
psi	%	%	%	ft/sec	psi	ft/sec	ft/sec
10	0.041927	0.013953	0.013987	845.296	16376.278	1309.171	1287.739
20	0.115302	0.038257	0.038523	1003.004	23057.043	1485.917	1468.598
30	0.173706	0.058565	0.057570	1108.567	28165.810	1600.171	1585.951
40	0.223873	0.077231	0.073321	1190.137	32463.251	1686.525	1674.859
50	0.265803	0.092614	0.086594	1257.518	36243.221	1756.703	1747.239

Table 4.17 Values of recovered elastic constants for MV specimens

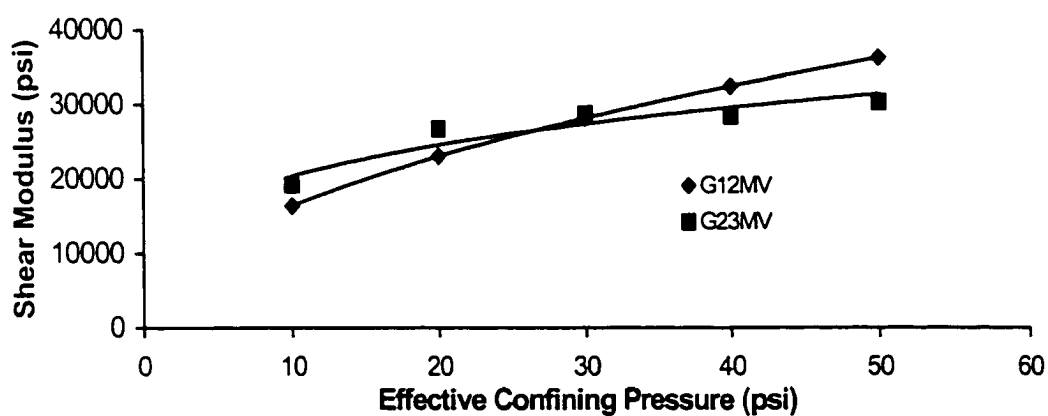
σ'	V_{12MV}	V_{21MV}	E_{1MV}	E_{2MV}	G_{12MV}	G_{23MV}
psi			psi	Psi	psi	psi
10	-0.016	-0.045	39119.559	37916.935	16376.278	19267.415
20	-0.091	-0.101	49634.773	48584.722	23057.043	26735.446
30	-0.004	-0.086	57803.446	57208.408	28165.810	28710.433
40	0.105	-0.095	63859.166	62862.232	32463.251	28456.166
50	0.130	-0.041	70445.245	68627.720	36243.221	30367.376

Table 4.18 Errors of the non-linear equations for MV specimens

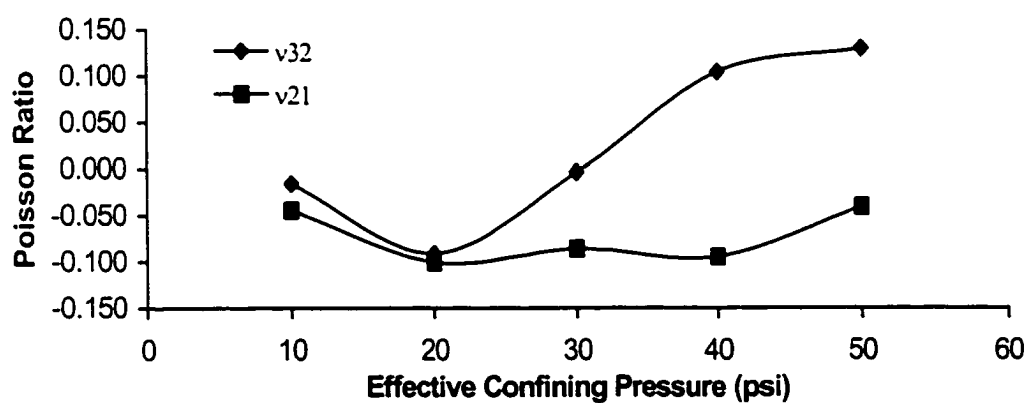
σ'	Equation 4.10	Equation 4.11	Equation 4.16	Equation 4.17
10	-2.84E-14	-2.84E-14	-4.76E-19	4.24E-19
20	0.00E+00	0.00E+00	-1.27E-18	8.47E-19
30	0.00E+00	0.00E+00	3.18E-19	5.54E-18
40	0.00E+00	0.00E+00	6.35E-19	-1.27E-18
50	0.00E+00	0.00E+00	0.00E+00	0.00E+00



(a)



(b)



(c)

Figure 4.17 Transversely isotropic elastic constants of MV specimens (a) Longitudinal modulus (b) shear modulus (c) Poisson's ratio

From Tables 4.10 to 18 and Figures 4.15 to 17, the following observations can be made:

First, based on previous studies, initial values of E_1 and E_2 were assigned as 30000 psi and the values of E_1 were recovered as 34624, 35143, and 39119 psi for AP, MT and MT specimens under 10 psi effective confining pressure, respectively. Based on the recovered values of E_1 , it appears that the amount of the rigidity in vertical direction of specimens increase in the order of AP<MT<MV as seen in Figure 4.18.

E_2 was found as 28383, 31421 and 37916 psi for AP, MT and MT specimens under 10 psi effective confining pressure, respectively. The amount of the compressional rigidity in horizontal direction or on isotropic planes of specimens increases in the order of AP<MT<MV as seen in Figure 4.19.

The highest values of longitudinal elastic moduli (E_1 and E_2) were obtained from MV specimen. The ratio of E_1 to E_2 for AP, MT and MV specimens were 1.2199, 1.035 and 1.032 under 10 psi effective confining pressure, respectively. It was clear that MV and MT specimens have a overall higher rigidity compare to AP specimens while the ratio of E_1 to E_2 for AP shows a very high cross anisotropy. The comparison of Figures 4.15(a) and (b) clearly implies that shear moduli are highly sensitive on soil fabric than longitudinal moduli in AP specimens.

G_{12} , shear modulus in the shear plane containing principal stresses σ_1 and σ_2 , was directly obtained from S-wave measurements in the vertical plane. G_{12} was found as 10589, 15028 and 16376 psi for AP, MT and MT specimens under 10 psi effective confining pressure, respectively. Based on the values of G_{12} , elastic shear moduli becomes higher in the order AP<MT<MV as seen in Figure 4.20. It is also seen G_{12} of AP specimen are significantly smaller than the ones of MT and MV specimens.

G_{23} , recovered elastic shear modulus, was found as 18998, 19367, and 19267 psi for AP, MT and MT specimens under 10 psi effective confining pressure, respectively. The amount of the stiffness G_{23} in horizontal direction and on the isotropic planes of specimens increase in the order AP<MV<MT. However, the values of the shear modulus were rather close as seen in Figure 4.21.

The ratios of G_{12} to G_{23} were 0.557, 0.776 and 0.850 for AP, MT and MV specimens under 10 psi effective confining pressure, respectively. It was shown that AP shows again distinguishable anisotropy compare to the other preparation techniques, but the differences are not large as compared with G_{12} .

Regarding the recovered Poisson's ratios, based on previous studies, initial values of ν_{21} and ν_{32} were assigned as 0.1 (Hardin and Richart 1963; Anadarajah and Kuganenthira, 1995; Bellotti et al. 1996; Zeng and Li 1999). Poisson's ratios were found so changeable under different effective confining pressures. Transversely composite materials can have Poisson's ratios fallen in the range of -1 to 0.5 . It implies that the results of our numerical studies were logical. The reason is that two independent tests were combined to obtain five independent elastic constants. Wave velocity measurements, which are low-strain tests, can be conducted without compromising the stress history of the soils. If during the tests an approximate magnitude of strain falls into the range between 10^{-6} to 10^{-5} , the range is acceptable to determine elastic characteristics of soils. However, after the results of the consolidation test were obtained by Equations 4.16 and 4.17, those axial strains fell into the range between 10^{-4} to 10^{-5} and the small axial range difference might significantly affect the Poisson ratios. A numerical study was made to understand this behavior. Values of P-wave velocities in vertical and horizontal directions were reduced 1% from the original values and run the recovery

program again and Poisson's ratios changed 47% but the other longitudinal modulus did not change more than 2%. It is clear that these errors come from experiments and/or recovery technique. The results may not affect significantly longitudinal moduli values, but the Poisson's ratios are affected.

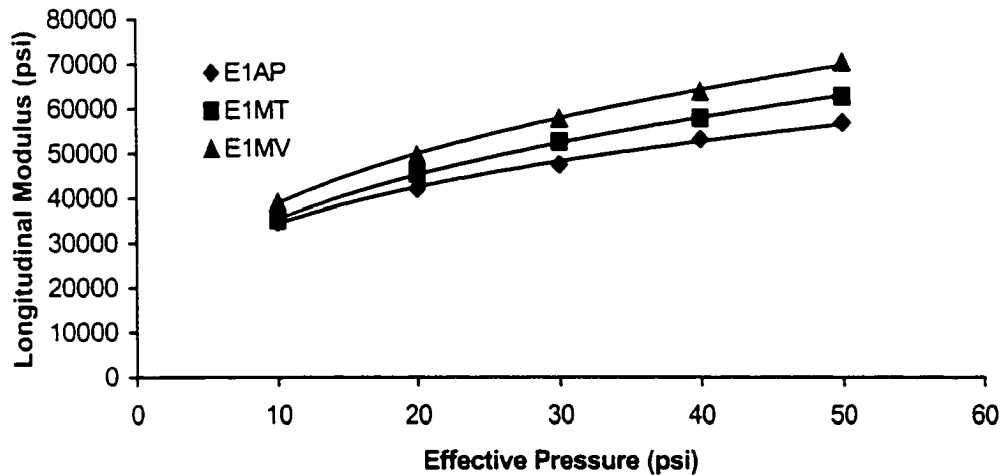


Figure 4.18 Influence of preparation techniques on longitudinal modulus in vertical direction, E_1

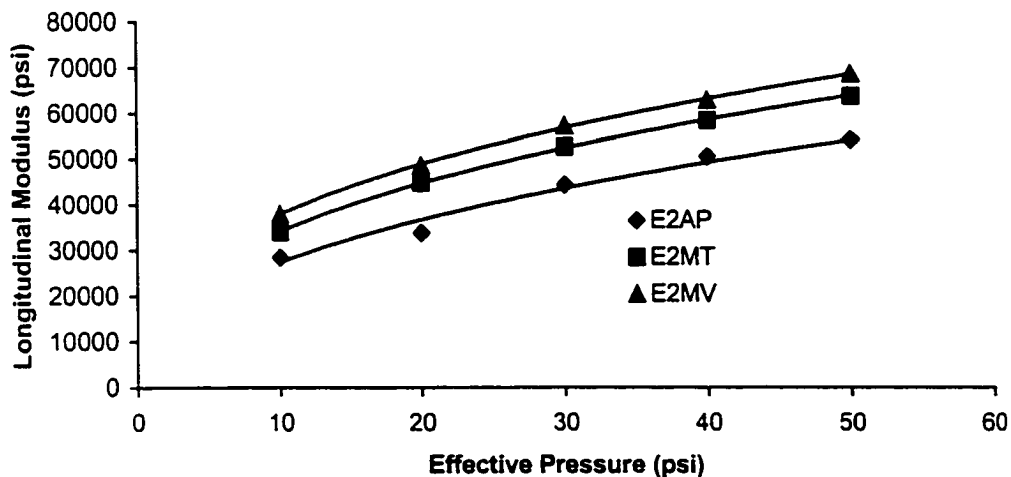


Figure 4.19 Influence of preparation techniques on longitudinal modulus in horizontal direction, E_2

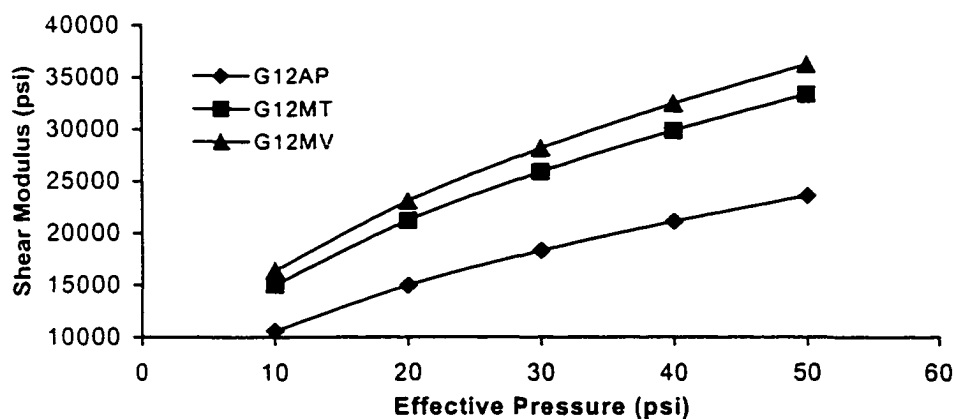


Figure 4.20 Influence of preparation techniques on shear modulus in vertical plane, G_{12}

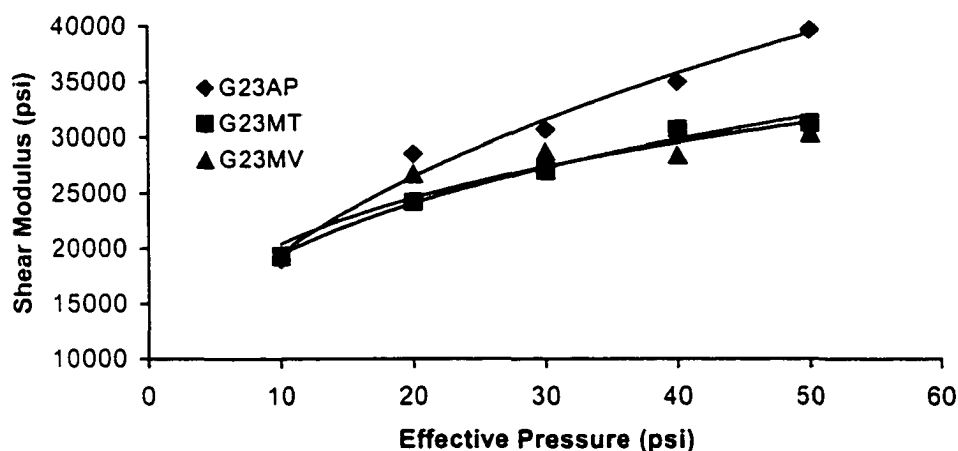


Figure 4.21 Influence of preparation techniques on shear modulus in vertical plane, G_{23}

4.5.3 Determination of Inherent Anisotropy

Many researchers indicated that the anisotropy of soils can be qualitatively identified by elastic constants determined in different directions in the granular materials (Schmertman, 1977; Ishibashi and Agarwal, 1991; Agarwal and Ishibashi, 1992; Ishibashi and Kiku, 1995; Santamarina et al., 1996; Hoque et al., 1996; Zeng et al., 1998 and 1999). As discussed in Section 4.5.2, the effects of the anisotropy on elastic wave measurements were explained quantitatively in terms of the elastic constants. It was observed that the recovered elastic constants of the reconstituted specimens were related

to the soil fabric. Here, an anisotropy indexes A^E for transversely isotropic AP, MT and MV specimens was defined as:

$$A^E = \frac{S^E}{E^E} \quad (4.18)$$

where

$$S^E = \frac{G_{12}}{G_{23}} \quad (4.19)$$

$$E^E = \frac{E_1}{E_2} \quad (4.20)$$

S^E is the ratio of shear modulus in vertical to horizontal planes for the reconstituted specimen. E^E is ratio of longitudinal modulus in vertical to horizontal planes. The values of A^E are shown in Table 4.19 and Figure 4.22 for AP, MT and MV specimens using the same subscripts, respectively. It is observed that A^E is very sensitive to the sample preparation techniques. If the specimens were isotropic material, A^E values should be unity. The closest A^E values to unity were given by MV specimen. It can be said that MV technique creates more isotropic soil structure than AP and MT. AP specimen gave the farthest values from unity and MT is intermediate. Based on these observations, A^E values might be useful tool to explain their anisotropy levels.

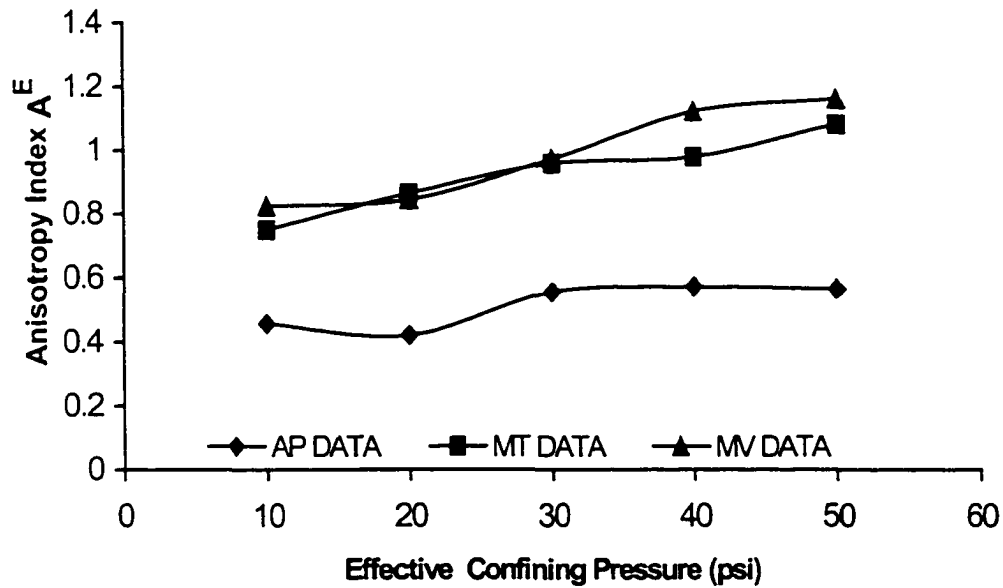


Figure 4.22 Anisotropy index (A^E) calculated from elastic constants

Table 4.19 Values of anisotropy index (A^E) for the specimens under different effective pressures

σ^j	AP			MT			MV		
	G_{12}/G_{23AP}	E_1/E_{2AP}	A^E_{AP}	G_{12}/G_{23MT}	E_1/E_{2MT}	A^E_{MT}	G_{12}/G_{23MV}	E_1/E_{2MV}	A^E_{MV}
Psi									
10	0.557	1.2199	0.457	0.776	1.035	0.750	0.850	1.032	0.824
20	0.524	1.2466	0.420	0.875	1.013	0.863	0.862	1.022	0.844
30	0.596	1.0713	0.556	0.958	1.001	0.958	0.981	1.010	0.971
40	0.603	1.0522	0.573	0.971	0.992	0.979	1.141	1.016	1.123
50	0.594	1.0507	0.566	1.066	0.985	1.082	1.193	1.026	1.163

4.5.4 Relationship between Anisotropy Index and Liquefaction Resistance

As mentioned earlier, Ishibashi and Kiku (1995) numerically simulated liquefaction experiments and directional wave measurements to propose a parameter, which was used to define the effects of anisotropy on liquefaction resistance. The proposed parameter, $G_{avg}/(E_v/E_h)^3$, included directional rigidities. A similar attempt is made to correlate anisotropic indexes, A_{AP}^E , A_{MT}^E and A_{MV}^E to liquefaction resistance.

The results of cyclic triaxial tests such as the one in Figure 4.2 can be expressed by the best fit curves with exponential decay function (Ferrito et al., 1979). Cyclic stress ratio (CSR) can be written as a function of N as:

$$CSR = ae^{\frac{b}{N}} \quad (4.21)$$

where N is the number of cycles, a and b are constants. Previous studies informed that “a” and “b” vary with:

- Relative density
- Unit weight
- Soil fabric
- Fine content
- Aging and cementation
- Grain characteristic
- Saturation degree

In this study, all parameters listed above are the same for AP, MT and MV specimens except soil fabric. Therefore, it can be assumed that “a” in Equation 4.21 is only a function of soil fabric when b=1 is assigned for a simplicity. Here, by assuming

that “a” in Equation 4.21 can be expressed by means of anisotropic, a pseudo cyclic stress ratio (CSR^*) is proposed and defined as:

$$CSR^* = (A^E)^n e^{\frac{1}{N}} \quad (4.22)$$

It should be noted that CSR^* values are assigned individually for AP, MT and MV specimens, using indexes A_{AP}^E , A_{MT}^E and A_{MV}^E , respectively.

To get similar tendencies of CSR^* variation as in CSR values, $n=1.5$ was chosen and CSR^* values were then computed using anisotropic indexes A_{AP}^E , A_{MT}^E and A_{MV}^E values obtained from the wave measurement experiments. Calculated CSR^* values are listed in the right side of Table 4.20 alongside the experimentally obtained CSR values at the right side of the table.

Table 4.20 Experimental CSR and pseudo CSR^* at different number of cycles (N)

N	CSR			CSR*		
	AP	MT	MV	AP	MT	MV
5	0.295	0.693	0.798	0.377	0.793	0.913
10	0.262	0.588	0.639	0.341	0.718	0.826
15	0.252	0.544	0.591	0.330	0.694	0.799
20	0.247	0.521	0.567	0.325	0.683	0.786
25	0.245	0.506	0.553	0.321	0.676	0.778
30	0.243	0.496	0.544	0.319	0.671	0.773

Table 4.21 Ratio of experimental CSR to pseudo CSR*

N	CSR/CSR*		
	AP	MT	MV
5	0.781	0.873	0.874
10	0.767	0.819	0.774
15	0.763	0.785	0.739
20	0.762	0.763	0.722
25	0.761	0.749	0.711
30	0.760	0.740	0.704

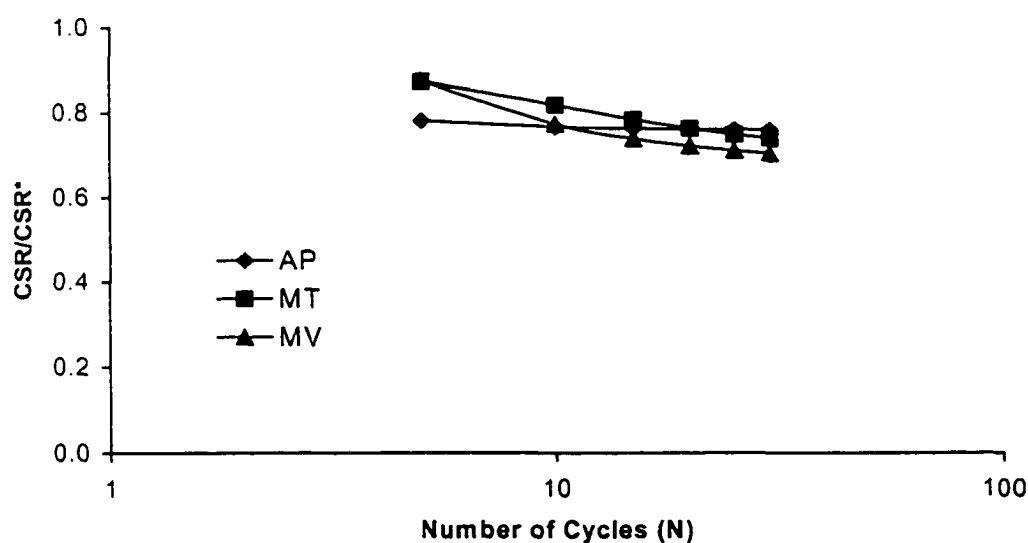


Figure 4.23 Ratio of CSR to CSR* against the number of cycles

Next, CSR values were normalized with the corresponding pseudo CSR* values. Those normalized CSR/CSR* are seen Table 4.21 and plotted against N in Figure 4.23. It is clear from the figure that the parameter $(A^E)^{1.5}$ eliminates the effect of specimen preparation techniques.

4.5.5 Relationship between Liquefaction Resistance and Shear Wave Velocity

Numerous studies have been conducted focusing on the assessment of the liquefaction resistance of soils in both laboratory and field studies. The results indicated

that using shear wave velocities for evaluating liquefaction potential of soils is to give good correlations. (Tokimatsu et al. 1986; Tokimatsu and Uchida, 1990; Andrus, 1999; Stokoe et al. 1999, Kayabali, 1998).

When the evaluation of liquefaction resistance of soil from shear wave velocity (V_s) is considered, the correlation of V_s and anisotropy might be exist. It is known that shear wave velocity is a function of shear modulus and density of the soil. In this case, density or mass is same for AP, MT and MV specimens. Therefore, anisotropy should be directly related to shear modulus.

In this section, a simpler anisotropic parameter is tested to see the effect of induced anisotropy on liquefaction resistance. As mentioned previously, Hardin and Richart (1963), and Hardin and Black (1968) specified shear modulus as:

$$G = A^S \cdot F(e) \cdot g(\sigma) \quad (4.23)$$

$$A^S = f(H, S, \tau_0, C, a, f, \vartheta, T) \quad (4.24)$$

where A^S is a function of several parameters: H , ambient stress and vibration history; S , degree of saturation; τ_0 , octahedral shear stress; C , grain characteristics; a , amplitude of strain; f , frequency of vibration; ϑ , soil fabric; and T , temperature parameter. $g(\sigma')$ is a function of effective confining stress. Previous studies pointed out that shear modulus (G) is function of effective pressure (σ') with n^{th} power, and n is approximately 0.5 for sand. Lastly, $F(e)$ is a function of void ratio and is defined as:

$$F(e) = \frac{(2.17 - e)^2}{e} \quad (4.25)$$

where e is void ratio of soil specimens, and G and σ' are expressed in psi. Considering effective pressure and void ratio effects, Equation 4.23 is rewritten to define shear modulus anisotropic index A^S :

$$A^S = \frac{G}{F(e)(\sigma')^{0.5}} \quad (4.26)$$

Here, void ratio (e) is 0.705 for 50% relative density. Equation 4.26, and G values were obtained from Equations 4.1c, 4.2c and 4.3c. The values of A^S are shown in Table 4.23. A_{AP}^S , A_{MT}^S and A_{MV}^S are functions of the parameters given in Equation 4.24. All parameters are eliminated in Equation 4.26 for all reconstituted specimens except soil fabric. Therefore, differences among A_{AP}^S , A_{MT}^S and A_{MV}^S values only reflect the effect of soil fabric. If the ratios of A_{AP}^S , A_{MT}^S , A_{MV}^S to A_{AP}^S are taken, as seen in the right side of Table 4.23, the ratios represent the effects of soil-fabric on the specimens relative to AP specimen. In fact, the ratio A_{MT}^S / A_{AP}^S , as an example, is reduced to G_{12MT} / G_{12AP} since $F(e)$ and $(\sigma')^{0.5}$ are the same for both specimens. If the ratios with power of 2nd ($n=2$) is put into Equation 4.22, the second pseudo CSR** can be defined as:

$$CSR_{AP}^{**} = \left(\frac{A_{AP}^S}{A_{AP}^S} \right)^2 e^{\frac{1}{N}} = \left(\frac{G_{12AP}}{G_{12AP}} \right)^2 e^{\frac{1}{N}} \quad (4.27)$$

$$CSR_{MT}^{**} = \left(\frac{A_{MT}^S}{A_{AP}^S} \right)^2 e^{\frac{1}{N}} = \left(\frac{G_{12MT}}{G_{12AP}} \right)^2 e^{\frac{1}{N}} \quad (4.28)$$

$$CSR_{MV}^{**} = \left(\frac{A_{MV}^S}{A_{AP}^S} \right)^2 e^{\frac{1}{N}} = \left(\frac{G_{12MV}}{G_{12AP}} \right)^2 e^{\frac{1}{N}} \quad (4.29)$$

where N is the number of cycles. $N=2$ was selected based on trial and error method to best fit the results.

Table 4.22 Shear wave anisotropic index A^S for AP, MT, and MV under different effective confining pressures ($S=0\%$)

σ	A_{AP}^S	A_{MT}^S	A_{MV}^S	$\frac{A_{AP}^S}{A_{AP}^S}$	$\frac{A_{MT}^S}{A_{AP}^S}$	$\frac{A_{MV}^S}{A_{AP}^S}$
psi						
10	2660.341	3775.394	4114.000	1.000	1.419	1.546
20	2656.288	3764.419	4095.791	1.000	1.417	1.542
30	2653.919	3758.014	4085.176	1.000	1.416	1.539
40	2652.240	3753.476	4077.661	1.000	1.415	1.537
50	2650.938	3749.960	4071.842	1.000	1.415	1.536

Table 4.23 Experimental CSR and pseudo CSR** at different number of cycles (N) ($S=0\%$)

N	CSR			CSR**		
	AP	MT	MV	AP	MT	MV
5	0.295	0.693	0.798	1.221	2.460	2.921
10	0.262	0.588	0.639	1.105	2.226	2.643
15	0.252	0.544	0.591	1.069	2.153	2.556
20	0.247	0.521	0.567	1.051	2.117	2.514
25	0.245	0.506	0.553	1.041	2.096	2.489
30	0.243	0.496	0.544	1.034	2.082	2.472

The CSR** values are computed in Table 4.23 alongside the experimental CSR values for AP, MT and MV specimens. Then, CSR values are normalized by corresponding CSR** values as shown in Table 4.24 and Figure 4.24. Figure 4.24 shows a unique relationship between liquefaction resistance and the number of cycles regardless of preparation techniques. The results in Table 4.24 and Figure 4.24 indicate that the differences of shear moduli of soil specimens also give a very selective distinction in terms of relationship of liquefaction resistance to initial soil fabric.

In the previous discussion, S-wave values were obtained from initially dry soil specimens. On the other hand, in the field, soil deposits are almost fully saturated and S-wave measurements may be obtained under fully saturated condition. Therefore, saturation effects on S-wave velocity are considered next.

Table 4.24 Ratio of experimental CSR to pseudo CSR**

N	CSR/CSR**		
	AP	MT	MV
5	0.241	0.282	0.273
10	0.237	0.264	0.242
15	0.236	0.253	0.231
20	0.235	0.246	0.226
25	0.235	0.242	0.222
30	0.235	0.238	0.220

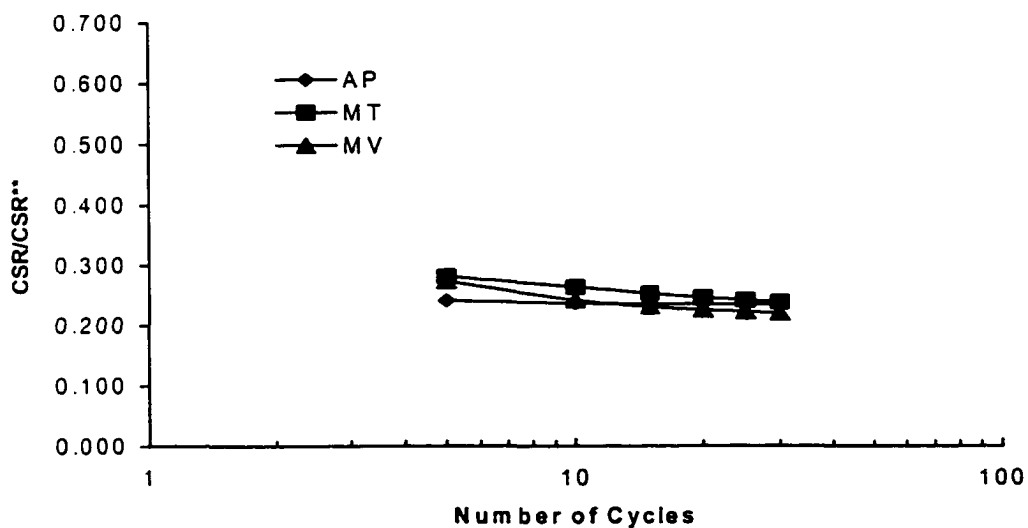


Figure 4.24 Ratio of CSR to CSR** against the number of cycles

Similarly obtained values of A^S are shown in Table 4.25 for S=100% conditions.

A_{AP}^S , A_{MT}^S and A_{MV}^S are obtained from Equations 4.1d, 4.2d and 4.3d for fully saturation

conditions. The values of S-wave measurements in saturated specimens are used to obtain further modified CSR^{***} as:

$$CSR_{AP}^{***} = \left(\frac{A_{AP}^S}{A_{AP}^S} \right)^{2.5} e^{\frac{1}{N}} = \left(\frac{G_{12AP}}{G_{12AP}} \right)^{2.5} e^{\frac{1}{N}} \quad (4.30)$$

$$CSR_{MT}^{***} = \left(\frac{A_{MT}^S}{A_{AP}^S} \right)^{2.5} e^{\frac{1}{N}} = \left(\frac{G_{12MT}}{G_{12AP}} \right)^{2.5} e^{\frac{1}{N}} \quad (4.31)$$

$$CSR_{MV}^{***} = \left(\frac{A_{MV}^S}{A_{AP}^S} \right)^{2.5} e^{\frac{1}{N}} = \left(\frac{G_{12MV}}{G_{12AP}} \right)^{2.5} e^{\frac{1}{N}} \quad (4.32)$$

This is a slight modification from Equations 4.27 to 4.29 (dry case), where the power n was 2.0, instead 2.5 used in CSR^{***}. The values of the pseudo cyclic stress ratios (CSR^{***}) are given in Table 4.26. alongside the experimental CSR values for AP, MT and MV specimens. Then CSR values are normalized by corresponding CSR^{***} values as shown in Table 4.27. According to Table 4.27 and Figure 4.25, for full saturation condition, this normalization also gives very selective and good relation based on cyclic triaxial test data.

Table 4.25 Shear wave anisotropy index A^S for AP, MT, and MV under different effective pressures (S=100%)

σ	A_{AP}^S	A_{MT}^S	A_{MV}^S	$\frac{A_{AP}^S}{A_{AP}^S}$	$\frac{A_{MT}^S}{A_{AP}^S}$	$\frac{A_{MV}^S}{A_{AP}^S}$
psi						
10	2878.095	3872.263	4205.275	1.000	1.345	1.461
20	2849.116	3760.637	4086.881	1.000	1.320	1.434
30	2832.299	3696.837	4019.176	1.000	1.305	1.419
40	2820.428	3652.228	3971.820	1.000	1.295	1.408
50	2811.255	3617.998	3935.472	1.000	1.287	1.400

Table 4.26 Experimental CSR and pseudo CSR^{***} at different number of cycles (N)
(S=100%)

N	CSR			CSR ^{***}		
	AP	MT	MV	AP	MT	MV
5	0.295	0.693	0.798	1.221	2.565	3.152
10	0.262	0.588	0.639	1.105	2.320	2.852
15	0.252	0.544	0.591	1.069	2.244	2.759
20	0.247	0.521	0.567	1.051	2.207	2.713
25	0.245	0.506	0.553	1.041	2.185	2.686
30	0.243	0.496	0.544	1.034	2.171	2.668

Table 4.27 Ratio of experimental CSR to pseudo CSR^{***}

N	$(CSR/CSR^{***})_{AP}$		
	AP	MT	MV
5	0.241	0.270	0.253
10	0.237	0.253	0.224
15	0.236	0.243	0.214
20	0.235	0.236	0.209
25	0.235	0.232	0.206
30	0.235	0.229	0.204

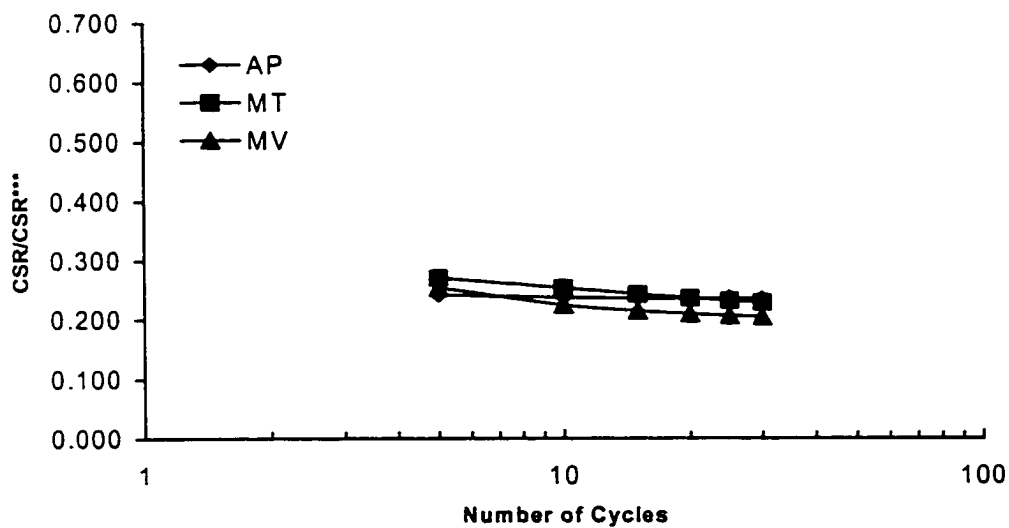


Figure 4.25 ratio of CSR to CSR^{***} against the number of cycles

4.5.6 Examination of Liquefaction Resistance by Anisotropy Index Parameters

From the preceding observations, it is apparent that anisotropy due to soil fabric has a significant effect on the resulting cyclic stress ratio of Virginia Beach sand. Therefore, three similar anisotropy indexes were identified by elastic constants for each type of reconstituted soil specimens. To investigate relationship between the anisotropy indexes and the liquefaction resistances of reconstituted specimens under cyclic loading, pseudo cyclic stress ratios were created in terms of anisotropy indexes as summarized Table 4.28. Cyclic stress ratios of the specimens were normalized with corresponding pseudo cyclic stress ratios.

As seen in Figures 4.23, 4.24 and 4.25, the effects of sample preparation techniques on the liquefaction resistance are apparently eliminated by normalized cyclic stress ratios with CSR^* , CSR^{**} and CSR^{***} . All these results confirm the presumptions of this study; the differences between the liquefaction cyclic stress ratios of reconstituted specimens are related to inherent anisotropy and those anisotropy can be quantitatively identified by anisotropic elastic constants.

Another conclusion is made that S-wave velocities in vertical direction are also sensitive to identify the level of anisotropy. To obtain CSR^* , it was assumed that the specimens were transversely isotropic. Five independent elastic constants (G_{12} , E_1 , E_2 , ν_{12} and ν_{23}) were quantitatively recovered by the results of directional elastic wave measurements and consolidation tests. Therefore, CSR^* represents all directional mechanical characteristics of the specimens and it requires a complex procedure. However, CSR^{**} and CSR^{***} gave also very good correlations and they were just obtained from the results of S-wave velocities in vertical direction. Those are much simpler than CSR^* and yet gave good correlations. It is practical to say that S-wave

velocities are enough to represents the level of inherent anisotropy and can be a useful tool to define the effect of anisotropy on the liquefaction resistance.

Table 4.28 Pseudo cyclic stress ratios of AP, MT, and MV specimens

Pseudo Cyclic Stress Ratio	AP	MT	MV
CSR*	$\left(\frac{G_{12,AP}^S}{G_{23,AP}^E} \frac{E_{1,AP}^E}{E_{2,AP}^E} \right)^{1.5} e^{\frac{1}{N}}$	$\left(\frac{G_{12,MT}^S}{G_{23,MT}^E} \frac{E_{1,MT}^E}{E_{2,MT}^E} \right)^{1.5} e^{\frac{1}{N}}$	$\left(\frac{G_{12,MV}^S}{G_{23,MV}^E} \frac{E_{1,MV}^E}{E_{2,MV}^E} \right)^{1.5} e^{\frac{1}{N}}$
CSR**	$\left(\frac{G_{12,AP}^S}{G_{12,AP}^S}_{S=0.0\%} \right)^2 e^{\frac{1}{N}}$	$\left(\frac{G_{12,MT}^S}{G_{12,AP}^S}_{S=0.0\%} \right)^2 e^{\frac{1}{N}}$	$\left(\frac{G_{12,MV}^S}{G_{12,AP}^S}_{S=0.0\%} \right)^2 e^{\frac{1}{N}}$
CSR***	$\left(\frac{G_{12,AP}^S}{G_{12,AP}^S}_{S=100\%} \right)^{2.5} e^{\frac{1}{N}}$	$\left(\frac{G_{12,MT}^S}{G_{12,AP}^S}_{S=100\%} \right)^{2.5} e^{\frac{1}{N}}$	$\left(\frac{G_{12,MV}^S}{G_{12,AP}^S}_{S=100\%} \right)^{2.5} e^{\frac{1}{N}}$

Lastly, if CSR** and CSR*** are compared to each other, saturation degree also has some effects on initial mechanical characteristics of the specimens. Since natural sand deposits under the investigation of liquefaction resistance are almost fully saturated, CSR*** is to be a possible solution to eliminate the effects of anisotropy on the liquefaction resistance of a soil.

CHAPTER 5 SUMMARY AND CONCLUSIONS

5.1 Summary of Research

In this study, the effects of inherent anisotropy due to different sample preparation techniques on liquefaction resistance and its relation to the elastic properties of soil specimens were investigated. Cyclic triaxial test, elastic wave measurement, and consolidation tests were conducted under isotropic stress condition ($\sigma_1=\sigma_2=\sigma_3$) and thus, the effects of stress induced anisotropy were eliminated. Virginia Beach (VB) sand, a highly liquefiable uniform sand with 50% relative density, was chosen for the testing.

By using three different preparation techniques (air pluviation (AP), moist tamping (MT), and moist vibration (MV)), three different soil fabrics were created. Specimens were fully saturated and consolidated under the same effective stress ($\sigma' = 10$ psi), and undrained cyclic triaxial tests were performed to determine the liquefaction resistance of each soil specimen. A relationship of liquefaction resistance in terms of cyclic stress ratio (CSR) to the number of cyclic loads was established for AP, MT and MV specimens. It was observed that inherent anisotropy was highly influential on the liquefaction resistance of VB sand.

Before each cyclic triaxial test, elastic wave velocities were measured by means of a pulse transmission method to determine the mechanical properties of each specimen. Thus, the effects of the anisotropy on the liquefaction resistance were investigated in a quantitative way. Isotropic consolidation tests were also conducted to determine the compressibility of each specimen. During the consolidation tests, elastic wave velocities

were also measured to examine the effects of effective confining stress and degree of saturation.

Anisotropic elastic constants of soil specimens were recovered quantitatively from elastic wave measurements and consolidation test data. Inherent anisotropy due to different preparation techniques was identified by recovered anisotropic constants. Several anisotropic indexes based on anisotropic elastic constants were identified to relate liquefaction resistance to these anisotropic indexes.

5.2 Conclusions

The following conclusions were drawn from this research:

1. The liquefaction resistances of AP specimens were found to be the lowest of all specimens. The liquefaction resistances of MV specimens gave the strongest responses.
2. It was found that P-wave velocities in both directions are nearly identical for MT and MV, but not for AP specimens. The AP technique, in comparison with the others, creates a slightly rigid specimen in a vertical direction, while MT and MV techniques create rather isotropic grain structures. In addition, the highest P-wave velocities in any direction are given by MV technique. At 10 psi effective confining pressure, the ratios of V_{p_v} to V_{p_h} for AP, MT and MV specimens are 1.085, 1.007 and 0.998, respectively.
3. During the water saturation process, compression wave velocities were measured as a function of saturation degree. There were some differences between theoretical P-wave velocities and the experimental values. It may be quite possible in the experiment that the pores of specimens might not be distributed uniformly. Flushing de-aired water travels from the bottom of the specimens to the top and air bubbles

could be stacked at the top. However, P-waves can be transmitted through the fully saturated pathways in the media.

4. V_{pv} and V_{ph} velocities are highly affected by the presence of air in the porous media. P-wave velocity increases with increasing confining pressure when specimens are dry. When the same porous volume is filled with de-aired water, fully saturated specimens give similar magnitudes of V_{pv} at different effective pressures.

5. Under dry and saturated conditions, S-waves of all reconstituted specimens increased with an increasing effective confining pressure. In addition, the effects of AP, MT and MV techniques on S-waves can be clearly distinguished in comparison with the curves of P-wave velocities. The smallest magnitudes of S-wave velocities at dry and saturated conditions are obtained by the AP technique, while the highest S-wave velocities occurred for the MV specimens for all levels of the effective confining pressure. Under 10 psi effective confining pressure, the differences in S-wave velocity of MV and AP specimens were about 21.76 % at $S=0\%$ and 21.52% at $S=100\%$. This shows a clear relationship between the anisotropy and shear modulus of the specimens.

6. According to isotropic consolidation test results, It was clear that the preparation techniques caused significant differences in terms of the volumetric and axial strains. It was observed that the amount of volumetric strain (ϵ_v), and the axial strain (ϵ_1) were highest for the AP specimens, followed by the MT, and the MV specimens in that order. It was also indicated from these experiments that the AP technique creates a highly anisotropic soil structure as evidence by the high ratio of ϵ_1 / ϵ_v .

7. By assuming transverse isotropy of the specimens the five elastic constants (E_1 , E_2 , G_{12} , ν_{21} and ν_{23}) were recovered numerically by a commercial computer program,

“Mathematica,” for AP, MT and MV specimens under different effective confining pressures. Only G_{12} was directly calculated from S-wave measurements. Longitudinal moduli E_1 and E_2 did not show clear distinguishable differences, while G_{12} showed clear differences due to preparation techniques.

8. Three anisotropy indexes were identified by elastic constants for each type of reconstituted soil specimens. Pseudo cyclic stress ratios were then created based on anisotropy indexes and liquefaction cyclic stress ratios were further normalized with corresponding pseudo cyclic stress ratios in following manner.

9. First normalization by CSR^* : $S^E (=G_{12}/G_{23})$, the ratio of shear modulus in vertical to horizontal planes, and $E^E (=E_1/E_2)$, ratio of longitudinal modulus in vertical to horizontal planes were obtained. By taking further the ratio of S^E to E^E , an anisotropy index parameter $A^E (S^E/E^E)$ was created. A pseudo cyclic stress ratio ($CSR^*=(A^E)^{1.5} e^{1/N}$) was then created. The values of CSR of the specimens were normalized with CSR^* . The CSR/CSR^* ratio showed a rather unique curve against the number of cyclic load, N regardless of differently prepared specimens.

10. Second and third normalizations by CSR^{**} and CSR^{***} : It was observed that shear modulus in vertical plane (G_{12}) showed as a promising variation for the sample preparation techniques. Pseudo cyclic stress ratios, CSR^{**} and CSR^{***} , were created as $(G_{12}/G_{12AP})^{2.0} e^{1/N}$ and $(G_{12}/G_{12AP})^{2.5} e^{1/N}$, respectively, for $S=0\%$ and $S=100\%$ conditions. Then, the values of CSR of the specimens were normalized with CSR^{**} and CSR^{***} depending on the saturation condition. It was observed that both of the normalized cyclic stress ratios had very good correlation and merged the values of CSR of the AP, MT and MV specimens into a very narrow band. It was confirmed

that the influence of the anisotropy induced by soil fabric on liquefaction resistance is to be eliminated simply using shear moduli ratio of different fabric specimens.

5.3 Recommendations for Future Works

In this study, one type of soil with a density was used. By using different types of soils, this research could be expanded to find standard correction factors for all kinds of soils. Some other factors include granular shapes and fine content and chemical aging of sand deposits. These could be future works of this research. As mentioned in Chapter 2, evaluating liquefaction resistance using shear wave velocity measurements in the field has been started and several researchers have been attempting to simplify the procedures. Still there is a gap between laboratory and in-situ experiments. Based on the conclusions and considering the values of shear wave velocities of sand samples in the field and laboratory, this gap can be filled. Therefore, the current research should be expanded to recover in-situ conditions and its relationship to laboratory reconstituted specimens.

REFERENCES

- Agarwal, T. K. (1991). *Micromechanics of granular materials and its relation to wave velocity*. PhD thesis, Old Dominion University.
- Agarwal, T. K. & Ishibashi, I. (1992). Anisotropic elastic constants of granular assembly from wave velocity measurements, *Advances in Micromechanics of Granular Materials*, Elsevier, 51-60.
- Anadarajah, A. & Kuganenthira, N. (1995). Some aspects of fabric anisotropy of soil. *Geotechnique* **45**, No. 1, 69-81.
- Andrus, R. D., & Stokoe, K. H. (1997). Guidelines for evaluation of liquefaction resistance using shear wave velocity, *Proc. NCEER Workshop on Evaluation of Liquefaction Resistance of Soils, Technical Report*.
- Andrus, R. D., (1999). Draft guidelines for evaluating liquefaction resistance using shear wave velocity measurements and simplified procedures, NISTIR 6277, *National Institute of Standards and Technology*, Gaithersburg, Maryland.
- Arulmoli, K. & Arulanandan, K. (1994). Review of an electrical method for evaluation of stress ratio required to cause liquefaction and dynamic modulus. *Dynamic Geotechnical Testing II, ASTM STP 1213*, 118-133.
- Arulnathan, R., Boulanger, R. W. & Riemer, M. F. (1998). Analysis of bender element tests. *Geotechnical Testing Journal* **21**, No. 2, 120-131.
- Ashraf, A. Ibrahim and Takaaki Kagawa (1991). Microscopic measurement of sand fabric from cyclic tests causing liquefaction. *Geotechnical Testing Journal*, **24** No. 4, 371-382.
- Bellotti, R., Jamiolkowski, M., Lo Presti, D. C. F. & O'Neill, D. A. (1996). Anisotropy of small strain stiffness in Ticino sand. *Geotechnique* **46**, No. 1, 115-131.
- Boulanger, R. W., Arulnathan, R., Harder, L. F., Torres, R. A. & Driller, M. W. (1998). Dynamic properties of Sherman Island peat. *Journal of Geotechnical and Geoenvironmental Engineering* **124**, No. 1, 12-20.
- Brignoli, E. G. M., Gotti, M. & Stokoe, K. H., II (1996). Measurement of shear waves in laboratory specimens by means of piezoelectric transducers. *Geotechnical Testing Journal* **19**, No. 4, 384-397.
- De Alba, P., Chan, C.K., & Seed, H.B. (1975). Determination of soil liquefaction characteristics by large-scale laboratory tests, *Report, Earthquake Engineering Research Center*, University of California, Berkeley.

- De Alba, P., Baldwin, K., Janoo, V., Roe, G. & Celikkol, B. (1984). Elastic-wave velocities and liquefaction potential. *Geotechnical Testing Journal* 7, No. 2, 77-87.
- Dyvik, R. & Madshus, C. (1985). Lab measurements of G_{max} using bender elements, *Advances in the Art of Testing Soils under Cyclic Conditions*, Conference, Geotechnical Engineering Division, ASCE, 79-107.
- Ferrito, J. M., Forrest, J. B. & Wu, G. (1979). A compilation of cyclic triaxial liquefaction test data. *Geotechnical Testing Journal* 2, No. 2, 106-113.
- Hall, J. R., Jr. & Richart, F. E., Jr. (1963). Dissipation of elastic wave energy in granular soils. *Journal of the Soil Mechanics and Foundations Division* 89, 27-56.
- Hardin, B. O. & Richart, F. E., Jr. (1963). Elastic wave velocities in granular soils. *Journal of the Soil Mechanics and Foundations Division* 89, 33-65.
- Hardin, B.O. & Black, W.L. (1968). Vibration modulus of normally consolidated clay, *Journal of Soil Mechanics and Foundation*, ASCE, 94, SM2, 353-69.
- Hoque, E., Tatsuoka, F. & Sato, T. (1996). Measuring anisotropic elastic properties of sand using a large triaxial specimen. *Geotechnical Testing Journal* 19, No. 4, 411-420.
- Iami, T. (1977). P- and S-wave velocities of the ground in Japan. *Proceedings of the 9th International Conference in Soil Mechanics and Foundation Engineering*, Tokyo, Vol.2, pp. 257-260.
- Ibrahim, A. A. & Kagawa, T. (1991). Microscopic measurement of sand fabric from cyclic tests causing liquefaction. *Geotechnical Testing Journal* 14, No.4, 371-382.
- Ishibashi, I. & Agarwal, T. K. (1991). Multi-directional wave velocity by piezoelectric crystals. *Proceedings of the Session on Recent Advances in Instrumentation Data Acquisition and Testing in Soil Dynamics*, 102-117.
- Ishibashi, I. & Kiku, H. (1995). Effect of initial anisotropy on liquefaction potential by discrete element model. *Earthquake Geotechnical Engineering*, A. A. Balkema, Rotterdam, Brookfield, 863-868.
- Ishihara, K. (1968). Propagation of compressional waves in a saturated soil. *Proceedings of the International Symposium on Wave Propagation and Dynamic Properties of Earth Materials*, University of New Mexico Press, Albuquerque, New Mexico, 195-206.
- Ishihara, K. (1970). Approximate forms of wave equations for water-saturated porous materials and related dynamic modulus. *Soils and Foundations, Japanese Society of Soil Mechanics and Foundation Engineering* 10, No. 4, 11-38.

- Ishihara, K. (1993). Liquefaction and flow failure during earthquakes. *Geotechnique* **43**, No. 3, 351-415.
- Ishihara, K. (1996). Soil behavior in earthquake geotechnics, *Oxford Science Publications*.
- Jovicic, V. & Coop, M. R. (1998). The measurement of stiffness anisotropy in clays with bender element tests in the triaxial apparatus. *Geotechnical Testing Journal* **21**, No. 1, 3-10.
- Jovicic, V., Coop, M. R. & Simic, M. (1996). Objective criteria for determining G_{max} from bender element tests. *Geotechnique* **46**, No. 2, 357-362.
- Kayabali, K. (1996). Soil liquefaction evaluation using shear wave velocity. *Engineering Velocity* **44**, 121-127.
- Ladd, R.S.(1974). Specimen Preparation and Liquefaction of Sands, *Journal of Geotechnical Engineering Division*, ASCE **100**, No.GT10, 1180-1184.
- Mogami, T., & Kubo, K. (1953). The behavior of soil during vibration, *Proceedings, 3rd International Conference on Soil Mechanics and Foundation Engineering*, Zurich I, 152-155.
- Mulilis, J. P., Chan, C. K. & Seed, H. B. (1975). The effects of method sample preparation on the cyclic stress-strain behavior of sands. University of California. Berkeley, California. *Technical Report*, 1-75.
- Mulilis, J. P., Seed, H. B., Chan, C. K., Mitchell, J. K. & Arulanandan, K. (1977). Effects of sample preparation on sand liquefaction. *Journal of the Geotechnical Engineering Division* **103**, 91-108.
- Nakagawa, K., Soga, K. & Mitchell, J. K. (1996). Pulse transmission system for measuring wave propagation in soils. *Journal of Geotechnical Engineering* **122**, No. 4, 302-308.
- Nakagawa, K., Soga, K. & Mitchell, J. K. (1997). Observation of Biot compressional wave of the second kind in granular soils. *Geotechnique* **47**, No. 1, 133-147.
- Nemat-Nasser, S. & Takahashi, K. (1984). Liquefaction and fabric of sand. *Journal of Geotechnical Engineering* **110**, No. 9, 1291-1306.
- Nemat-Nasser, S. & Tobita, Y. (1982). Influence of fabric on liquefaction and desiccation potential of cohesionless sand. *Mechanics of Materials* **1**, 43-62.
- Richart, F.E., Hall, J.R., & Woods, R.D.(1970). *Vibration of Soils and Foundations*, Prentice Hall.

- Robertson, P. K., Samasitharan, S., Cunning, J. C. Sego, D. C. (1995). Shear-wave velocity to evaluate in-situ state of Ottawa sand. *Journal of Geotechnical Engineering* **121**, 262-273.
- Roesler, S.K. (1979). Anisotropic shear modulus due to stress anisotropy, *Journal of Geotechnical Engineering Division*, ASCE, **105**, No. GT7.
- Santamarina, J. C. & Casacante, G. (1996). Stress anisotropy and wave propagation: a micromechanical view. *Canadian Geotechnical Journal* **33**, 770-782.
- Sasithran, S., Robertson, P. K. & Sego, D. C. (1994). Sample disturbance from shear wave velocity measurements. *Canadian Geotechnical Journal* **31**, No. 1, 119-124.
- Schmertman, J.H. (1977). Effect of shear stress on the dynamic bulk modulus of sand, *Final Report to Waterways Experiment Sta. Corps of Engrs.*, U.S. Army, Contract DACW 39-76-M-6676
- Seed, H.B., & Peacock, W.H. (1971a). Test Procedures for Measuring Soil Liquefaction Characteristics, *Journal of The Soil Mechanics and Foundations Division*, ASCE, **97**, No. SM8, 1099-1199.
- Seed, H.B., & Idriss, I.M. (1971b). Simplified Procedure for Evaluating Soil Liquefaction Potential, *Journal of The Soil Mechanics and Foundations Division*, ASCE, **97**, No. SM9, 1249-1273.
- Seed, H.B., Mori, K.L., Idriss, I.M., & Maksidi, F.I. (1975). Influence of seismic history on the liquefaction characteristics of sands, *Report EERC 75-25*, Earthquake Engineering Center, University of California, Berkeley.
- Seed, H. B. (1979). Soil liquefaction and cyclic mobility evaluation for level ground during earthquakes, *Journal of Geotechnical Engineering Division*, ASCE, **97**, SM9, 1249-1243.
- Seed, H.B., and Idriss, I.M. (1982). Ground Motions and Soil Liquefaction during Earthquakes, EERI, *Monograph*, 134
- Seed, H.B., Tokimatsu, K., Harder, L.F., & Chung, R.M. (1985). Influence of SPT procedures in soil liquefaction resistance evaluations, *Journal of Geotechnical Engineering Division*, ASCE, **111**. No.12, 1425-1445.
- Sherif, M. A., Ishibashi, I. & Tsuchiya, C. (1977). Saturation effects on initial soil liquefaction. "Pure Pressure Rise of Saturated Sands during Cyclic Loading." *Soil Research Report*, No. 17, University of Washington, Seattle,
- Skempton, A. W. (1954). The pore-pressure coefficients *A* and *B*, *Geotechnique*, **4**. 143-152.

- Souto, A., Hartikainen, J. & Ozudogru, K. (1994). Measurement of dynamic parameters of road pavement materials by the bender element and resonant column tests. *Geotechnique* **44**, No. 3, 519-525.
- Strachan, P. (1985). Alternative test method for ensuring full saturation in triaxial samples. *Geotechnical Testing Journal* **8**, No. 1, 43-46.
- Tatsuoka, F., Ochi, K., Fuji, S., & Okamoto, M.(1986). Cyclic undrained triaxial and torsional shear strength of sands for different sample preparation methods, *Soils and Foundations*, **26**, No.3, 23-41.
- Thomann, T. G. & Hryciw, R. D. (1990). Laboratory measurement of small strain modulus under κ_0 conditions. *Geotechnical Testing Journal* **13**, No. 2, 97-105.
- Toki, S. Tatsuoka, F. Miura, S., Yoshimi, Y., Yasuda, S., & Makihara, Y.(1986). Cyclic undrained triaxial strength of sand by a cooperative test program, *Soils and Foundations*, **26**, No.3, 117-138.
- Tokimatsu, K. Yamazaki, T. & Yoshimi, Y. (1986). Soil liquefaction evaluations by elastic shear moduli. *Journal of the Japanese Society of Soil Mechanics and Foundation Engineering* **26**, No. 1, 25-35.
- Tokimatsu, K. & Uchida, A.(1990). Correlation Between Liquefaction Resistance and shear wave velocity, *Japanese Society of Soil Mechanics and Foundation Engineering*, **30**, No.2, 33-42.
- Vaid, Y. P., Sivathayalan, S. & Stedman, D. (1999). Influence of specimen-reconstructing method on the undrained response of sand. *Geotechnical Testing Journal* **22**, No. 3, 187-195.
- Viggiani, G. & Atkinson, J. H. (1995). Interpretation of bender element tests. *Geotechnique* **45**, No. 1, 149-154.
- Viggiani, G. & Atkinson, J. H. (1995). Stiffness of fine-grained soil at very small strains. *Geotechnique* **45**, No. 2, 249-265.
- Yamamoto, T. & Turgut, A. (1988). Acoustic wave propagation through porous media with arbitrary pore size distributions. *The Journal of the Acoustical Society of America* **83**, No. 5, 1744-1751.
- Yoshimi, Y., Tokimatsu, K., Kaneko, O., & Makihara, Y. (1984). Undrained cyclic shear strength of a Niigata sand, *Soil and Foundation*, **24**, 131-145.
- Yoshimi, Y., Tokimatsu, K. & Hosaka, Y. (1989). Evaluation of liquefaction resistance of clean sands based on high-quality undisturbed samples. *Journal of the Japanese Society of Soil Mechanics and foundation Engineering* **29**, No. 1, 93-104.

- Zeng, X. & Ni, B. (1998). Application of bender elements in measuring G_{\max} of sand under κ_0 condition. *Geotechnical Testing Journal* **21**, No. 3, 251-263.
- Zeng, X. & Ni, B. (1999). Stress-induced anisotropic G_{\max} of sands and its measurement. *Journal of Geotechnical and Geoenvironmental Engineering* **125**, No. 9, 741-749.

APPENDIX A

CYCLIC TRIAXIAL TEST RECORDS

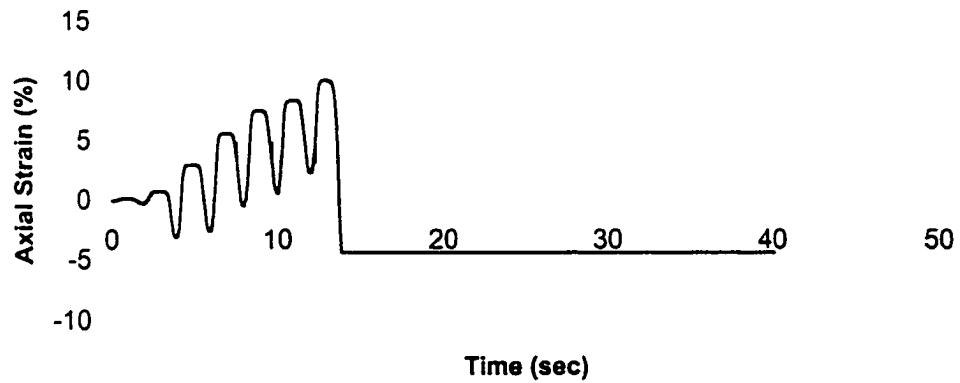
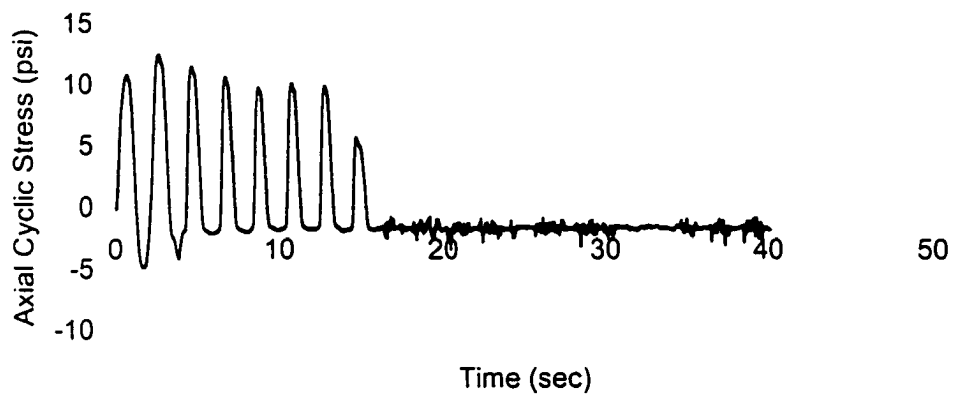
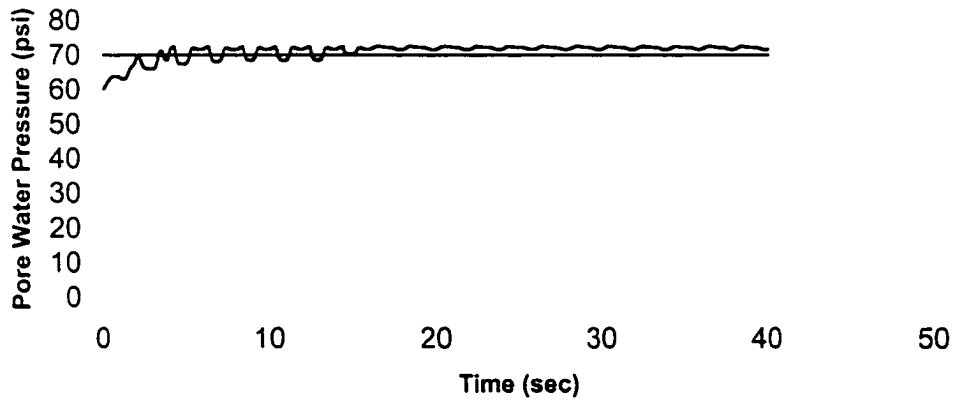


Figure A.1 Results of cyclic triaxial test on AP Specimen at Initial Conditions:

$D_r=49.99\%$, $\sigma'_0=10$ psi, $B=0.96$

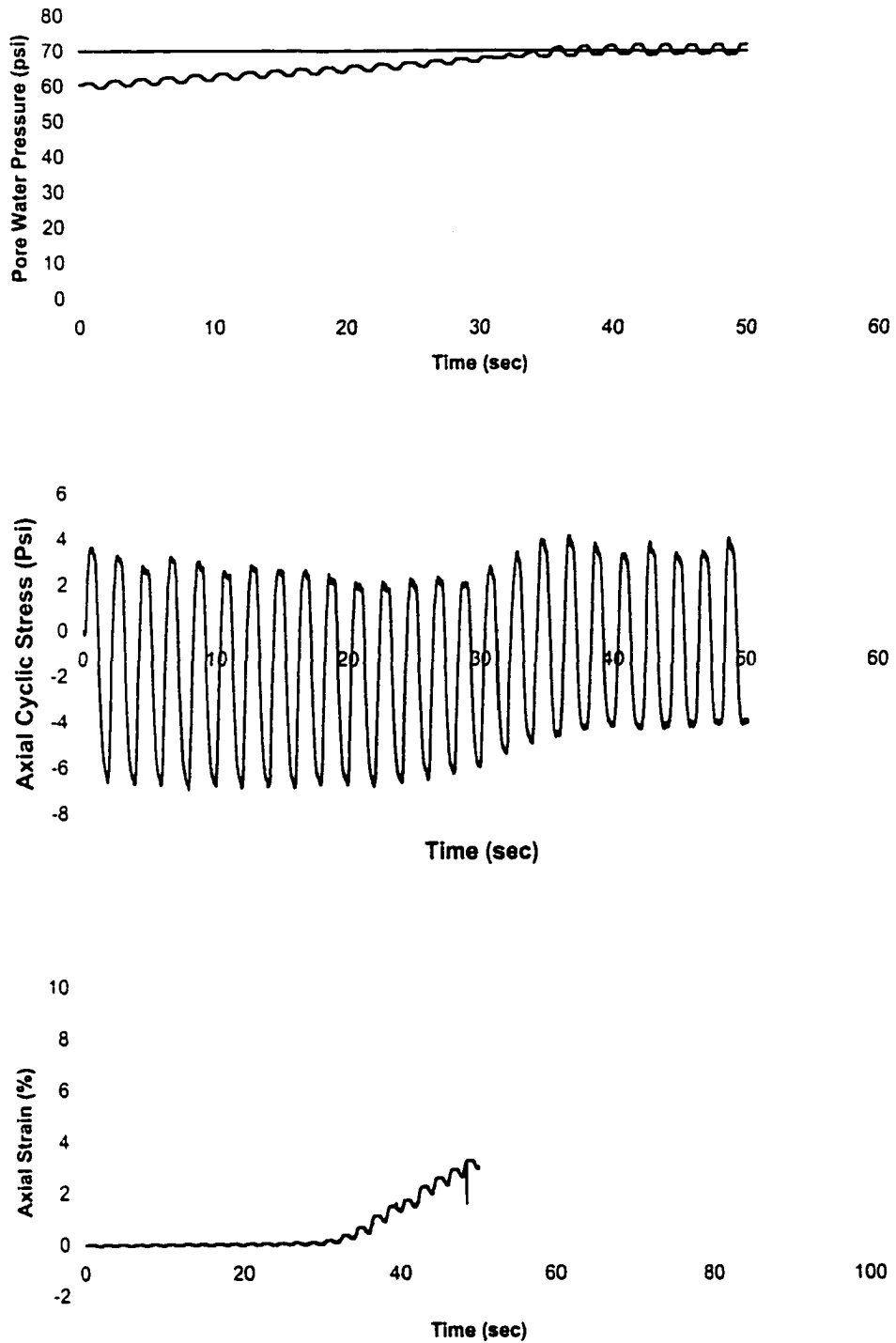


Figure A.2 Results of cyclic triaxial test on AP Specimen at Initial Conditions:

$D_r=51.36\%$, $\sigma'_0=10$ psi, $B=0.95$

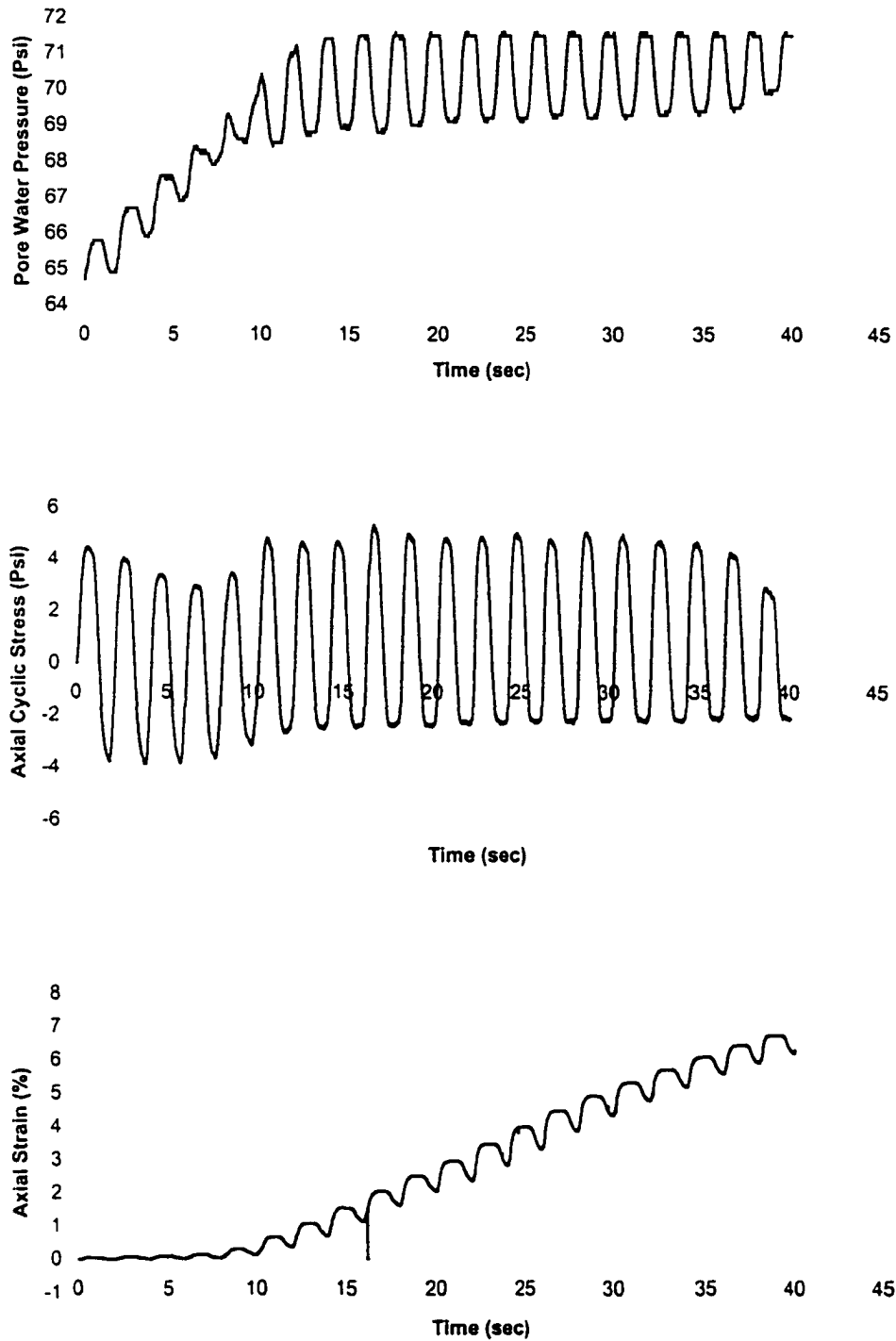


Figure A.3 Results of cyclic triaxial test on AP Specimen at Initial Conditions:

$D_r=51.35\%$, $\sigma'_0=10$ psi, $B=0.99$

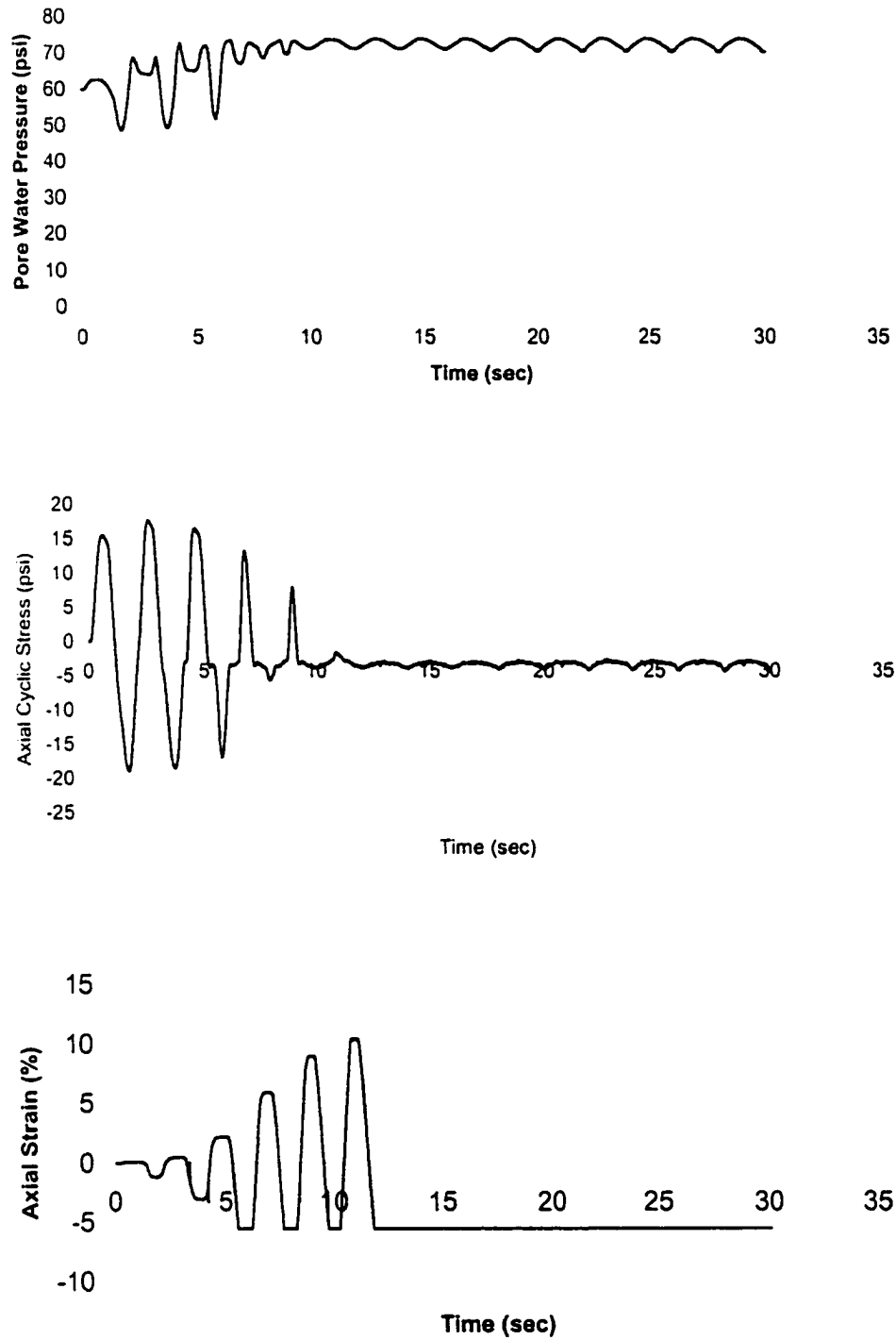


Figure A.4 Results of cyclic triaxial test on MT Specimen at Initial Conditions:

$D_r=49.07\%$, $\sigma'_0=10$ psi, $B=0.98$

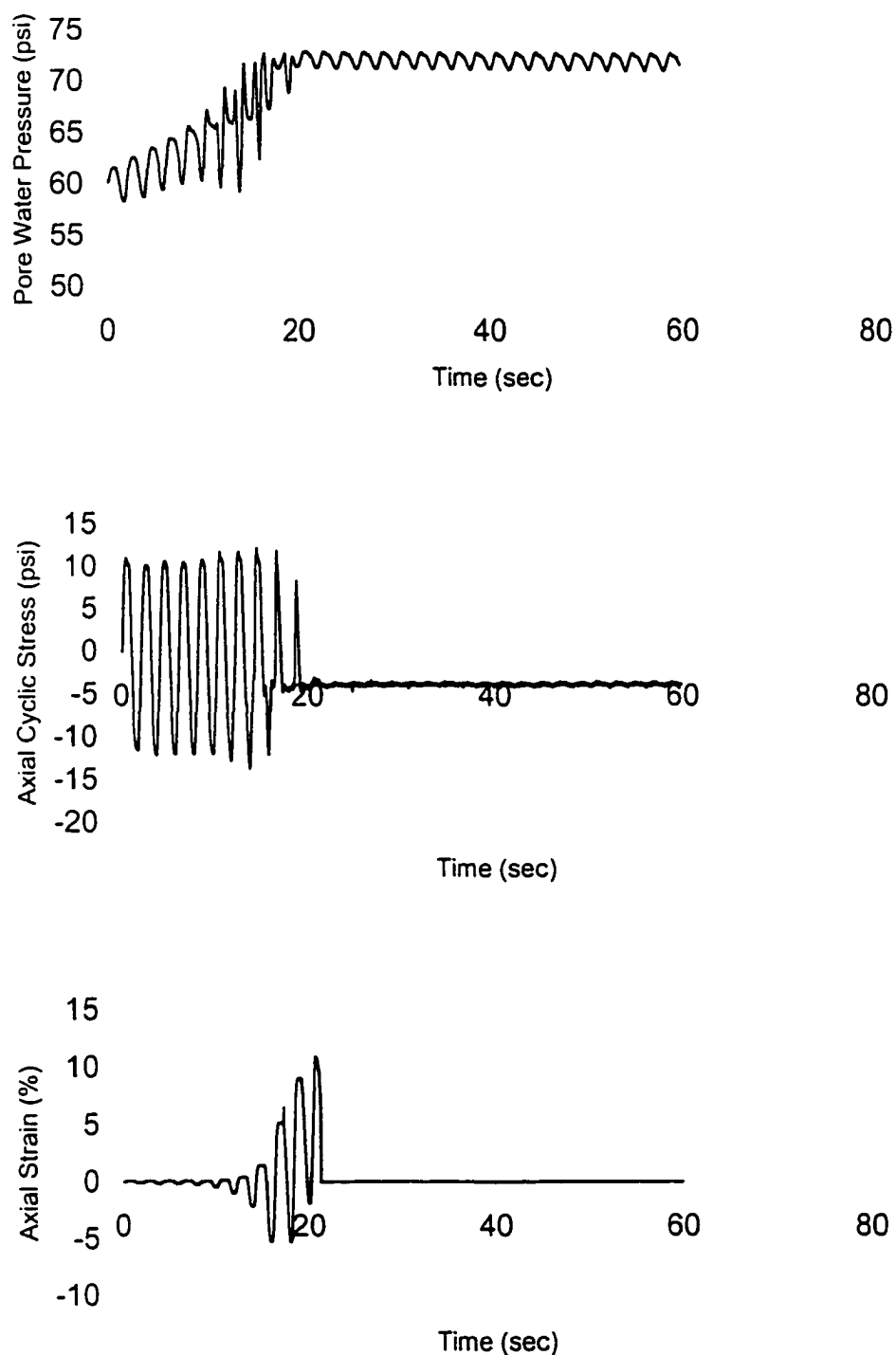


Figure A.5 Results of cyclic triaxial test on MT Specimen at Initial Conditions:

$D_r=48.28\%$, $\sigma'_0=10$ psi, $B=0.94$

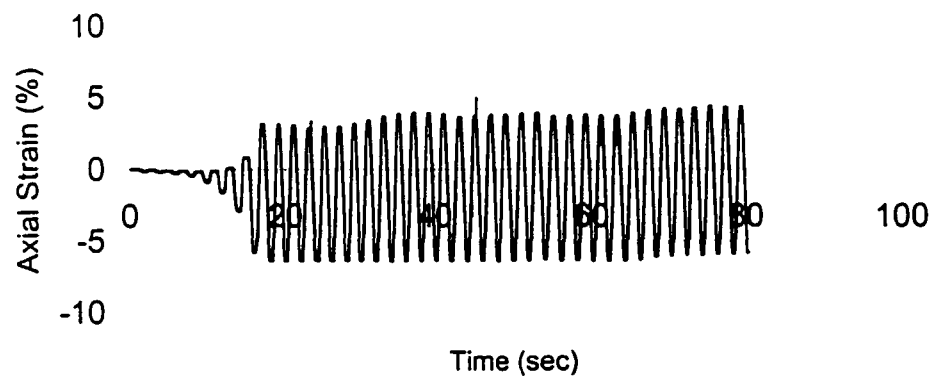
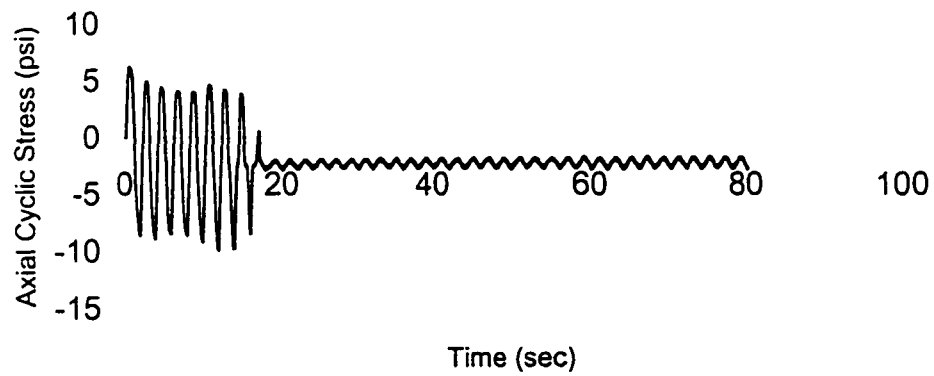
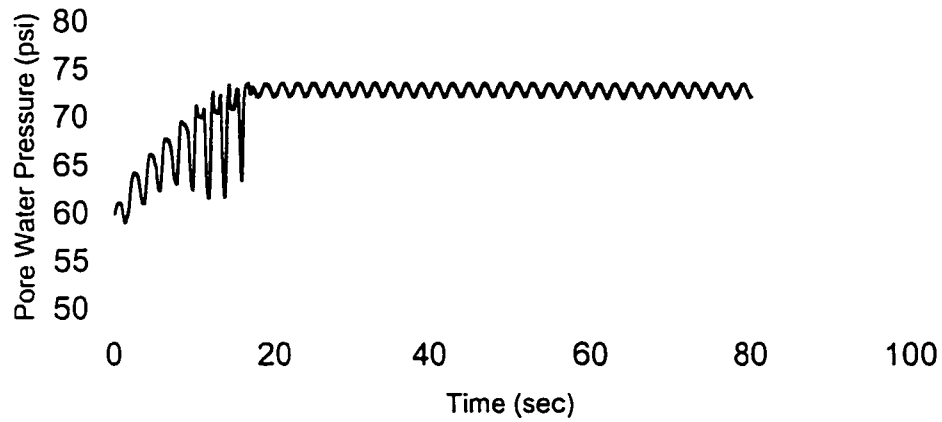


Figure A.6 Results of cyclic triaxial test on MT Specimen at Initial Conditions:

$D_r=48.36\%$, $\sigma'_0=10$ psi, $B=0.95$

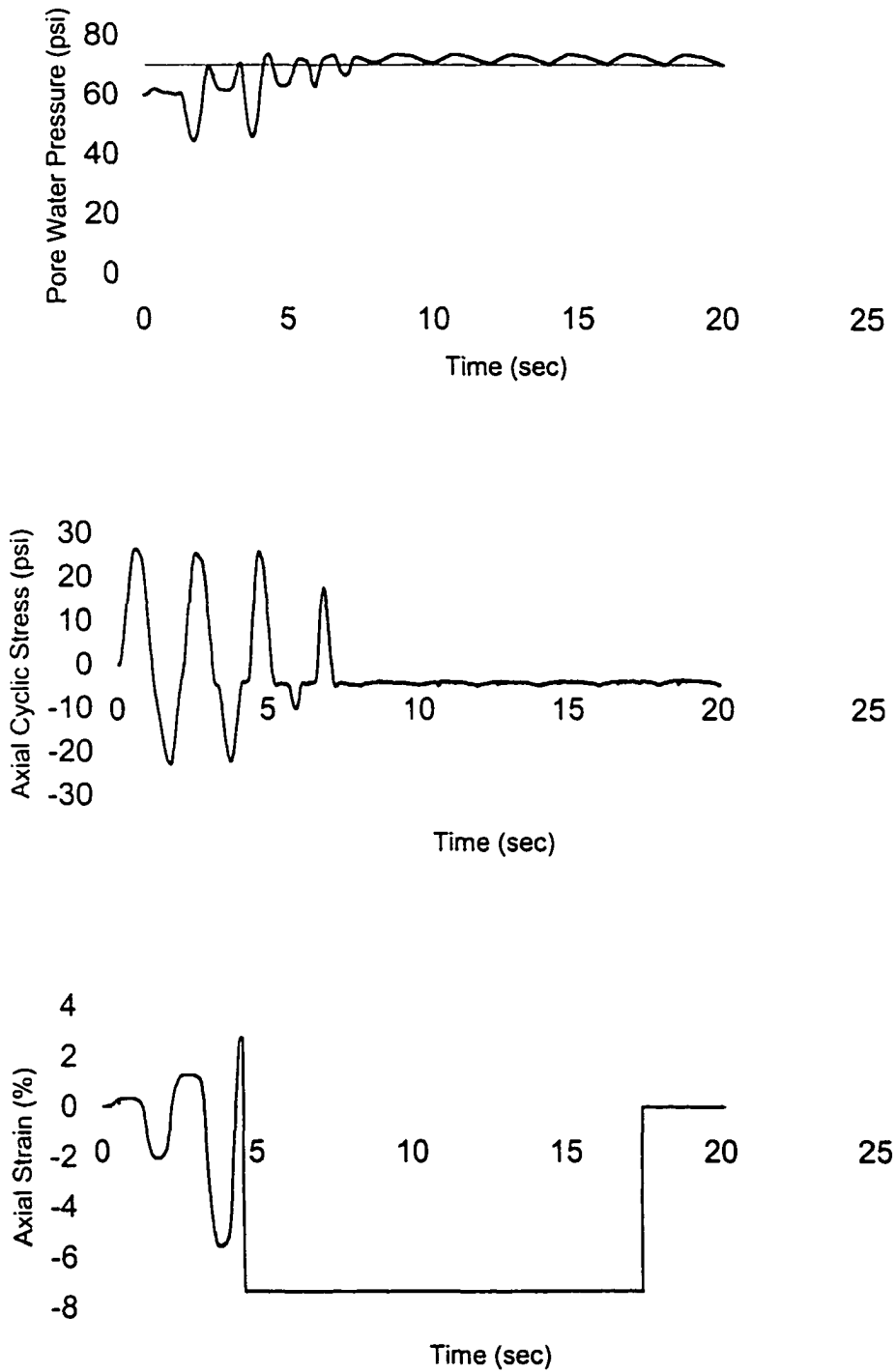


Figure A.7 Results of cyclic triaxial test on MV Specimen at Initial Conditions:

$D_r=48.74\%$, $\sigma'_0=10$ psi, $B=0.96$

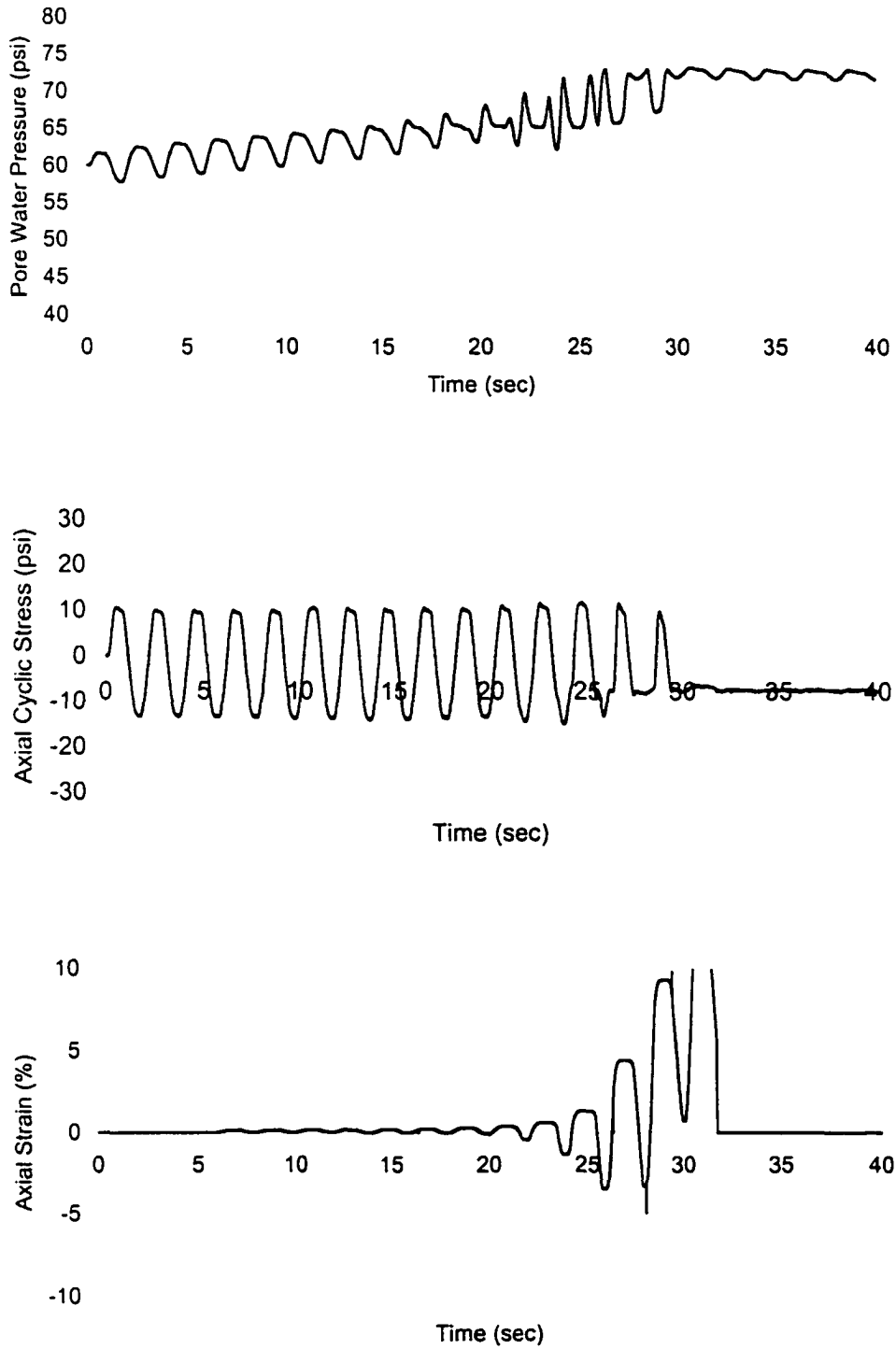


Figure A.8 Results of cyclic triaxial test on MV Specimen at Initial Conditions:

$D_r=48.0\%$, $\sigma'_0=10$ psi, $B=0.98$

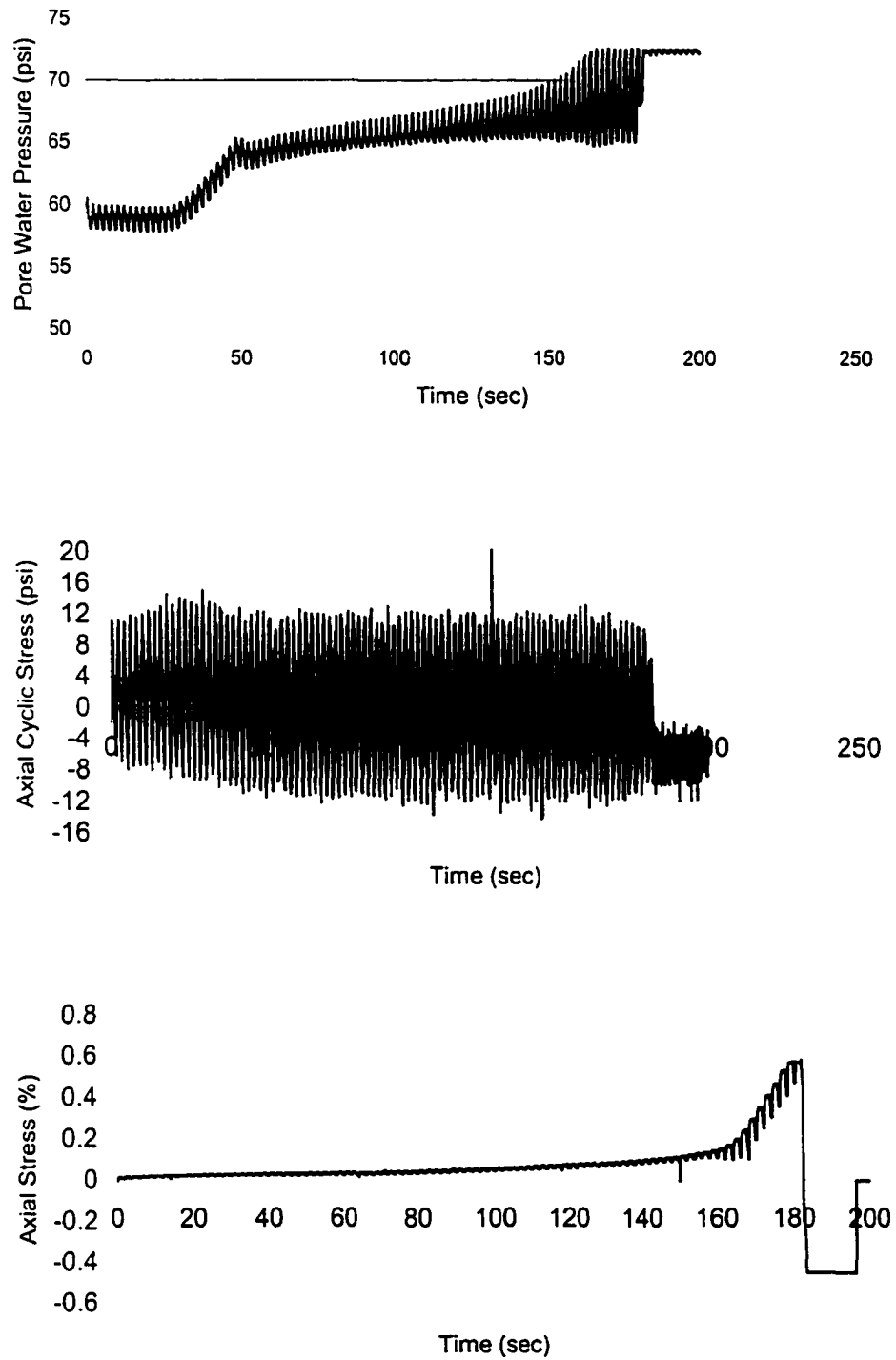


Figure A.9 Results of cyclic triaxial test on MV Specimen at Initial Conditions:

$D_r=49.32\%$, $\sigma'_0=10$ psi, $B=0.94$

APPENDIX B

FREQUENCY EFFECT ON ELASTIC WAVE VELOCITIES

Frequency effects were investigated for all elastic waves. All elastic wave records here were obtained under 5 psi effective pressure for V_{p_v} , V_{p_h} , V_{s_v} of AP specimen. Frequency was changed from 3 kHz to 30 kHz.

All wave records here were obtained from the hard copies of the oscilloscope display.

Figures B1 through B9 show wave records for V_{p_v} , under different frequencies.

Figures B10 through B19 show wave records for V_{p_h} , under different frequencies.

Figures B20 through B28 show wave records for V_{s_v} , under different frequencies.

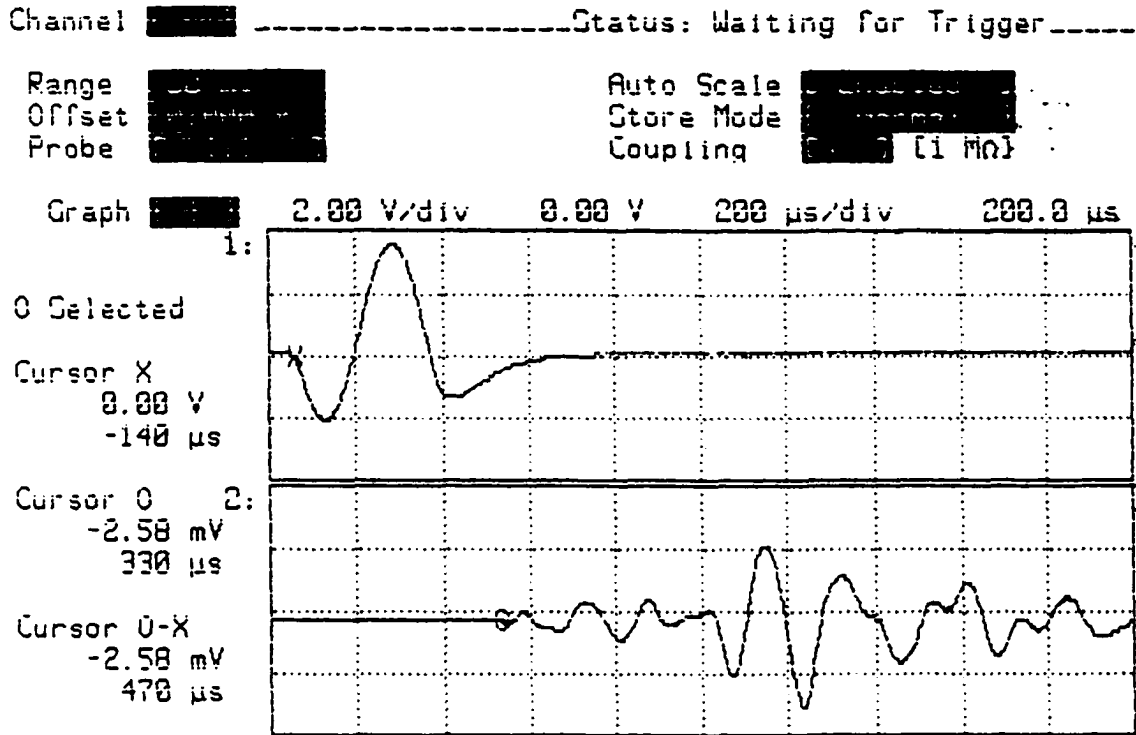


Figure B-1 Measurement of P-wave travel time in vertical direction (V_{pv}) for AP specimen at $D_r=50.35\%$, $\sigma=5$ psi, $S=0\%$, input frequency (f) = 3.0 kHz

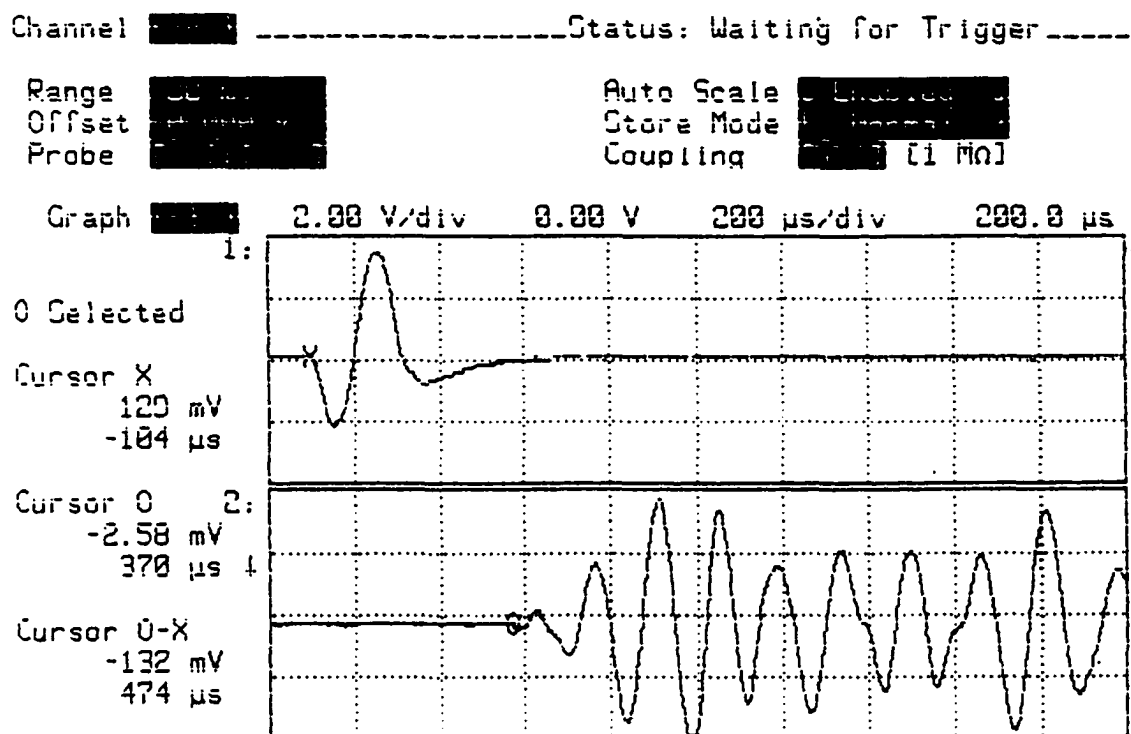


Figure B-2 Measurement of P-wave travel time in vertical direction (V_{p_v}) for AP specimen at $D_r=50.35\%$, $\sigma=5$ psi, $S=0\%$, input frequency (f) = 5.0 kHz

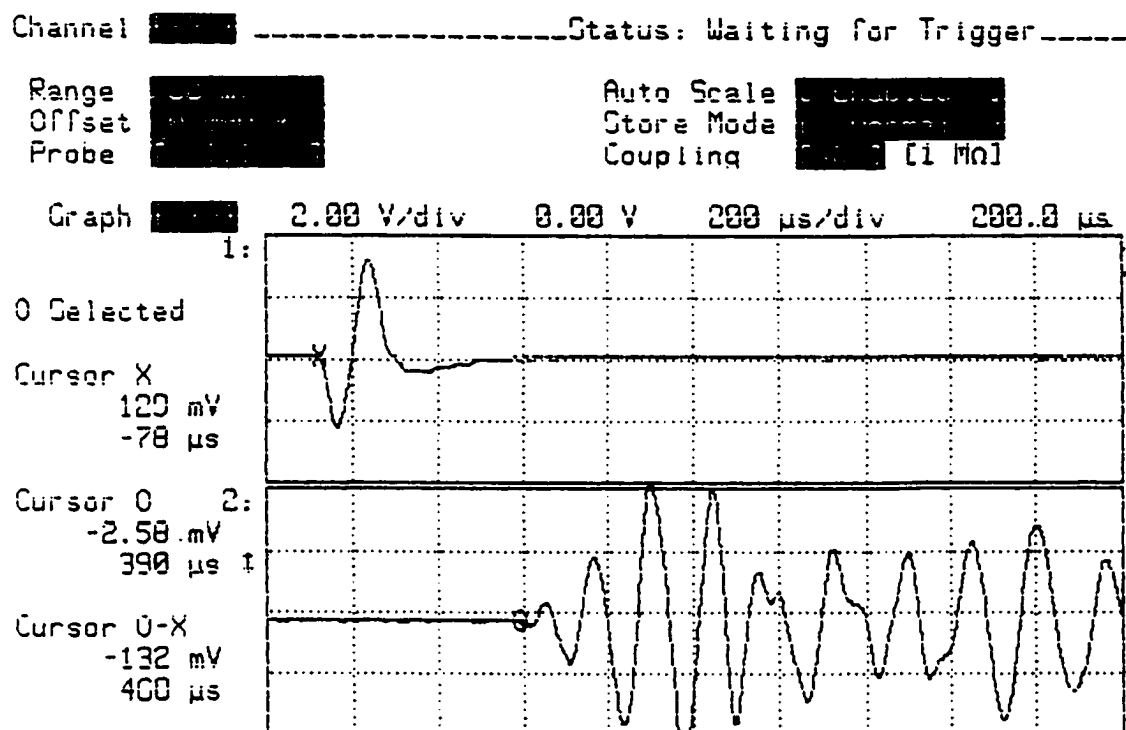


Figure B-3 Measurement of P-wave travel time in vertical direction (V_{p_v}) for AP specimen at $D_r=50.35\%$, $\sigma=5$ psi, $S=0\%$, input frequency (f) = 7.0 kHz

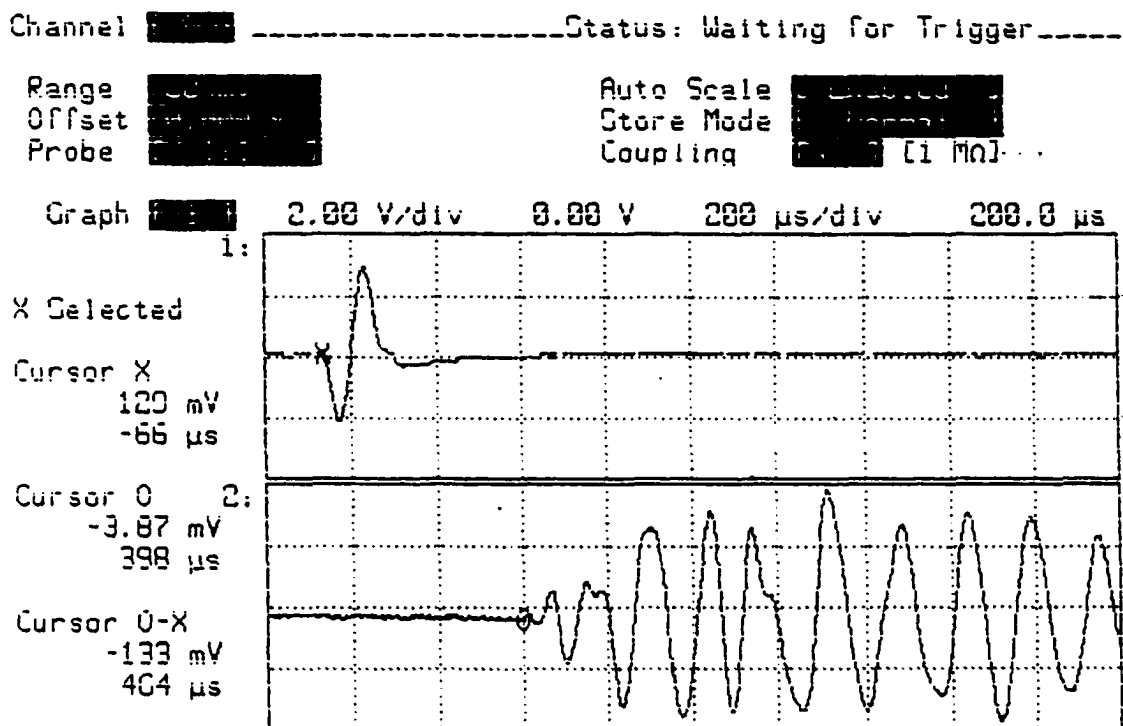


Figure B-4 Measurement of P-wave travel time in vertical direction (V_p) for AP specimen at $D_r=50.35\%$, $\sigma=5$ psi, $S=0\%$, input frequency (f) = 9.0 kHz

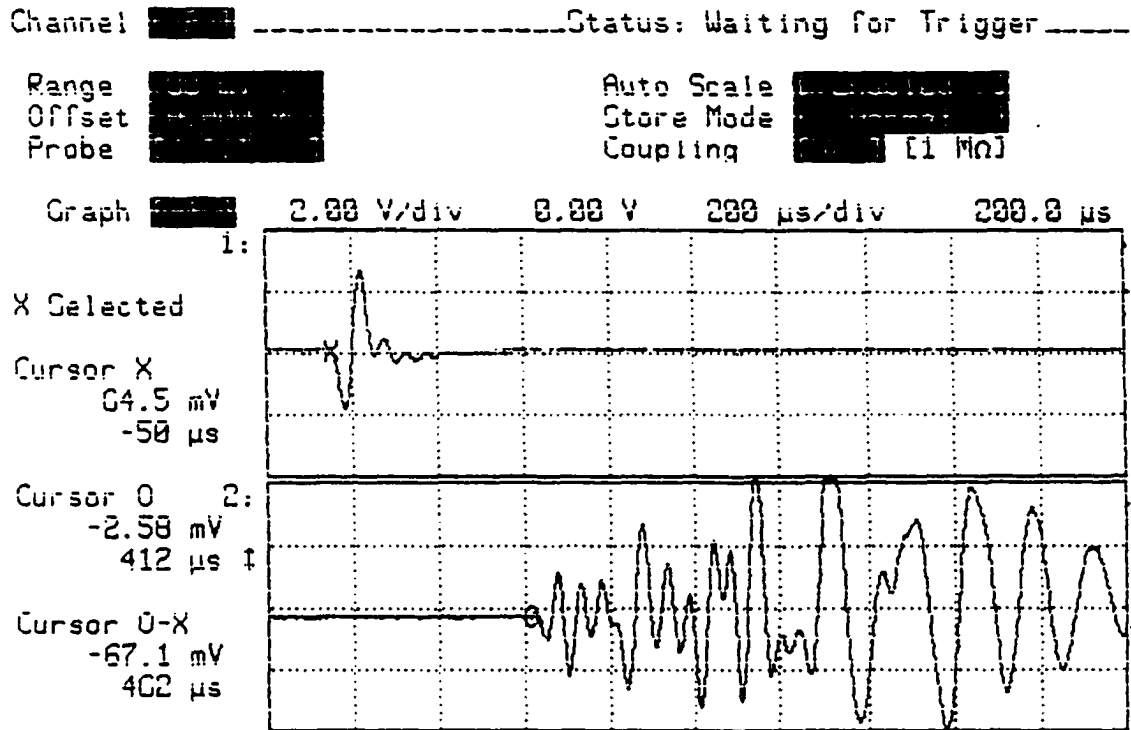


Figure B-5 Measurement of P-wave travel time in vertical direction (V_{pv}) for AP specimen at $D_r=50.35\%$, $\sigma=5$ psi, $S=0\%$, input frequency (f) = 11.0 kHz

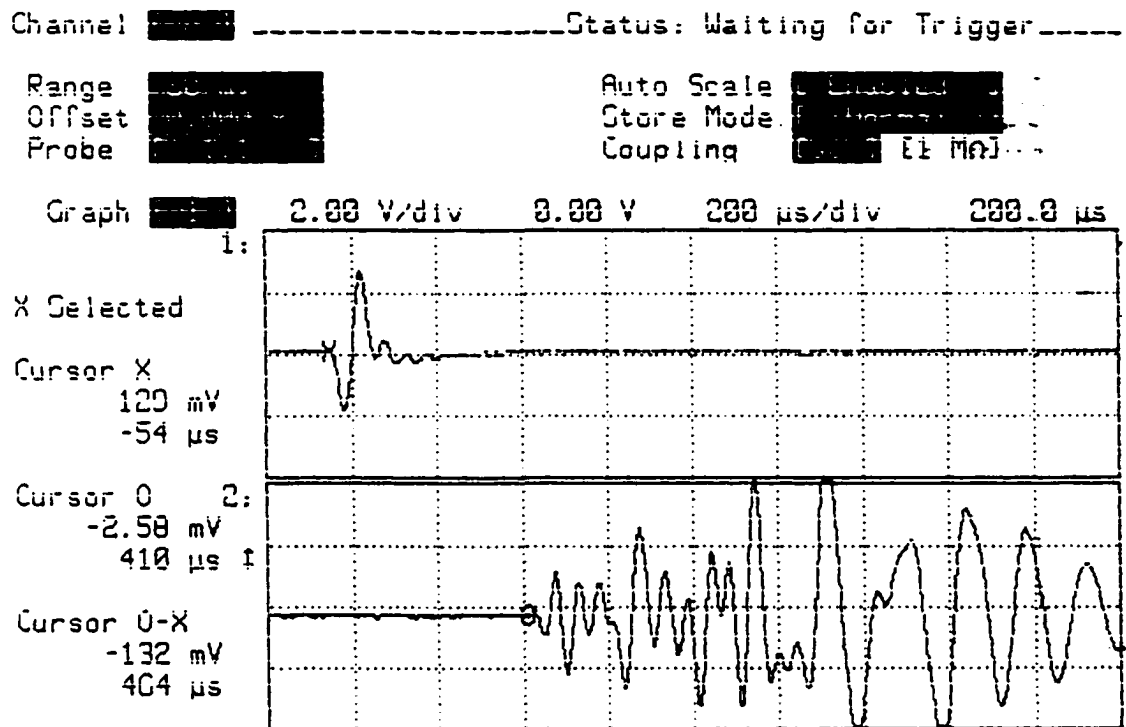


Figure B-6 Measurement of P-wave travel time in vertical direction (V_{pv}) for AP specimen at $D_r=50.35\%$, $\sigma=5$ psi, $S=0\%$, input frequency (f) = 13.5 kHz

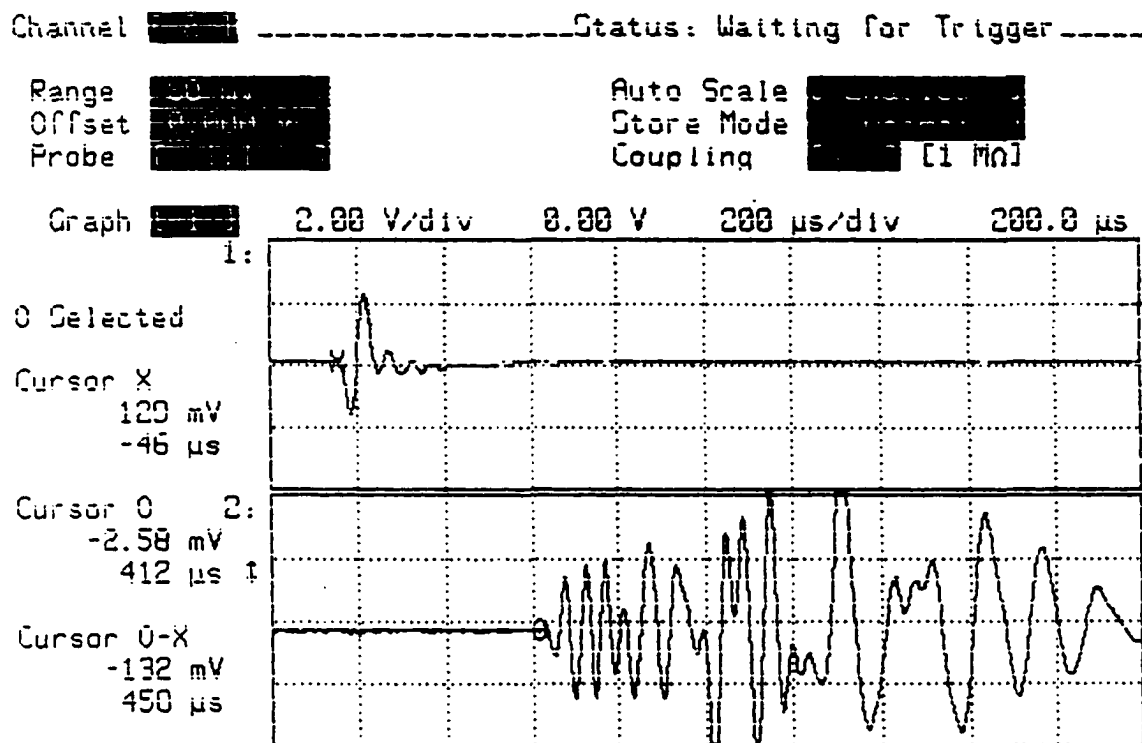


Figure B-7 Measurement of P-wave travel time in vertical direction (V_{pv}) for AP specimen at $D_r=50.35\%$, $\sigma'=5$ psi, $S=0\%$, input frequency (f) = 17 kHz

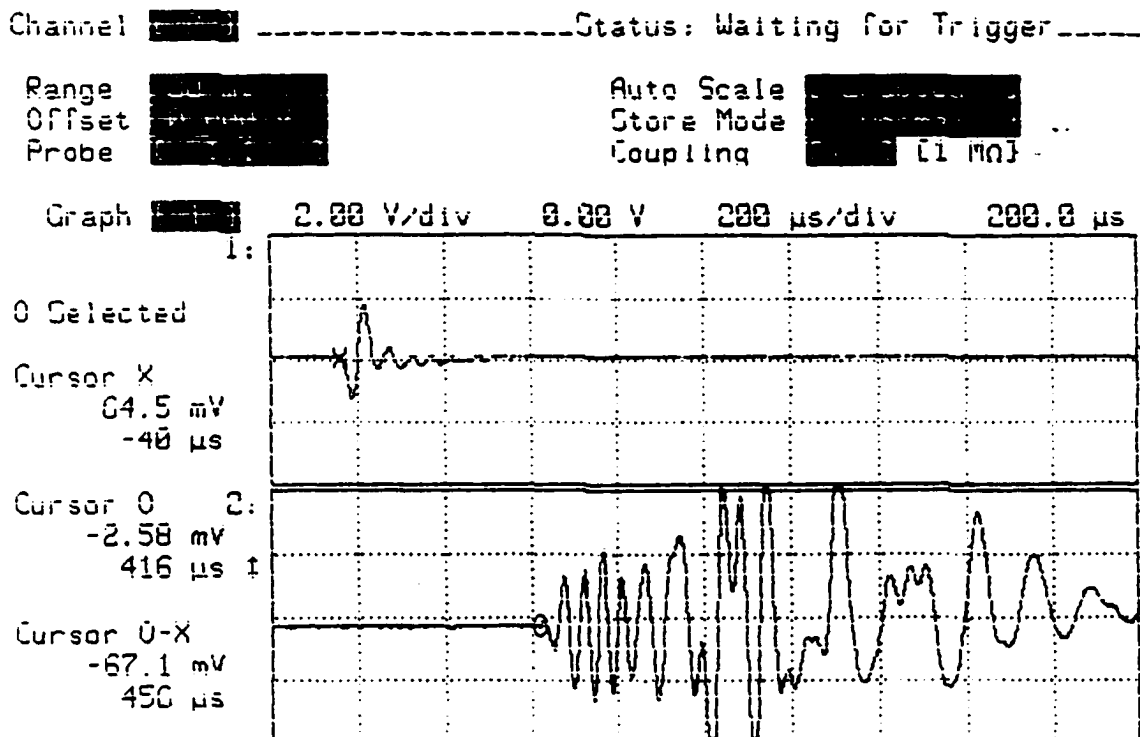


Figure B-8 Measurement of P-wave travel time in vertical direction (V_{p_v}) for AP specimen at $D_r=50.35\%$, $\sigma=5$ psi, $S=0\%$, input frequency (f) = 22.0 kHz

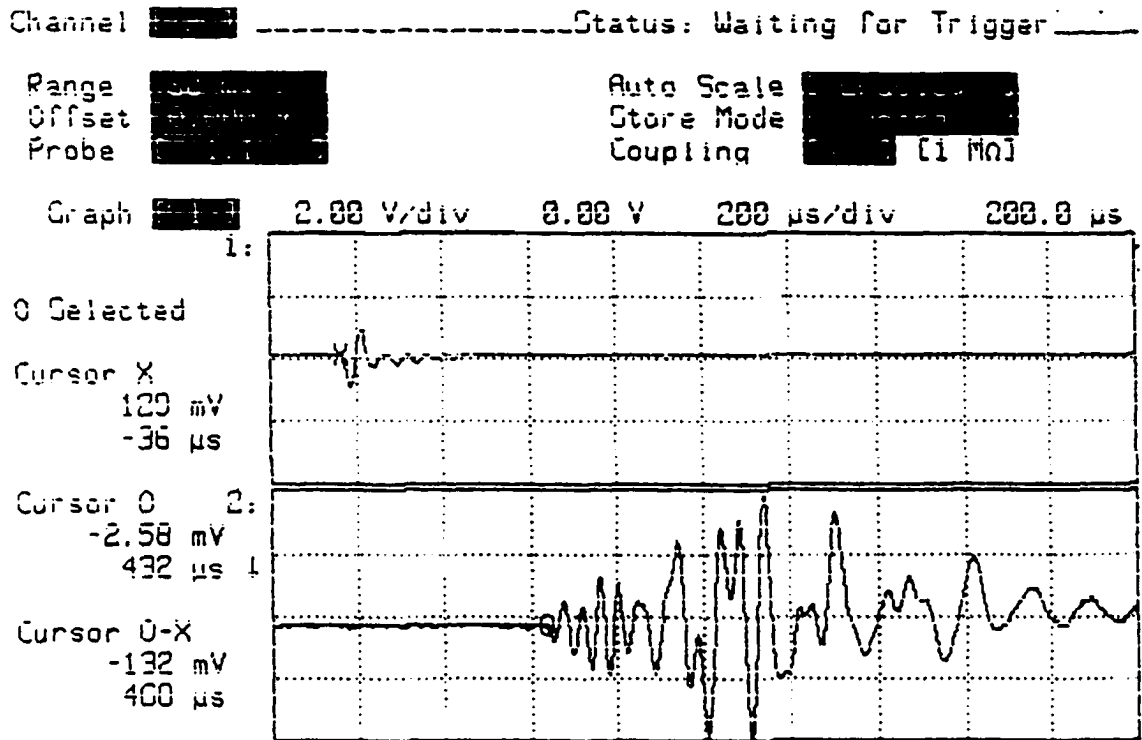


Figure B-9 Measurement of P-wave travel time in vertical direction (V_{pv}) for AP specimen at $D_r=50.35\%$, $\sigma'=5$ psi, $S=0\%$, input frequency (f) = 30 kHz

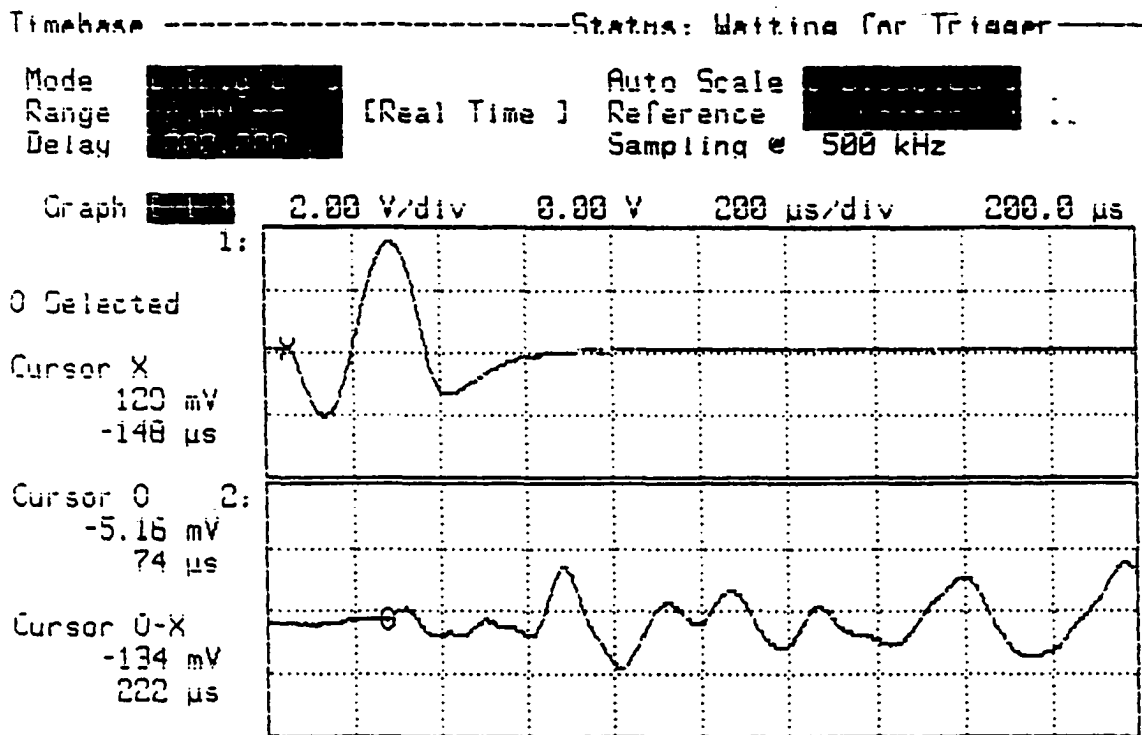


Figure B-10 Measurement of P-wave travel time in horizontal direction (V_{ph}) for AP specimen at $D_r=50.35\%$, $\sigma'=5$ psi, $S=0\%$, input frequency (f) = 3 kHz

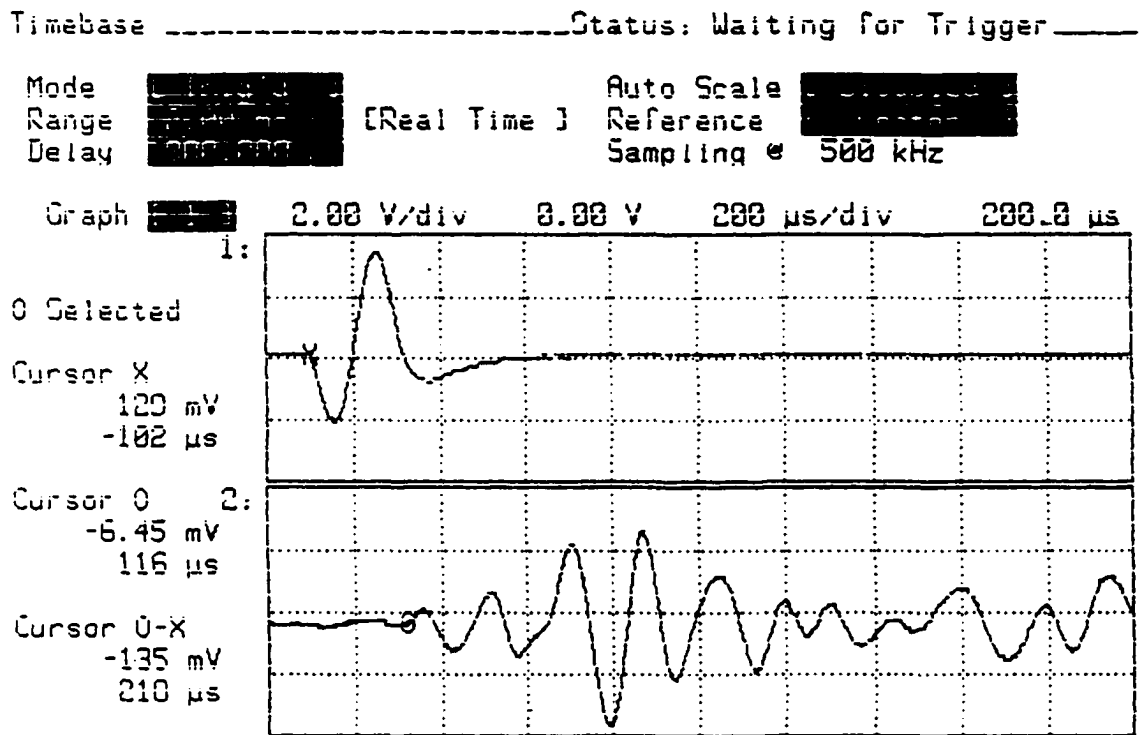


Figure B-11 Measurement of P-wave travel time in horizontal direction (V_{ph}) for AP specimen at $D_r=50.35\%$, $\sigma'=5$ psi, $S=0\%$, input frequency (f) = 5 kHz

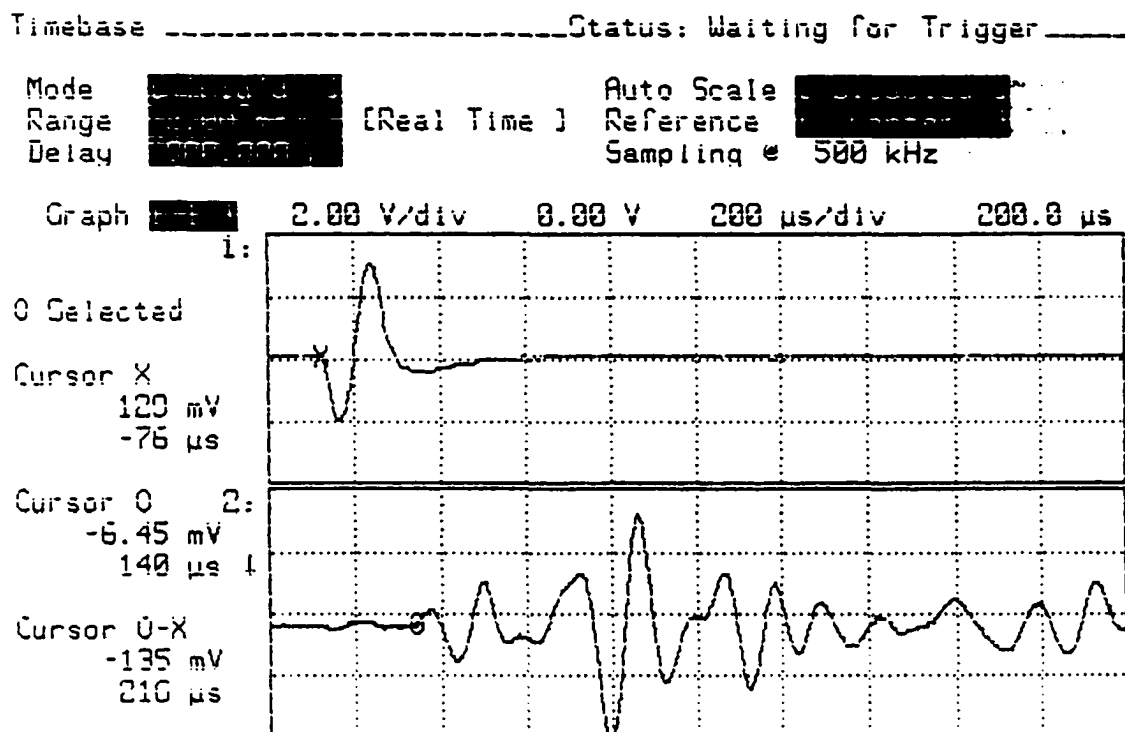


Figure B-12 Measurement of P-wave travel time in horizontal direction (V_{ph}) for AP specimen at $D_r=50.35\%$, $\sigma'=5$ psi, $S=0\%$, input frequency (f) = 7 kHz

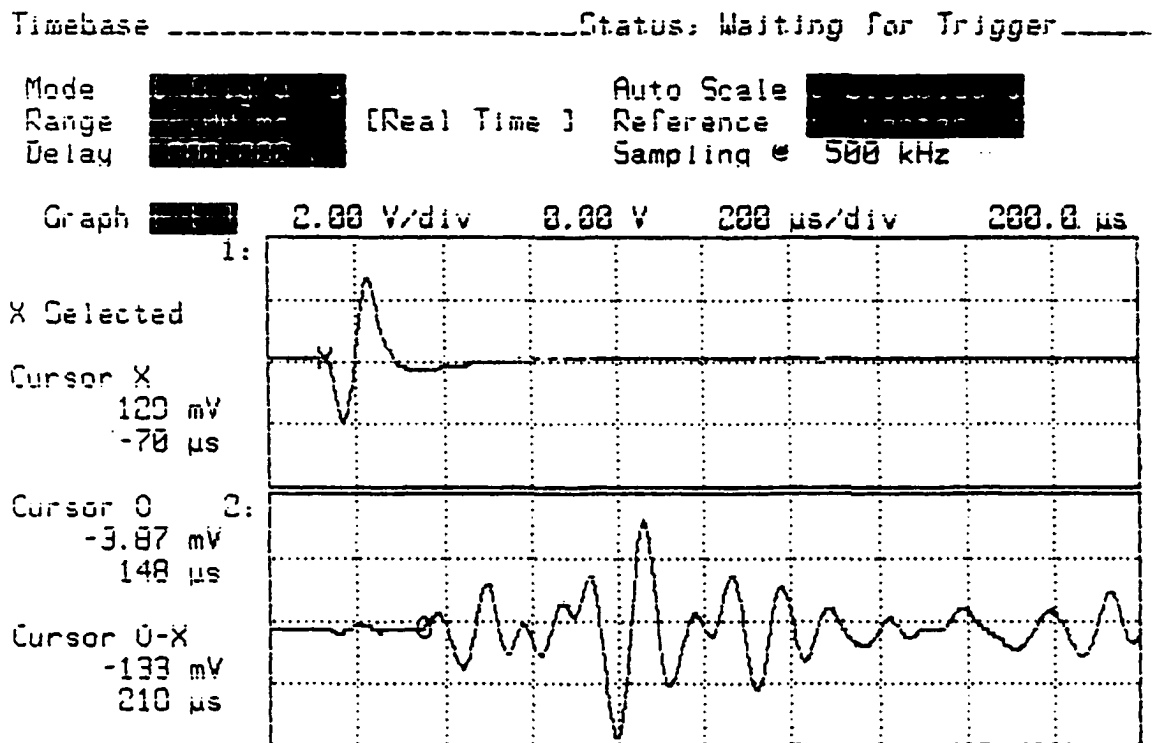


Figure B-13 Measurement of P-wave travel time in horizontal direction (V_{ph}) for AP specimen at $D_r=50.35\%$, $\sigma=5$ psi, $S=0\%$, input frequency (f) = 9 kHz

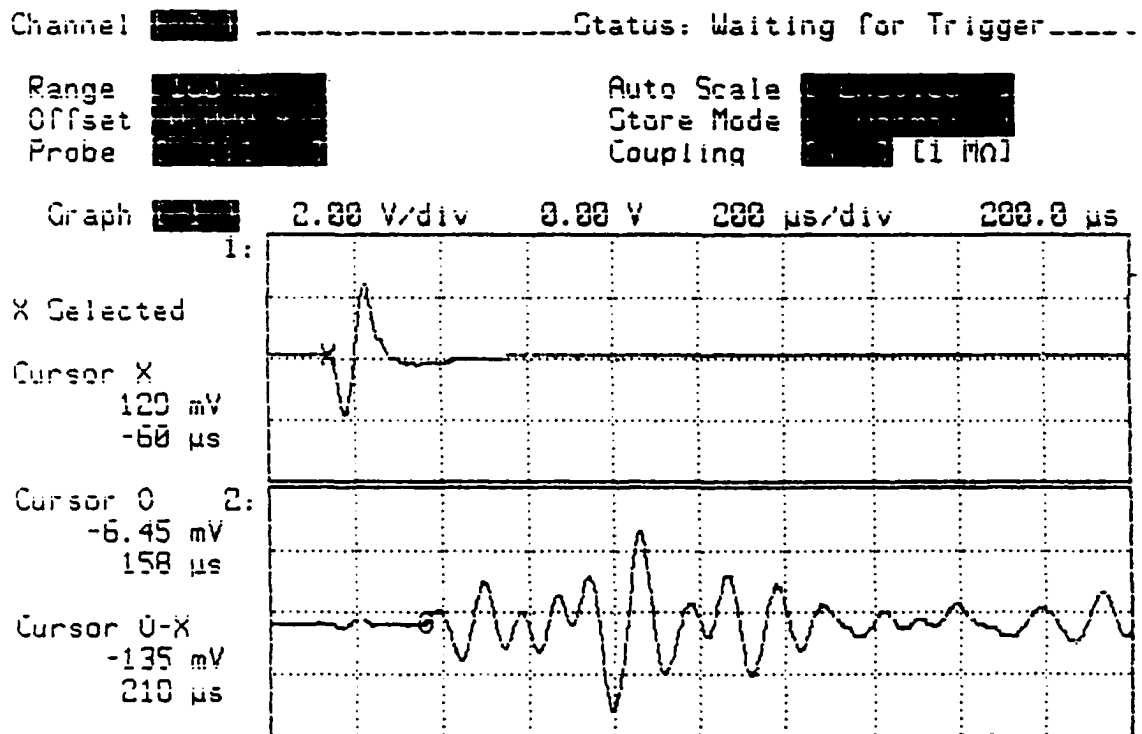


Figure B-14 Measurement of P-wave travel time in horizontal direction (V_{ph}) for AP specimen at $D_r=50.35\%$, $\sigma=5$ psi, $S=0\%$, input frequency (f) = 11 kHz

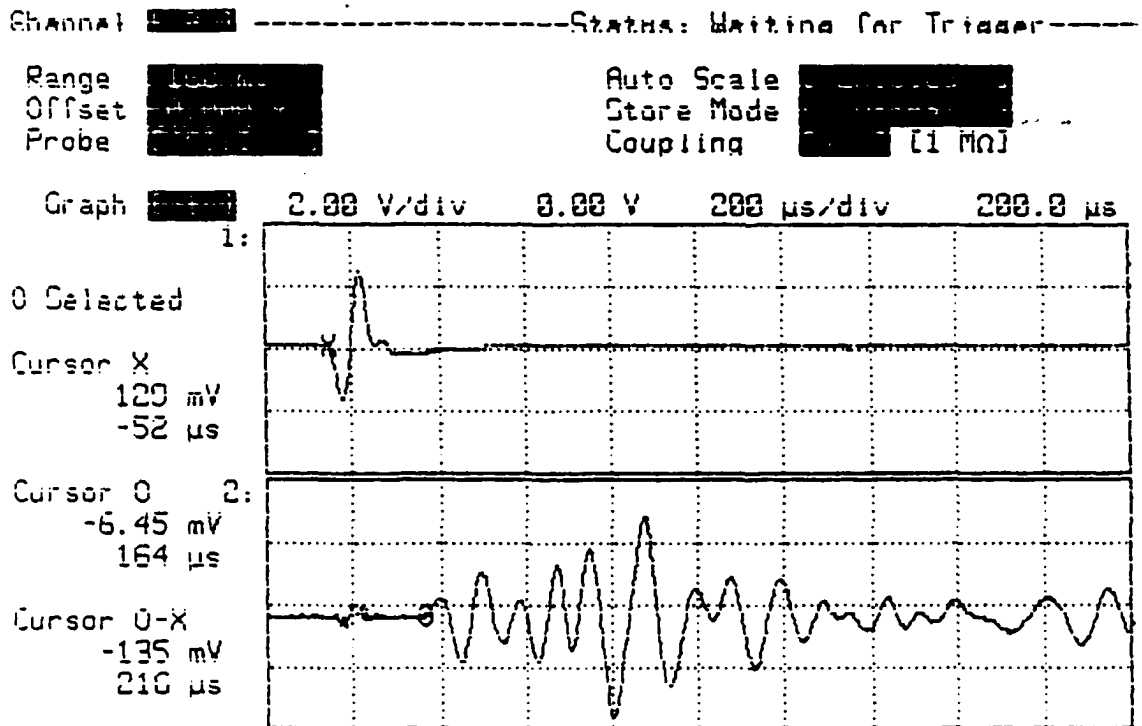


Figure B-15 Measurement of P-wave travel time in horizontal direction (V_{ph}) for AP specimen at $D_r=50.35\%$, $\sigma=5$ psi, $S=0\%$, input frequency (f) = 13.5 kHz

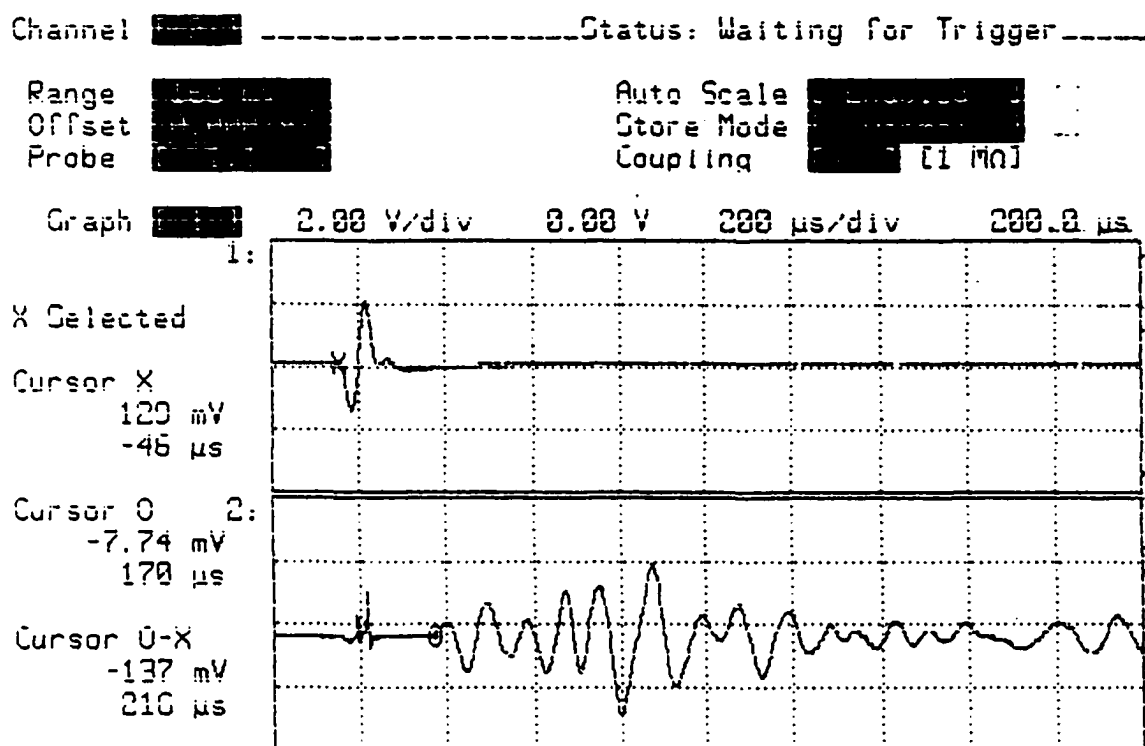


Figure B-16 Measurement of P-wave travel time in horizontal direction (V_{ph}) for AP specimen at $D_r=50.35\%$, $\sigma=5$ psi, $S=0\%$, input frequency (f) = 17 kHz

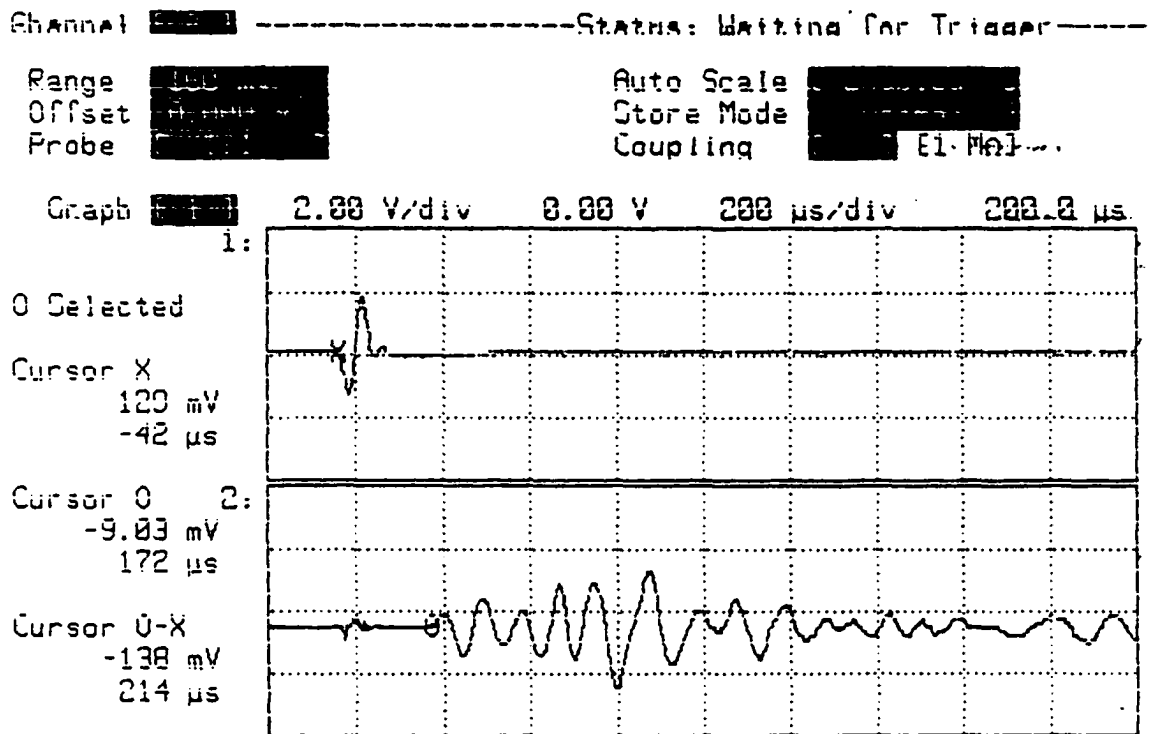


Figure B-17 Measurement of P-wave travel time in horizontal direction (V_{ph}) for AP specimen at $D_r=50.35\%$, $\sigma=5$ psi, $S=0\%$, input frequency (f) = 20 kHz

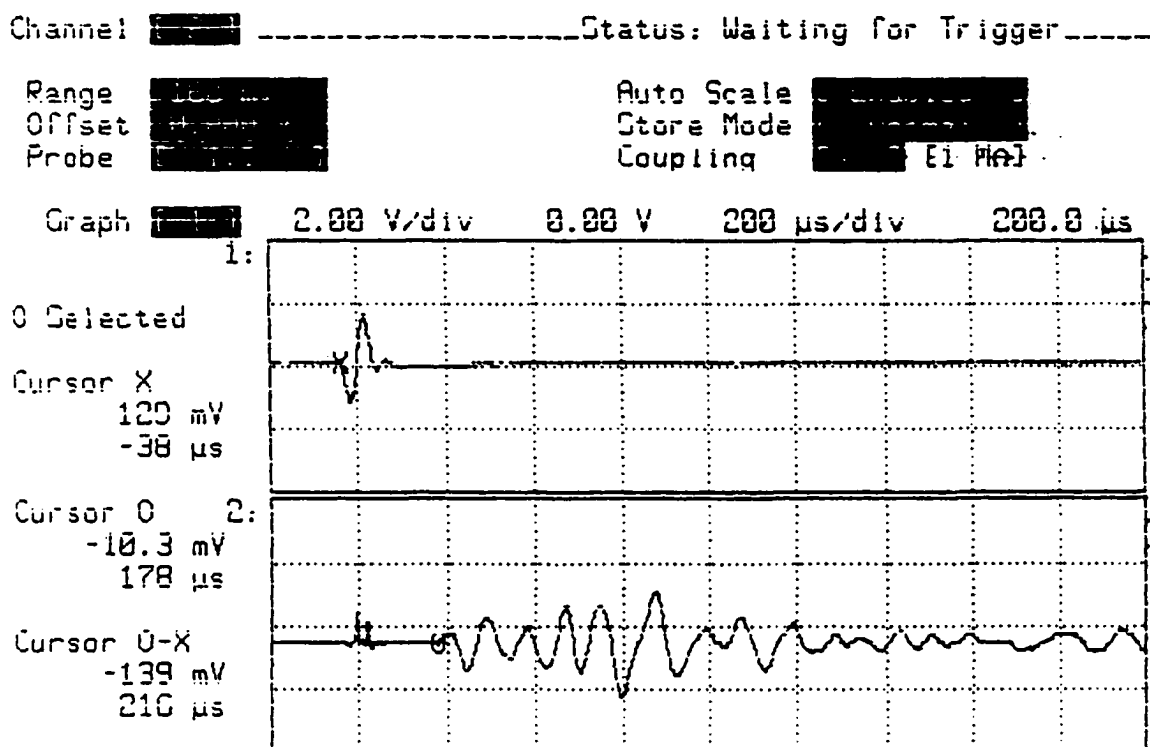


Figure B-18 Measurement of P-wave travel time in horizontal direction (V_{ph}) for AP specimen at $D_r=50.35\%$, $\sigma=5$ psi, $S=0\%$, input frequency (f) = 22 kHz

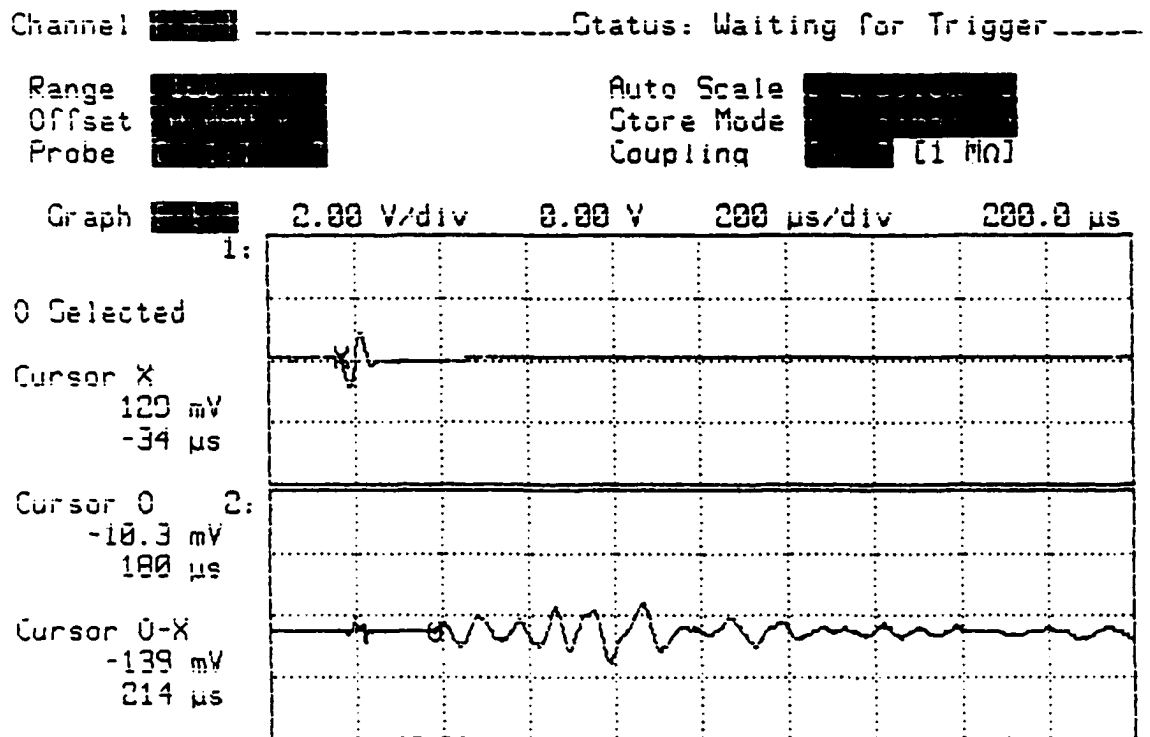


Figure B-19 Measurement of P-wave travel time in horizontal direction (V_{ph}) for AP specimen at $D_r=50.35\%$, $\sigma=5$ psi, $S=0\%$, input frequency (f) = 30 kHz

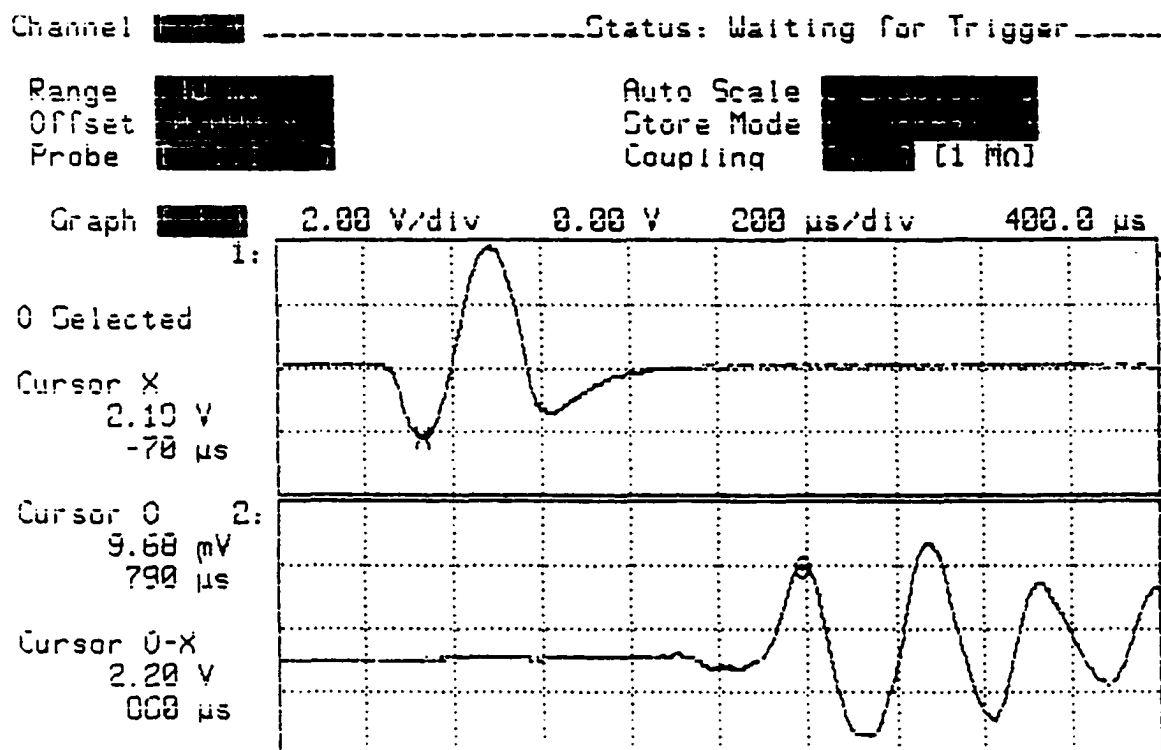


Figure B-20 Measurement of S-wave travel time in horizontal direction (V_{s_v}) for AP specimen at $D_r=50.35\%$, $\sigma'=5$ psi, $S=0\%$, input frequency (f) = 3 kHz

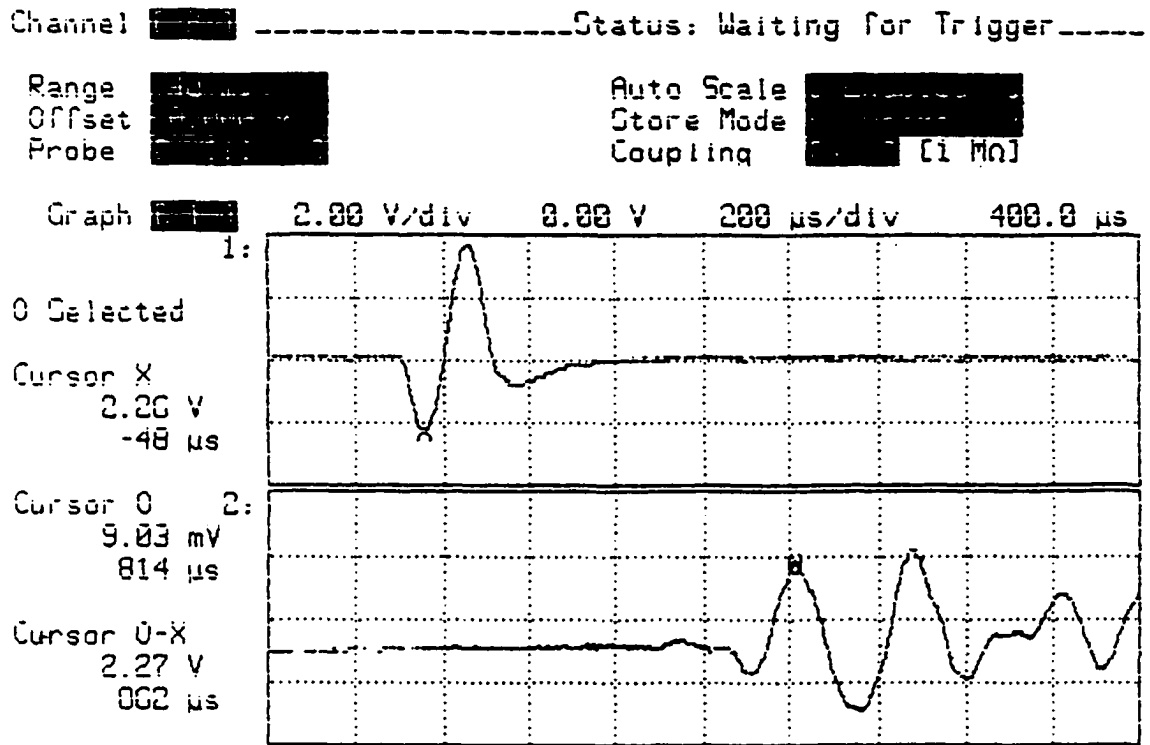


Figure B-21 Measurement of S-wave travel time in horizontal direction (V_{s_v}) for AP specimen at $D_r=50.35\%$, $\sigma'=5$ psi, $S=0\%$, input frequency (f) = 5 kHz

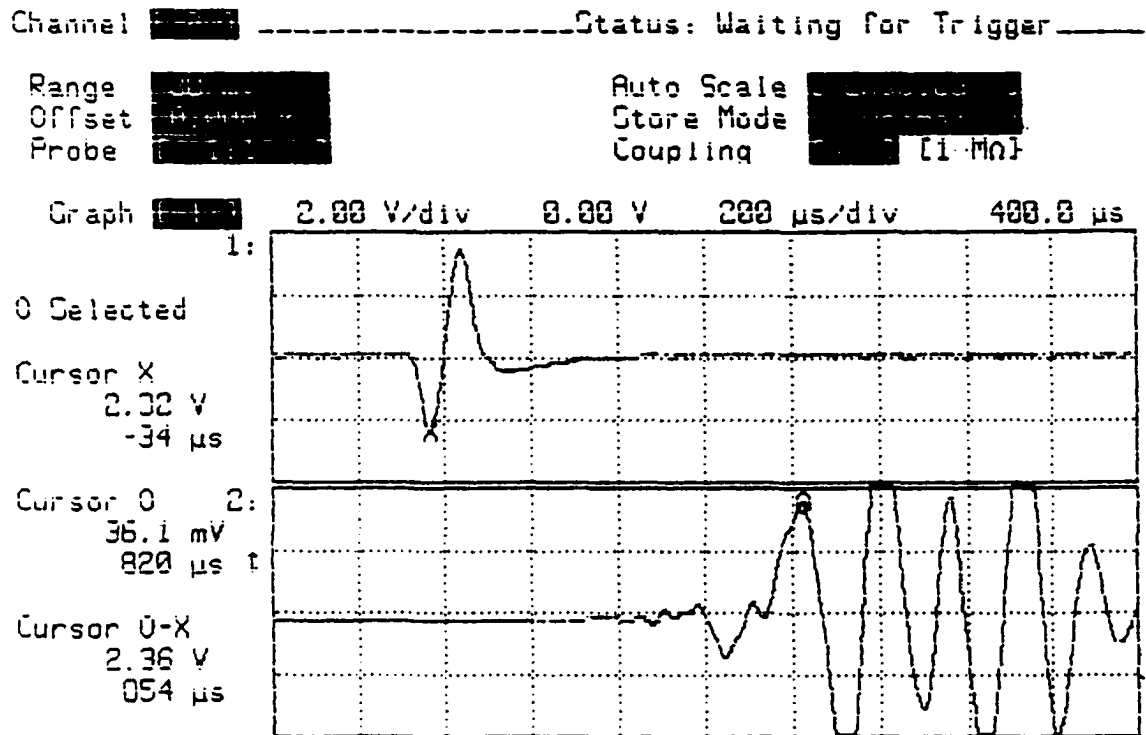


Figure B-22 Measurement of S-wave travel time in horizontal direction (V_{sv}) for AP specimen at $D_r=50.35\%$, $\sigma=5$ psi, $S=0\%$, input frequency (f) = 7 kHz

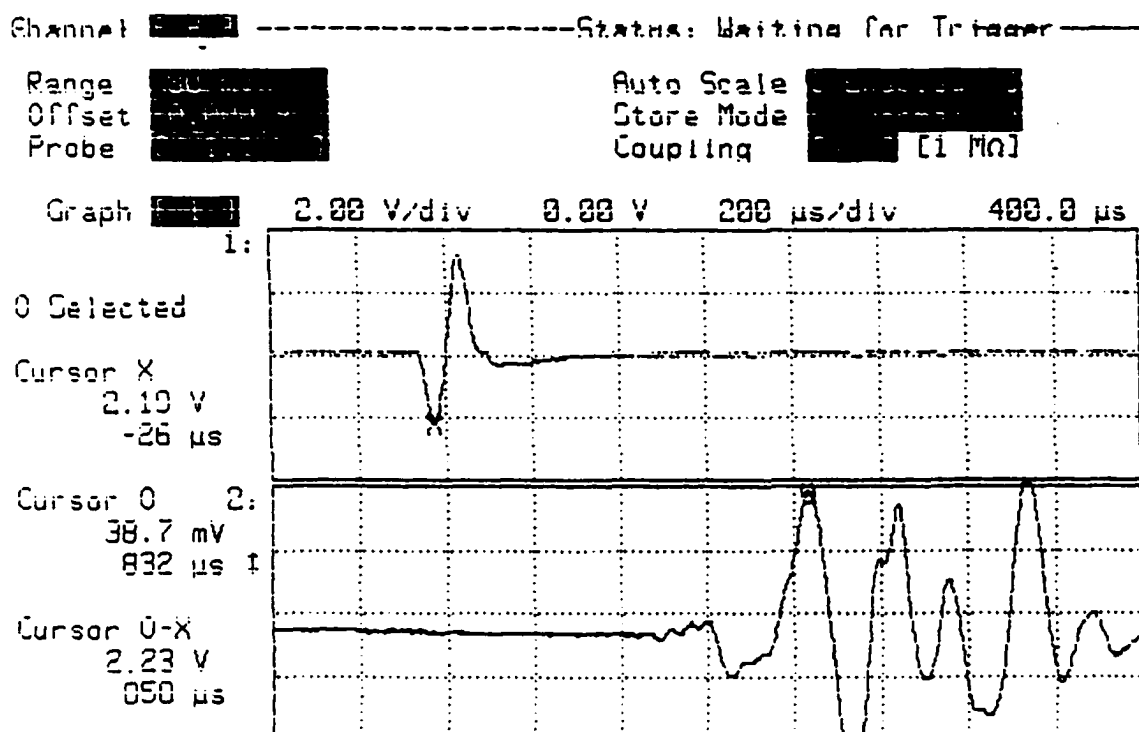


Figure B-23 Measurement of S-wave travel time in horizontal direction (V_{sv}) for AP specimen at $D_r=50.35\%$, $\sigma=5$ psi, $S=0\%$, input frequency (f) = 9 kHz

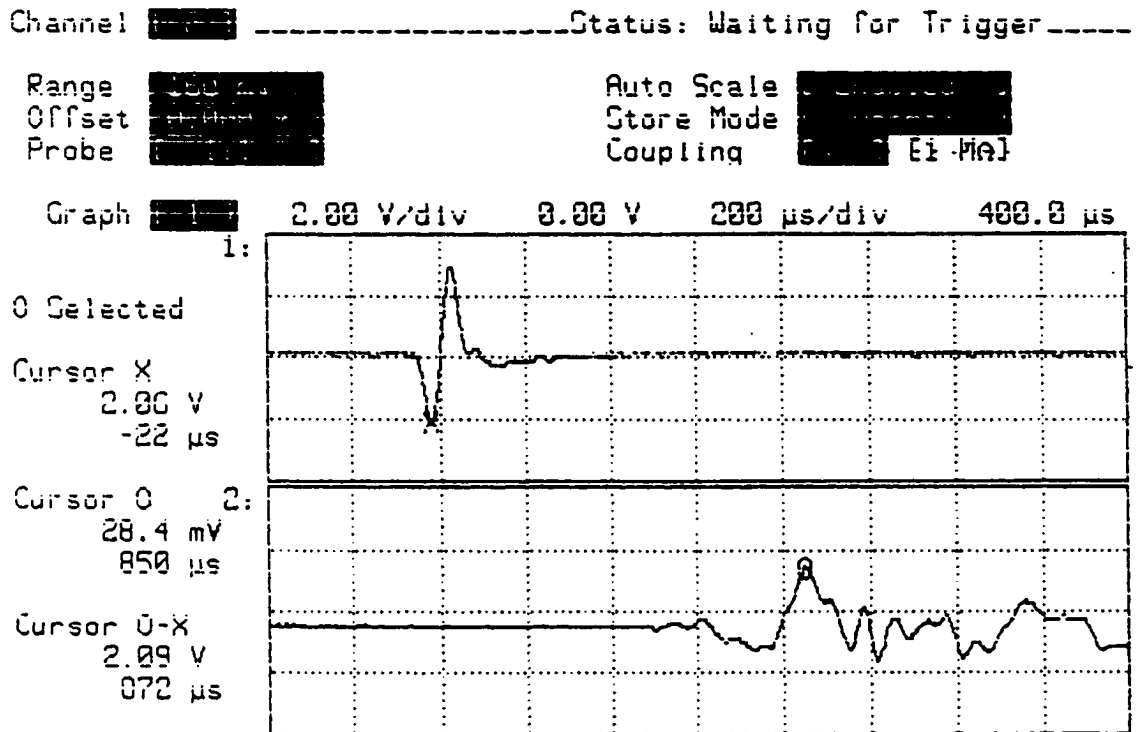


Figure B-24 Measurement of S-wave travel time in horizontal direction (V_{sv}) for AP specimen at $D_r=50.35\%$, $\sigma=5$ psi, $S=0\%$, input frequency (f) = 11 kHz

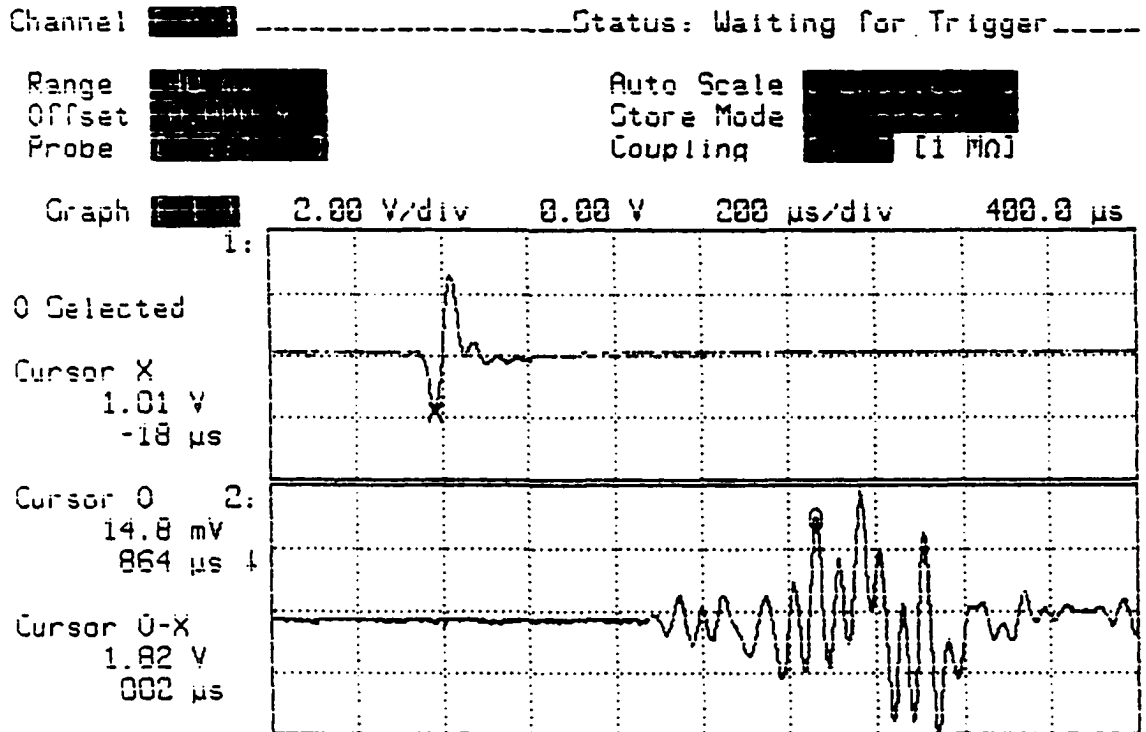


Figure B-25 Measurement of S-wave travel time in horizontal direction (V_{s_v}) for AP specimen at $D_r=50.35\%$, $\sigma=5$ psi, $S=0\%$, input frequency (f) = 13.5 kHz

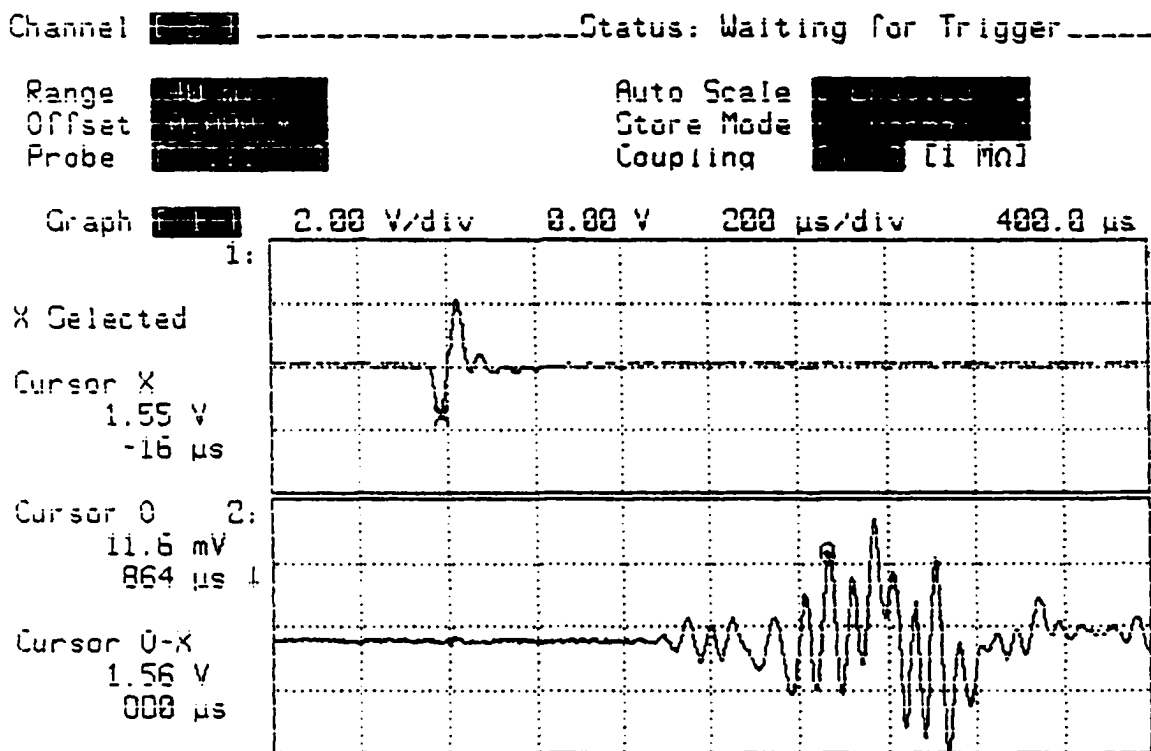


Figure B-26 Measurement of S-wave travel time in horizontal direction (V_{sv}) for AP specimen at $D_r=50.35\%$, $\sigma'=5$ psi, $S=0\%$, input frequency (f) = 17.0 kHz

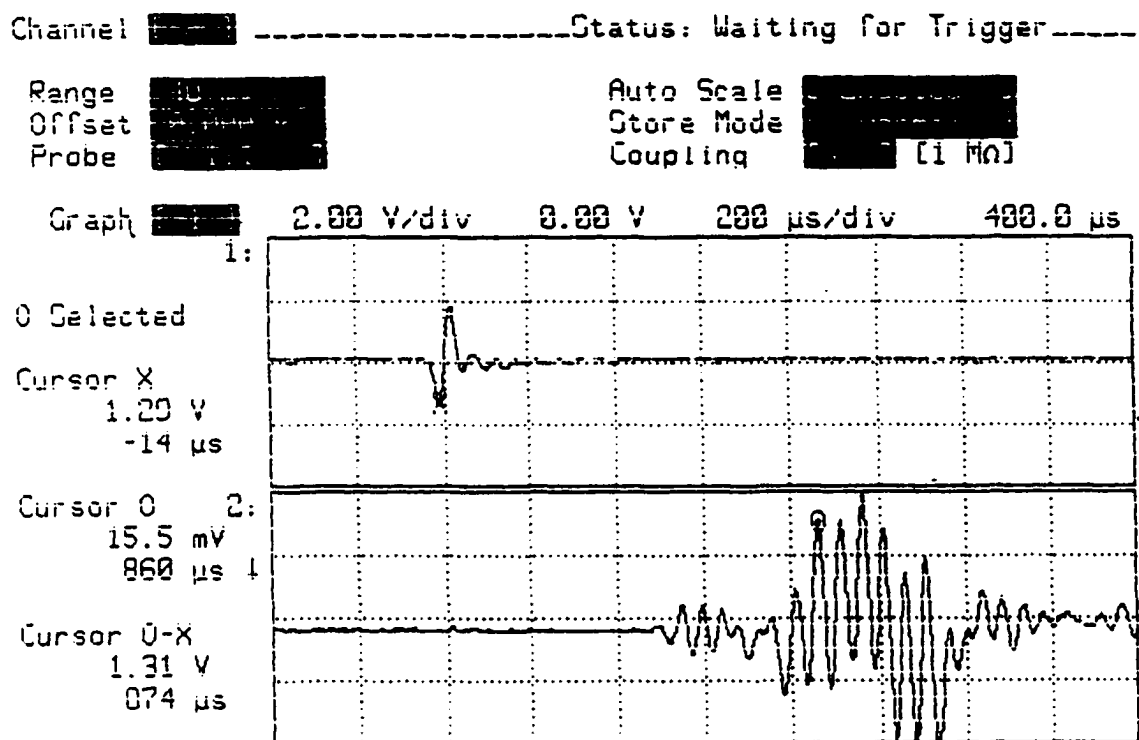


Figure B-27 Measurement of S-wave travel time in horizontal direction (V_{s_v}) for AP specimen at $D_r=50.35\%$, $\sigma'_v=5$ psi, $S=0\%$, input frequency (f) = 22.0 kHz

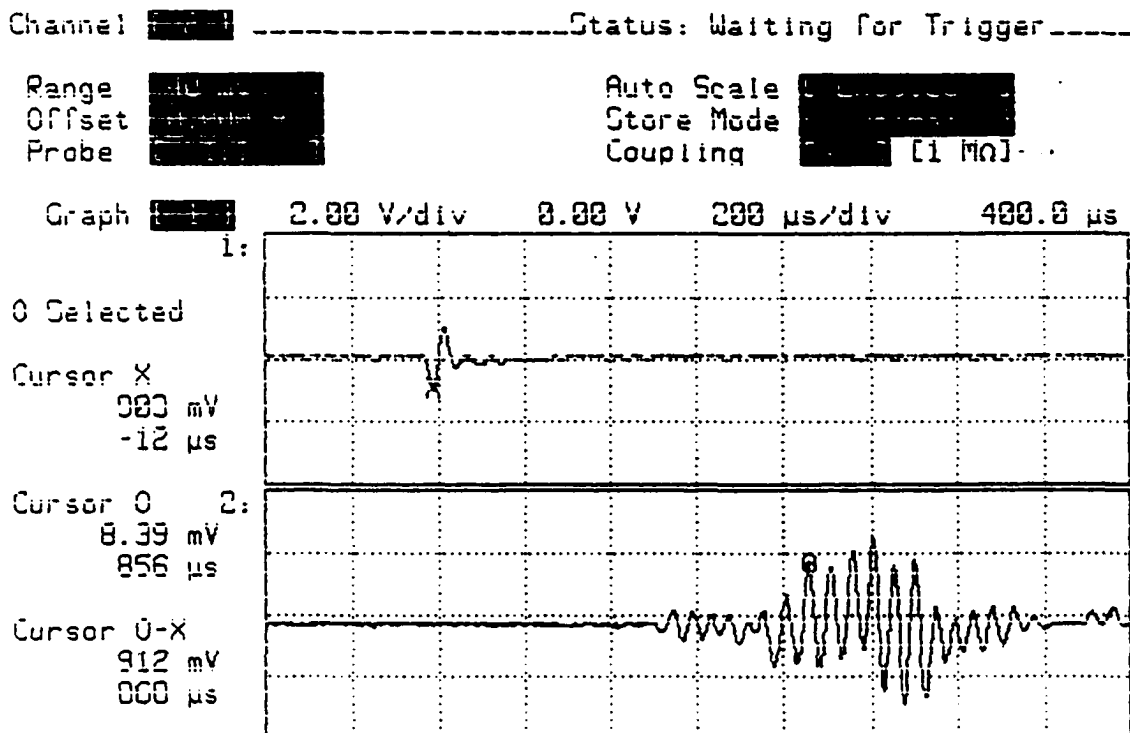


Figure B-28 Measurement of S-wave travel time in horizontal direction (V_{sv}) for AP specimen at $D_r=50.35\%$, $\sigma=5$ psi, $S=0\%$, input frequency (f) = 30.0 kHz

APPENDIX C
SATURATION EFFECT ON ELASTIC WAVE
VELOCITIES

Water saturation effects were investigated for the elastic wave velocities in vertical direction. All elastic wave records here were obtained under 5 psi effective pressure for V_{p_v} , V_{s_v} , of a MV specimen.

All wave records here were obtained from the hard copies of the oscilloscope display. Figure C1 through C4 show wave records for V_{p_v} under different saturation degrees. Figure C5 through C8 show wave records for V_{s_v} under different frequencies.

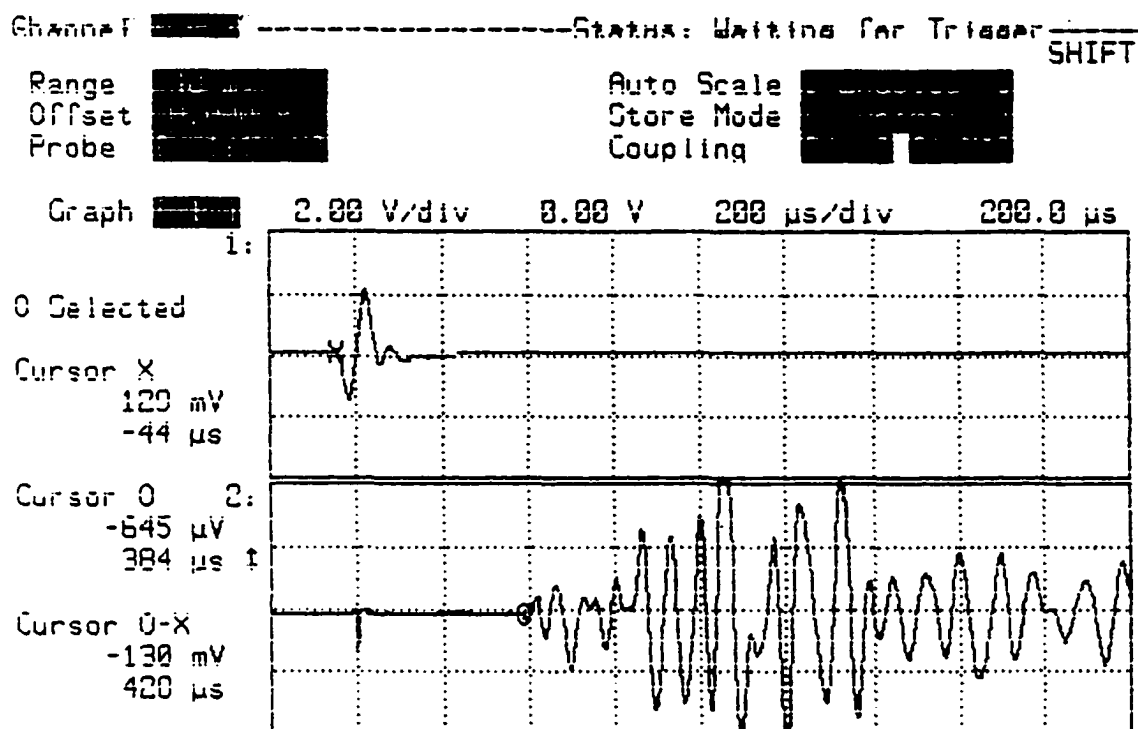


Figure C-1 Measurement of P-wave travel time in vertical direction (V_{pv}) for MV specimen at $D_r=49.07\%$, $\sigma=5$ psi, $B=0$, input frequency (f) = 17 kHz

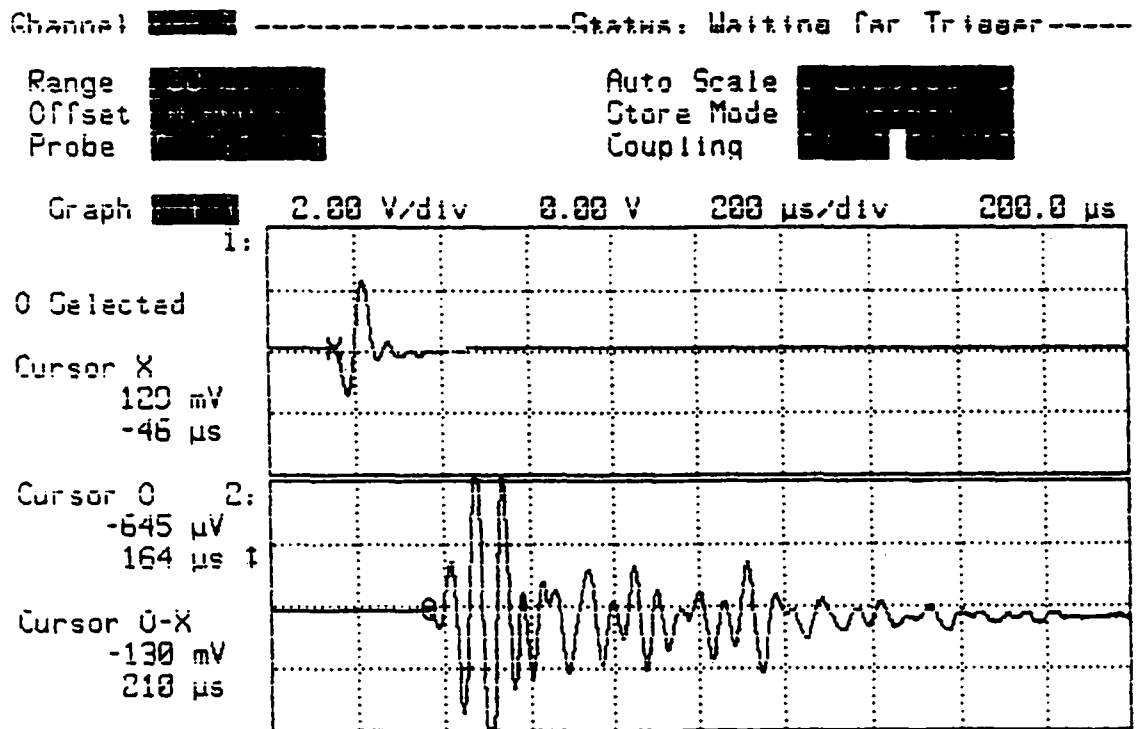


Figure C-2 Measurement of P-wave travel time in vertical direction (V_{pv}) for MV specimen at $D_r=49.07\%$, $\sigma'_v=5$ psi, $B=43$, input frequency (f) = 17 kHz

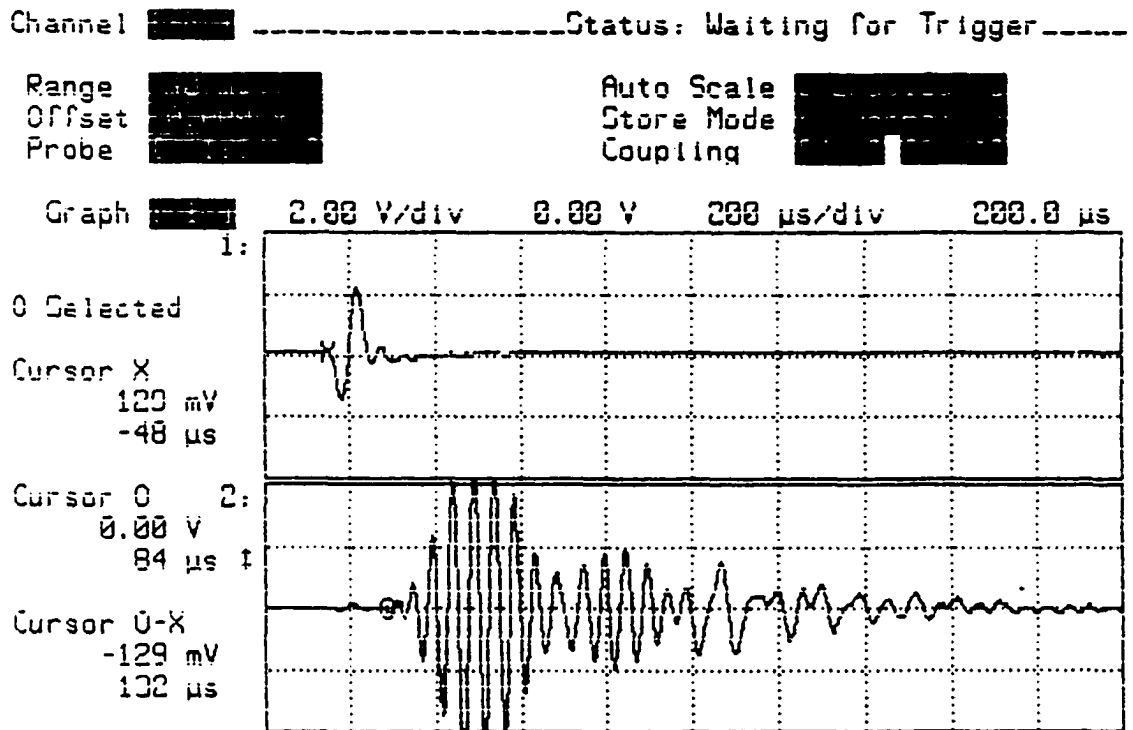


Figure C-3 Measurement of P-wave travel time in vertical direction (V_{pv}) for MV specimen at $D_r=49.07\%$, $\sigma'=5$ psi, $B=76$, input frequency (f) = 17 kHz

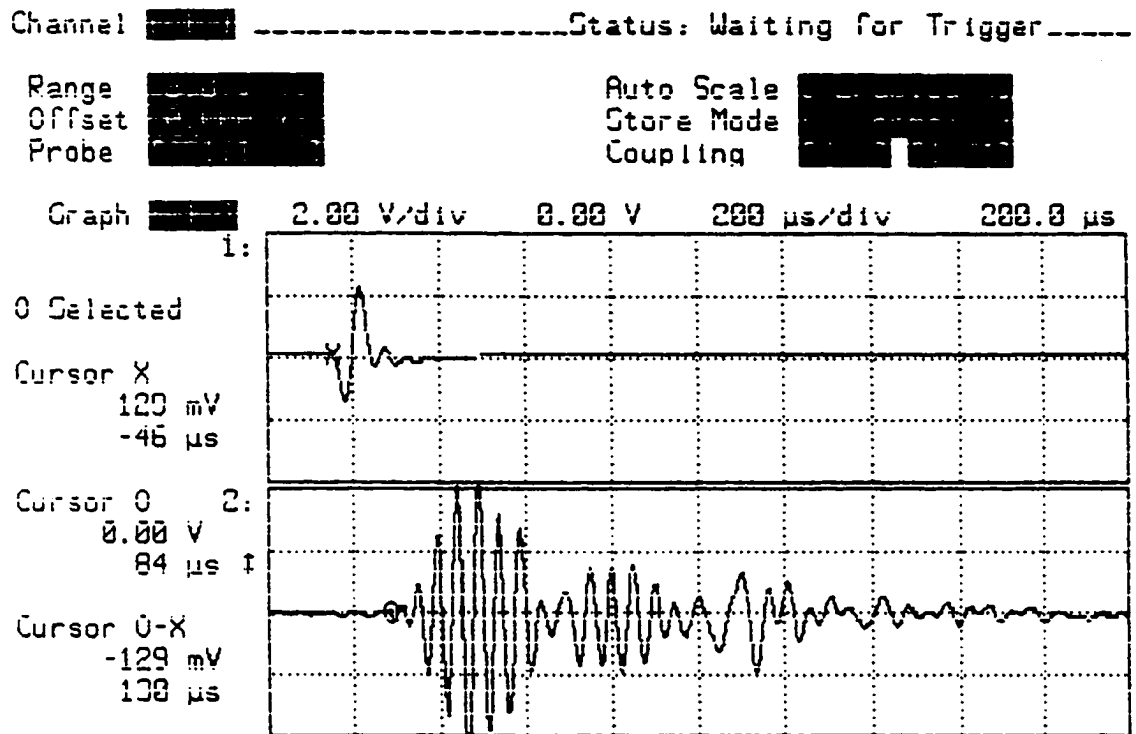


Figure C-4 Measurement of P-wave travel time in vertical direction (V_{pv}) for MV specimen at $D_r=49.07\%$, $\sigma'=5$ psi, $B=88$, input frequency (f) = 17 kHz

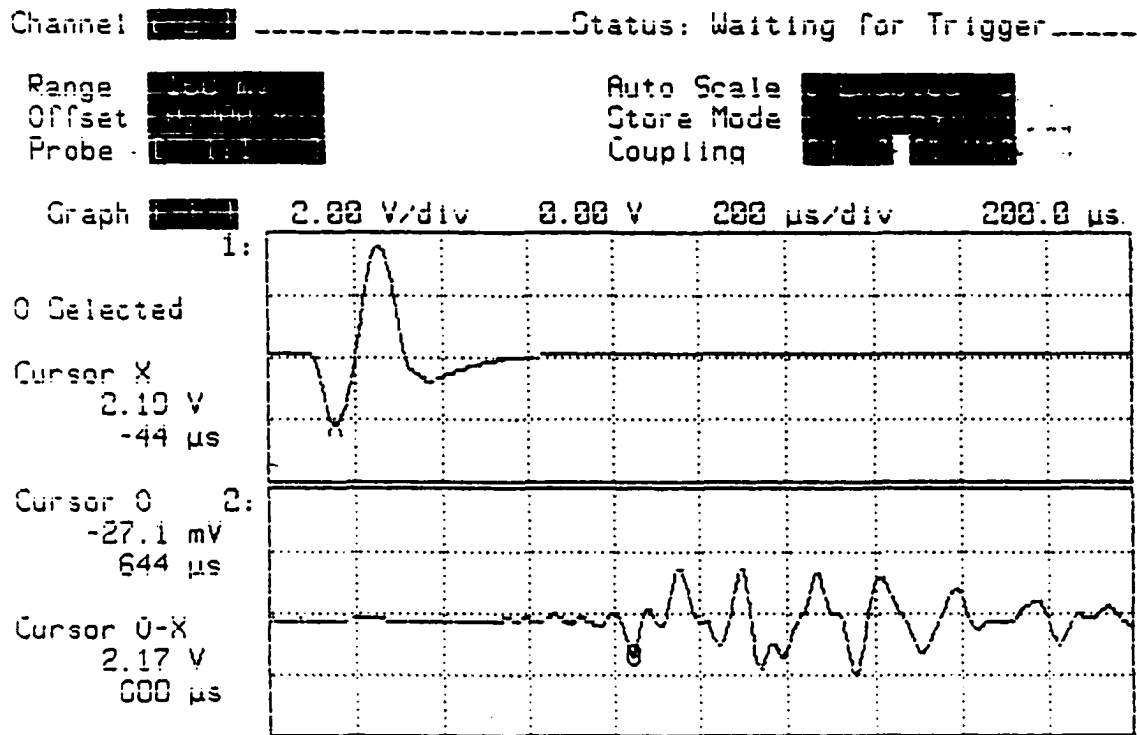


Figure C-5 Measurement of S-wave travel time in vertical direction (V_{sv}) for MV specimen at $D_r=49.07\%$, $\sigma=5$ psi, $\mathbf{B}=\mathbf{0}$, input frequency (f) = 5.0 kHz

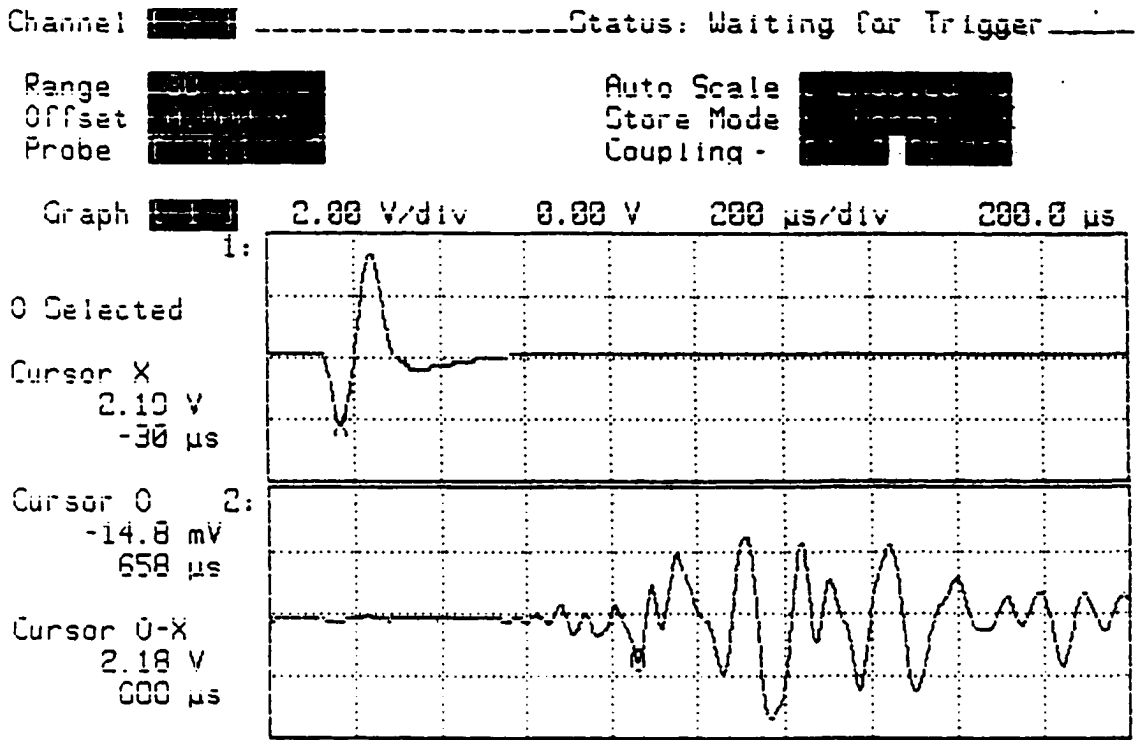


Figure C-6 Measurement of S-wave travel time in vertical direction (V_{sv}) for MV specimen at $D_r=49.07\%$, $\sigma=5$ psi, $B=0$, input frequency (f) = 7.0 kHz

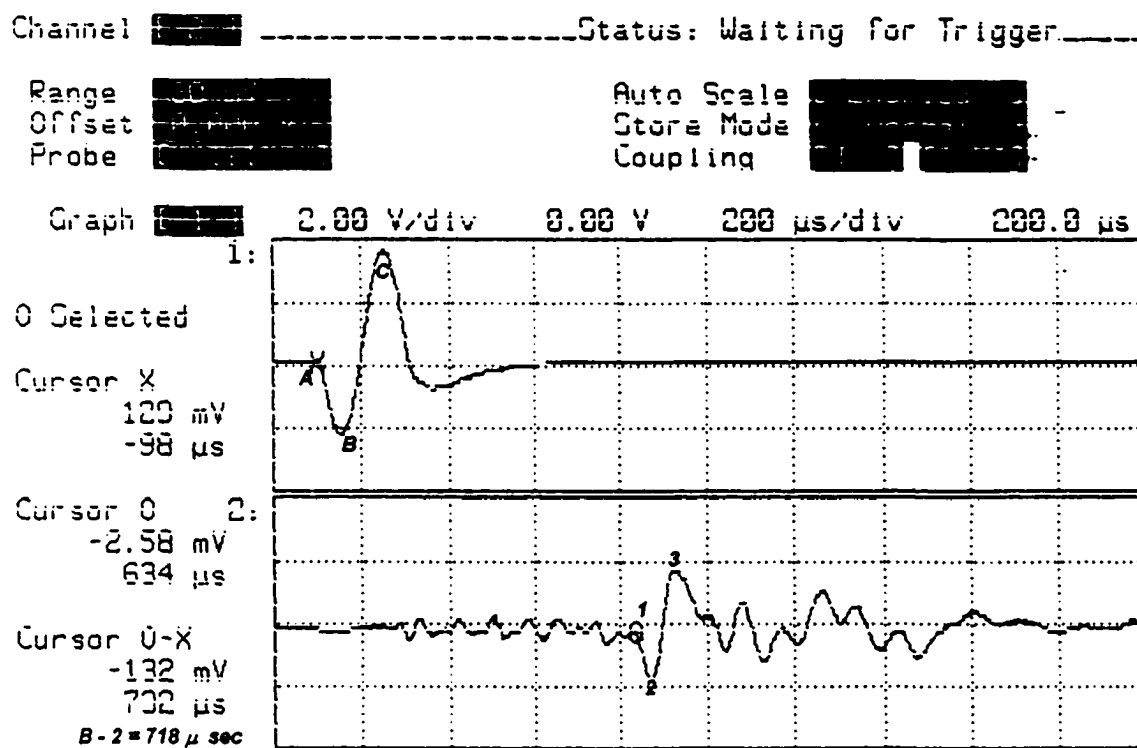


Figure C-7 Measurement of S-wave travel time in vertical direction (V_{sv}) for MV specimen at $D_r=49.07\%$, $\sigma=5$ psi, $B=94$, input frequency (f) = 5 kHz

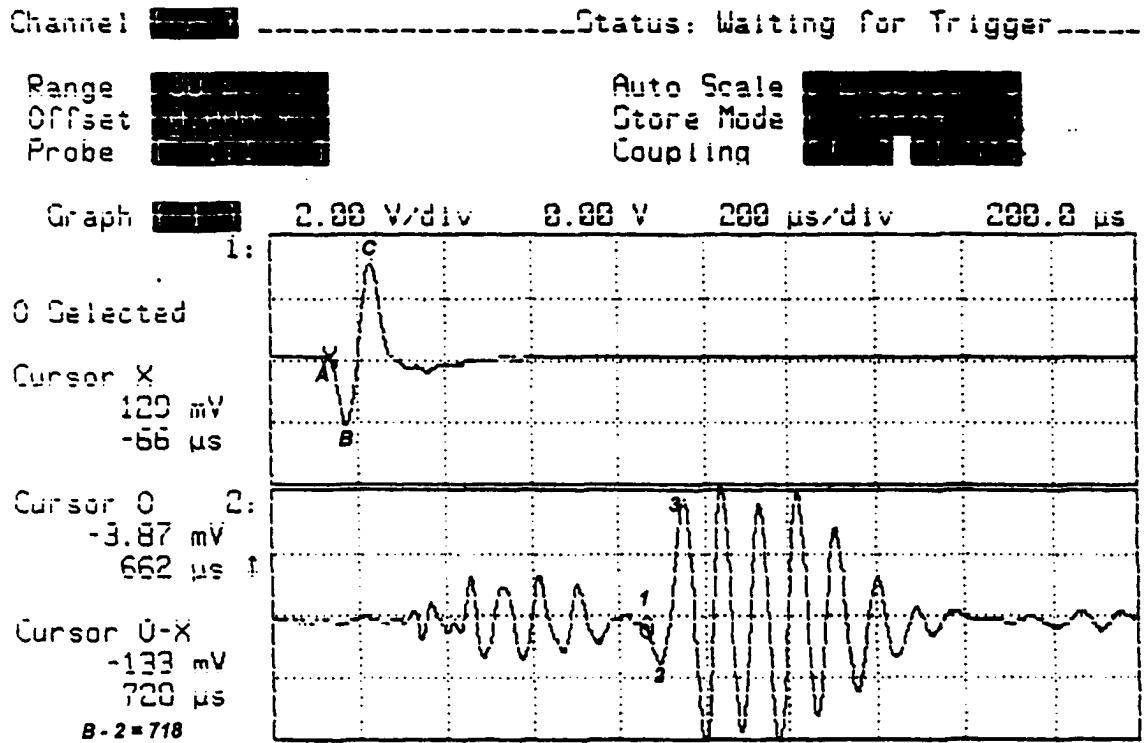


Figure C-8 Measurement of S-wave travel time in vertical direction (V_{sv}) for MV specimen at $D_r=49.07\%$, $\sigma'=5$ psi, $B=94$, input frequency (f) = 9.0 kHz

APPENDIX D

**ELASTIC WAVE MEASUREMENTS UNDER DIFFERENT
EFFECTIVE CONFINING PRESSURE AT DRY CONDITION**

The effect of effective confining pressure (σ') on elastic wave velocities were investigated. Specimens were first prepared at 5 psi vacuum pressure and effective pressure (σ') was then increased to 10, 20, 30, 40, and 50 psi. P-wave velocities in vertical and horizontal directions (V_{pv} and V_{ph}) and S-wave velocity in vertical direction (V_{sv}) were measured. Some wave records here are presented for a MV specimen. All wave records here were obtained from the hard copies of the oscilloscope display.

Figure D1 through D6 show wave records for V_{pv} under different effective stress at dry condition (S=0%).

Figure D7 through D12 show wave records for V_{ph} under different effective stress at dry condition (S=0%).

Figure D13 through D17 show wave records for V_{sv} under different effective stress at dry condition (S=0%).

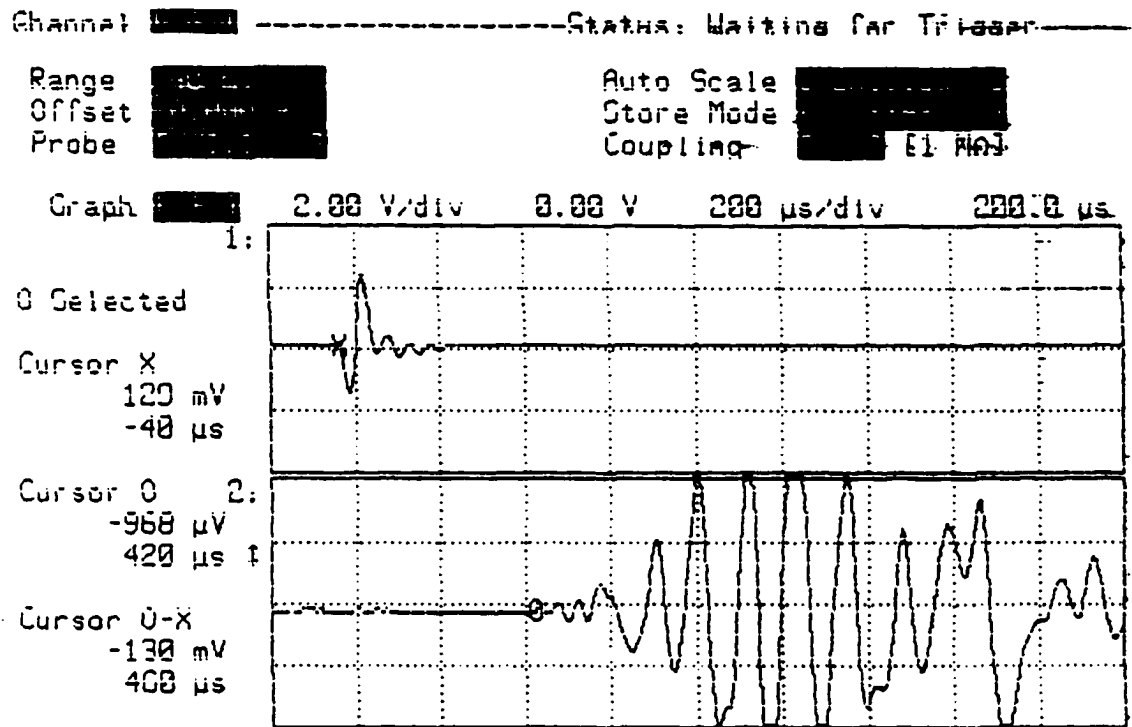


Figure D-1 Measurement of P-wave travel time in vertical direction (V_{pv}) for MV specimen at $D_r=48.20\%$, $\sigma'=5$ psi, $B=0$, input frequency (f) = 17.0 kHz

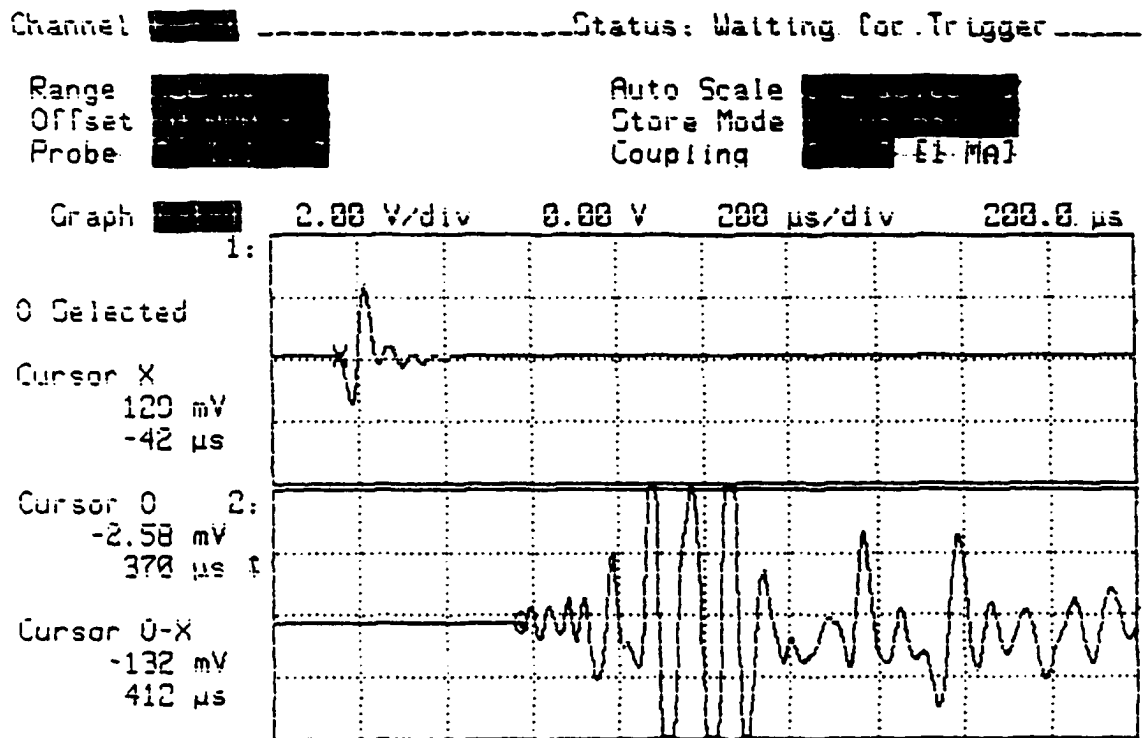


Figure D-2 Measurement of P-wave travel time in vertical direction (V_{p_v}) for MV specimen at $D_r=48.20\%$, $\sigma=10$ psi, $B=0$, input frequency (f) = 17.0 kHz

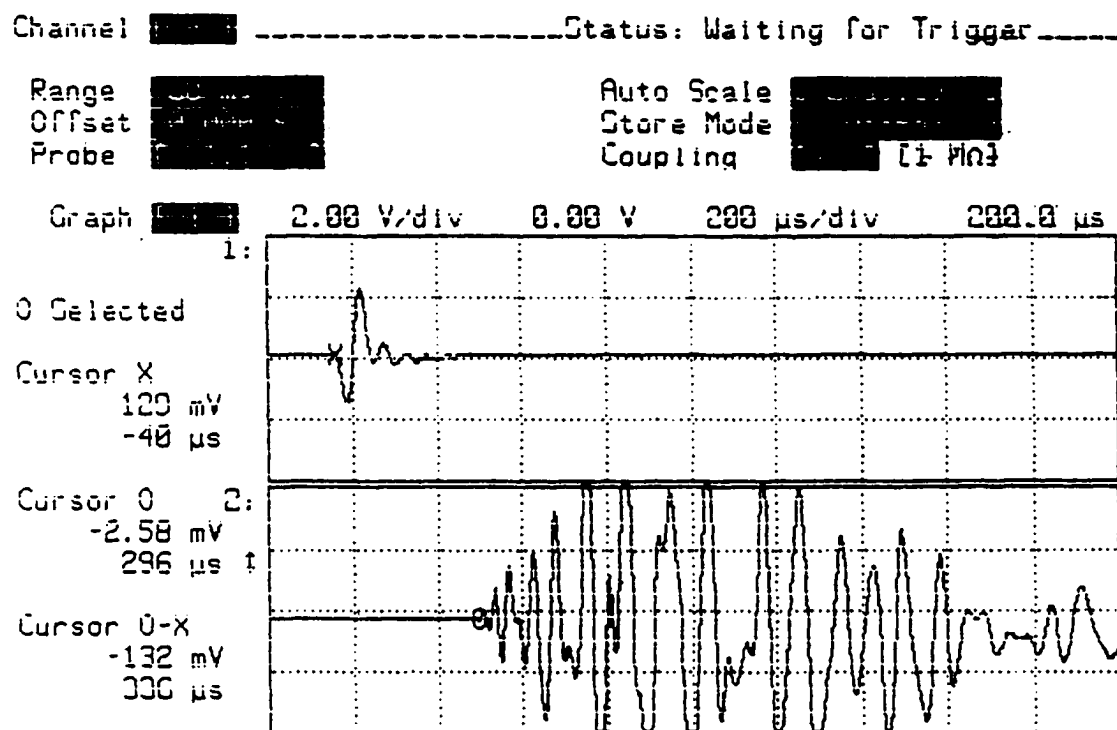


Figure D-3 Measurement of P-wave travel time in vertical direction (V_{pv}) for MV specimen at $D_r=48.20\%$, $\sigma'=20$ psi, $B=0$, input frequency (f) = 17.0 kHz

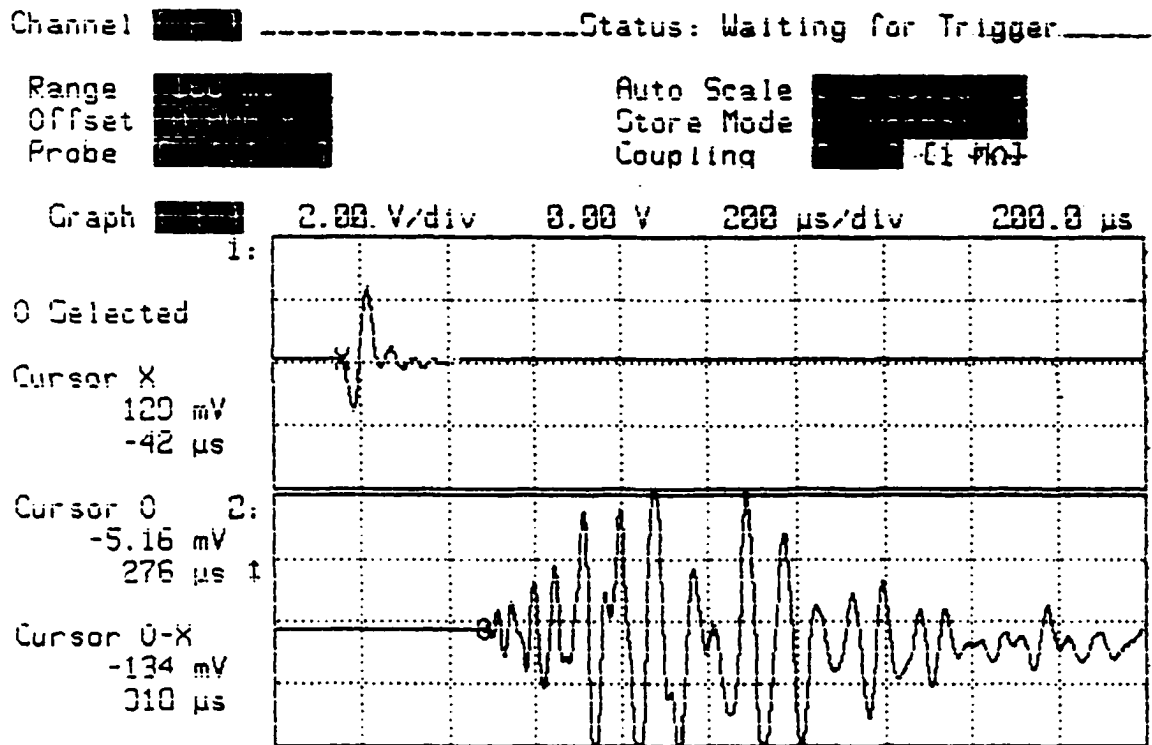


Figure D-4 Measurement of P-wave travel time in vertical direction (V_{pv}) for MV specimen at $D_r=48.20\%$, $\sigma=30$ psi, $B=0$, input frequency (f) = 17.0 kHz

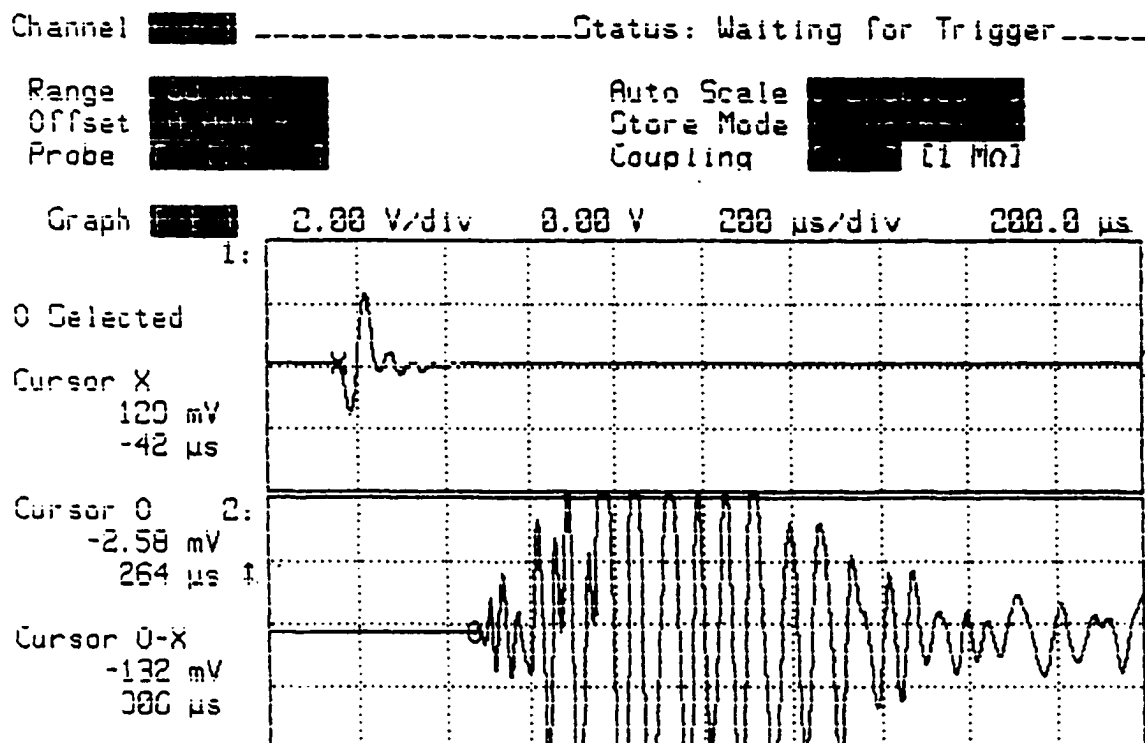


Figure D-5 Measurement of P-wave travel time in vertical direction (V_{pv}) for MV specimen at $D_r=48.20\%$, $\sigma'_v=40$ psi, $B=0$, input frequency (f) = 17.0 kHz

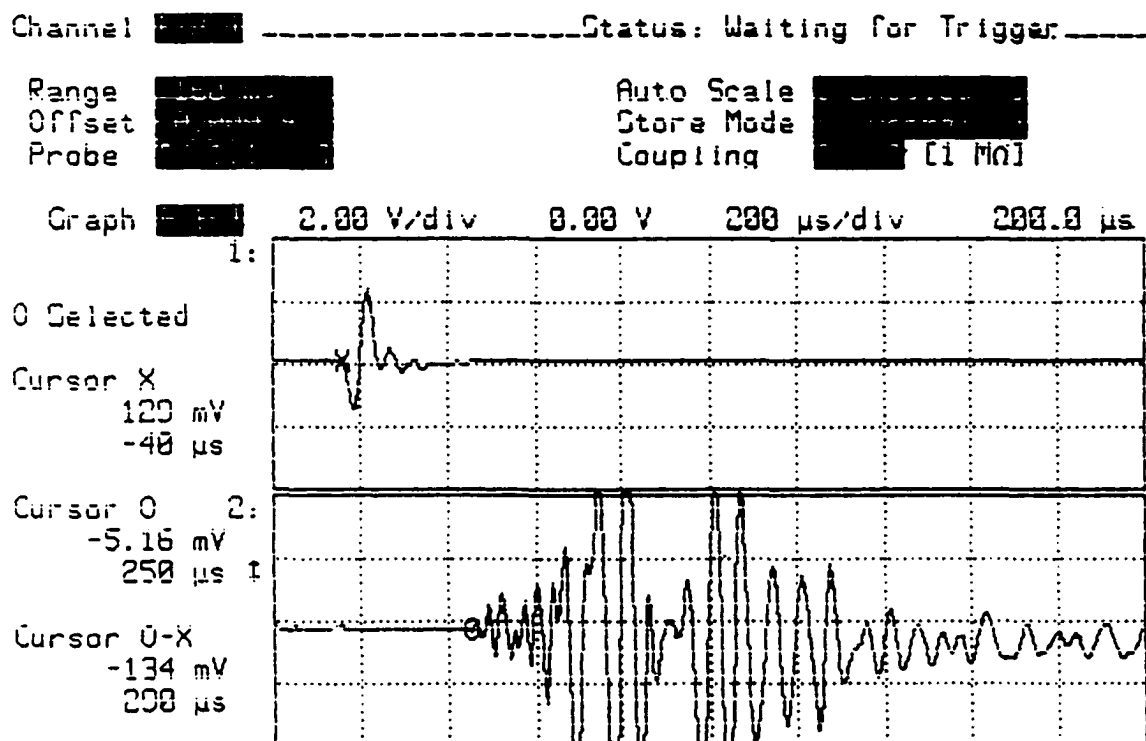


Figure D-6 Measurement of P-wave travel time in vertical direction (V_{pv}) for MV specimen at $D_r=48.20\%$, $\sigma'_v=50$ psi, $B=0$, input frequency (f) = 17.0 kHz

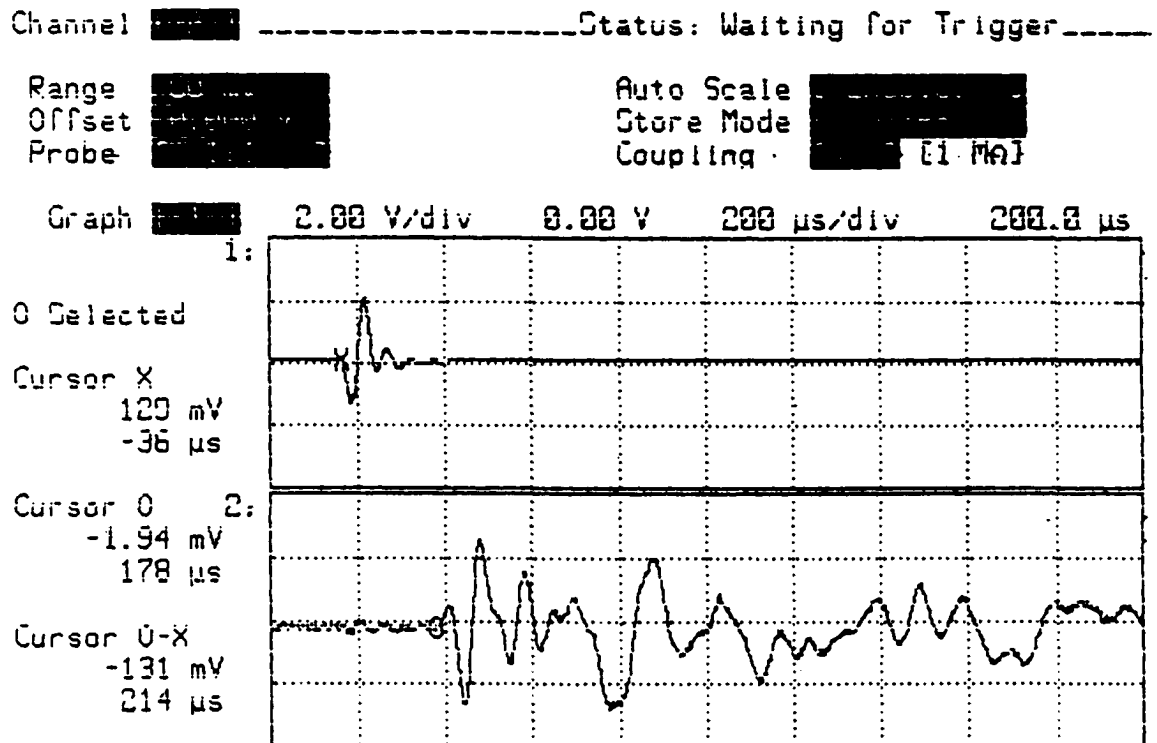


Figure D-7 Measurement of P-wave travel time in horizontal direction (V_{ph}) for MV specimen at $D_r=48.20\%$, $\sigma'_v=5$ psi, $B=0$, input frequency (f) = 20 kHz

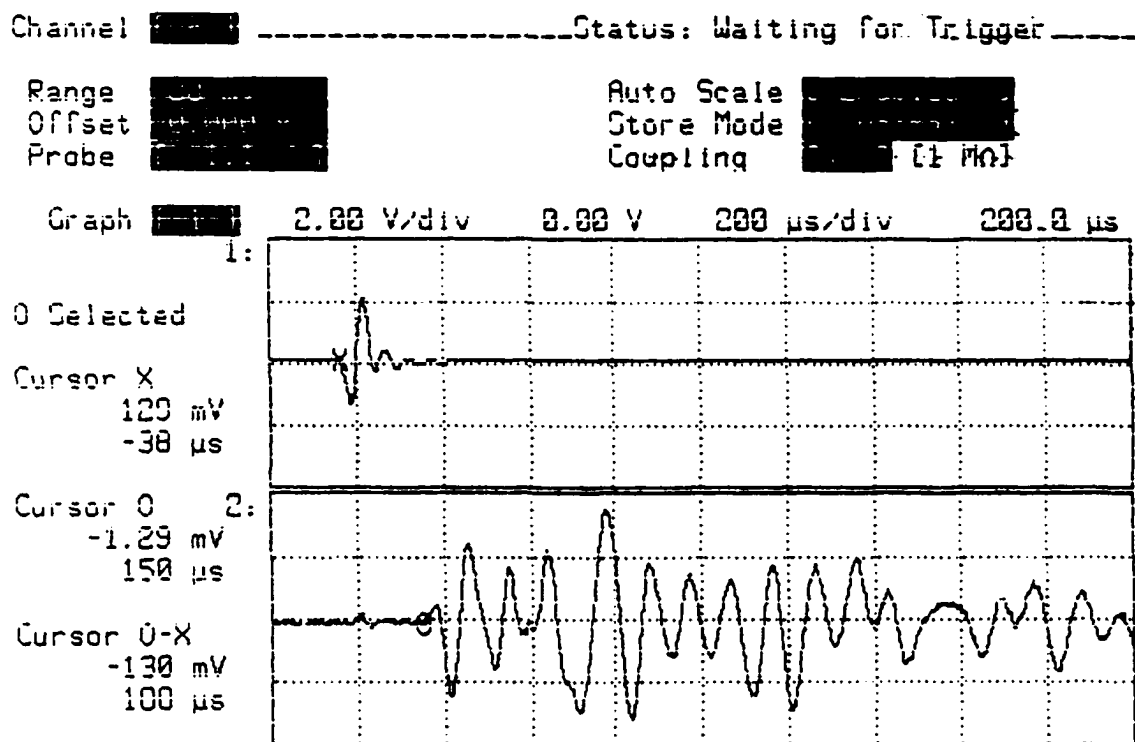


Figure D-8 Measurement of P-wave travel time in horizontal direction (V_{ph}) for MV specimen at $D_r=48.20\%$, $\sigma'_v=10$ psi, $B=0$, input frequency (f) = 20 kHz

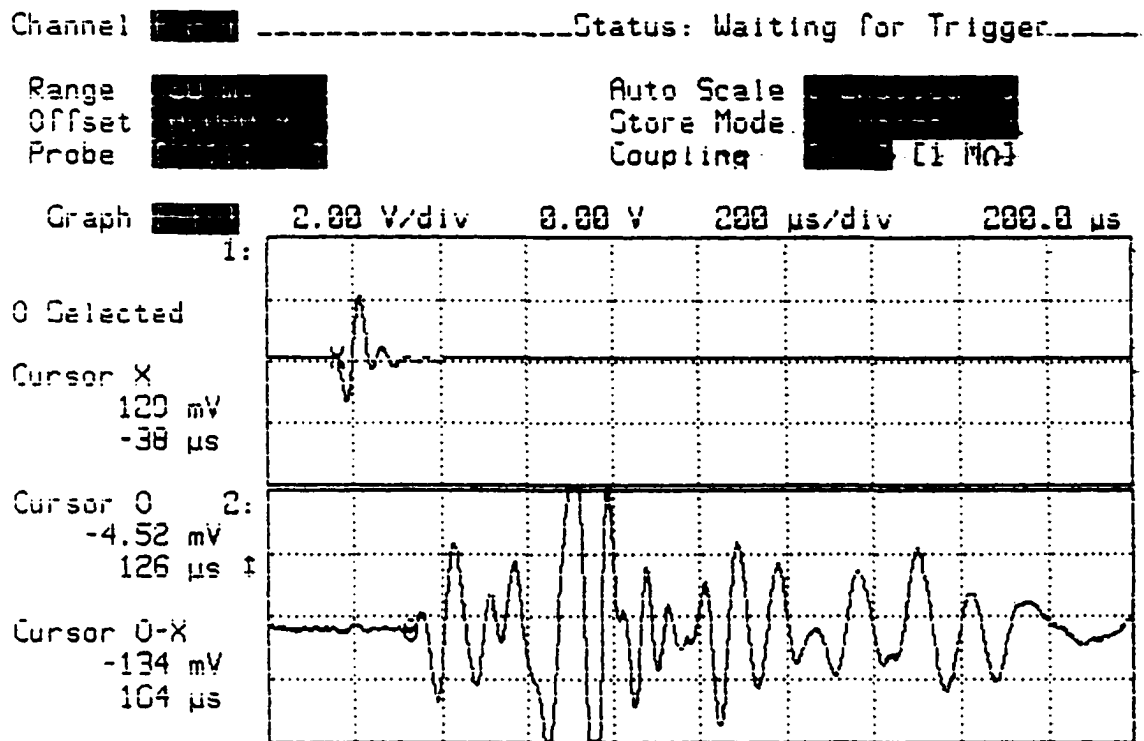


Figure D-9 Measurement of P-wave travel time in horizontal direction (V_{ph}) for MV specimen at $D_r=48.20\%$, $\sigma' = 20$ psi, $B=0$, input frequency (f) = 20 kHz

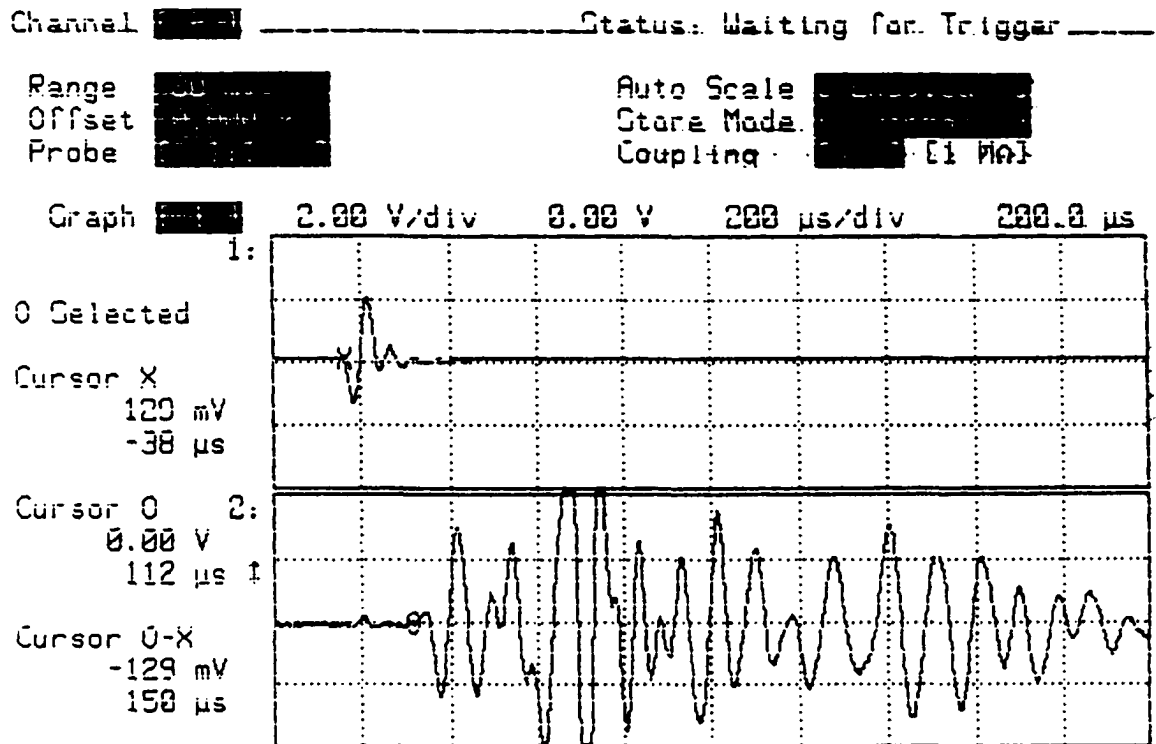


Figure D-10 Measurement of P-wave travel time in horizontal direction (V_{ph}) for MV specimen at $D_r=48.20\%$, $\sigma=30$ psi, $B=0$, input frequency (f) = 20 kHz

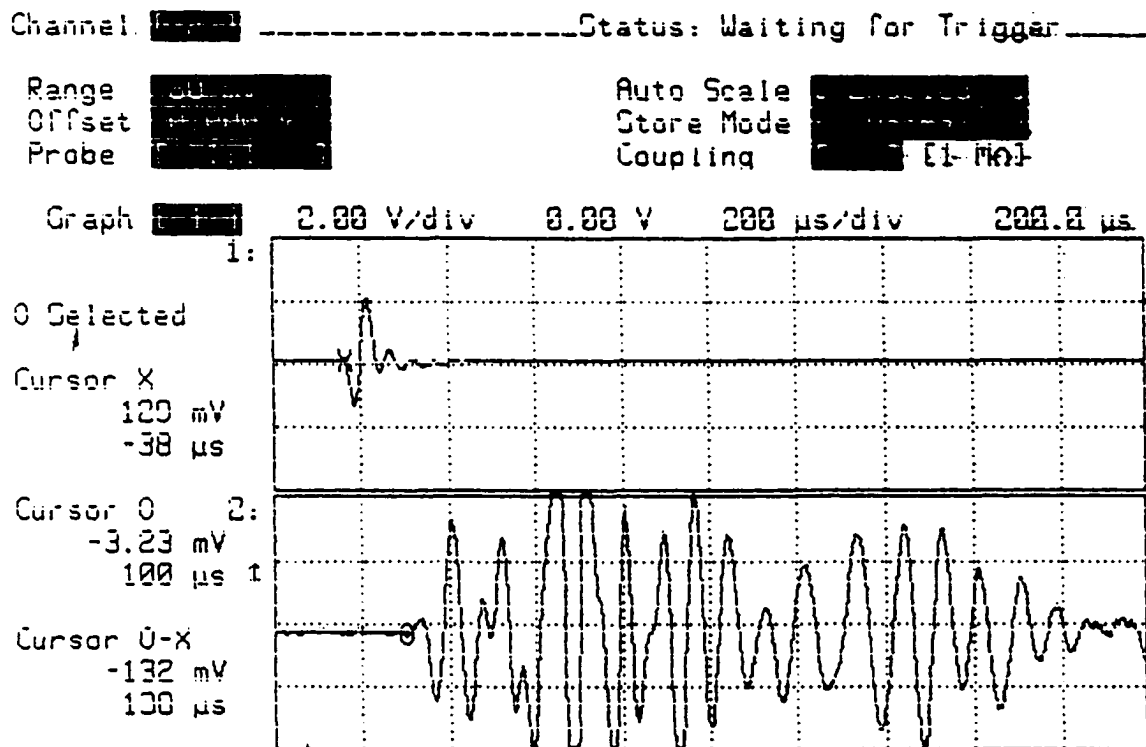


Figure D-11 Measurement of P-wave travel time in horizontal direction (V_{ph}) for MV specimen at $D_r=48.20\%$, $\sigma=40$ psi, $B=0$, input frequency (f) = 20 kHz

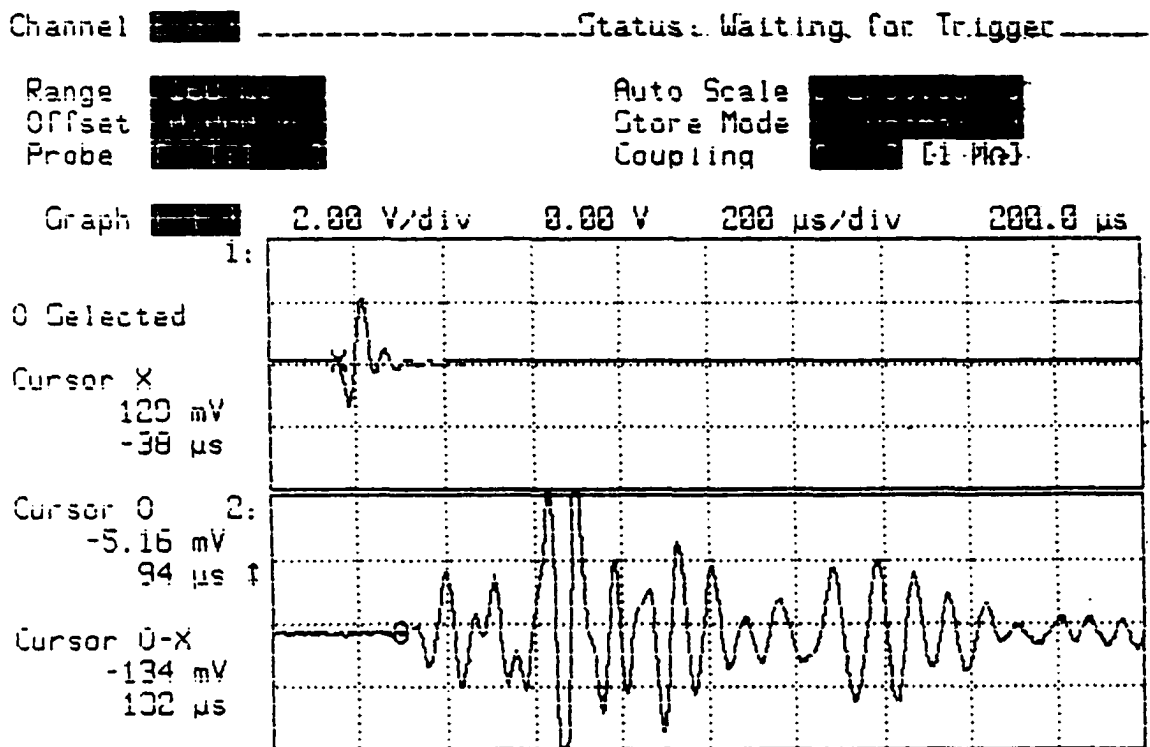


Figure D-12 Measurement of P-wave travel time in horizontal direction (V_{ph}) for MV specimen at $D_r=48.20\%$, $\sigma'_v=50$ psi, $B=0$, input frequency (f) = 20 kHz

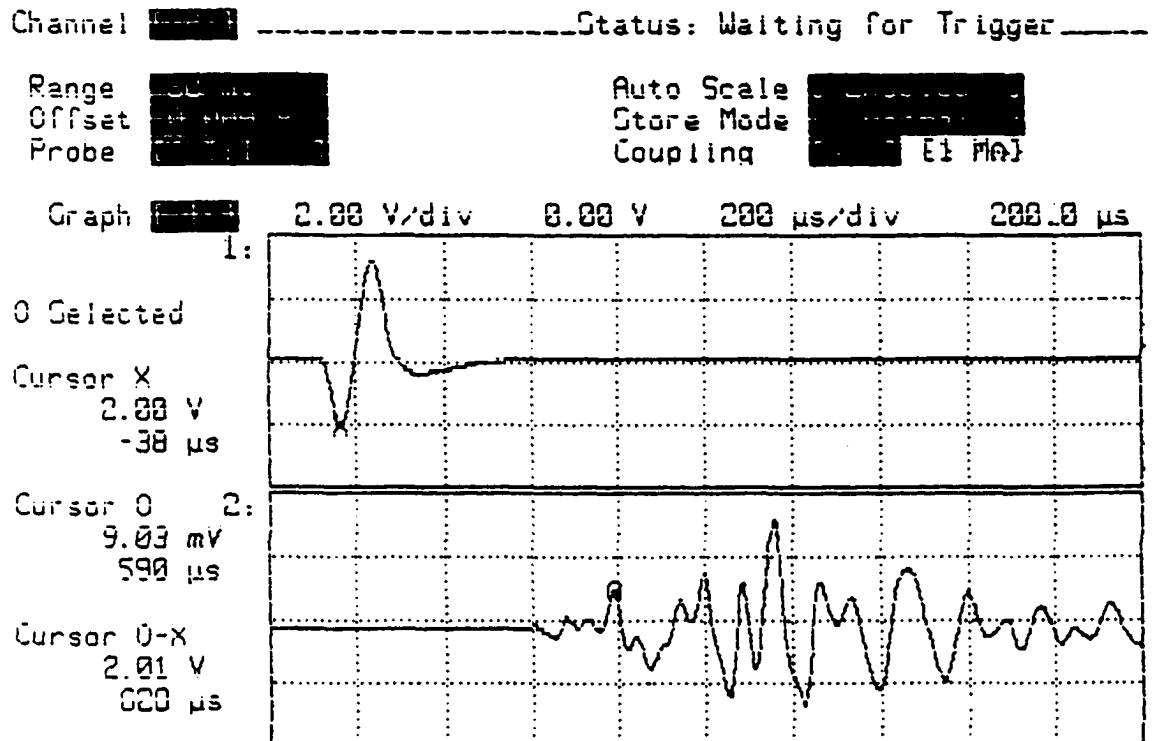


Figure D-13 Measurement of S-wave travel time in vertical direction (V_{sh}) for MV specimen at $D_r=48.20\%$, $\sigma'_v=10$ psi, $B=0$, input frequency (f) = 7 kHz

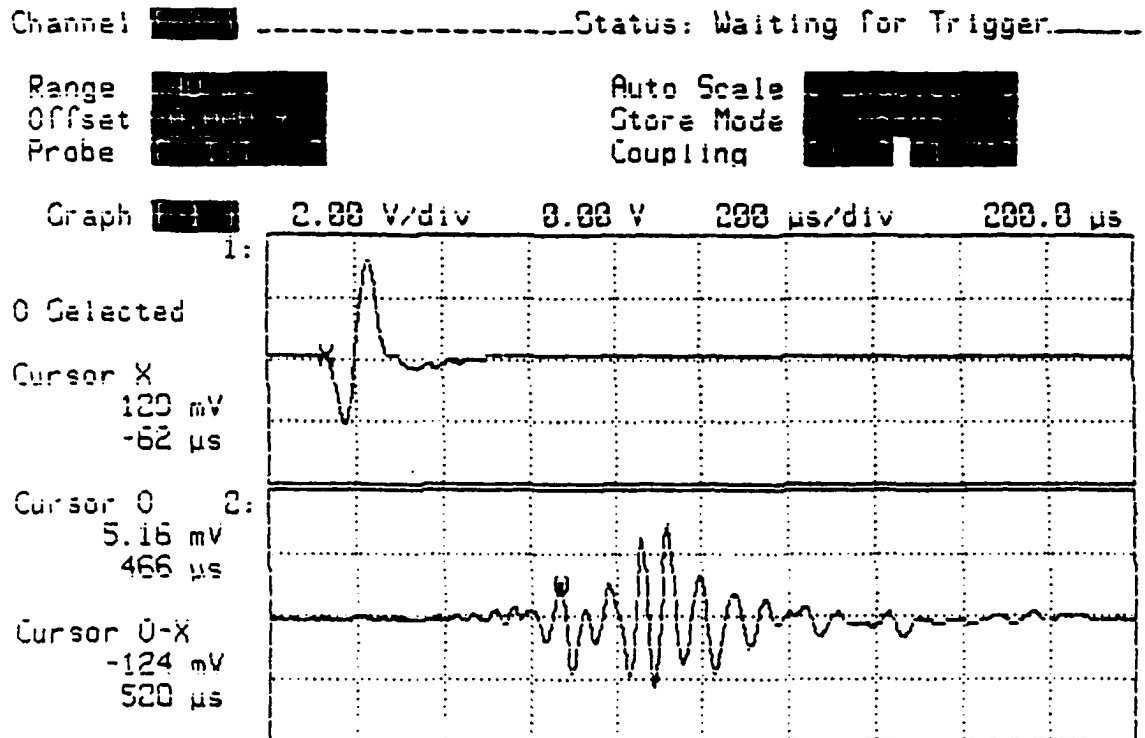


Figure D-14 Measurement of S-wave travel time in vertical direction (V_{sh}) for MV specimen at $D_r=48.20\%$, $\sigma' = 20$ psi, $B=0$, input frequency (f) = 9 kHz

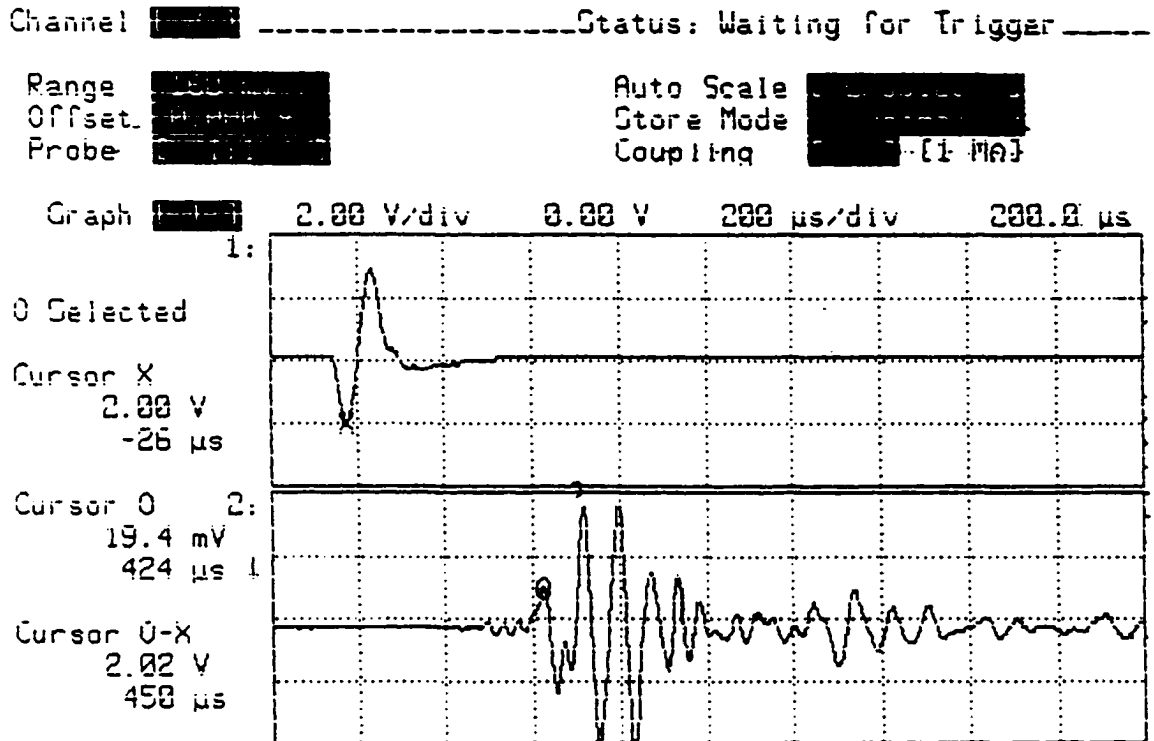


Figure D-15 Measurement of S-wave travel time in vertical direction (V_{sh}) for MV specimen at $D_r=48.20\%$, $\sigma'_v=30$ psi, $B=0$, input frequency (f) = 9 kHz

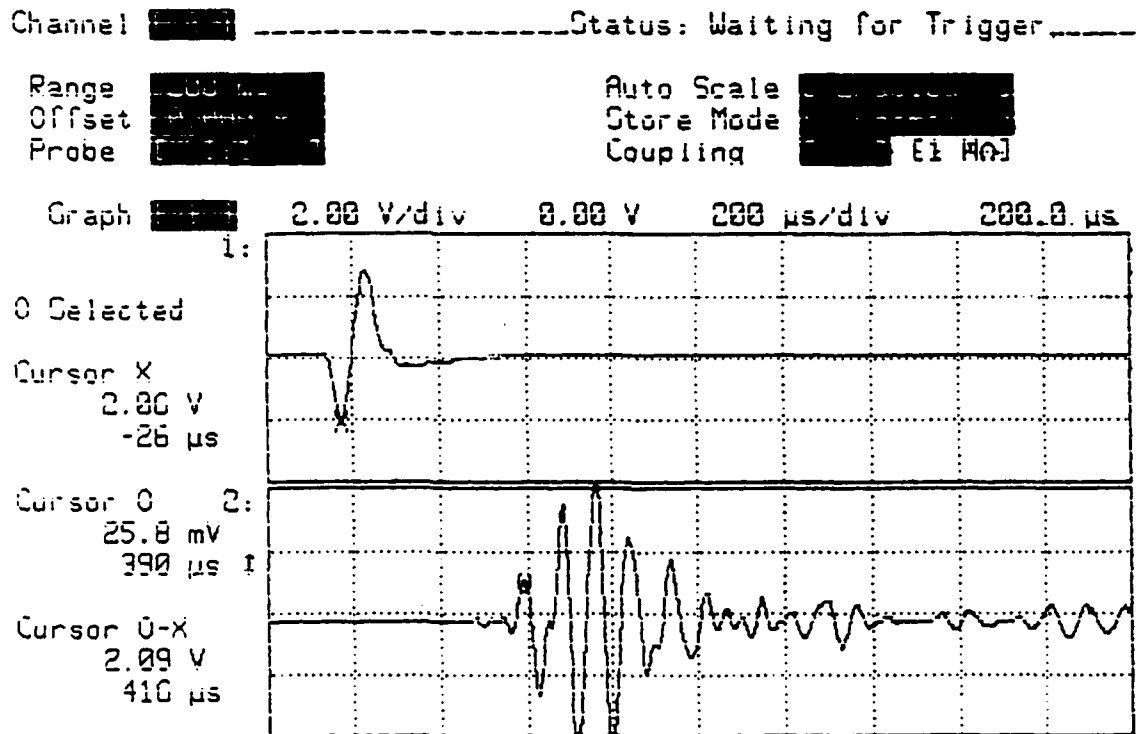


Figure D-16 Measurement of S-wave travel time in vertical direction (V_{sh}) for MV specimen at $D_r=48.20\%$, $\sigma=40$ psi, $B=0$, input frequency (f) = 9 kHz

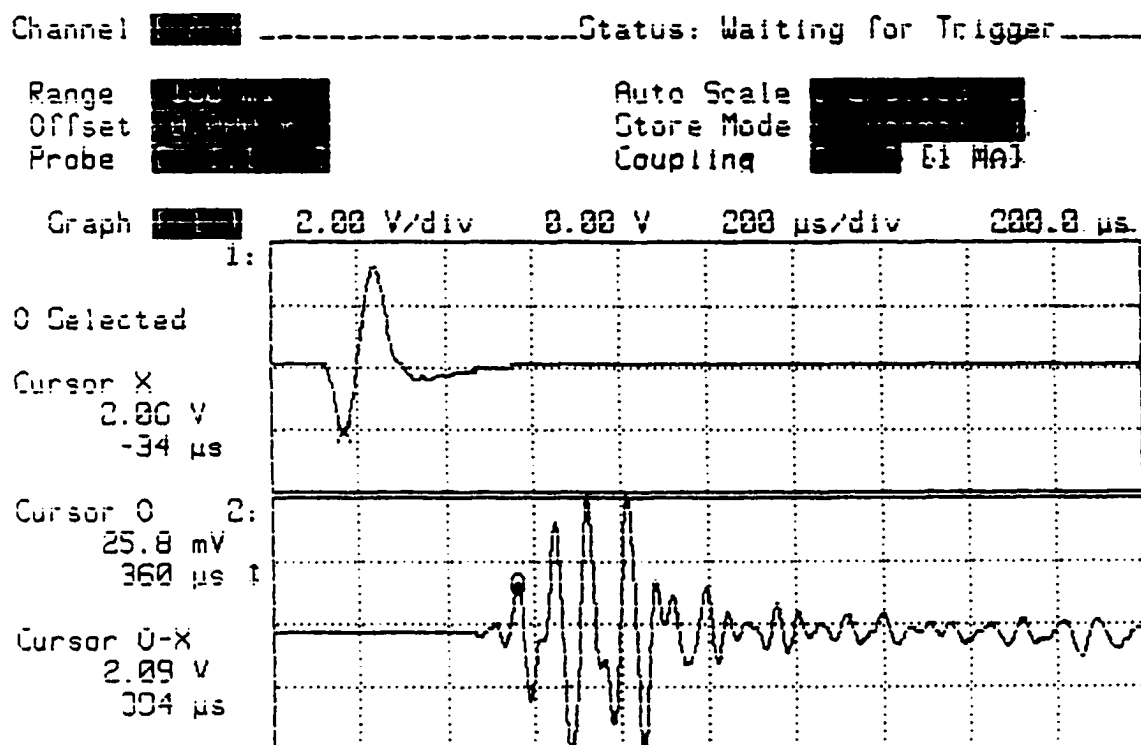


Figure D-17 Measurement of S-wave travel time in vertical direction (V_{sh}) for MV specimen at $D_r=48.20\%$, $\sigma'_v=50$ psi, $B=0$, input frequency (f) = 9 kHz

APPENDIX E

**ELASTIC WAVE MEASUREMENTS UNDER DIFFERENT
EFFECTIVE CONFINING PRESSURE AT SATURATED CONDITION**

Under different effective confining pressures (σ') in the range from 10 to 50 psi, P-wave velocities and S-wave velocities in vertical direction were measured after saturated the specimens were saturated.

Some wave records of P and S-wave arrival times are presented. All wave records here were obtained from the hard copies of the oscilloscope display.

Figure E-1 through E-7 show wave records for V_{p_v} under different effective stress at initially, $S=0\%$, and then $S=100\%$ for a MT specimen.

Figure E-8 through E-12 show wave records for V_{s_v} under different effective stress for a AP specimen at $S=100\%$

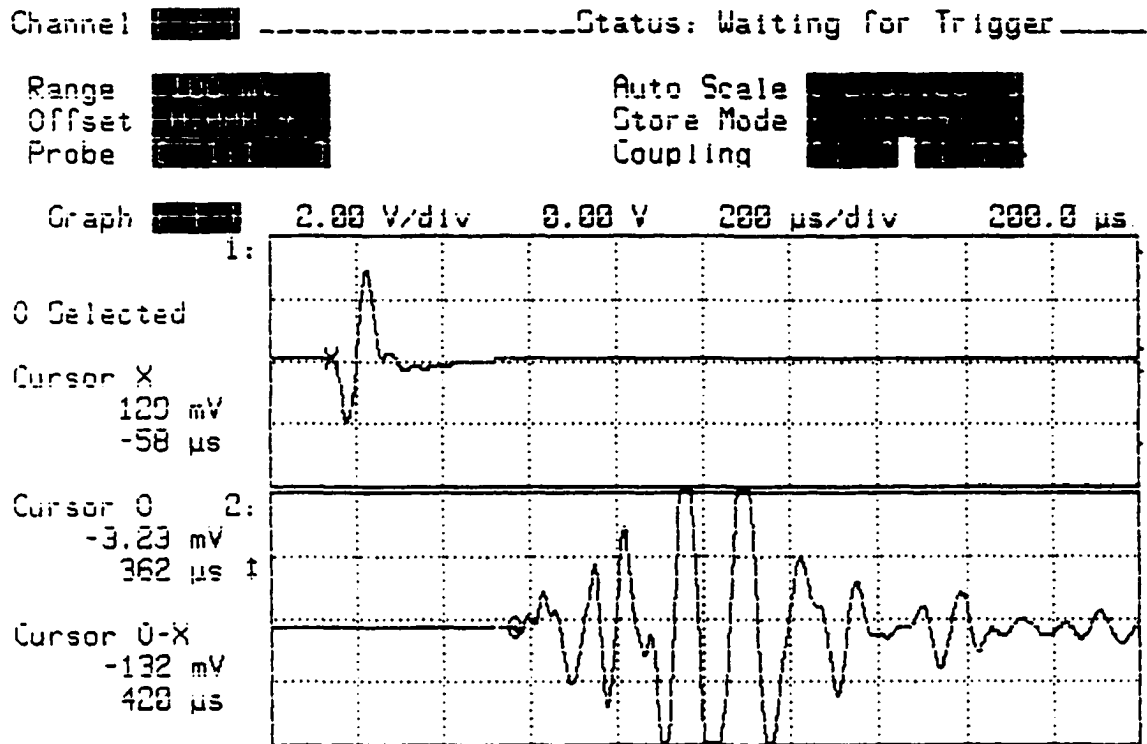


Figure E-1 Measurement of P-wave travel time in vertical direction (V_{pv}) for MT specimen at $D_r=49.2\%$, $\sigma'=10$ psi, $S=0\%$, input frequency (f) = 11.0 kHz

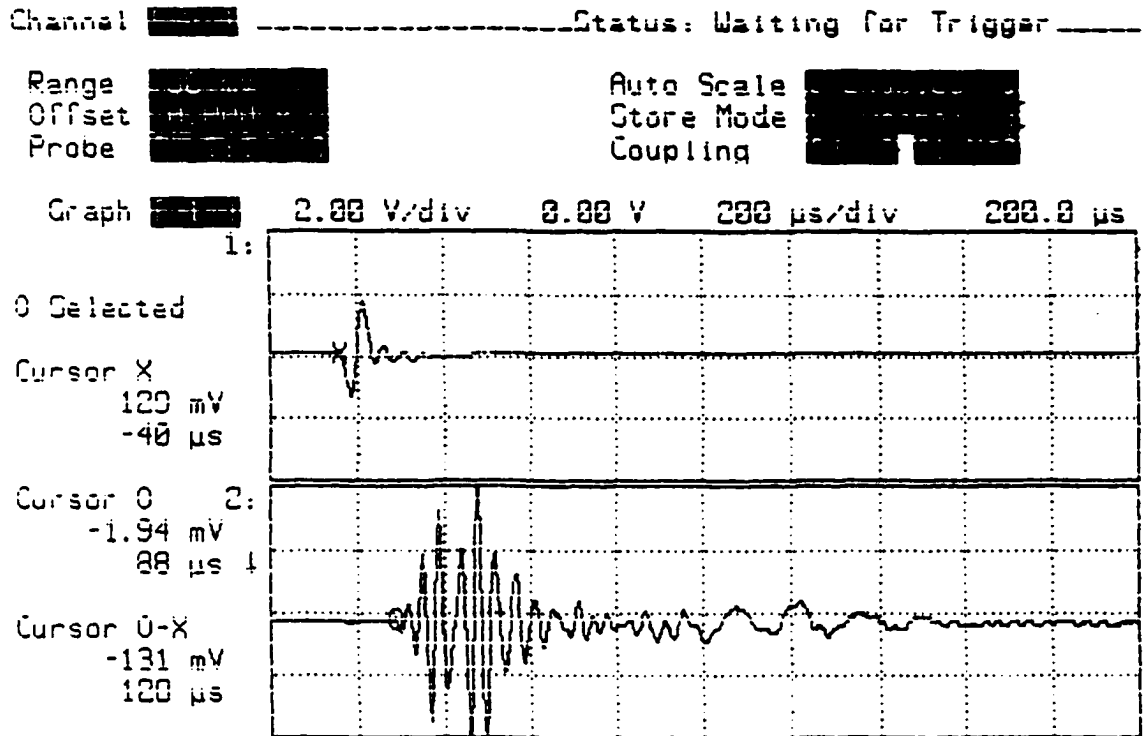


Figure E-2 Measurement of P-wave travel time in vertical direction (V_p) for MT specimen at $D_r=49.2\%$, $\sigma=10$ psi, $S=100\%$, input frequency (f) = 22.0 kHz

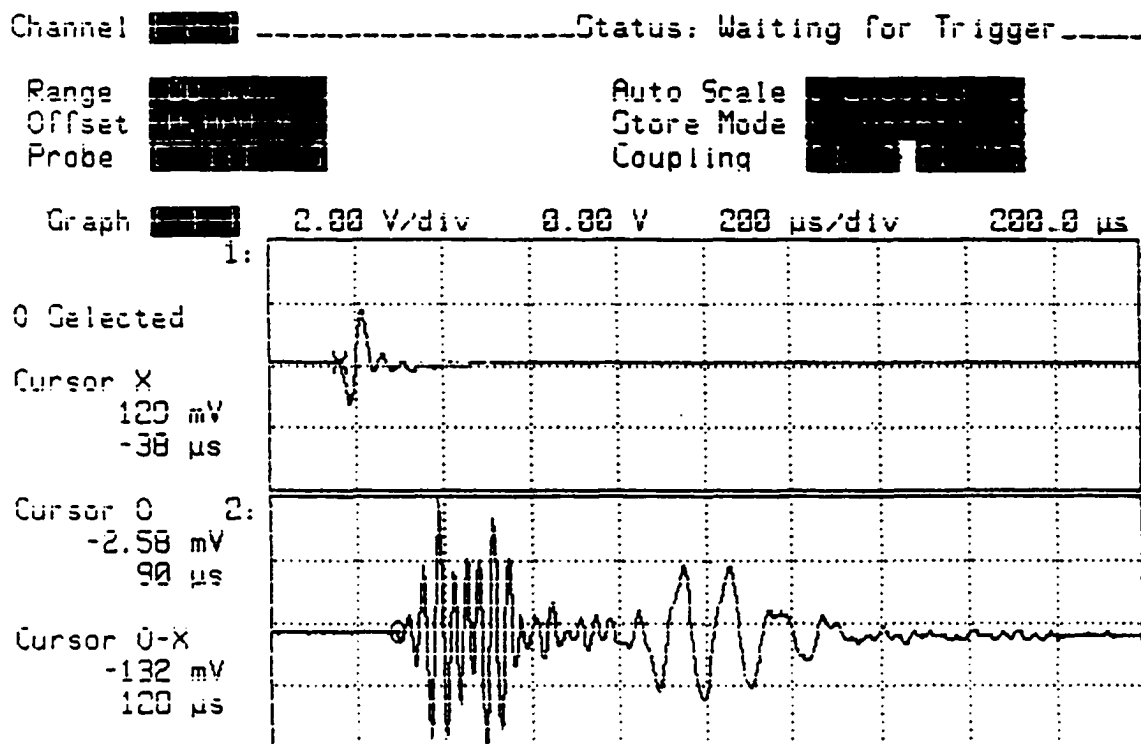


Figure E-3 Measurement of P-wave travel time in vertical direction (V_{pv}) for MT specimen at $D_r=49.2\%$, $\sigma'_v=20$ psi, $S=100\%$, input frequency (f) = 22.0 kHz

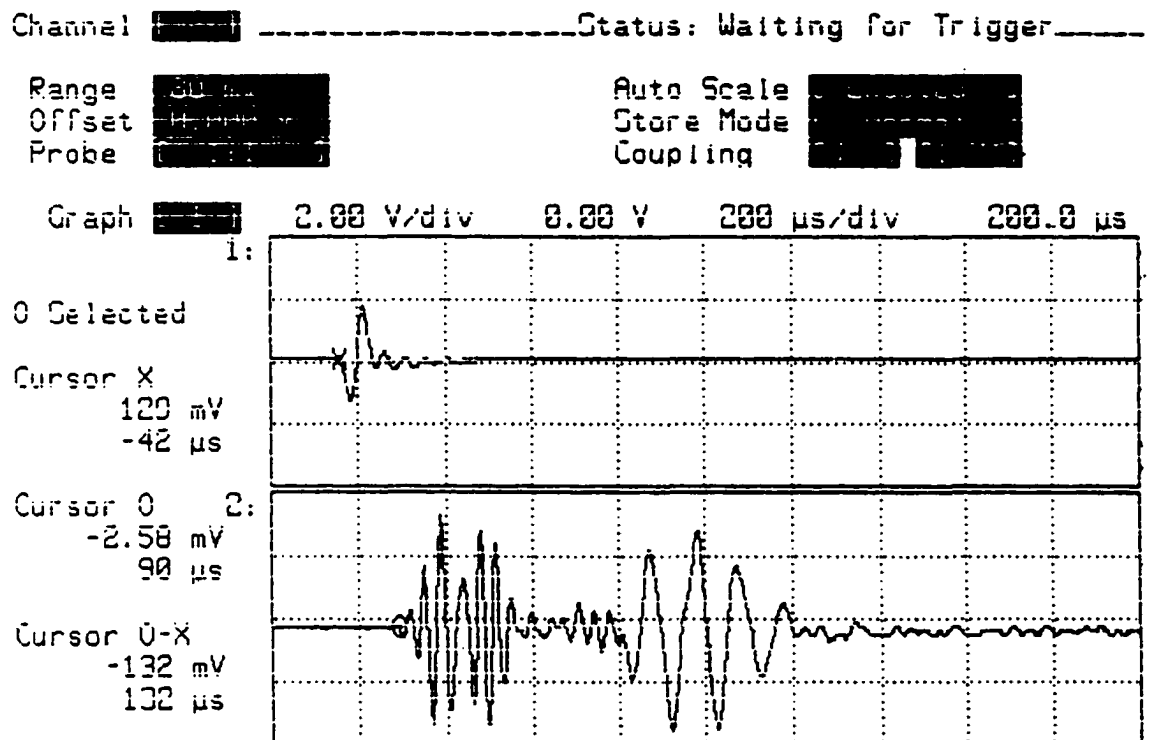


Figure E-4 Measurement of P-wave travel time in vertical direction (V_{pv}) for MT specimen at $D_r=49.2\%$, $\sigma=30$ psi, $S=100\%$, input frequency (f) = 22.0 kHz

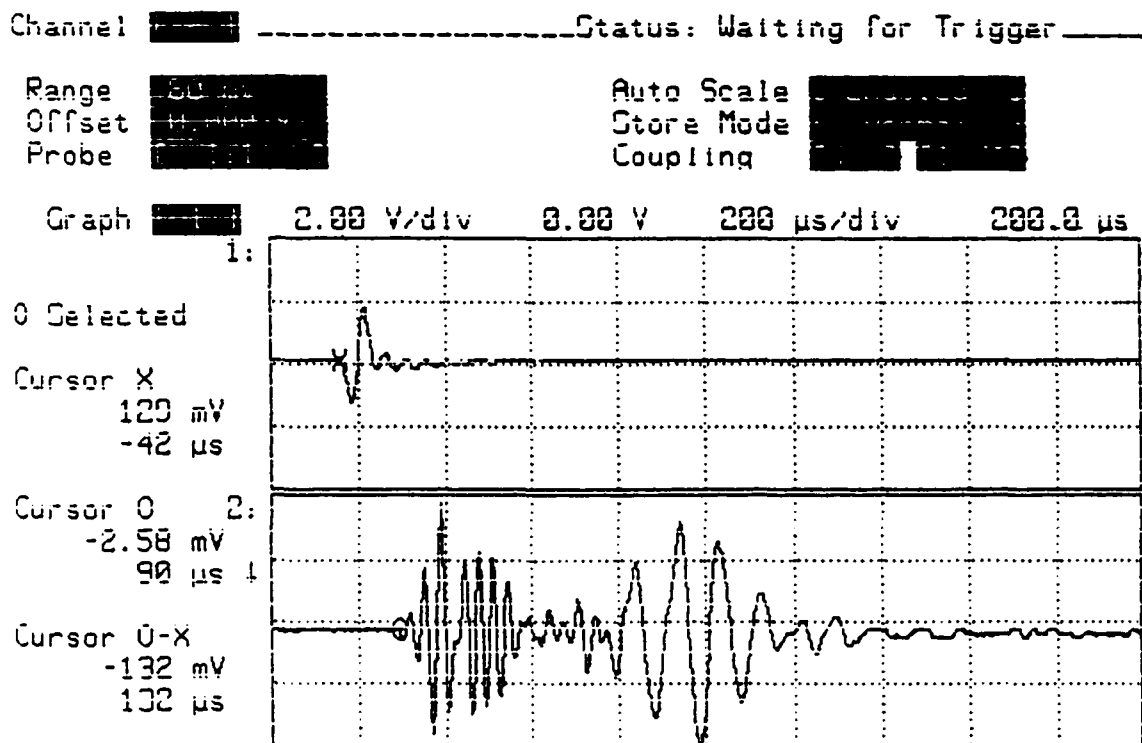


Figure E-5 Measurement of P-wave travel time in vertical direction (V_{pv}) for MT specimen at $D_r=49.2\%$, $\sigma=40$ psi, $S=100\%$, input frequency (f) = 22.0 kHz

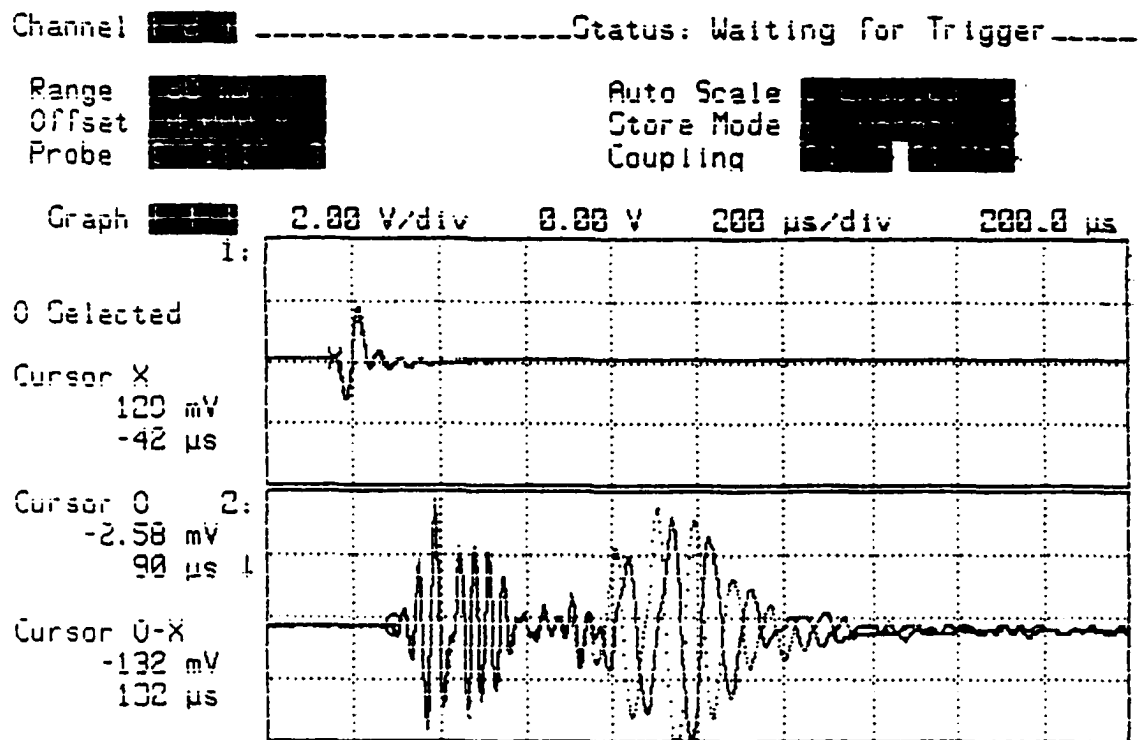


Figure E-6 Measurement of P-wave travel time in vertical direction (V_{pv}) for MT specimen at $D_r=49.2\%$, $\sigma=40-50$ psi, $S=100\%$, input frequency (f) = 22.0 kHz

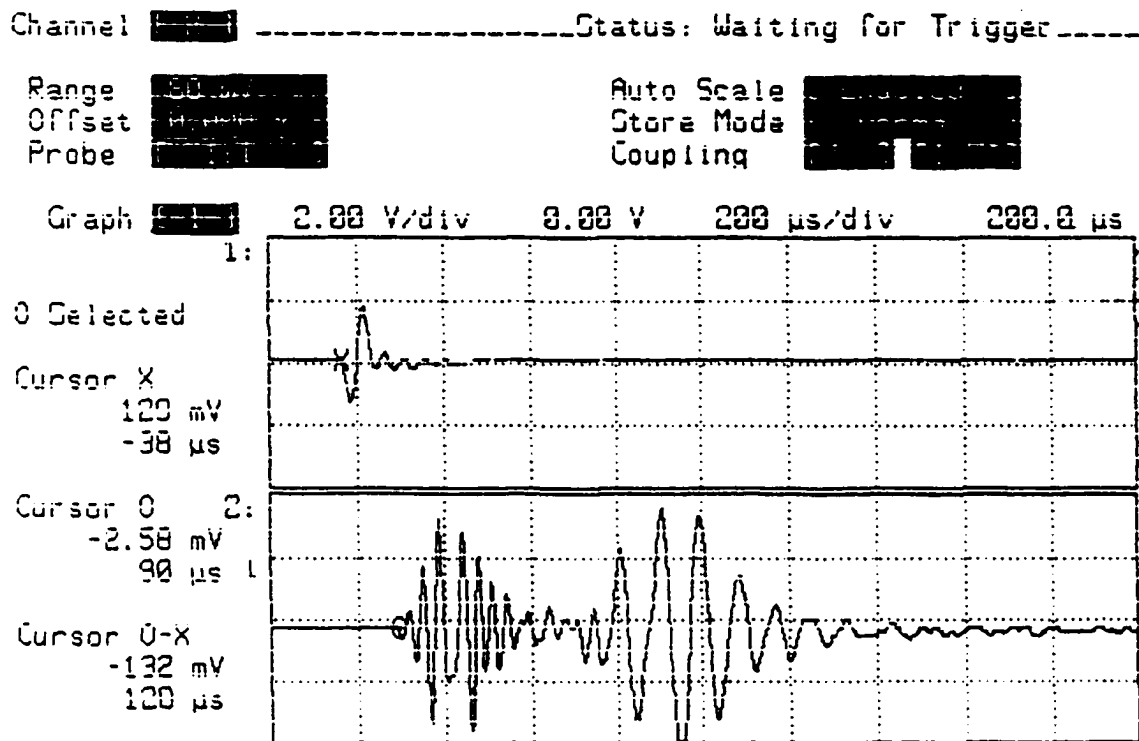


Figure E-7 Measurement of P-wave travel time in vertical direction (V_{pv}) for MT specimen at $D_r=49.2\%$, $\sigma=50$ psi, $S=100\%$, input frequency (f) = 22.0 kHz

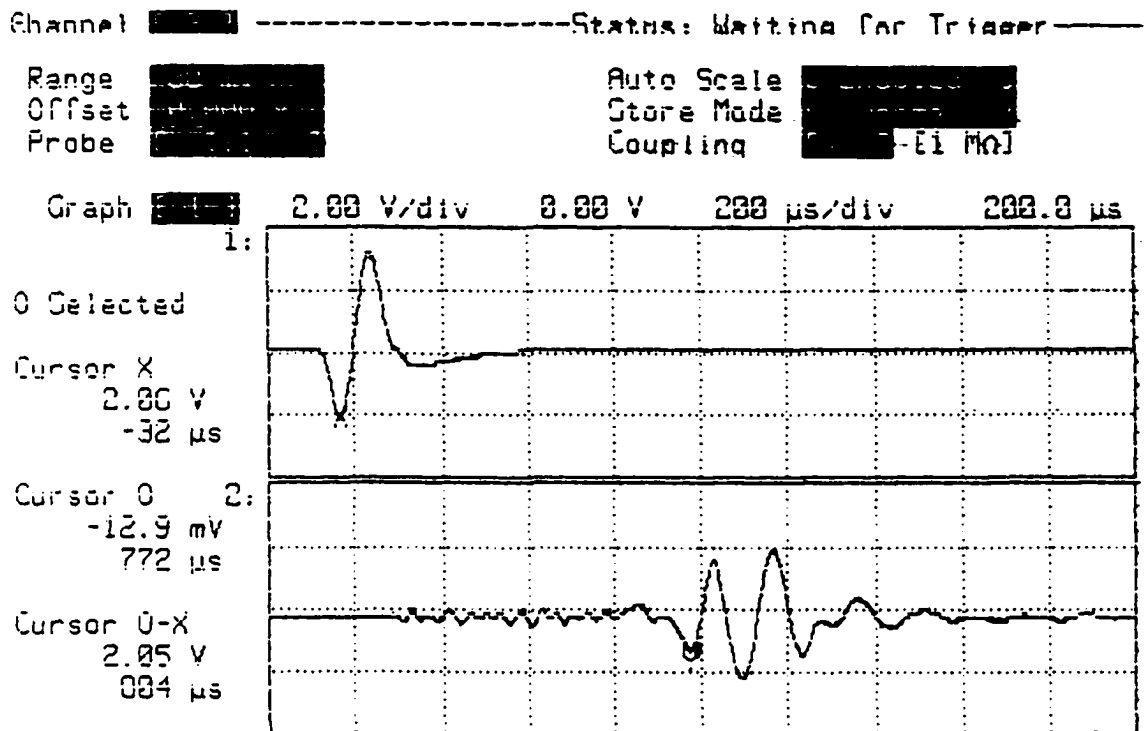


Figure E-8 Measurement of S-wave travel time in vertical direction (V_{Sh}) for AP specimen at $D_r=50.02\%$, $\sigma=10$ psi, $S=100\%$, input frequency (f) = 7 kHz

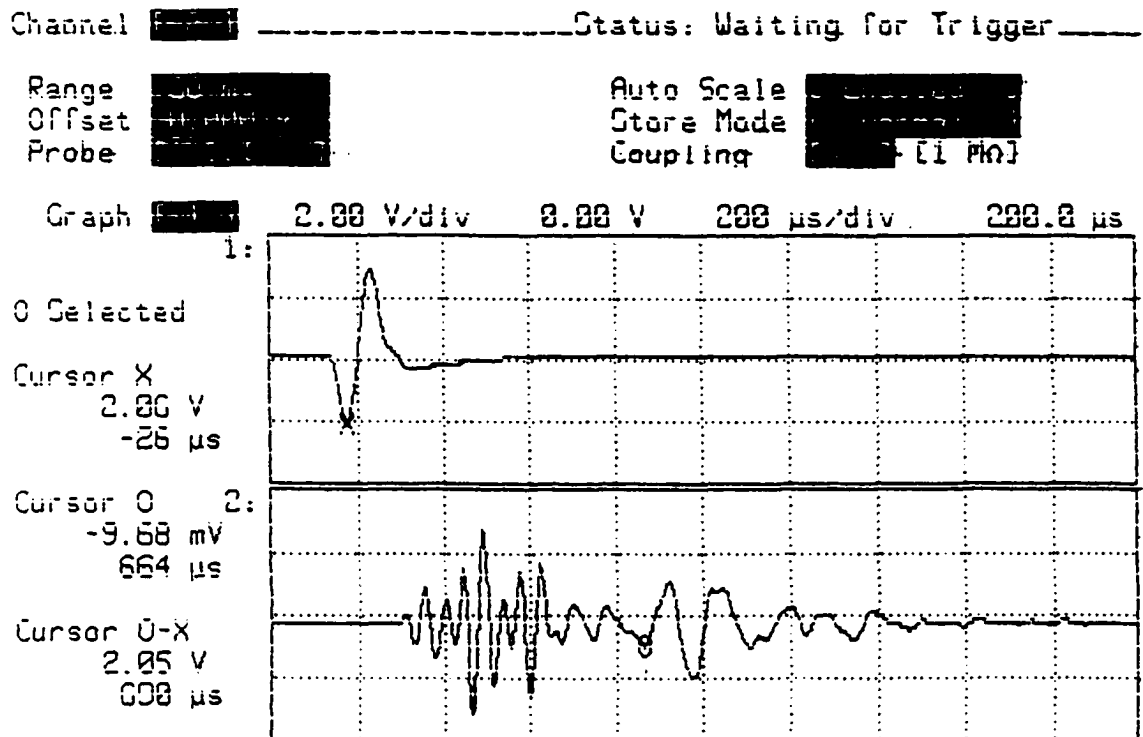


Figure E-9 Measurement of S-wave travel time in vertical direction (V_{sh}) for AP specimen at $D_r=50.02\%$, $\sigma'_v=20$ psi, $S=100\%$, input frequency (f) = 9 kHz

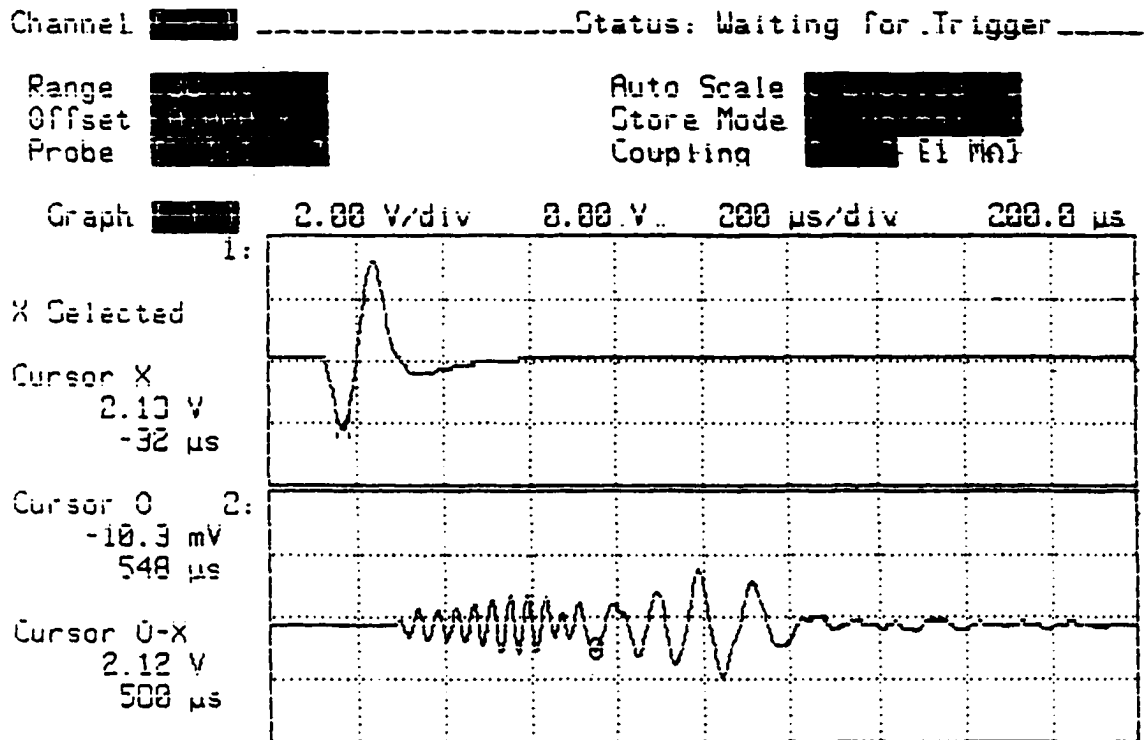


Figure E-10 Measurement of S-wave travel time in vertical direction (V_{sh}) for AP specimen at $D_r=50.02\%$, $\sigma=30$ psi, $S=100\%$, input frequency (f) = 9 kHz

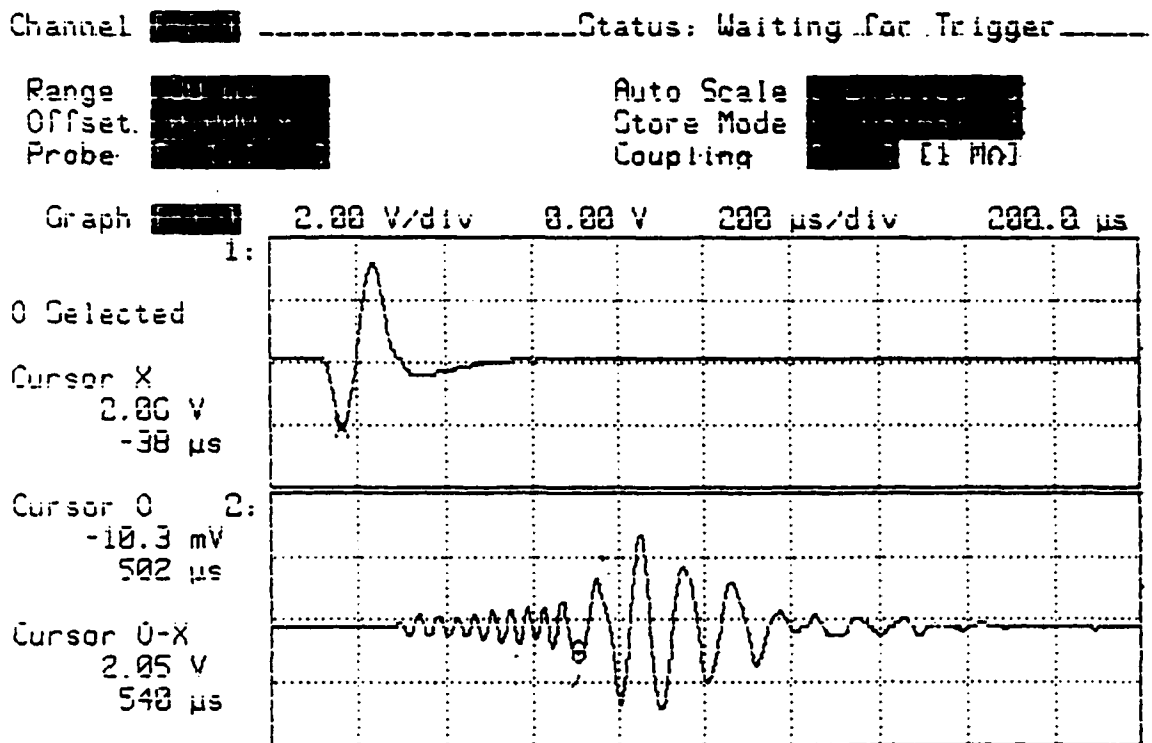


Figure E-11 Measurement of S-wave travel time in vertical direction (V_{sh}) for AP specimen at $D_r=50.02\%$, $\sigma'_c=40$ psi, $S=100\%$, input frequency (f) = 7 kHz

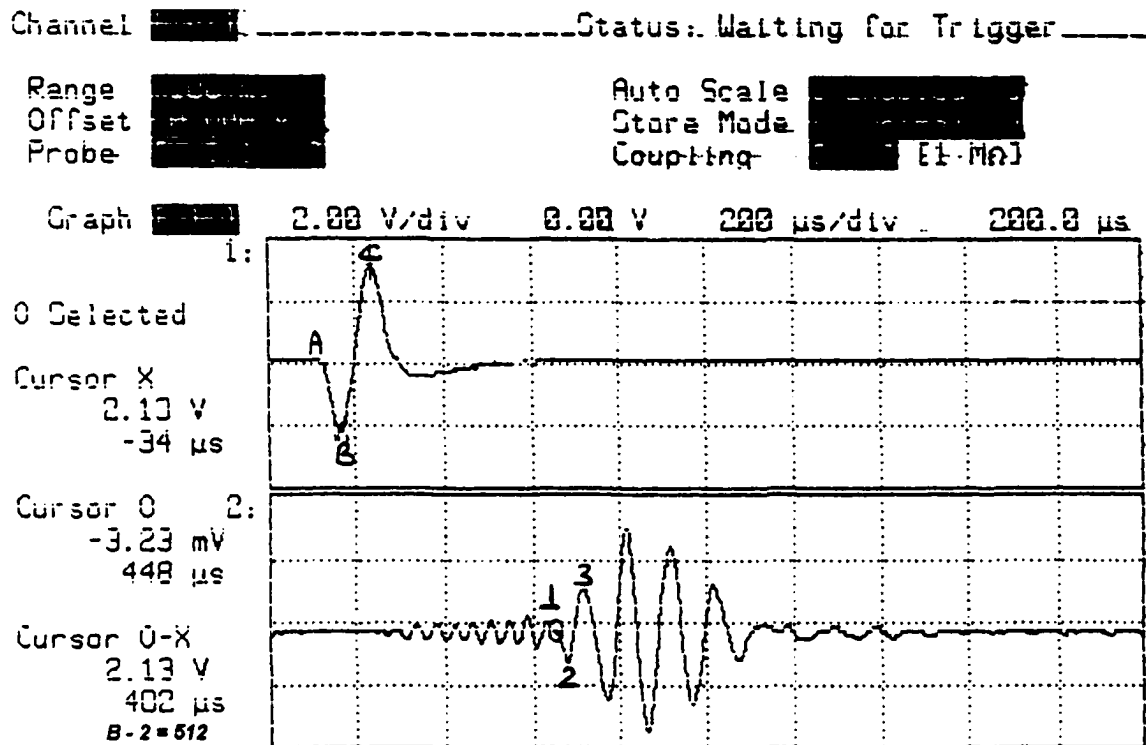


Figure E-12 Measurement of S-wave travel time in vertical direction (V_{Sh}) for AP specimen at $D_r=50.02\%$, $\sigma=50$ psi, $S=100\%$, input frequency (f) = 7 kHz

CURRICULUM VITA

for

Omer Faruk Capar**NAME: Omer Faruk Capar****DATE OF BIRTH: November 19, 1968****DEGREES:**

Doctor of Philosophy (Civil Engineering), Old Dominion University, Norfolk, VA, December 2000

Master of Science (Civil Engineering), Cukurova University, Adana, Turkey, 1992

Bachelor of Science (Civil Engineering), Cukurova University, Adana, Turkey, 1989

PROFESSIONAL CHRONOLOGY:

Department of Civil Engineering, Zonguldak Karaelmas University, Zonguldak Turkey

Research Assistant 1994 to Present

Department of Civil Engineering, Cukurova University, ADANA Turkey

Research and Teaching Assistant 1989 to 1994

MEMBERSHIP IN PROFESSIONAL SOCIETIES:

American Society of Civil Engineers

HONOR AND AWARDS:

Scholarship for Junior Faculty in "New" Universities (Turkish Higher Education Council Scholarships), May 1995 to May 1999.

TECHNICAL REPORTS:

Geotechnical Evaluation Report: Clayey Soil Samples for Antakya Waste Water Treatment Facility July 1992, Department of Civil Engineering, Cukurova University, Adana, Turkey.

Geotechnical Evaluation Report: BaYer Holding Multi-Family Apartment Complexes in Adana, April 1993, Department of Civil Engineering, Cukurova University, Adana, Turkey.

Geotechnical Evaluation Report: Tarsus-Mersin Police Department Headquarter Complex, July 1993, Department of Civil Engineering, Cukurova University, Adana, Turkey

Geotechnical Evaluation Report: Mersin S.S. Ilkevim Multi Apartment Complexes. July 1993, Department of Civil Engineering, Cukurova University, Adana Turkey.

Geotechnical Evaluation Report: Merta Joint-Stock Co. Pozteks Apartments, October 1993, Department of Civil Engineering, Cukurova University, ADANA Turkey.

Geotechnical Evaluation Report: A&Z Architecture, Multi-Family Housing Complexes January 1994, Department of Civil Engineering, Cukurova University, Adana, Turkey.

PUBLICATIONS:

TEKINSOY, M.A. and CAPAR, O. F., 1993, *Compaction of Well Graded Non-Plastic Silty and Sandy Gravels Symposium of Problems of Soil Mechanics in Earth Fill Dams*. Gumuldur-Izmir Turkey, 20-25 Sept. 1993, (pp. 461-475) in Turkish.

HAKTANIR, T. and CAPAR, O. .F., 1994, *Computer Package for Flood Frequency Analysis Comprising Recent Models*, 15th Anniversary proceedings. of Cukurova University, Engineering and Architecture Faculty, Adana, Turkey, April 1994, (pp. 37-42) in Turkish